Measurement of the ZZ production cross section and limits on anomalous neutral triple gauge couplings with the ATLAS detector

Nicholas Charles Edwards

School of Physics & Astronomy
College of Science & Engineering

Submitted in fulfilment of the requirements
for the degree of Doctor of Philosophy
at the University of Glasgow

July 2013

Abstract

This thesis presents measurements of the ZZ production cross section in proton-proton collisions at $\sqrt{s} = 7$ TeV and at $\sqrt{s} = 8$ TeV, using data recorded by the ATLAS experiment at the LHC in 2011 and 2012. Events are selected which are consistent with two Z bosons decaying to electrons or muons. The cross section is first measured in a fiducial phase-space corresponding closely to the detector acceptance. For the 7 TeV measurement, this phase-space is defined by requiring four electrons or muons with $p_{\mathrm{T}} > 7$ GeV and $|\eta| < 3.16$, with a minimum separation between any pair of leptons (electrons or muons) of $\Delta R = 0.2$. The leptons must form two opposite-sign same-flavour pairs, each with invariant mass $66 < m_{\ell^-\ell^+} < 116$ GeV. The fiducial cross section times branching ratio to four electrons or muons measured in a dataset corresponding to an integrated luminosity of 4.6 fb^{-1} is $25.2\,^{+3.3}_{-3.0}\,(\mathrm{stat})\,^{+1.2}_{-1.0}\,(\mathrm{syst})\,^{+1.1}_{-0.9}\,(\mathrm{lumi})$ fb. For the 8 TeV measurement, the fiducial phase-space is defined in the same way, except with the lepton pseudo-rapidity requirement tightened to $|\eta| < 2.7$. The fiducial cross section measured in a dataset corresponding to an integrated luminosity of 20 fb^{-1} is $20.8\,^{+1.3}_{-1.2}\,(\mathrm{stat})\,^{+1.0}_{-0.9}\,(\mathrm{syst})\,^{+0.6}_{-0.6}\,(\mathrm{lumi})$ fb. Additionally, a fiducial cross section allowing one of the Z bosons to be off shell is measured at $\sqrt{s} = 7$ TeV by relaxing the mass requirement on one of the lepton pairs to $m_{\ell^-\ell^+} > 20$ GeV. This is found to be $27.8\,^{+3.6}_{-3.4}\,(\mathrm{stat})\,^{+1.8}_{-1.6}\,(\mathrm{syst})\,^{+1.1}_{-1.0}\,(\mathrm{lumi})$ fb.

These results are then used to derive the total cross section for ZZ production with Z bosons in the mass range 66 GeV to 116 GeV, by correcting for the acceptance of the fiducial phase-space and the $Z \to \ell\ell$ branching fractions. The total cross section is measured to be $7.0\,^{+0.9}_{-0.8}\,(\mathrm{stat})\,^{+0.4}_{-0.3}\,(\mathrm{syst})\,^{+0.3}_{-0.2}\,(\mathrm{lumi})$ pb at $\sqrt{s} = 7$ TeV and $7.1\,^{+0.4}_{-0.4}\,(\mathrm{stat})\,^{+0.4}_{-0.3}\,(\mathrm{syst})\,^{+0.2}_{-0.2}\,(\mathrm{lumi})$ pb at $\sqrt{s} = 8$ TeV, which is consistent with the Standard Model expectation of $5.9\,^{+0.2}_{-0.2}$ pb at $\sqrt{s} = 7$ TeV and $7.2\,^{+0.3}_{-0.2}$ pb at $\sqrt{s} = 8$ TeV, calculated to next-to-leading order in QCD. The differential cross section in bins of three kinematic variables is also presented.

The differential event yield as a function of the transverse momentum of the highest transverse momentum Z boson is used to set limits on the strength of anomalous ZZZ and $ZZ\gamma$ neutral triple gauge boson couplings, which are forbidden in the Standard Model. The limits obtained with the $\sqrt{s} = 8$ TeV data are the most constraining to date.

Acknowledgements

I acknowledge and thank the Science and Technology Facilities Council (STFC) for their financial support over the last three and a half years, including support for a fantastic two years spent on Long Term Attachment at CERN.

Many thanks to my supervisor Aidan Robson for expert guidance and support throughout my PhD, particularly for pointing me onto the path of ZZ measurements in the first place. I believe it a very rewarding decision, even if Aidan's original motivation for encouraging me to work on ZZ physics unfortunately didn't come to pass! Thanks also to Tony Doyle for acting as my second supervisor. I would like to thank the other (current and former) Glasgow PhD students who put up with me and helped keep me sane: Big Mike, Donny, Will, Paul, Ginger Mike, Cristina, Gen, Alistair, and everyone else in the Glasgow PPE group for making it a very friendly environment to work in.

For my work on the SCT temperature monitoring I thank Saverio D'Auria for helping me get started, for exhaustive knowledge of all things SCT, and for letting me share his office for two years. Thank you also to Steve McMahon.

I am indebted to Shih-Chieh Hsu, for very enthusiastic support, guidance and constructive criticism in my initial work on ZZ, and also for having the confidence in me to appoint me as analysis contact for the preliminary 8 TeV measurement. I would also like to thank Kostas Kordas, Andrew Nelson, Advait Nagarkar, Joshua Moss, and the rest of the ZZ analysis group, who were all wonderful people to work with, even after multiple sleepless nights! Thank you to Vasiliki Kouskoura for helping me get started with the nTGC limit setting, and to Will Buttinger for many discussions regarding the limit setting procedure (amongst many other things ZZ related).

Thank you to all of the friends I made in Geneva, in particular the former residents of Rue de L'Athenee for many stimulating discussions on all aspects of particle physics, ATLAS politics, and much else besides!

I would like to give thanks to Cigdem Issever for encouraging me to do a PhD in the first place.

Finally, I of course have to thank my parents, Rod and Angie, for their unedning support. And lastly, but by no means least, thank you Kayleigh for putting up with me moaning and being stressed over the last few years!

Declaration

I declare that the results presented here are the product of my own work, unless explicit references are given in the text to the work of others. This thesis is the result of the research I carried out in the Experimental Particle Physics group in the School of Physics & Astronomy of the University of Glasgow between September 2009 and March 2013. It has not been submitted for any other degree at the University of Glasgow or any other institution.

Nicholas Charles Edwards

Author's Contributions

Due to the large size of modern particle physics experiments, results are produced in a very collaborative manner, and the work presented in this thesis relies on the work of many other members of the ATLAS collaboration. The main individual contributions of the author are outlined below:

- **Chapter 4, SCT Temperature Monitoring:** The SCT temperature monitoring study was carried out entirely by the author, under the guidance of Saverio D'Auria and Steve McMahon, and involved writing software using the existing Oracle database.

- **Chapter 6, Object and Event Selection:** The author played a leading role in the development and optimisation of the selection requirements, and produced the estimates of the selection efficiencies and systematics.

- **Chapter 7, Background Estimate:** The author contributed to the development of the data-driven background estimate method, in association with other members of the ATLAS ZZ working-group, and provided a cross-check of the final results (the results presented in the chapter being entirely the work of the author). The author produced the Monte Carlo based background estimates.

- **Chapter 8, Cross Section:** The author produced all results for this chapter.

- **Chapter 9, TGC Limits:** The After-Burner reweighting code and the TGC limit setting methodology were developed by other members of the ATLAS collaboration. The 7 TeV TGC limit results were initially produced by other members of the ZZ working-group, using inputs from the author on expected yields and systematics. The author subsequently cross-checked these results. For the 8 TeV limits, the author carried out the bin optimisation study and produced the limits.

Contents

List Of Figures 14

List Of Tables 17

Introduction 18

I Background 20

1 Theory 21

1.1 The Standard Model . . . 21

1.1.1 Fundamental Fermions . . . 21

1.1.2 Fundamental Forces and the Bosons . . . 22

1.1.3 The Electroweak Theory . . . 24

1.1.4 Electroweak Symmetry Breaking . . . 28

1.1.5 Quantum Chromodynamics . . . 30

1.2 Interactions in Proton-Proton Collisions . . . 31

1.3 Monte-Carlo Simulation . . . 33

1.3.1 Monte Carlo Generators . . . 34

2 ZZ Production 37

2.1 ZZ Production at Hadron Colliders . . . 37

2.1.1 ZZ Decay Modes . . . 38

2.1.2 Cross Section Definition . . . 39

2.1.3 Theoretical Cross Section Predictions . . . 41

2.2 Kinematic Distributions . . . 43

2.2.1 Comparison of $ZZ \to \ell^-\ell^+\ell^-\ell^+$ at 7 TeV and 8 TeV . . . 43

2.2.2 Comparison of $gg \to ZZ$ and $qq \to ZZ$ . . . 46

2.2.3 Z Mass Distributions . . . 46

2.2.4 Generator Comparisons for $ZZ \to \ell^-\ell^+\ell^-\ell^+$ . . . 46

2.3 Nominal Signal Sample . . . 52

2.4 Anomalous Triple Gauge Couplings . . . 53

2.4.1 Origin of nTGCs . . . 54

2.4.2 Signatures at Hadron Colliders . . . 55

2.5 Previous Experimental Results 56

II Experimental Description 61

3 The ATLAS Detector at the LHC 62
3.1 The Large Hadron Collider 62
3.1.1 Machine Design 62
3.1.2 LHC Operation in 2011 and 2012 64
3.2 The ATLAS Detector 66
3.2.1 ATLAS Co-ordinate System 67
3.2.2 Inner Detector 68
3.2.3 Calorimetry 72
3.2.4 Forward Calorimeter 75
3.2.5 Muon Spectrometer 76
3.3 Trigger 77
3.4 Detector Simulation 79
3.5 Luminosity Measurement 79
3.6 Data Samples 81

4 SCT Temperature Monitoring 82
4.1 Introduction 82
4.1.1 Effects of Radiation Damage on Semiconductor Detectors . 82
4.1.2 SCT Module Design 83
4.1.3 The Inner Detector Cooling System 84
4.2 Methodology 85
4.3 Monitoring Variables 86
4.3.1 Front-Back Temperature Difference - ΔT 86
4.3.2 Difference In Temperature To Local Average - T_{diff} 88
4.4 Time Evolution of Monitoring Variables 91
4.4.1 Number of Problem Modules 91
4.5 Behaviour of Problematic Modules 92
4.6 Long Term Trends in Monitoring Variables 94
4.7 Conclusions 97

5 Particle Reconstruction 98
5.1 Tracking 99
5.1.1 Inside-Out Tracking 100

5.1.2 Outside-In Tracking . . . 101
5.2 Vertex Finding . . . 101
5.3 Electron Reconstruction and Identification . . . 102
5.3.1 Electron Triggers . . . 102
5.3.2 Electron Reconstruction . . . 103
5.3.3 Electron Identification . . . 110
5.4 Muon Reconstruction and Identification . . . 121
5.4.1 Muon triggers . . . 121
5.4.2 Reconstruction and Identification . . . 122
5.5 Jet Reconstruction . . . 129

III Analysis 131

6 Object and Event Selection 132
6.1 Electron Selection . . . 132
6.1.1 Central Electron Selection . . . 132
6.1.2 Forward Electron Selection . . . 135
6.1.3 Electron Distributions . . . 136
6.2 Muon Selection . . . 138
6.2.1 Central Muon Selection . . . 138
6.2.2 Forward Muon Selection . . . 140
6.2.3 Calorimeter Tagged Muon Selection . . . 142
6.2.4 Muon Distributions . . . 142
6.3 Trigger Selection . . . 144
6.3.1 Trigger Efficiencies . . . 145
6.4 Dilepton Control Plots . . . 146
6.5 ZZ Event Selection . . . 152
6.5.1 Z Candidate Definitions . . . 152
6.5.2 Event Selection Requirements . . . 152
6.6 Selection Efficiencies . . . 154
6.6.1 Mis-pairing Rates . . . 154
6.6.2 Effect of Minimum ΔR Requirement . . . 156
6.6.3 Reconstruction Acceptance C_{ZZ} . . . 156
6.6.4 Comparison of Reconstruction Acceptances at 7 TeV and 8 TeV . . . 161
6.6.5 Contribution from $ZZ \to \tau\tau\ell\ell$ and $ZZ \to \tau\tau\tau\tau$ . . . 161

6.6.6 Contribution from $H \to ZZ \to \ell^-\ell^+\ell^-\ell^+$ 162
6.7 Systematic Uncertainties 164
6.7.1 Sources of Systematic Uncertainty 164
6.7.2 Estimates of Systematic Uncertainties on C_{ZZ} 169
6.7.3 Estimates of Systematic Uncertainties on Expected Signal 169

7 Background Estimate 173
7.1 Monte Carlo Background Estimates 174
7.2 Data Driven Background Estimates 178
7.2.1 Methodology 178
7.2.2 Lepton-Like-Jet Definitions 179
7.2.3 Fake-Factor Measurement 180
7.2.4 Statistical and Systematic Uncertainties 183
7.2.5 Monte Carlo Closure Test 184
7.2.6 Results 184
7.2.7 Cross-Check with Same-Sign Events 185
7.3 Background Shape 195
7.4 Final Background Estimate 195

8 Observed Events and Cross Section Measurement 197
8.1 Observed Events 197
8.2 Kinematic Distributions 199
8.3 Cross Section Measurement 207
8.3.1 Fiducial Cross Section 207
8.3.2 Total Cross Section 208
8.4 Unfolded Kinematic Distributions 213

9 Limits on Anomalous Neutral Triple Gauge Couplings 217
9.1 Limit Setting Procedure 217
9.1.1 Matrix Element Reweighting 218
9.1.2 Validation of Reweighting Procedure 220
9.1.3 Yield Coefficients 220
9.1.4 Limit Setting 222
9.2 Bin Optimisation 226
9.3 Robustness of Limits 230
9.4 Expected and Observed Limits 230

10 Conclusions 236

Bibliography **239**

Appendix **251**

A Additional Material for nTGC Limits **251**

A.1 Robustness of nTGC Limits 251

List of Figures

1.1 Illustration of a proton-proton collision. 31

2.1 Leading order Feynman diagrams for ZZ production in proton-proton collisions. 38
2.2 Feynman diagrams for $gg \to ZZ$. 38
2.3 Comparison of generator level distributions, normalised to unit area, for $ZZ \to \ell^-\ell^+\ell^-\ell^+$ at $\sqrt{s} = 7$ TeV and $\sqrt{s} = 8$ TeV. 44
2.4 Comparison of generator level distributions, normalised to unit area, for $ZZ^* \to \ell^-\ell^+\ell^-\ell^+$ at $\sqrt{s} = 7$ TeV and $\sqrt{s} = 8$ TeV. . . . 45
2.5 Comparison of generator level distributions, normalised to unit area, for $ZZ \to \ell^-\ell^+\ell^-\ell^+$ proceeding via qq and gg interactions. . 47
2.6 Z boson invariant mass distributions in $ZZ \to \ell^-\ell^+\ell^-\ell^+$ events at 7 TeV after applying the lepton kinematic requirements. 48
2.7 Comparison of generator level distributions, normalised to unit area, for $qq \to ZZ \to e^-e^+\mu^-\mu^+$ as produced by different generators. 49
2.8 Comparison of generator level m_Z distributions, normalised to unit area, for $qq \to ZZ \to e^-e^+\mu^-\mu^+$ as produced by different generators. 50
2.9 Generator level m_Z distributions, comparing the distributions obtained from Sherpa using two different models for QED radiation. 51
2.10 Production of a ZZV vertex through a heavy fermion loop. . . . 55
2.11 $m(ZZ)$ and p_{T} of the leading Z boson in Standard Model $ZZ \to \ell^-\ell^+\ell^-\ell^+$ decays, as well as $ZZ \to \ell^-\ell^+\ell^-\ell^+$ decays in four samples generated with anomalous nTGCs included in the simulation. 56
2.12 Measurements of the ZZ production cross section in e^+e^- collisions at LEP as a function of centre of mass energy $\sqrt{s}$. 57
2.13 Negative log-likelihood curves for nTGC couplings from the four LEP experiments and their combination. 58

3.1 Peak instantaneous luminosity delivered by the LHC per run as a function of time from 2010 to 2012. 65
3.2 Cumulative integrated luminosity as a function of time in 2011 and 2012. 65

3.3 Cut-away view of the ATLAS detector. 68
3.4 Cut-away view of the inner detector. 69
3.5 Plan view of a quarter section of the inner detector showing the positions and pseudo-rapidity coverage of the various subdetectors. 70
3.6 Photograph of an SCT barrel module. 71
3.7 Cut-away view of the ATLAS calorimeter system. 73
3.8 Diagram of the ATLAS liquid argon calorimeter, showing the accordion structure and the different granularity in the different layers. 75
3.9 Cut away view showing the various components of the ATLAS muon spectrometer. 76
3.10 An overview of the ATLAS trigger and DAQ system. 78

4.1 Diagrams of SCT barrel and endcap modules. 83
4.2 Schematic of the SCT evaporative cooling system. 85
4.3 ΔT distributions for the SCT Barrels for 01:20 22/9/2012 to 01:20 23/9/2012. 87
4.4 T_{diff} distributions for the SCT barrel and endcaps for 01:20 22/9/2012 to 01:20 23/9/2012 89
4.5 Problem modules on barrel 5 in April 2010. 91
4.6 The number of 'problematic' modules with large ΔT and T_{diff} per day as a function of time between 20/01/2010 to 16/10/2012. . . 92
4.7 The temperature difference between the front and back of the module (ΔT) for barrel module Q3/B6/L126/I/P29/A5 and barrel module Q3/B6/L126/O/P30/C6 as a function of time between 20/1/2010 to 18/7/2010. 93
4.8 The difference in temperature between the module and the average temperature of modules on the same cooling structure (T_{diff}) as a function of time for module Q2/B5/L102/I/P24/C3 and for module Q4/ECA/D4/L160/RO/07 between 20/1/2010 and 18/7/2010. . 94
4.9 The width and mean of the module ΔT distribution as a function of time. 95
4.10 The mean and width of the module temperature distribution as a function of time. 96
4.11 The width of the T_{diff} distribution as a function of time. 96

5.1 Schematic view of the progression of different types of particle through the ATLAS detector. 99

5.2 Distribution of the inner detector material for each sub-detector as a function of the pseudorapidity. 105
5.3 Distribution of the simulated transverse impact parameter significance for GSF and standard electrons from Z-boson decays. . . . 107
5.4 Electron reconstruction efficiency in 2011 and 2012 as a function of the cluster η and the cluster E_{T}. 109
5.5 Electron energy-scale correction factor α derived from fits to $Z \to ee$. 111
5.6 Di-electron mass distribution after applying the energy scale calibration. 112
5.7 Distributions of electron identification variables for electrons and hadrons with $|\eta| < 1.47$: R_{had}, R_{η}. $w_{\eta 2}$, E_{ratio}, w_{stot}, f_3 117
5.8 Distributions of electron identification variables for electrons and hadrons with $|\eta| < 1.47$: $\Delta\eta$, $\Delta\phi$, d_0, E/p, f_3 118
5.9 Distributions of forward electron identification variables for electrons and hadrons: $\lambda_{\mathrm{centre}}$, $\langle\lambda^2\rangle$, $\langle r^2\rangle$, f_{max}, Normalised longitudinal moment, Normalised lateral moment 119
5.10 Electron identification efficiency in 2011 and 2012 as a function of the number of reconstructed primary vertices in the event. 120
5.11 Efficiency of the `Loose++` identification requirements as a function of the cluster transverse energy. 120
5.12 Cross sectional view of the muon trigger chambers. 122
5.13 Muon reconstruction efficiency in 2011 as a function of the pseudorapidity and the transverse momentum of the muon. 126
5.14 Di-muon mass resolutions for muon tracks in different detector subsystems. 128

6.1 Distributions of relative track and calorimeter isolation, $d_0/\sigma(d_0)$ and z_0 for additional electron candidates in events containing a dilepton pair with mass $66 < m_{\ell^-\ell^+} < 116$ GeV in 7 TeV data. . . 137
6.2 Fraction of forward muons which are Combined muons as a function of η 141
6.3 Distributions of relative track and calorimeter isolation, $d_0/\sigma(d_0)$ and z_0 for additional muon candidates in events containing a dilepton pair with mass $66 < m_{\ell^-\ell^+} < 116$ GeV in 7 TeV data. 144
6.4 Dilepton invariant mass and transverse momentum in the 7 TeV data. 148

6.5 Dilepton invariant mass and transverse momentum in the 8 TeV data. 149
6.6 Lepton kinematic distributions for di-lepton events in the 7 TeV data. 150
6.7 Lepton kinematic distributions for di-lepton events in the 8 TeV data. 151
6.8 Effect of the $\Delta R < 0.2$ requirement on sensitivity to boosted four-lepton systems. 163
6.9 Efficiency-correction scale-factors for the d_0 significance, $z_0 \cdot sin(\theta)$ and track isolation cuts for electrons and muons in the 8 TeV data, as a function p_T of the lepton. 166

7.1 p_{T} and η distributions for selected electrons L and lepton-like-electrons J in the Z-tag sample for 7 TeV data. 182
7.2 p_{T} and η distributions for selected electrons L and electron-like-jets J in the Z-tag sample for 8 TeV data. 183
7.3 p_{T} and η distributions for selected muons L and muons-like-jets J in the Z-tag sample for 7 TeV data. 190
7.4 p_{T} and η distributions for selected muons L and muon-like-jets J in the Z-tag sample for 8 TeV data. 191
7.5 Electron Fake-Factors as a function of p_{T} and η for 7 TeV data. . 192
7.6 Electron Fake-Factors as a function of p_{T} and η for 8 TeV data. . 192
7.7 Muon Fake-Factors as a function of p_{T} and η for 7 TeV data. . . . 193
7.8 Muon Fake-Factors as a function of p_{T} and η for 8 TeV data. . . . 194

8.1 Mass of the leading lepton pair versus the mass of the sub-leading lepton pair for candidate ZZ events in the 7 TeV data. 200
8.2 Mass of the leading lepton pair versus the mass of the sub-leading lepton pair for candidate ZZ events in the 8 TeV data. 201
8.3 Transverse momentum of lepton pairs versus the opening angle between the leptons forming the pair, for events passing the ZZ^* selection in 7 TeV data. 202
8.4 Invariant masses of the leading and subleading lepton pair in candidate ZZ events in the 7 TeV data. 202
8.5 Invariant masses of the leading and subleading lepton pair in candidate ZZ events in the 8 TeV data. 203

8.6 Kinematic distributions for events passing the ZZ selection in the 7 TeV data. 204
8.7 Kinematic distributions for events passing the ZZ selection in the 8 TeV data. 205
8.8 Kinematic distributions for events passing the ZZ^* selection in the 7 TeV data. 206
8.9 Comparison of experimental measurements and theoretical predictions of the total ZZ production cross section as a function of centre-of-mass energy $\sqrt{s}$. 212
8.10 Unfolded ZZ fiducial cross sections. 216

9.1 Validation of the TGC reweighting procedure for the 8 TeV samples. 221
9.2 Expected total event yield for the 8 TeV analysis as a function of the nTGC parameters. 224
9.3 Expected limits on f_4^γ obtained in a binned fit of the p_{T} distribution of the leading Z boson candidate, as a function of the lower boundary of the last bin in p_{T}. 228
9.4 Percentage uncertainties for different choices of binning in the p_{T} of the leading Z boson. 229
9.5 Candidate Z boson transverse momentum distributions with the binning used for nTGC limit setting. 231
9.6 Two dimensional 95% confidence intervals for anomalous neutral gauge boson couplings (nTGCs) for form factor scale $\Lambda = \infty$. . . . 234
9.7 Anomalous neutral triple gauge coupling (nTGC) 95% confidence intervals from the ATLAS, CMS, LEP and Tevatron experiments. 235

List of Tables

1.1 The fundamental particles and their properties. 23

2.1 Cross Sections calculated at NLO in QCD for $pp \to ZZ \to e^-e^+\mu^-\mu^+$. 42
2.2 Total $pp \to ZZ$ cross sections at 7 TeV and at 8 TeV. 42
2.3 Percentage contribution of the $gg \to ZZ$ process relative to the total cross section. 43
2.4 95 % confidence level limits on anomalous triple gauge coupling parameters obtained from LEP, D0 and CMS. 60

3.1 LHC operational parameters. 65
3.2 Performance goals of the ATLAS detector. 67

4.1 The width, goodness of fit and mean of a Gaussian fit to the ΔT distribution averaged over stable periods between 20/1/2010 and 20/6/2010. 88
4.2 Number and percentage of modules with $|\Delta T|$ greater than the threshold for identifying problem modules at least 5 times during the period 20/1/2010 - 19/6/2010 for each barrel. 88
4.3 The width of a Gaussian fit to the T_{diff} distribution for each stable period between 20/1/2010 and 20/6/2010. 90
4.4 Number and percentage of modules with $|T_{\text{diff}}|$ greater than the threshold for identifying problem modules at least 5 times during the period 20/1/2010 - 19/6/2010 for each barrel and for each of the endcaps. 91

6.1 Electron selection requirements. 133
6.2 Efficiency of the central electron selection requirements. 135
6.3 Efficiency of the forward electron selection requirements. 136
6.4 Muon selection requirements. 139
6.5 Efficiency of the central muon selection requirements. 140
6.6 Efficiency of the forward muon selection requirements. 142
6.7 Efficiency of the calorimeter-tagged muon selection requirements. 143
6.8 Electron triggers used in the different data taking periods. 145
6.9 Muon triggers used in the different data taking periods. 145

6.10 Trigger efficiencies for ZZ events. 146
6.11 Expected number of events in the 7 TeV data by cut for 4.6 fb^{-1}. 154
6.12 Expected number of events in the 8 TeV data by cut for 20 fb^{-1}. . 154
6.13 Mis-pairing rates in percent for different algorithms for choosing the di-lepton pairs in four-lepton events. 155
6.14 Details of the acceptance and selection efficiencies and contaminations for the 7 TeV analysis. 159
6.15 Details of the acceptance and selection efficiencies and contaminations for the 8 TeV analysis. 160
6.16 Comparison of the fiducial acceptance C_{ZZ} between the 7 TeV analysis and the 8 TeV analysis. 161
6.17 Reconstruction Acceptance C_{ZZ}, compared between different MC generators for the 7 TeV analysis. 168
6.18 Reconstruction Acceptance C_{ZZ}, compared between different MC generators for the 8 TeV analysis. 168
6.19 Systematic uncertainties on the reconstruction acceptance C_{ZZ} for the 7 TeV analysis. 170
6.20 Systematic uncertainties on the reconstruction acceptance C_{ZZ} for the 8 TeV analysis. 171
6.21 Systematic uncertainties on the expected signal yield. 172

7.1 Monte Carlo generators used to model background processes. . . . 174
7.2 MC predicted number of events passing various levels of selection for the Z+X, $W^{\pm}Z/W^{+}W^{-}$, top quark, ZZZ/WWZ and $t\bar{t}+V$ backgrounds for the 7 TeV analysis. 176
7.3 MC estimated number of events passing various levels of selection for the Z+X, $W^{\pm}Z/W^{+}W^{-}$, top quark, ZZZ/WWZ and $t\bar{t}+V$ backgrounds for the 8 TeV analysis. 177
7.4 Definition of selected-leptons L and lepton-like-jets J 180
7.5 Event selection requirements for the Z-tag sample used to measure the fake-factor. 181
7.6 Unparameterised (average) fake-factors for different lepton types. 183
7.7 Results of the Monte Carlo closure test for the data driven background estimate. 185
7.8 Details of the background estimate for 4.6 fb^{-1} of 7 TeV data. . . 186
7.9 Details of the background estimate for 20 fb^{-1} of 8 TeV data. . . 187

7.10 Comparison of background estimates for the 7 TeV analysis, using different criteria to define the lepton-like-jets J. 187
7.11 Comparison of background estimates for the 8 TeV analysis, using different criteria to define the lepton-like-jets J. 188
7.12 Final data-driven fake background estimates. 188
7.13 Background estimate cross-check to the 8 TeV ZZ analysis using same-sign events. 188
7.14 Final background estimates. The irreducible background estimate is taken from Monte Carlo, whilst the reducible background is estimated using the data driven (D.D.) technique described in this chapter. 196

8.1 Expected and observed events in 4.6 fb^{-1} of 7 TeV data. 198
8.2 Expected and observed events in 20 fb^{-1} of 8 TeV data. 198
8.3 Fiducial Cross Section measurements at 7 TeV and at 8 TeV. . . . 209
8.4 Systematic uncertainties to the fiducial acceptance factors, A_{ZZ}, at 7 TeV and at 8 TeV. 210
8.5 Fiducial acceptance factors, A_{ZZ}, at 7 TeV and at 8 TeV. 211
8.6 Total ZZ Cross Section measurements at 7 TeV and at 8 TeV. . . 211

9.1 Yield coefficients for the 8 TeV analysis with form-factor $n = 3, \Lambda = 3$ TeV. 223
9.2 Yield coefficients for the 8 TeV analysis with no form-factor. . . . 223
9.3 Expected and observed 95% confidence interval limits for anomalous neutral gauge boson couplings (nTGCs), set using the 7 TeV data. 232
9.4 Expected and observed 95% confidence interval limits for anomalous neutral gauge boson couplings (nTGCs), set using the 8 TeV data. 233

A.1 Robustness of expected 95% confidence intervals for anomalous neutral gauge boson couplings (nTGCs) for the 8 TeV analysis. . . 252

Introduction

The LHC began high energy proton-proton collisions in 2010, and since then has accumulated high statistics datasets at centre of mass energies of $\sqrt{s} = 7$ TeV, and from 2012, $\sqrt{s} = 8$ TeV. These high statistics samples allow for precision measurements of the Standard Model of particle physics, as well as searches for physics beyond the Standard Model.

Of particular interest are the diboson production processes, where gauge bosons, the force-carriers of the Standard Model, are produced in pairs. Such processes are relatively rare, occurring as rarely as one in every 10^{13} collisions. This thesis is concerned with diboson ZZ production, where the Z boson is produced in pairs. Measuring diboson processes such as ZZ production gives a direct probe of the gauge structure of the electroweak sector of the Standard Model. In the Standard Model, the so called *neutral triple gauge couplings (nTGCs)* ZZZ and $ZZ\gamma$ are forbidden, and diboson production may only proceed by combinations of $Zq\bar{q}$ vertices. Anomalous ZZZ and $ZZ\gamma$ couplings are predicted in some models of physics beyond the Standard Model, and would lead to an increased production rate of diboson events, particularly when the diboson system is produced with high energy. By studying the rate of ZZ production and the kinematic distributions of the observed events, one can search for anomalous nTGCs, and in the absence of any evidence for them, set limits on the maximum size of the couplings.

Diboson production rates are also sensitive to direct contributions from new physics, where resonantly-produced heavy new particles decay to diboson pairs, and so such processes provide ideal search channels for new particles. Non-resonant diboson production is also a major background process to searches for, and studies of, the Higgs boson, which until recently was a major missing component of the Standard Model. Recently, the ATLAS and CMS experiments both reported the discovery of a new particle with mass around 125 GeV, with properties consistent with the Higgs. The good understanding of non-resonant diboson production was a key ingredient to this discovery.

This thesis is divided into three parts. Firstly, Part I gives the theoretical background and motivation to the work presented in this thesis. Chapter 1 gives an introduction to the Standard Model, with particular emphasis on the electroweak theory, and gives an introduction to the phenomenology of particle collisions at

the LHC and the computational tools available for simulating them. Chapter 2 gives a more detailed introduction to ZZ production, nTGCs, and previous experimental results.

Secondly, Part II describes the experimental setup. Chapter 3 gives an outline of the LHC and its experiments, and a description of the ATLAS detector. Chapter 4 describes work done by the author monitoring the performance of the cooling system of the Semiconductor Tracker (SCT), part of the ATLAS inner detector. An overview of the particle reconstruction and identification algorithms and their performance is given in Chapter 5.

Thirdly, Part III describes the main topic of this thesis, the measurement of the ZZ production cross section and limits on nTGCs. Chapter 6 describes requirements used to select ZZ events and reject background processes. Chapter 7 describes estimates of the size of the contribution from background processes. Chapter 8 presents the observed events passing the selection requirements, their kinematic distributions, and measurements of the ZZ cross section. Separate measurements of the cross section at $\sqrt{s} = 7$ TeV and $\sqrt{s} = 8$ TeV are made. These are described 'side-by-side', with small differences in the methodology between the two measurements discussed as appropriate. At each centre-of-mass energy, two measurements of the cross section are given: firstly a measurement in a restricted fiducial phase-space corresponding closely to the experimental kinematic selections, termed the *fiducial cross section*, and secondly a *total* cross section, correcting for the acceptance of the fiducial phase-space. These events are then used to set limits on nTGCs, which is described in Chapter 9.

The work and results presented in this thesis contributed to a number of ATLAS conference notes and publications. An initial measurement of the ZZ cross section at $\sqrt{s} = 7$ TeV and limits on nTGCs using the four-lepton final state in the first 1 fb^{-1} of 2011 data was presented in [1] and later published in [2]. An updated measurement of the cross section using the full 2011 7 TeV dataset of 4.7 fb^{-1} was given in [3], and later a paper published [4], giving combined results with an analysis of $ZZ \to \ell^-\ell^+\nu\bar{\nu}$ decays, including nTGC limits and differential cross sections. A first measurement of the ZZ cross section at $\sqrt{s} = 8$ TeV cross section using the first 5.8 fb^{-1} of the 2012 dataset was given in [5], and an updated measurement using the full 2012 dataset of 20 fb^{-1} was given in [6].

Part I

Background

Chapter 1

Theory

1.1 The Standard Model

The Standard Model of particle physics is a gauge theory describing the fundamental components of matter and their interactions, and encompasses our current understanding of the world at the level of elementary particles. The Standard Model was formulated in the 1970s, and since then has been tested to an unprecedented level of precision. A brief outline of the Standard Model is given here; it is described in great detail elsewhere (e.g. [7–9]).

In the Standard Model there are two classes of particles: fermions, with half-integer spin, and bosons, with integer spin. Fermions are the building blocks of matter, whilst bosons carry the forces and mediate interactions between the fermions. The bosons responsible for carrying the fundamental forces all have spin-1 and are known as *gauge bosons*. The language of the Standard Model is Quantum Field Theory, and every particle in the Standard Model is associated with a field. The fundamental fermions and the fundamental forces and their bosons are described in the next two sections, followed by an overview of electroweak theory and of quantum chromodynamics (QCD).

1.1.1 Fundamental Fermions

There are two types of fermions: *quarks* and *leptons*. The quarks are the constituents of hadrons such as protons and neutrons, whilst the most common lepton, the electron, is found orbiting the nucleus in the atom. The quarks and leptons are arranged into three generations, with each generation having identical quantum numbers [1] but progressively higher mass. The different quark and lepton

[1] "Quantum numbers" are constants of motion in a quantum-mechanical system, for example a particle's charge or spin.

types are referred to as 'flavours'. Each generation of quarks consists of an up-type quark with electric charge $+2/3$ (named 'up', 'charm' and 'top' in the three generations) and a down-type quark with electric charge $-1/3$ (named 'down', 'strange' and 'bottom' in the three generations); they are shown schematically below

$$\begin{pmatrix} u \\ d \end{pmatrix} \begin{pmatrix} c \\ s \end{pmatrix} \begin{pmatrix} t \\ b \end{pmatrix} \tag{1.1}$$

Each generation of leptons consists of an electrically neutral *neutrino* and an electrically charged lepton with charge -1 (the 'electron' e^-, 'muon' μ^- and 'tau' τ^-); they are shown schematically below

$$\begin{pmatrix} \nu_e \\ e^- \end{pmatrix} \begin{pmatrix} \nu_\mu \\ \mu^- \end{pmatrix} \begin{pmatrix} \nu_\tau \\ \tau^- \end{pmatrix} \tag{1.2}$$

The neutrinos are assumed to be massless in the Standard Model, although experimental evidence indicates that they do in fact have a small mass.

All of the fundamental fermions described above have spin $1/2$, and they all have an antiparticle partner, with identical mass but opposite electrical charge[2]. Properties of the fundamental fermions are summarised in Table 1.1.

1.1.2 Fundamental Forces and the Bosons

At present four fundamental forces are known, and these successfully describe almost all observed interactions at microscopic levels. They are the *gravitational force*, the *electromagnetic force*, the *strong force* and the *weak force*.

The gravitational force describes the attraction between masses. It is by far the weakest of the known forces (about 10^{38} times weaker than the electromagnetic force), and so has negligible impact on microscopic particle interactions. It is also the only of the four forces not yet formulated as a Quantum Field Theory and does not enter into the Standard Model, and so is not discussed any further here.

The electromagnetic force is responsible for interactions between electrically charged particles, and is responsible for many of the phenomena of the everyday world, such as light, electricity, the binding of electrons and nuclei into atoms, and the binding of atoms to form more complicated structures. It is mediated by the

[2]It is an open question whether or not the neutrino is its own antiparticle.

Particle	Spin	Charge	Mass [GeV]
Gauge Bosons			
Photon γ	1	0	0
Gluon g	1	0	0
$W^{\pm}$	1	± 1	80.39 ± 0.02
Z	1	0	91.188 ± 0.002
Quarks			
Up (u)	$1/2$	$+2/3$	$2.3\ ^{+0.7}_{-0.5} \times 10^{-3}$
Down (d)	$1/2$	$-1/3$	$4.8\ ^{+0.7}_{-0.3} \times 10^{-3}$
Charm (c)	$1/2$	$+2/3$	$1.27\ ^{+0.07}_{-0.09}$
Strange (s)	$1/2$	$-1/3$	0.095 ± 0.005
Top (t)	$1/2$	$+2/3$	173.5 ± 1.0
Bottom (b)	$1/2$	$-1/3$	4.7 ± 0.03
Leptons			
Electron (e^-)	$1/2$	-1	0.511×10^{-3}
Electron neutrino (ν_e)	$1/2$	0	$< 2 \times 10^{-9}$
Muon (μ^-)	$1/2$	-1	0.106
Muon neutrino (ν_μ)	$1/2$	0	$< 2 \times 10^{-9}$
Tau (τ^-)	$1/2$	-1	1.7768 ± 0.0002
Tau neutrino (ν_τ)	$1/2$	0	$< 2 \times 10^{-9}$
Higgs H	0	0	~ 125

Table 1.1: The fundamental particles and their properties [10].

photon (γ), which couples to particles carrying electrical charge with a strength given by the particle's charge and a coupling strength of $\alpha = 1/137$. The photon is chargeless, so does not self interact; and has zero mass, so electromagnetism is a long range force. The theory describing the electromagnetic force in the Standard Model is known as *Quantum Electrodynamics (QED)*.

The weak force is mediated by the $W^{\pm}$ and Z bosons, which couple to particles carrying weak isospin and is so named as it is approximately 1000 times weaker than the electromagnetic force. It is responsible for many radioactive decays, the best known of which is beta decay. The $W^{\pm}$ have integer electric charge, whilst the Z is electrically neutral. Unlike the other gauge bosons (γ, g), they are both massive and have rather large masses; consequently the weak interaction is a very short range interaction. Uniquely amongst the known forces, weak interactions allow quarks to change flavour and violate CP-symmetry.

The strong force describes interactions between particles carrying a 'colour' charge, and is so named as it is roughly 100 times stronger than the electromagnetic force. Colour charge is analogous to electrical charge, but comes in three 'types' referred to as red, green and blue, rather than just one as in the case of electromagnetism. The strong force is mediated by massless gluons. Gluons carry colour charge, and thus unlike photons can interact with other gluons. This self-interaction leads to the remarkable property that the strength of the strong force *increases* with distance between two colour-charged particles. This in turn leads to *confinement*: bare quarks are never observed in nature, but are only observed bound together into colour neutral *hadrons* such as protons and neutrons. The strong force is also responsible for binding protons and neutrons together into atomic nuclei. The theory describing the strong force in the Standard Model is known as *Quantum Chromodynamics (QCD)*.

Properties of the gauge bosons are summarised in Table 1.1.

1.1.3 The Electroweak Theory

In the 1960s Weinberg [11] and Salam [12] proposed the unification of the electromagnetic and weak forces into a single theory which later became known as the *electroweak* theory. The theory is a gauge theory, guided by requiring that the theory be invariant under *local gauge transformations*, that is that the Lagrangian be invariant under a set of continuous transformations whose parameters have a space-time dependence. Requiring invariance under a local gauge transformation leads to the emergence of vector *gauge fields* with associated *gauge bosons*.

Interactions between the fermions and the gauge bosons give rise to the forces.

The unified electroweak theory has gauge group:

$$U(1)_Y \times SU(2) \tag{1.3}$$

The associated gauge bosons are a massless singlet B_μ associated with the $U(1)_Y$ group and a massless triplet $\mathbf{W}_\mu = \{W^1_\mu, W^2_\mu, W^3_\mu\}$ associated with the $SU(2)$ group. The field associated with the $U(1)_Y$ gauge group is analogous to the electromagnetic field, but is instead associated with hypercharge Y.

It is observed that weak interactions violate parity conservation; this leads to different interactions for the *left-handed* and the *right-handed* components of a particle. A Dirac field, ψ, can be expressed as the sum of left-handed and right-handed components:

$$\psi = \psi_L + \psi_R \tag{1.4}$$

with:

$$\psi_L = P_L\psi = \frac{1}{2}(1-\gamma^5)\psi \tag{1.5}$$

$$\psi_R = P_R\psi = \frac{1}{2}(1+\gamma^5)\psi \tag{1.6}$$

$$\tag{1.7}$$

where γ^5 is the product of the Dirac gamma matrices γ^μ: $\gamma^5 = \gamma^0\gamma^1\gamma^2\gamma^3$. P_L and P_R project out the left-handed and right-handed *chiral* states of the fermion. Chirality is a property of the fermion, but is not a physical observable. In the limit of massless fermions, the chirality is equal to the helicity of the particle, i.e. its spin projected onto its direction of motion (either $+1/2$ or $-1/2$ for a spin $1/2$ fermion). Experimentally the W boson is seen only to couple to left-handed chiral states. This is expressed in the theory by arranging the left-handed particles into $SU(2)$ doublets and the right-handed particles into $SU(2)$ singlets. Considering only the first generation of fermions, we have:

$$\ell_L = \begin{pmatrix} \nu_L \\ e_L \end{pmatrix},\ e_R,\ \nu_R{}^{3},\ q_L = \begin{pmatrix} u_L \\ d_L \end{pmatrix},\ u_R,\ d_R \tag{1.8}$$

[3]The right-handed neutrino need not exist in a model with massless neutrinos, however given experimental evidence for a small neutrino mass it is included here for completeness.

The $SU(2)$ singlets e_R, ν_R, u_R, d_R are invariant under $SU(2)$ transformations and thus do not couple to the $\mathbf{W}_\mu$ gauge bosons, whilst the doublets transform as:

$$\ell_L \to \ell'_L = e^{-iw^a \mathbf{T^a}} \ell_L \tag{1.9}$$

where the $\mathbf{T^a}$ are the three generators of the $SU(2)$ group. These can be expressed in terms of the Pauli matrices as $\frac{1}{2}\tau^{\mathbf{a}}$, where:

$$\tau^1 = \begin{pmatrix} 0 & 1 \\ 1 & 0 \end{pmatrix},\ \tau^2 = \begin{pmatrix} 0 & -i \\ i & 0 \end{pmatrix},\ \tau^3 = \begin{pmatrix} 1 & 0 \\ 0 & 1 \end{pmatrix} \tag{1.10}$$

Under $U(1)_Y$ both the singlets and the doublets transform in the same way:

$$\psi \to \psi' = e^{-iw'Y(\psi)}\psi \tag{1.11}$$

where Y is the hypercharge of the particle in question.

The Lagrangian for a massless free fermion field ψ is given by the Dirac Lagrangian:

$$\mathcal{L}_{Dirac} = \bar{\psi}(i\gamma^\mu \partial_\mu)\psi \tag{1.12}$$

where $\bar{\psi} = \psi^\dagger \gamma^0$ is the conjugate field. In order to make this Lagrangian invariant under local $U(1)$ and $SU(2)$ transformations it is necessary to introduce the gauge fields B_μ and $\mathbf{W}_\mu$ as described above, and to replace the derivative ∂_μ with the *covariant derivative* D_μ, defined such that the quantity $D_\mu\psi$ transforms in the same way as ψ under gauge transforms. This gives rise to interactions between the fermions and the gauge fields. The covariant derivative operators include the $U(1)_Y$ and $SU(2)$ operators as needed, and for a fermion multiplet f take the following form:

$$D_\mu = \partial_\mu + i2gI_W(f)\mathbf{T^a}W^a_\mu + ig'Y(f)B_\mu \tag{1.13}$$

where $I_W(f)$ is the weak isospin and $Y(f)$ is the hypercharge of fermion f and g and g' are the couplings of the $SU(2)$ and hypercharge fields. The explicit values of I_W and Y are as follows:

$$\begin{aligned} Y(\ell_L) = -\frac{1}{2},\ Y(e_R) = -1,\ Y(\nu_R) = 0,\ Y(q_L) = \frac{1}{6},\ Y(u_R) = \frac{2}{3},\ Y(d_R) = -\frac{1}{3} \\ I_W(\ell_L) = I_W(q_L) = \frac{1}{2},\ I_W(e_R) = I_W(\nu_R) = I_W(u_R) = I_W(d_R) = 0 \end{aligned} \tag{1.14}$$

This ensures the desired property that the $SU(2)$ field couples only to the left handed multiplets.

The Lagrangian for the electroweak theory is:

$$\begin{aligned}\mathcal{L}_{EW} = &-\frac{1}{4}B_{\mu\nu}B^{\mu\nu} - \frac{1}{4}F^a_{\mu\nu}F^{a\,\mu\nu} \\ &+ i\overline{\ell_L}^T\gamma^\mu D_\mu \ell_L + i\overline{e_R}^T\gamma^\mu D_\mu e_R + i\overline{\nu_R}^T\gamma^\mu D_\mu \nu_R \\ &+ i\overline{q_L}^T\gamma^\mu D_\mu q_L + i\overline{u_R}^T\gamma^\mu D_\mu u_R + i\overline{d_R}^T\gamma^\mu D_\mu d_R \end{aligned} \tag{1.15}$$

The first line gives kinematic terms for the gauge fields, where $B_{\mu\nu} = \partial_\mu B_\nu - \partial_\nu B_\mu$ is the hypercharge field strength, and $F^a_{\mu\nu} = \partial_\mu W^a_\nu - \partial_\nu W^a_\mu - g f^{abc} W^b_\mu W^c_\nu$ is the weak $SU(2)$ field strength. The last term in the second expression gives rise to triple and quartic couplings of the W^a bosons. The second and third lines of Equation 1.15 describe the kinematics of the fermions in the theory.

Substituting Equations 1.10,1.13 and 1.14 into Equation 1.15 gives the following interaction terms between the leptons and the gauge bosons:

$$\begin{aligned}-\frac{g}{2}\begin{pmatrix}\overline{\nu_L}\\ \overline{e_L}\end{pmatrix}^T\gamma^\mu\left(\begin{pmatrix}W^3_\mu & \sqrt{2}W^+_\mu\\ \sqrt{2}W^-_\mu & -W^3_\mu\end{pmatrix} - \tan\theta_{\mathrm{W}} B_\mu\right)\begin{pmatrix}\nu_L\\ e_L\end{pmatrix} \\ +g\tan\theta_{\mathrm{W}}\,\overline{e_R}\,\gamma^\mu B_\mu e_R\end{aligned} \tag{1.16}$$

where the W^1, W^2 have been rewritten as $W^\pm = (W^1 \mp iW^2)/\sqrt{2}$, and θ_{W} is the weak mixing angle, defined such that:

$$g\sin\theta_{\mathrm{W}} = g'\cos\theta_{\mathrm{W}} \tag{1.17}$$

In Equation 1.16 four gauge bosons are seen: a charged W^+ and W^- which mediate transitions between electrons and neutrinos, and a neutral W^3_μ and B_μ which both couple to pairs of electrons and neutrinos. These can not be identified with the physical Z boson and photon, since the photon does not couple to the neutrino. However, the physical bosons can be obtained by a 'rotation', replacing the fields W^3_μ and B_μ by the physical particles Z_μ and A_μ:

$$Z_\mu = \cos\theta_{\mathrm{W}} W^3_\mu - \sin\theta_{\mathrm{W}} B_\mu \tag{1.18}$$

$$A_\mu = \cos\theta_{\mathrm{W}} B_\mu + \sin\theta_{\mathrm{W}} B_\mu \tag{1.19}$$

Substituting these into Equation 1.16 and collecting terms relating to each of the gauge bosons, it is found that the charged $W^\pm$ bosons mediate transitions

between left-handed electrons and neutrinos with the term:

$$-\frac{g}{2\sqrt{2}}\left(\overline{\nu_L}\gamma^\mu e_L W_\mu^+ \;+\; \overline{e_L}\gamma^\mu \nu_L W_\mu^-\right) \tag{1.20}$$

The Z boson couples to left- and right-handed electrons and to neutrinos, with slightly different couplings to the left- and right-handed electrons:

$$\frac{g}{2\cos\theta_\mathrm{W}}\left((1-2\sin^2\theta_\mathrm{W})\,\overline{e_L}\gamma^\mu e_L - 2\sin^2\theta_\mathrm{W}\,\overline{e_R}\gamma^\mu e_R - \overline{\nu_L}\gamma^\mu\nu_L\right) Z_\mu \tag{1.21}$$

Finally, the photon couples equally to left- and right-handed electrons, but not to the neutrinos:

$$g\sin\theta_\mathrm{W}\left(\overline{e_L}\gamma^\mu e_L \;+\; \overline{e_R}\gamma^\mu e_R\right) A_\mu = g\sin\theta_\mathrm{W}\,\overline{e}\,\gamma^\mu e A_\mu \tag{1.22}$$

The quantity $g\sin\theta_\mathrm{W}$ can thus be associated with the electromagnetic charge e. The $W^\pm$ and Z bosons are associated with the weak force, and the photon with the electromagnetic force.

Similarly, it is found that the $W^\pm$ boson mediates transitions between left-handed u and d quarks, that the Z boson couples to quarks proportionally to their weak isospin and electric charge, with different couplings for the different chiral states, and that the photon couples to quarks with couplings proportional to their electric charge.

Generally, the covariant derivative of Equation 1.13 can be written in terms of the physical fields $W_\mu^\pm$, Z_μ, A_μ as:

$$D_\mu = \partial_\mu + i\frac{g}{\sqrt{2}}(W_\mu^+ + W_\mu^-) + i\frac{g}{\cos\theta_\mathrm{W}}(I_3^f - Q^f\sin^2\theta_\mathrm{W})Z_\mu + igQ^f\sin\theta_\mathrm{W}A_\mu \tag{1.23}$$

for a fermion f possessing a third component of weak isospin I_3^f and an electromagnetic charge Q^f. The electromagnetic charge can be related to the hypercharge as $Q = I_3 + Y$. The second term in (1.23) describes the weak Charged Current (CC) interaction, the third the weak Neutral Current (NC) and the fourth the electromagnetic neutral current.

1.1.4 Electroweak Symmetry Breaking

The gauge bosons and fermions in the electroweak Lagrangian given in Equation 1.15 are massless. This is clearly a problem as the fermions are observed to be massive, and more worryingly the W and Z bosons are observed to be ex-

tremely massive. Unfortunately, explicit mass terms for the gauge bosons may not be added to the theory without violating local gauge invariance, and it is not possible to include explicit mass terms for the fermions as this mixes the left- and right-handed components, which have been assigned to different $SU(2)$ multiplets.

In order to give mass to the gauge bosons, the symmetry must be broken somehow. The simplest way to do so would be to simply add mass terms for the gauge bosons by hand, however this would lead to a non-renormalisable theory which would contain an infinite number of divergences. Instead, gauge bosons are given masses by 'spontaneous symmetry breaking' in the Higgs mechanism[4] by introducing an $SU(2)$ doublet of complex scalar fields (the *Higgs Field*), with a potential of the form:

$$V(\Phi) = \mu^2 \Phi^\dagger \Phi + \lambda (\Phi^\dagger \Phi)^2 \tag{1.24}$$

If $\mu^2 < 0$ then the field has a minimum at $\Phi^\dagger \Phi = -\frac{1}{2}\mu^2/\lambda$, and thus has a non-zero vacuum expectation value. Gauge invariance of the Lagrangian is preserved, however the vacuum state is no longer invariant under gauge transformations. The gauge bosons acquire mass by interactions with the field, and it is found that:

$$M_W = \frac{1}{2} g v, \;\; M_Z = \frac{g v}{2 \cos \theta_{\mathrm{W}}} \tag{1.25}$$

where $v = \mu/\sqrt{\lambda}$ is the vacuum expectation value.

Terms can also be introduced describing interactions of the fermions with this field, giving masses to the fermions without mixing the left- and right-handed components. Such an interaction is called the 'Yukawa interaction'. The couplings strengths are given by the *Yukawa couplings*, which can be different for each fermion and are not fixed by the theory, requiring experimental determination.

The introduction of the Higgs field predicts the existence of one further fundamental particle, a massive scalar boson known as the *Higgs Boson* with mass $m_H = \sqrt{2}|\mu|$. Again, the mass is not predicted by the theory. There has been much experimental activity in the search for the Higgs boson, and for many years it proved elusive. Recently, the CMS [13] and ATLAS [14] collaborations reported evidence for a new boson with properties consistent with the Higgs.

[4] More properly the Brout-Englert-Higgs mechanism.

1.1.5 Quantum Chromodynamics

Quantum Chromodynamics is the theory of the strong interaction, and is a non-abelian gauge theory with gauge group $SU(3)$. The charge associated with $SU(3)$ is the *colour charge*, so named because the three charges are referred to as red, blue and green. The theory is constructed in a similar way to the electroweak theory, requiring invariance under local gauge transformations generated by the group. This is again achieved by replacing the derivative in the Dirac equation with a covariant derivative, necessitating the introduction of gauge boson fields. Since there are eight generators of $SU(3)$, an octet of gauge fields is introduced, which are the eight gluons $G_\mu^{1..8}$.

The Lagrangian for QCD is given by:

$$\mathcal{L}_{QCD} = -\frac{1}{4} G^a_{\mu\nu} G^{\mu\nu}_a + \bar{q}_a (i\gamma^\mu D_\mu)_{ab}\, q_b \tag{1.26}$$

where the index a runs over colour charge. The covariant derivative is defined as:

$$D_\mu = \partial_\mu + i g_s \mathbf{T}^a G^a_\mu \tag{1.27}$$

where $\mathbf{T}^a$ are the generators of $SU(3)$ and $G^a_{\mu\nu}$ is the colour field strength tensor:

$$G^a_{\mu\nu} = \partial_\mu G^a_\nu - \partial_\nu G^a_\mu - g_s f^{abc} G^b_\mu G^c_\nu \tag{1.28}$$

The f^{abc} are the structure functions of the $SU(3)$ group. As in the case of W bosons in the weak interaction, the last term in Equation 1.28 gives rise to triple and quartic interactions between the gluons. g_s is the strong coupling constant, usually expressed as α_S, given by:

$$\alpha_S = \frac{g_s}{4\pi} \tag{1.29}$$

Since the gluons are massless, QCD contains UV divergences which lead to infinite results in cross section calculations. This is clearly unphysical, so a renormalisation procedure must be used to cancel the divergences, for example by introducing a gluon mass or setting a UV cutoff scale to regularise the divergence. The divergences are then absorbed by a redefinition of the 'bare' parameters of the theory to the physically observable parameters. Renormalised parameters such as α_S are dependent on the *renormalisation scale* μ_R, the scale at which this subtraction is done. A result of this procedure is that α_S becomes dependent on

the momentum squared of the external particles coming into a vertex, Q^2:

$$\alpha_S(Q^2) = \alpha_S(\mu_R^2) - \alpha_S(\mu_R^2)\beta_0 \ln(Q^2/\mu_R^2) \tag{1.30}$$

The parameter β_0 is positive, and so the effective coupling *decreases* as the momentum scale Q^2 increases, a phenomena referred to as the *running of the coupling*. For momentum scales below $\sim$ 2 GeV, α_S becomes large, and it is not possible to perform perturbative calculations in QCD. In this *non-perturbative* regime phenomenological models are needed.

The running of the coupling gives rise to two additional phenomena: *confinement* and *asymptotic freedom*. Since α_S increases as Q^2 decreases, the strong force between two quarks increases as the distance between them increases, leading to stronger and stronger binding as they are pulled apart. At sufficiently large separation, the colour 'string' connecting the quark snaps, and a new pair of quarks is produced. A result of this is that quarks and gluons may only ever be observed as colourless bound-states (hadrons), and never as 'bare' colour charges. Conversely, at large momentum scales (such as in a high energy particle collision) or short distances (such as within a hadron) the strong coupling between quarks becomes very small and they behave more like free particles.

1.2 Interactions in Proton-Proton Collisions

An illustration of a proton-proton collision at a hadron collider is shown in Figure 1.1. In proton-proton collisions it is not the protons themselves that interact but their quark and gluon constituents. The interaction between two *incoming* partons (quarks or gluons) from the two initial protons is known as the *hard scatter*, which will lead to two or more hard outgoing particles. The incoming and any

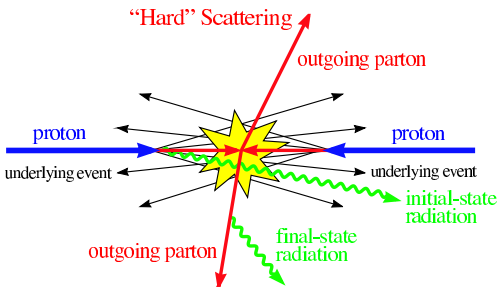

(a)

Figure 1.1: Illustration of a proton-proton collision. Figure from [15].

coloured outgoing particles will emit further QCD radiation known as *initial state radiation (ISR)* and *final state radiation (FSR)* in the form of gluons, which in turn can split into further partons. Once the outgoing quarks and gluons become far enough from one other, the coupling between them becomes strong and they form into colour neutral hadrons in a process known as hadronisation. Charged incoming and outgoing particles will also emit electromagnetic (QED) radiation in the form of photons.

The interaction between the incoming particles leaves behind other partons from the breakup of the original proton. There may also be other secondary collisions between these residual partons, referred to as *multiple interactions*. Particles from ISR and FSR, the breakup of the proton and multiple interactions are collectively referred to as the *underlying event (UE)*.

In a basic picture, the proton consists of three *valence quarks*: two up-quarks and one down-quark, bound together by the strong force. These quarks will spontaneously exchange gluons, which can in turn split into additional quark pairs, known as *sea quarks*. As the energy of a particle used to probe the proton is increased, the fraction of the proton momentum observed to be carried by sea quarks and gluons increases, as a more energetic probe is able to resolve the structure of the proton at a finer level. The parton content of the proton thus depends on the momentum transfer of the interaction Q^2. Perturbative QCD is not able to describe the soft splittings within the proton, and so the structure of the proton be described by fits to experimental data. *Parton Density Functions (PDFs)* of the form $f_i(x_i, Q^2)$ are used to describe the probability of finding a parton of flavour i carrying a fraction x_i of the incoming proton momentum at a momentum scale Q^2. The DGLAP equations [16] model interactions within the proton using splitting functions and use perturbative QCD to evolve the PDFs between different Q^2.

An important concept in calculating cross section for interactions involving hadrons is the *factorisation theorem* [17], which allows the hard short-distance component of a scattering process, which can be calculated exactly with perturbative QCD, to be 'factorised' from the soft long-distance component, which can not and must be modelled with phenomenological models and parametrised functions fit to experimental data. Thus in the above model of proton-proton collisions the hard scattering cross section can be calculated exactly whilst the PDF is used to describe the behaviour of the partons within the proton. The cross section for

a scattering initiated by two protons with momenta P_1, P_2 can be written as:

$$\sigma(P_1, P_2, Q^2) = \sum_{i,j} \int dx_1 dx_2 \, f_i(x_1, \mu_F) f_j(x_2, \mu_F) \times \hat{\sigma}_{i,j\to X}(x_1.P_1, x_2.P_2, \alpha_s(\mu_R^2), \frac{Q^2}{\mu_F}, \frac{Q^2}{\mu_R}) \tag{1.31}$$

where the sum i, j is over parton flavour, $\hat{\sigma}_{i,j\to X}$ is the partonic cross section for partons i and j scattering to give X, and $f_i(x_1, \mu_F)$ are the PDFs. μ_F is the factorisation scale, the scale at which the PDF is evaluated, setting the boundary between hard, perturbative QCD and soft, non-perturbative QCD and μ_R is the renormalisation scale, discussed in Section 1.1.5.

When performing calculations to all orders of perturbation theory, the results do not depend on the choice of the scales μ_R and μ_F; however since for most processes it is only possible to calculate the first few terms of the expansion, the results will heavily depend on the choice of scale. The dependence on the choice of scale is expected to decrease as the calculation is performed to higher order.

1.3 Monte-Carlo Simulation

Simulated events are a crucial ingredient to a particle physics measurement for a number of reasons. It is of course important to be able to compare experimentally measured quantities such as cross sections and kinematic distributions with predictions from the theory. Furthermore, simulated events are important for calibrating the detector response and for estimating selection efficiencies in order to translate from observed events to a physical quantity such as a cross section.

Simulated events are generated by means of Monte Carlo simulation, which uses numerical integration to calculate matrix elements and generate events. Generating events suitable for the purposes outlined in the last paragraph typically consists of four steps: calculation of the matrix element for the hard scattering, adding initial and final state radiation using a parton shower, simulating the hadronisation, and finally embedding in the underlying event. An outline of these steps is given below. For more details see e.g. [15, 18].

The calculation of the matrix element (ME) is made at a fixed order in perturbative QFT, where the expansion is in terms of the strong coupling constant α_S. The event generators used in this thesis are either *Leading Order (LO)*, where only the simplest diagrams contributing to a process are calculated, or *Next to*

Leading Order (NLO), where contributions from one loop diagrams are included.

FSR and ISR are modelled by the parton shower (PS), which models successive splittings of the incoming or outgoing partons. In the case of outgoing partons they are radiated until they reach an energy of $\sim$ 1 GeV, at which point the predictions of perturbative QCD become invalid and the partons hadronise. For the incoming partons, the shower is run in reverse to model the evolution of the parton back from its state at the point of the hard scatter through splittings occurring within the proton, with progressively lower energy until a cutoff scale of $\sim$ 1 GeV is reached.

The process of hadronisation is not well described theoretically, but relies on a number of phenomenological models. A common set of models are the *string models*, in which the force between two coloured charges is modelled as an elastic string with rising tension as the particles separate. If the string is stretched too far it will snap, creating a new pair of colour charges. If a pair of opposite colour charges are found close to each other, they are combined into a hadron.

When calculating cross sections and generating events, an important consideration is the choice of factorisation and renormalisation scales, μ_R and μ_F, defined in Section 1.2. Since at LO and NLO the cross section is strongly dependent on the choice of scale, theoretical uncertainties must be assigned to account for the dependence on the (somewhat arbitrary) choice of scale. Typically, this is done by setting the scales to an energy similar to the characteristic energy scale Q of the interaction, then varying up and down by a factor of two to estimate systematic uncertainties.

Modern Monte Carlo integrators can calculate exact matrix elements with additional partons from FSR in the matrix element. Whilst this increases the accuracy of the cross section and kinematic distributions, it becomes necessary to 'match' the ME calculation to the PS to ensure no double counting, since otherwise a $2 \to 3$ event could either come from a $2 \to 3$ matrix element event or a $2 \to 2$ matrix element event with an additional parton coming from a splitting in the parton shower. One method of doing this is by vetoing any splitting in the PS above a certain threshold. Different generators use different models for the parton shower, hadronisation, and for ME-PS matching.

1.3.1 Monte Carlo Generators

A wide range of Monte Carlo integrators and event generators is available to simulate processes of interest at the LHC. The following generators are used in this

thesis. For each generator, an outline of how it is used and its general properties is given.

- MCFM [19] is designed to calculate cross sections for femtobarn-level processes at hadron colliders. Matrix elements are calculated at NLO, incorporating full spin correlations. MCFM is a cross section calculator only and cannot produce unweighted events suitable for use in a physics analysis. Nevertheless it provides a useful toolkit for calculating cross sections, estimating the acceptance of fiducial selections and studying the associated uncertainties due to PDF and scale uncertainties.

- POWHEGBOX [20] is a general framework for implementing NLO calculations. It uses the POWHEG method to match the NLO matrix elements to the parton shower. POWHEGBOX must be interfaced to an external program for the implementation of the parton shower; for this thesis, POWHEGBOX is interfaced to PYTHIA for showering. Specific details of the implementation of the ZZ process in POWHEGBOX are given in [21]. The $gg \to ZZ$ process is not included. Samples generated using POWHEGBOX are used as the main signal samples for the $qq \to ZZ$ process, used to optimise the selection, estimate selection acceptances and systematics and compare observed distributions with theory.

- GG2ZZ [22] is a specialist generator used to simulate the $gg \to ZZ$ process. Events generated with GG2ZZ are used in conjunction with the POWHEGBOX events as the main signal sample. It is interfaced to the HERWIG to provide the parton shower and JIMMY [23] to model the underlying event. Its sister generator, GG2WW, is used to simulate the background from $gg \to W^+W^-$ [24].

- SHERPA [25] is a LO generator, capable of simulating the $qq \to ZZ$ process with up to three additional hard partons in the matrix element. It uses an extended version of the CKKW scheme [26] to match to the matrix element to the parton shower, and provides its own simulation of the parton shower, QED radiation and the underlying event. SHERPA is also capable of simulating anomalous triple gauge couplings (aTGCs), discussed in Chapter 2. It is used as a cross-check to POWHEGBOX and to estimate the impact of uncertainties arising from different implementations of the parton shower and QED radiation. It is also used to simulate aTGC samples. Version

1.3.1 is used to simulate $qq \to ZZ \to \ell^-\ell^+\ell^-\ell^+$ at 7 TeV, and 1.4.0 is used at 8 TeV.

- PYTHIA is a LO generator which uses a library of $2 \to 2$ matrix elements covering almost all Standard Model processes to model the signal process and a p_{T} ordered parton shower to model additional radiation. The Fortran77 based PYTHIA 6 [27] is used at 7 TeV whilst the C++ based PYTHIA 8 [28] is used at 8 TeV. PYTHIA is used to provide showering for many of the other generators described here.

- HERWIG [29] is another general purpose LO generator, generating events in a similar way to PYTHIA, but using an angular-ordered parton shower. It is used for generating inclusive samples (all final states) of WW and WZ production, used in estimating background from other diboson processes.

- HERWIG++ [30] is a C++ based generator based on the Fortran HERWIG. It includes NLO calculations of a number of processes using the POWHEG matching scheme. HERWIG++ is only used for comparison of ZZ event kinematics at generator level.

- MC@NLO [31] is a NLO generator, and was the first generator to implement NLO ME to PS matching, using the so-called MC@NLO technique. MC@NLO is used to simulate the background processes $t\bar{t}$, $W^{\pm}t$ and single-top at 7 TeV. MC@NLO can simulate $qq \to ZZ$, but only in the zero-width approximation where the lineshape of the Z boson is not included. For this reason MC@NLO is not used for signal simulation, though the generator level predictions of MC@NLO are compared to other generators in the Chapter 2. MC@NLO is used to model the $t\bar{t}$, $W^{\pm}Z$ and W^+W^- backgrounds, for which it provides implementations including the widths of the bosons.

- ALPGEN [32] is a LO generator for simulating multi-parton processes in hadron interactions. It can simulate W and Z production with up to 6 additional partons in the matrix element. It is interfaced to HERWIG for the parton shower, using the MLM matching scheme [33]. It is used to simulate $W^{\pm}$ and Z bosons in association with jets, as well as low mass Drell-Yan and $W^{\pm}\gamma$ and $Z\gamma$.

Chapter 2

ZZ Production

The study of the production of pairs of Z bosons in particle collisions (so called *diboson ZZ production*) is of great interest as it provides a precision test of the Standard Model, and unique opportunity to probe the structure of the electroweak sector. The ZZZ and $ZZ\gamma$ neutral triple gauge boson couplings (nTGCs) are zero at tree-level in the Standard Model, and exist only at the level of $\mathcal{O}(10^{-4})$ in one-loop corrections [34]. The sizes of these nTGCs are, however, enhanced in many models of new physics. Measurement of these couplings thus provides a test of the structure of the electroweak sector of the Standard Model.

Non-resonant ZZ production is also the irreducible background to $H \to ZZ$ decays, one of the key channels in Higgs boson physics at the LHC. The CMS [13] and ATLAS [14] experiments both recently reported the discovery of a new boson with mass near 125 GeV in the search for the Higgs boson. $H \to ZZ$ decays were a key search channel for this discovery, contributing a local significance of 3.6σ to the overall local significance of 6.0σ (the other contributing channels were $H \to \gamma\gamma$ and $H \to WW$). The good understanding of non-resonant ZZ production obtained by the measurements presented in this thesis was essential for this discovery, and continues to be important for studying the properties of the new boson.

2.1 ZZ Production at Hadron Colliders

At hadron colliders, $qq \to ZZ$ proceeds at tree level via t- and u-channel quark-antiquark annihilation as shown in Figure 2.1. Since ZZZ and $ZZ\gamma$ couplings are forbidden in the Standard Model there is no contribution from s-channel $q\bar{q}$ annihilation. Final states involving an off shell photon in place of a Z are indistinguishable from the state with a Z, and so the $qq \to ZZ$ process involves a small contribution from γ^*, with interference between the Z diagrams and the γ^* diagrams. For the remainder of this thesis, Z is taken to mean Z/γ^*.

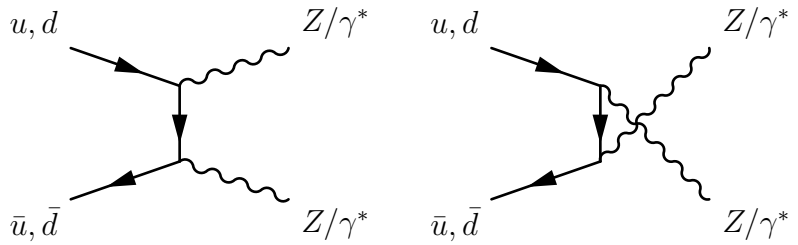

Figure 2.1: Leading order Feynman diagrams for ZZ production in proton-proton collisions. The left hand diagram shows t-channel $qq \rightarrow ZZ$, the right hand diagram the equivalent u-channel process. The tree level s-channel process is forbidden in the Standard Model.

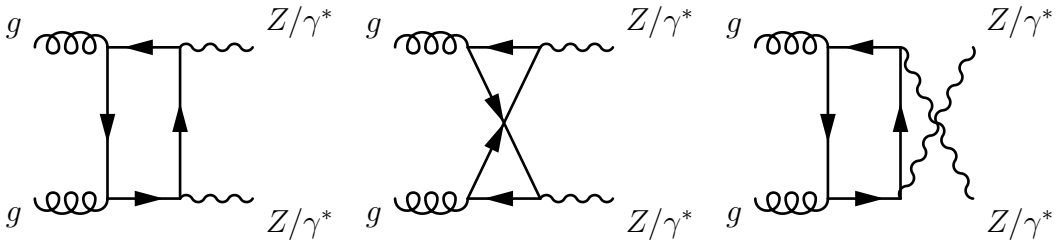

Figure 2.2: Feynman diagrams for $gg \rightarrow ZZ$. Although these are NNLO processes and are suppressed by a factor of α_s^2, they still make a significant contribution at LHC energies due to the high gluon content of the proton

Gluon-gluon fusion processes will also contribute via quark box diagrams, as shown in Figure 2.2. Although these are NNLO and are suppressed by a factor of α_s^2, due to the high gluon content of the proton at LHC energies they still contribute a sizeable fraction of the total ZZ production cross section, contributing approximately 5-10% [19], depending on the centre of mass energy and the mass range of the Z bosons.

2.1.1 ZZ Decay Modes

Z bosons can decay to a quark-antiquark pair, a neutrino-antineturino pair or a pair of oppositely charged leptons. The branching fractions to each of the final states are well known [10], and are 69.9% for $q\bar{q}$, 20.0% for $\nu\bar{\nu}$ and 10.1% for $\ell^-\ell^+$. In ZZ decays, each boson decays independently, so the branching fraction for a given final state is the product of the branching fractions for the two Z bosons. The measurements in this thesis are all based on measurements of $ZZ \rightarrow \ell^-\ell^+\ell^-\ell^+$, where $\ell = e, \mu$, giving three final states $e^-e^+e^-e^+$, $\mu^-\mu^+\mu^-\mu^+$ and $e^-e^+\mu^-\mu^+$. The branching fractions to these final states, obtained by multi-

plying the branching fractions from [10], are as follows:

$$\mathcal{B}(ZZ \to e^-e^+e^-e^+) = 0.113 \pm 0.008\,\% \tag{2.1}$$

$$\mathcal{B}(ZZ \to \mu^-\mu^+\mu^-\mu^+) = 0.113 \pm 0.014\,\% \tag{2.2}$$

$$\mathcal{B}(ZZ \to e^-e^+\mu^-\mu^+) = 0.226 \pm 0.016\,\% \tag{2.3}$$

2.1.2 Cross Section Definition

The cross section for non-resonant ZZ production can be defined in a number of ways. One definition is to use a *zero-width* approximation for the Z bosons and calculate a total cross section. Alternatively, the natural width of the Z bosons can be used, and requirements made on the invariant masses of the Z bosons to define a cross section. In this thesis, measurements of two total ZZ cross sections are presented: an *on-shell* cross section assuming natural width for the Z bosons and requiring both bosons have mass in the range $66 < m_Z < 116$ GeV, and a cross section allowing one of the Z bosons to be off shell with $m_Z > 20$ GeV.

Measurements are also presented in a restricted phase space, termed a *fiducial volume*, which corresponds closely to the experimental selection requirements described in Chapter 6. The corresponding *fiducial cross section* has smaller theoretical uncertainties than the total cross section, since in extrapolating from the experimentally measured fiducial cross section to the total cross section additional uncertainties arise due to uncertainties on the PDF and the factorisation and renormalisation scales. The fiducial volumes used for the 7 TeV and the 8 TeV measurements are are defined below; they are slightly different from each other, reflecting the different experimental selections. The fiducial cross sections are measured using decays where both Z bosons decay to either electrons or muons, denoted $ZZ \to \ell^-\ell^+\ell^-\ell^+$. They are then extrapolated to the total cross section, correcting for the geometric acceptance of the fiducial volume and the branching fractions to leptons.

7 TeV Fiducial Cross Section Definitions

The $ZZ \to \ell^-\ell^+\ell^-\ell^+$ on-shell (ZZ) fiducial cross section is defined as:

- $(Z/\gamma^*)(Z/\gamma^*) \to \ell^-\ell^+\ell^-\ell^+$, $\ell = e, \mu$;
- $66 < m_{12}(Z/\gamma^*) < 116$ GeV, where $m_{12}(Z/\gamma^*)$ is the mass of the Z reconstructed from the first and second leptons. The lepton pairings are assigned

by choosing the set of same-flavour, opposite-sign lepton pairs that minimises the sum of distances from the Z boson mass given in [10]:

$$|m_{1,2}(Z/\gamma^*) - m_Z^{\mathrm{PDG}}| + |m_{3,4}(Z/\gamma^*) - m_Z^{\mathrm{PDG}}| \tag{2.4}$$

- $66 < m_{34}(Z/\gamma^*) < 116$ GeV, where $m_{34}(Z/\gamma^*)$ is the mass of the Z reconstructed from the third and fourth leptons;
- All four leptons have transverse momentum satisfying $p_{\mathrm{T}}^{\ell} > 7$ GeV;
- All four leptons have pseudo-rapidity satisfying $|\eta^{\ell}| < 3.16$;
- The minimum distance between any two leptons in the event must satisfy $\min(\Delta R(\ell,\ell)) > 0.2$, where $\Delta R = \sqrt{\Delta\phi^2 + \Delta\eta^2}$.

The $ZZ^* \to \ell^-\ell^+\ell^-\ell^+$ fiducial cross section, allowing one Z to be off-shell (ZZ^*), is defined as:

- $(Z/\gamma^*)(Z/\gamma^*) \to \ell^-\ell^+\ell^-\ell^+$, $\ell = e, \mu$;
- $66 < m_{12}(Z/\gamma^*) < 116$ GeV;
- $m_{34}(Z/\gamma^*) > 20$ GeV;
- All leptons satisfying the same kinematics requirements as above: $p_{\mathrm{T}}^{\ell} > 7$ GeV, $|\eta^{\ell}| < 3.16$, and $\min(\Delta R(\ell,\ell)) > 0.2$.

In this case the tighter mass cut is applied to the dilepton pair closest to the Z boson mass.

8 TeV Fiducial Cross Section Definitions

For the 8 TeV data, only a measurement of the on-shell (ZZ) cross section is presented. The fiducial volume is defined as:

- $(Z/\gamma^*)(Z/\gamma^*) \to \ell^-\ell^+\ell^-\ell^+$, $\ell = e, \mu$;
- $66 < m_{12}(Z/\gamma^*) < 116$ GeV, where $m_{12}(Z/\gamma^*)$ is the mass of the Z boson reconstructed from the first and second leptons. The lepton pairings are assigned by choosing the set of same-flavour, opposite-sign lepton pairs that minimises the sum of distances from the Z boson mass given in [10]:

$$|m_{1,2}(Z/\gamma^*) - m_Z^{\mathrm{PDG}}| + |m_{3,4}(Z/\gamma^*) - m_Z^{\mathrm{PDG}}| \tag{2.5}$$

- $66 < m_{34}(Z/\gamma^*) < 116$ GeV, where $m_{34}(Z/\gamma^*)$ is the mass of the Z boson reconstructed from the third and fourth leptons;
- All four leptons have transverse momentum satisfying $p_{\mathrm{T}}^{\ell} > 7$ GeV;
- All four leptons have pseudo-rapidity satisfying $|\eta^{\ell}| < 2.7$;
- The minimum distance between any two leptons in the event must satisfy $\min(\Delta R(\ell,\ell)) > 0.2$, where $\Delta R = \sqrt{\Delta\phi^2 + \Delta\eta^2}$.

In calculating the invariant masses of the lepton pairs and the lepton p_{T} and η, photons within $\Delta R < 0.1$ of the lepton are included in the lepton four-momentum.

2.1.3 Theoretical Cross Section Predictions

Table 2.1 shows cross sections for the $ZZ \to e^-e^+\mu^-\mu^+$ process at 7 TeV and at 8 TeV, calculated using version 6.3 of the MCFM [19] program. The cross section in the zero-width approximation is shown, as well as the cross sections allowing for the natural width of the Z boson and applying mass cuts. The cross sections after applying the requirements defining the fiducial volume are also shown. In all cases, the CT10 [35] PDF set is used, and the factorisation and renormalisation scales are set to $\mu_R = \mu_F = \frac{1}{2}m(ZZ)$. The error due to the PDF uncertainty is evaluated by using the 52 CT10 error sets and by taking the difference in cross section obtained when using the MSTW08NLO [36] PDF set. The error due to the choice of factorisation and renormalisation scales is evaluated by varying them simultaneously up and down by a factor of two. The contribution from the γ^* diagram is included in the calculation.

Total cross sections are shown in Table 2.2. These are also calculated using the MCFM program as described above, by calculating the cross section for $ZZ \to e^-e^+\mu^-\mu^+$ then correcting for the branching fraction $\mathcal{B}(ZZ \to e^-e^+\mu^-\mu^+)$.

The percentage contributions from gluon-gluon fusion processes are shown in Table 2.3.

$\sqrt{s} = 7$ **TeV**	$\sigma(ee\mu\mu)$ **(fb)**	**Value shift (%)**	
		PDF	**Scale**
Zero-width	13.99 ± 0.01	$^{+2.9}_{-2.2}$	$^{+3.8}_{-2.7}$
$66 < m_{12} < 116$ GeV, $66 < m_{34} < 116$ GeV	13.33 ± 0.01	$^{+2.9}_{-2.2}$	$^{+3.7}_{-2.7}$
$66 < m_{12} < 116$ GeV, $66 < m_{34} < 116$ GeV, $p_{\mathrm{T}}(\ell) > 7$ GeV, $\lvert\eta(\ell)\rvert < 3.16$, $\Delta R > 0.2$	10.59 ± 0.01	$^{+3.5}_{-2.3}$	$^{+3.9}_{-2.7}$
$66 < m_{12} < 116$ GeV, $m_{34} > 20$ GeV	16.74 ± 0.02	$^{+2.7}_{-2.2}$	$^{+3.3}_{-2.5}$
$66 < m_{12} < 116$ GeV, $m_{34} > 20$ GeV, $p_{\mathrm{T}}(\ell) > 7$ GeV, $\lvert\eta(\ell)\rvert < 3.16$, $\Delta R > 0.2$	12.57 ± 0.02	$^{+3.2}_{-2.3}$	$^{+4.4}_{-2.2}$

$\sqrt{s} = 8$ **TeV**	$\sigma(ee\mu\mu)$ **(fb)**	**Value shift (%)**	
		PDF	**Scale**
Zero-width	17.21 ± 0.01	$^{+2.7}_{-2.0}$	$^{+3.7}_{-2.7}$
$66 < m_{12} < 116$ GeV, $66 < m_{34} < 116$ GeV	16.39 ± 0.01	$^{+2.7}_{-2.0}$	$^{+3.5}_{-2.5}$
$66 < m_{12} < 116$ GeV, $66 < m_{34} < 116$ GeV, $p_{\mathrm{T}}(\ell) > 7$ GeV, $\lvert\eta(\ell)\rvert < 2.7$, $\Delta R > 0.2$	10.54 ± 0.01	$^{+3.4}_{-2.2}$	$^{+3.8}_{-2.9}$

Table 2.1: Cross Sections calculated at NLO in QCD with MCFM version 6.3 for $pp \to ZZ \to e^-e^+\mu^-\mu^+$. The cross section for the $llll$ final state is equal to these cross sections multiplied by two. The columns labeled "PDF" give the error derived from the 52 CT10 error sets and the difference between CT10 and MSTW2008, while the ones labeled 'Scale' give the error from changing the factorisation and renormalisation scales up and down by a factor of two from the default value of $\frac{1}{2}m(ZZ)$. The absolute errors on the cross section are due to Monte Carlo statistics.

Selection	**7 TeV**	**8 TeV**
Zero-Width	6.18 $^{+0.27}_{-0.21}$ pb	7.61 $^{+0.31}_{-0.24}$ pb
$66 < m_{12} < 116$ GeV $66 < m_{34} < 116$ GeV	5.89 $^{+0.24}_{-0.21}$ pb	7.24 $^{+0.29}_{-0.24}$ pb

Table 2.2: Total $pp \to ZZ$ cross sections at 7 TeV and at 8 TeV, obtained using MCFM. The uncertainty quoted is the total theoretical uncertainty arising from PDF uncertainties and uncertainties on the factorisation and renormalisation scales, obtained as described in the text.

Selection	$\sqrt{s} = 7$ **TeV**
Zero-Width	5.5%
$66 < m_{12} < 116$ GeV, $66 < m_{34} < 116$ GeV	5.4%
$66 < m_{12} < 116$ GeV, $66 < m_{34} < 116$ GeV, $p_{\mathrm{T}}(\ell) > 7$ GeV, $\lvert\eta(\ell)\rvert < 3.16$, $\Delta R < 0.2$	5.8%
$66 < m_{12} < 116$ GeV, $m_{34} > 20$ GeV	4.6%
$66 < m_{12} < 116$ GeV, $m_{34} > 20$ GeV, $p_{\mathrm{T}}(\ell) > 7$ GeV, $\lvert\eta(\ell)\rvert < 3.16$, $\Delta R < 0.2$	5.1%

Selection	$\sqrt{s} = 8$ **TeV**
Zero-Width	5.9%
$66 < m_{12} < 116$ GeV, $66 < m_{34} < 116$ GeV	5.9%
$66 < m_{12} < 116$ GeV, $66 < m_{34} < 116$ GeV, $p_{\mathrm{T}}(\ell) > 7$ GeV, $\lvert\eta(\ell)\rvert < 2.7$, $\Delta R < 0.2$	6.8%

Table 2.3: Percentage contribution of the $gg \to ZZ$ process relative to the total cross section, obtained using MCFM.

2.2 Kinematic Distributions

2.2.1 Comparison of $ZZ \to \ell^-\ell^+\ell^-\ell^+$ at 7 TeV and 8 TeV

Figures 2.3 and 2.4 show comparisons of kinematic distributions in $ZZ \to \ell^-\ell^+\ell^-\ell^+$ decays at 7 TeV and 8 TeV, simulated using the POWHEGBOX[21] generator to model the quark-antiquark annihilation process and the GG2ZZ [22] generator to model the gluon-gluon fusion process, where the samples from the two generators are combined according to the percentages given in Table 2.3. In Figure 2.3 the kinematic distributions are plotted after requiring that both Z bosons have $66 < m_{\ell^-\ell^+} < 116$ GeV, whilst in Figure 2.4 the requirement on the most off-shell Z is relaxed to $m_Z > 20$ GeV. In both cases the distributions of $m(ZZ)$, $p_{\mathrm{T}}(ZZ)$, leading [1] Z p_{T} and the p_{T} of the highest and lowest p_{T} leptons are observed to tend towards slightly higher energies at 8 TeV than at 7 TeV. The pseudo-rapidity distributions of the highest and lowest p_{T} leptons are observed to be wider at 8 TeV, with a greater fraction of the leptons at high pseudo-rapidity.

[1] Throughout this thesis the 'leading' particle is defined as the one with highest p_{T}.

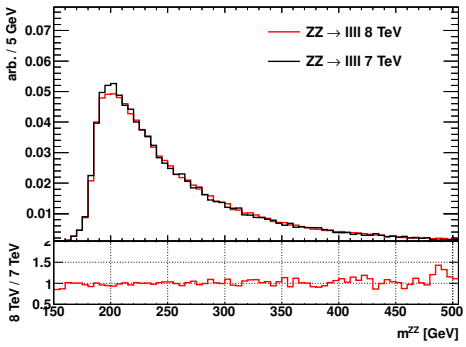

(a)

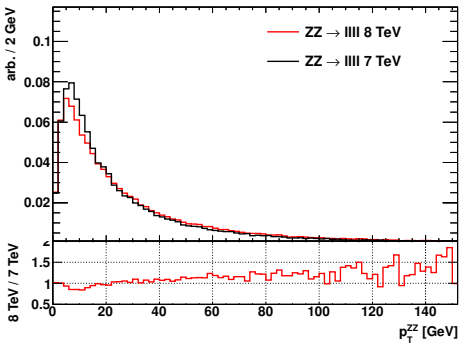

(b)

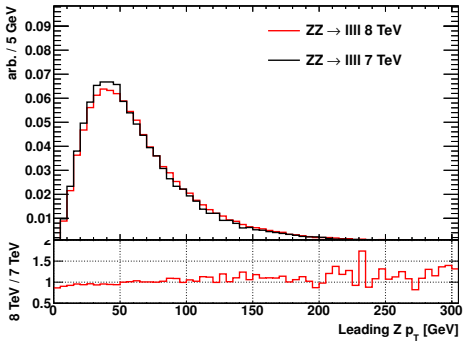

(c)

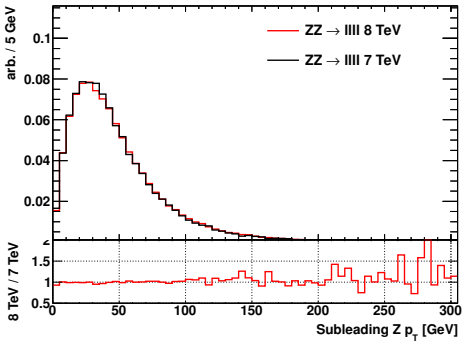

(d)

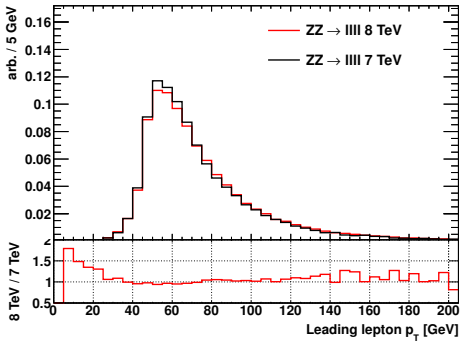

(e)

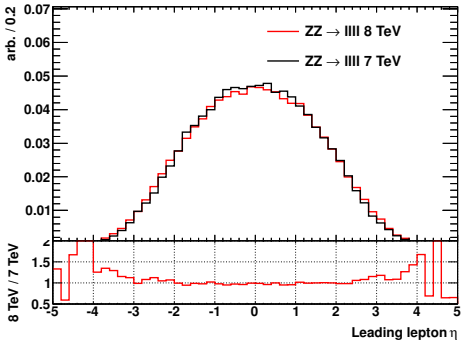

(f)

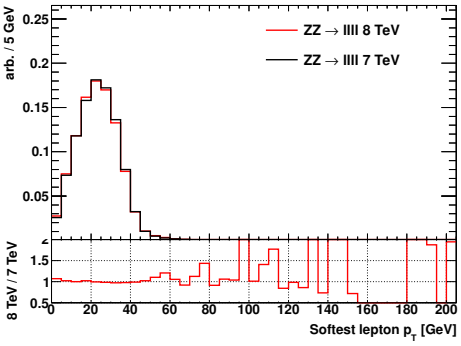

(g)

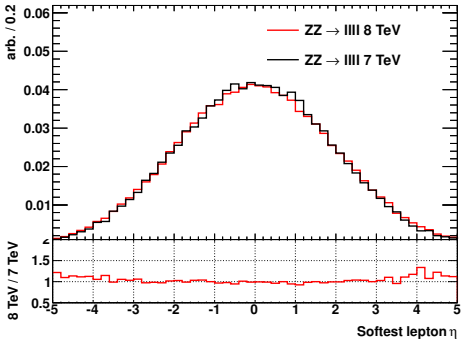

(h)

Figure 2.3: Comparison of generator level distributions, normalised to unit area, for $ZZ \to \ell^-\ell^+\ell^-\ell^+$ at $\sqrt{s} = 7$ TeV and $\sqrt{s} = 8$ TeV. Both Z bosons are required to have $66 < m_Z < 116$ GeV. Figures (a) and (b) show the mass and p_{T} of the ZZ system, respectively. Figures (c) and (d) show the p_{T} of the leading and subleading Z, respectively. Figure (e) shows the p_{T} of the highest p_{T} lepton in the event, and figure (f) shows its η. Similarly figures (g) and (h) show the p_{T} and η of the lowest p_{T} lepton in the event.

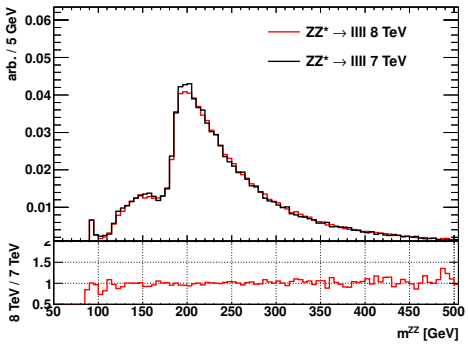

(a)

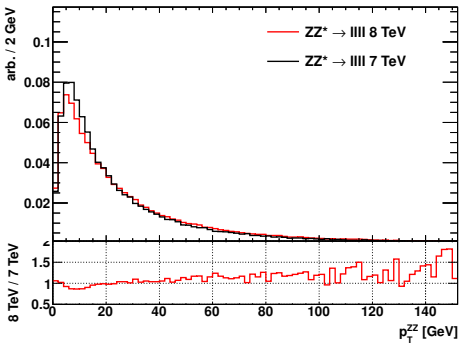

(b)

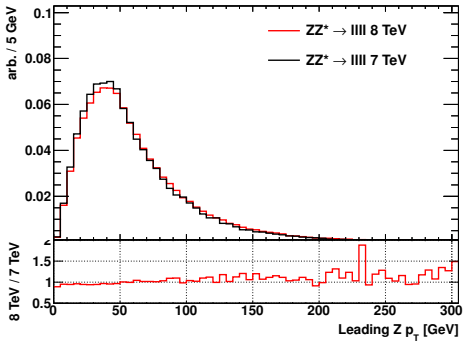

(c)

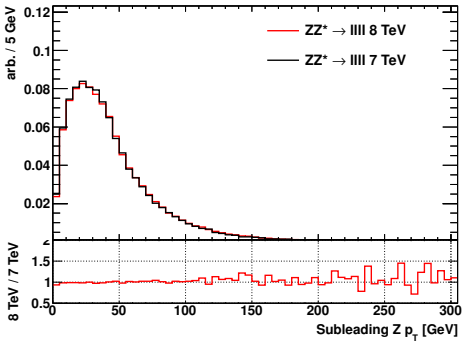

(d)

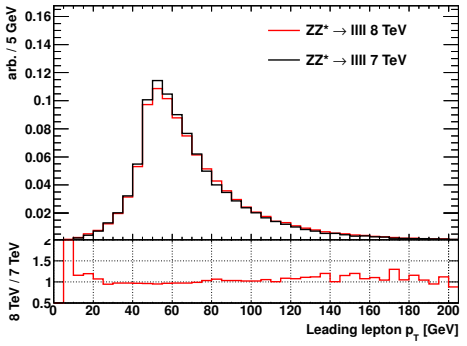

(e)

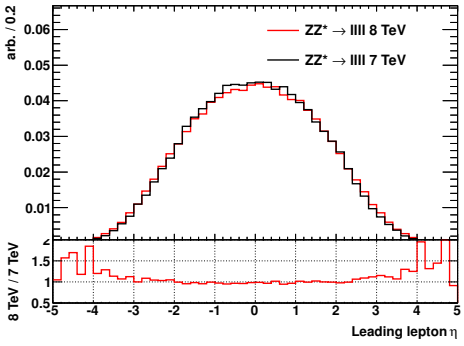

(f)

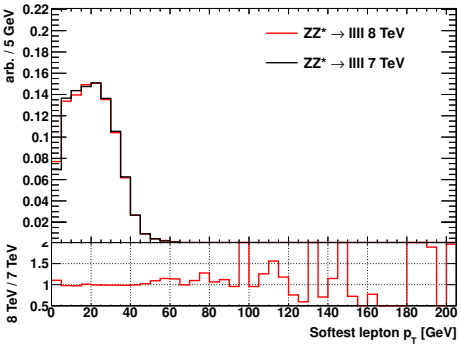

(g)

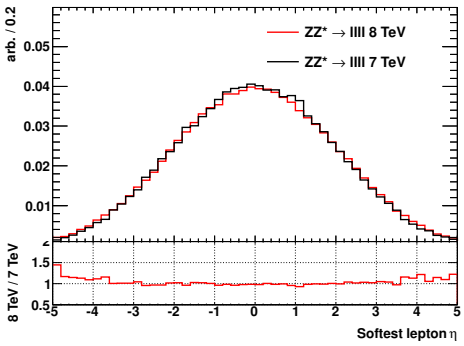

(h)

Figure 2.4: Comparison of generator level distributions, normalised to unit area, for $ZZ^* \to \ell^-\ell^+\ell^-\ell^+$ at $\sqrt{s} = 7$ TeV and $\sqrt{s} = 8$ TeV. One Z is required to have $66 < m_Z < 116$ GeV and the other $m_Z > 20$ GeV. Figures (a) and (b) show the mass and p_{T} of the ZZ system, respectively. Figures (c) and (d) show the p_{T} of the leading and subleading Z, respectively. Figure (e) shows the p_{T} of the highest p_{T} lepton in the event, and figure (f) shows its η. Similarly figures (g) and (h) show the p_{T} and η of the lowest p_{T} lepton in the event.

2.2.2 Comparison of $gg \to ZZ$ and $qq \to ZZ$

Figure 2.5 shows a comparison of kinematic distributions in $gg \to ZZ$ (simulated using GG2ZZ) and $qq \to ZZ$ events (simulated using POWHEGBOX), requiring that both Z bosons have $66 < m_{\ell^-\ell^+} < 116$ GeV. The $m(ZZ)$ distribution is similar in both processes, however the $p_{\mathrm{T}}(ZZ)$ distribution is much harder in the case of $gg \to ZZ$. This can be attributed to increased initial state radiation in the gluon-gluon fusion process. As a consequence of this, the leading Z p_{T} distribution is slightly harder in the $gg \to ZZ$ process, whilst the subleading Z p_{T} is slightly softer. The leptons produced in $gg \to ZZ$ decays are much more central in η, and have slightly higher p_{T} on average than in $qq \to ZZ$ decays.

2.2.3 Z Mass Distributions

Figure 2.6 shows the Z boson invariant mass distributions in $ZZ \to \ell^-\ell^+\ell^-\ell^+$ events at 7 TeV after applying the lepton kinematic requirements described in Section 2.1.2. Figure (a) shows the invariant mass of the Z boson closest to the Z pole, without applying any mass selections. Figure (b) shows the invariant mass of the remaining Z boson, after requiring that the first Z boson has $66 < m_{\ell^-\ell^+} < 116$ GeV. The rise in events around 60 GeV in figure (a) is due to singly-resonant $Z \to \ell^-\ell^+\ell^-\ell^+$ decays; these events are all rejected by the $66 < m_Z < 116$ GeV requirement.

2.2.4 Generator Comparisons for $ZZ \to \ell^-\ell^+\ell^-\ell^+$

Figures 2.7 and 2.8 show comparisons of kinematic distributions in $qq \to ZZ \to e^-e^+\mu^-\mu^+$ events generated using different Monte Carlo generators. The generators compared are SHERPA, MC@NLO, POWHEGBOX, HERWIG, HERWIG++ and PYTHIA; descriptions of these generators are given in Section 1.3.1. In all figures both Z bosons are required to have have $66 < m_{\ell^-\ell^+} < 116$ GeV.

There is generally good agreement between different generators in the four-lepton invariant mass ($m(ZZ)$) distribution, although SHERPA produces a larger low tail, and MC@NLO gives a much softer distribution. Similarly, MC@NLO gives a softer distribution for the four-lepton transverse momentum compared to the other generators, whilst PYTHIA gives a harder distribution. This distribution is particularly sensitive to ISR: in all of the generators other than PYTHIA and HERWIG one or more hard emissions are modelled exactly in the matrix element. It is somewhat surprising that HERWIG gives such good agreement with the NLO

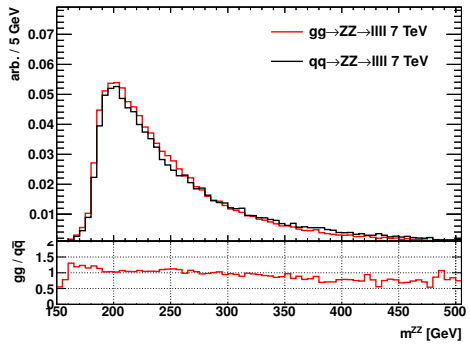

(a)

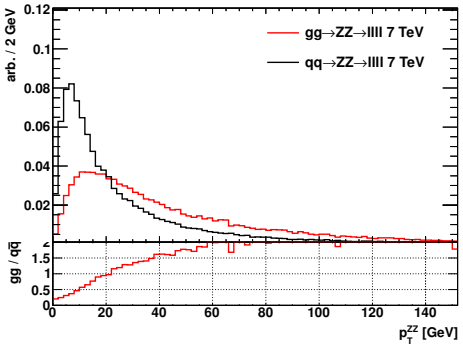

(b)

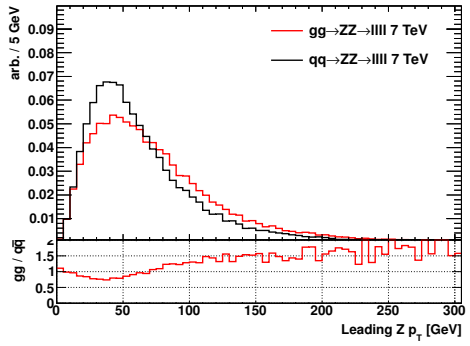

(c)

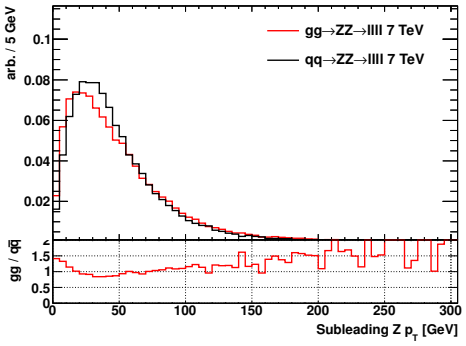

(d)

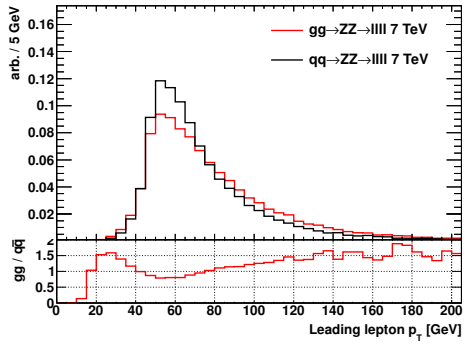

(e)

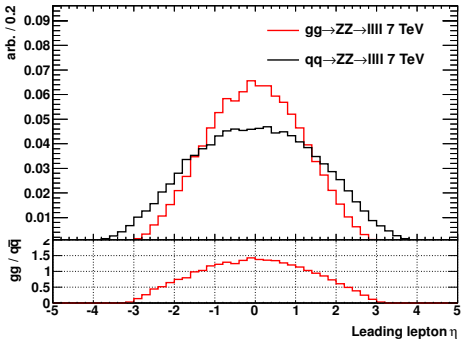

(f)

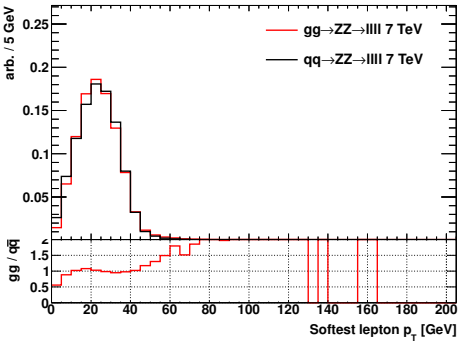

(g)

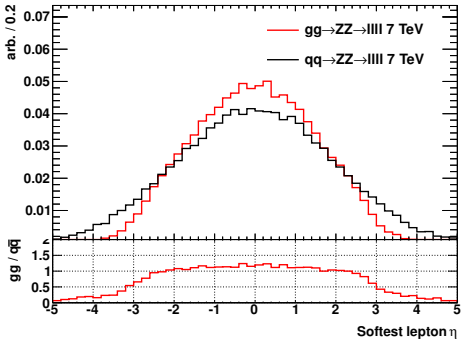

(h)

Figure 2.5: Comparison of generator level distributions, normalised to unit area, for $ZZ \to \ell^-\ell^+\ell^-\ell^+$ proceeding via qq and gg interactions. Both Z bosons are required to have $66 < m_Z < 116$ GeV. Figures (a) and (b) show the mass and p_{T} of the ZZ system, respectively. Figures (c) and (d) show the p_{T} of the leading and subleading Z, respectively. Figure (e) shows the p_{T} of the highest p_{T} lepton in the event, and figure (f) shows its η. Similarly figures (g) and (h) show the p_{T} and η of the lowest p_{T} lepton in the event.

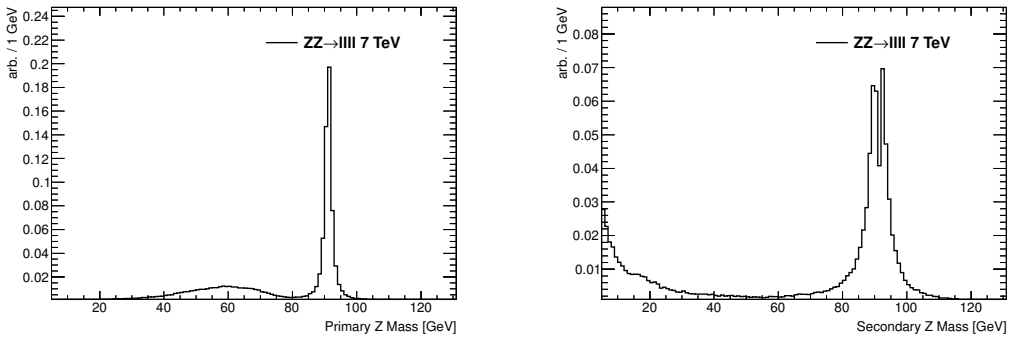

(a) (b)

Figure 2.6: Z boson invariant mass distributions in $ZZ \to \ell^-\ell^+\ell^-\ell^+$ events at 7 TeV after applying the lepton kinematic requirements. Figure (a) shows the invariant mass of the Z boson closest to the Z pole, without applying any mass selections. Figure (b) shows the invariant mass of the remaining Z boson, after requiring that the first Z boson has $66 < m_{\ell^-\ell^+} < 116$ GeV.

generators in this distribution. HERWIG gives much harder transverse momentum distributions for both Z bosons, and consequently harder distributions for the hardest and the softest lepton. Conversely, MC@NLO gives softer transverse momentum distributions for the Z bosons, and consequently softer transverse momentum distributions for the hardest and the softest lepton.

Figure 2.8 shows the invariant mass distribution of the di-electron and di-muon pairs. Good agreement is seen between the different generators, with the exception of MC@NLO, which uses a zero-width approximation for the Z bosons, and SHERPA, which is seen to have a slightly wider Z lineshape.

The difference in the Z line-shape observed between SHERPA and the other generators is attributed to the fact that SHERPA applies QED FSR in a different way. For all of the other generators compared in Figure 2.8, PHOTOS [37] is used to model QED radiation, whereas SHERPA has its own internal treatment, described below.

There are two ways of applying QED radiation to a $ZZ \to \ell^-\ell^+\ell^-\ell^+$ final state. The radiation can either be applied from the full four-lepton multipole, distributing the recoil within the multipole, or assuming two separate dipoles, $Z[\ell\ell]$ and $Z[\ell'\ell']$, each of which undergoes QED radiation independently from the other. The latter treatment leaves the mass of each dilepton pair and of the four-lepton system invariant, whereas the former treatment leaves only the mass of the four-lepton system invariant. PHOTOS uses the $(\ell\ell)(\ell'\ell')$ approach, whilst the SHERPA samples used in Figure 2.8 use the $(\ell\ell\ell\ell)$ approach.

Figure 2.9 shows the difference between the Z lineshape in SHERPA samples

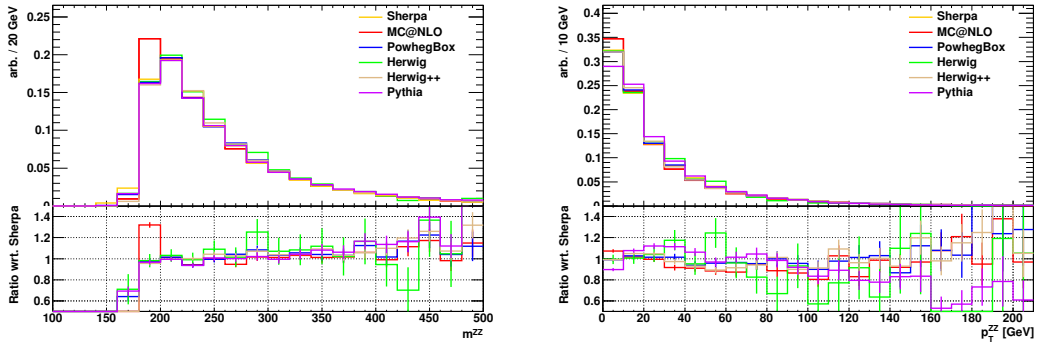

(a)

(b)

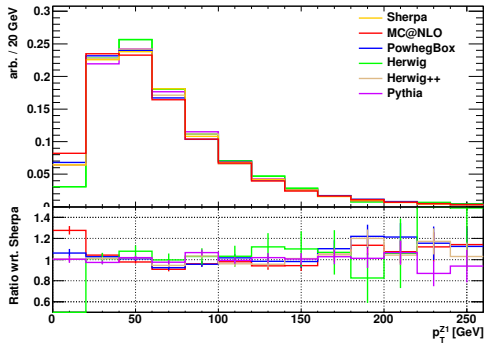

(c)

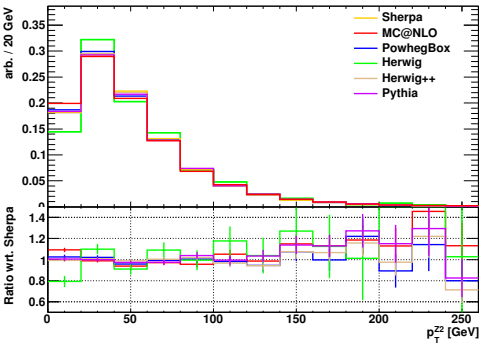

(d)

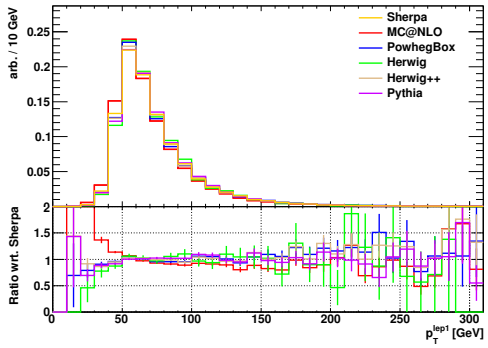

(e)

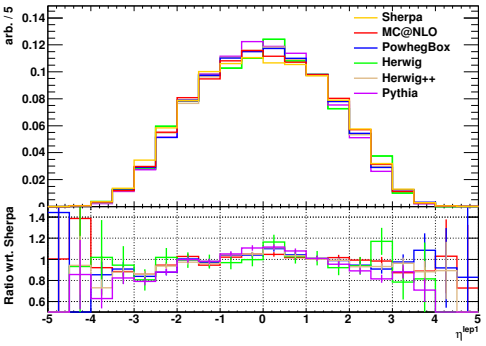

(f)

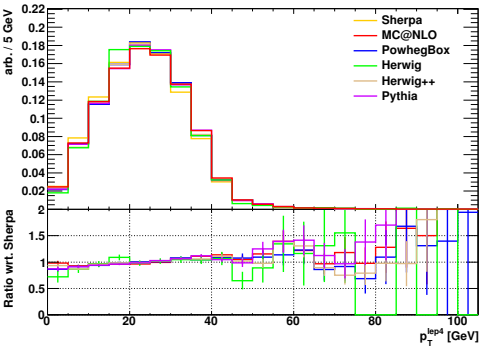

(g)

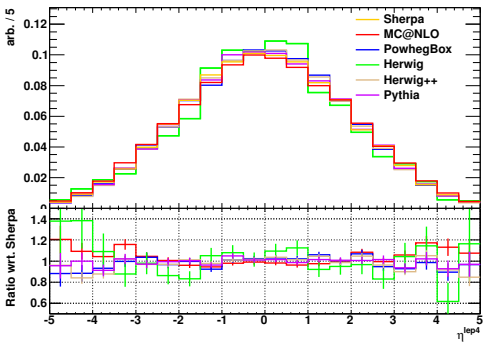

(h)

Figure 2.7: Comparison of generator level distributions, normalised to unit area, for $qq \to ZZ \to e^-e^+\mu^-\mu^+$ as produced by different generators. Both Z bosons are required to have $66 < m_{\ell^-\ell^+} < 116$ GeV. Figures (a) and (b) show the mass and p_{T} of the ZZ system, respectively. Figures (c) and (d) show the p_{T} of the leading and subleading Z, respectively. Figure (e) shows the p_{T} of the highest p_{T} lepton in the event, and figure (f) shows its η. Similarly figures (g) and (h) show the p_{T} and η of the lowest p_{T} lepton in the event.

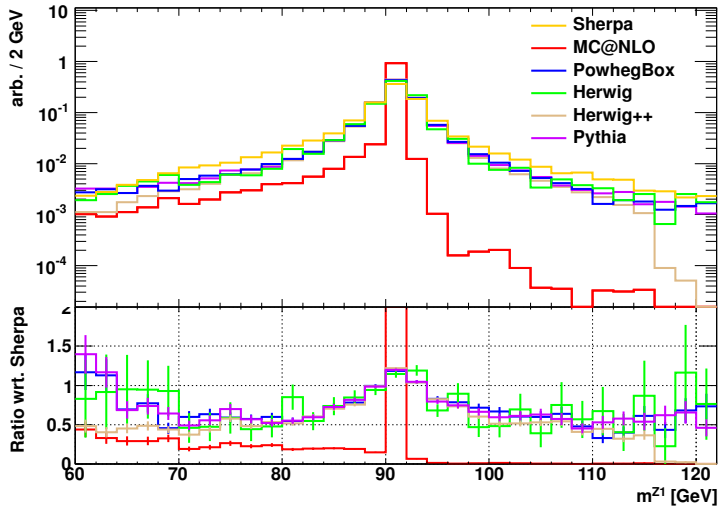

(a)

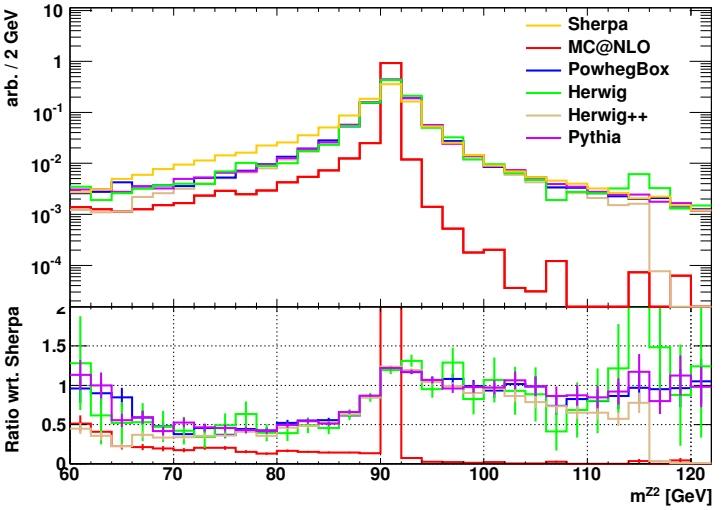

(b)

Figure 2.8: Comparison of generator level m_Z distributions, normalised to unit area, for $qq \to ZZ \to e^-e^+\mu^-\mu^+$ as produced by different generators. Both Z bosons are required to have $66 < m_{\ell^-\ell^+} < 116$ GeV. Figure (a) shows the invariant mass distribution for the di-electron pair whilst Figure (b) shows the invariant mass distribution for the di-muon pair.

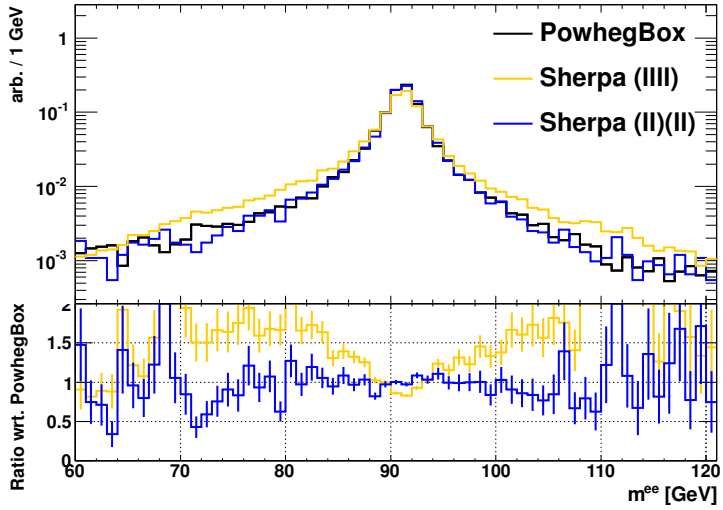

(a)

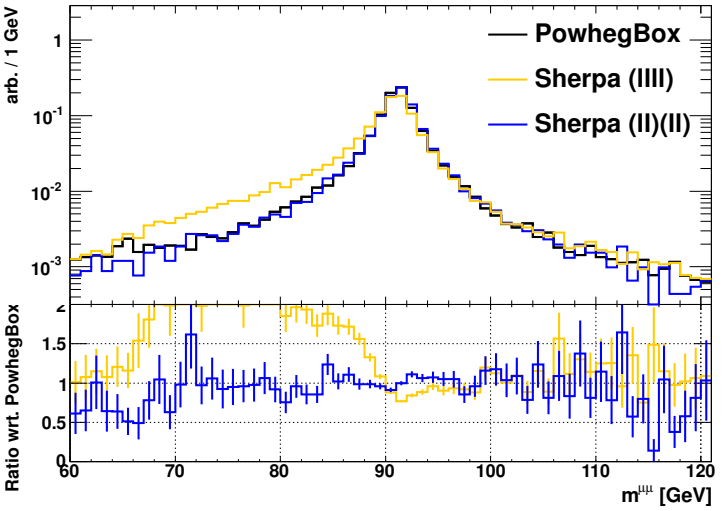

(b)

Figure 2.9: Generator level m_Z distributions, comparing the distributions obtained from SHERPA by applying the QED radiation from the full $llll$ multipole (labelled $(llll)$), and assuming two separate dipoles, $Z[\ell\ell]$ and $Z[\ell'\ell']$ and radiating from them (labelled $(ll)(ll)$). The distribution from POWHEGBOX, which uses the second approach, is also shown for comparison. All distributions are normalised to unit area, and both Z bosons are required to have $66 < m_{\ell^-\ell^+} < 116$ GeV. Figure (a) shows the invariant mass distribution for the di-electron pair whilst Figure (b) shows the invariant mass distribution for the di-muon pair.

generated using the two approaches; the Z lineshape in SHERPA samples generated using the $(\ell\ell)(\ell'\ell')$ approach agree with the predictions from the generators using PHOTOS. It is not clear which is the correct approach theoretically [38], so additional systematics are assigned to account for differences resulting from the two approaches.

In conclusion, rather good agreement is seen between the different generators, especially in the distributions to which the experimental selections are most sensitive (lepton p_{T} and η, and di-lepton invariant mass), with the exception of the different di-lepton mass distribution in SHERPA, for which the difference is understood.

2.3 Nominal Signal Sample

POWHEGBOX is used as the nominal Monte Carlo generator to model the $qq \to ZZ \to \ell^-\ell^+\ell^-\ell^+$ process. POWHEGBOX generates events to NLO in QCD, and will give NLO accuracy in inclusive distributions not making requirements on the p_{T} of additional parton emissions; most of the ZZ distributions of interest fall into this category, with the exception of distributions such as the p_{T} of the ZZ system. Additionally, the dependence on the choice of factorisation and renormalisation scales is expected to be smaller for a NLO calculation. MC@NLO is also a NLO generator, but is not chosen since it does not simulate the width of the Z bosons; HERWIG++ would be another choice of NLO generator, but is seen to give similar kinematic distributions to POWHEGBOX.

In addition, the GG2ZZ generator is used to model the $gg \to ZZ \to \ell^-\ell^+\ell^-\ell^+$ process. When estimating efficiencies and expected distributions, the samples generated using POWHEGBOX and GG2ZZ are combined, normalised according to the cross section of the two processes; this is referred to as POWHEGBOX+GG2ZZ. Both samples are generated using PDF set CT10 [35]. In POWHEGBOX the factorisation and renormalisation scales are set to the mass of the four-lepton system $m(ZZ)$; in GG2ZZ they are set to m_Z. Both samples are normalised to the cross section predicted by MCFM using the CT10 PDF set and scale set to $\frac{1}{2}m(ZZ)$, as given in the tables above. For the 8 TeV analysis, an event-by-event reweighting is applied to the POWHEGBOX sample to reweight to a scale of $\frac{1}{2}m(ZZ)$. This is done by assigning an weight to each event, which is the fractional difference in fiducial cross section predicted by MCFM at the two-scales, binned in terms of the leading Z boson. The changes in results after applying this

reweighting compared to just normalising to a cross section calculated using a scale of $\frac{1}{2}m(ZZ)$ are negligible.

SHERPA is used as an alternative Monte Carlo generator to cross-check efficiency estimates from POWHEGBOX. SHERPA is chosen because although it is only a LO generator, it simulates real additional parton emissions in the matrix-element, and so should give improved modelling of kinematic distributions; it also uses a different model for QED radiation from that used in the POWHEGBOX samples, as described above. SHERPA is also used to estimate the event yield in the presence of anomalous triple gauge couplings.

2.4 Anomalous Triple Gauge Couplings

The ZZZ and $ZZ\gamma$ (collectively ZZV) vertices are forbidden at tree level in the Standard Model, and arise and only at the level of $\mathcal{O}(10^{-4})$ in one-loop corrections [34]. Such couplings may however arise as the result of contributions from New Physics (NP). Anomalous neutral triple gauge couplings (henceforth referred to as nTGCs) are introduced by means of an effective Lagrangian framework. The basic assumption is that there is some NP beyond the Standard Model at a mass scale Λ, far beyond the reach of current experiments. The resulting new particles are thus not directly observable, and the only observable effect of the NP is anomalous interactions of SM particles. Since in ZZV couplings there are always at least two identical particles, Bose statistics forbid ZZV vertices with all particles on-shell; at least one of the bosons must thus be off-shell. The most general form of the anomalous couplings, assuming Lorentz and $U(1)_{EM}$ gauge invariance, gives two independent couplings for each of the ZZV vertices, or four parameters in total. Two of these, denoted f_4^Z and f_4^γ, give rise to CP violating interactions, whilst the remaining two, f_5^Z and f_5^γ, give CP conserving interactions. A priori there is no relation between these couplings.

The most general form of the Lagrangian for the effective theory is [39]:

$$\mathcal{L} = \frac{e}{m_Z^2}\left[f_4^V(\partial_\mu V^{\mu\beta})Z_\alpha(\partial^\alpha Z_\beta) + f_5^V(\partial^\mu V_{\mu\alpha})(\tilde{Z}^{\alpha\beta}Z_\beta)\right] \tag{2.6}$$

where $V = Z, A$ for the Z or photon tensor, $\tilde{Z}_{\mu\nu} = \frac{1}{2}\epsilon_{\mu\nu\rho\sigma}Z^{\rho\sigma}$ and $V_{\mu\nu} = \partial_\mu V_\nu - \partial_\nu V_\mu$.

Since the departure from the SM prediction grows rapidly with the partonic

centre of mass energy $\sqrt{\hat{s}}$, and may eventually violate unitarity, it is conventional to apply a *form-factor* to the basic couplings given above, in order to maintain unitarity at high $\sqrt{\hat{s}}$. The form-factor is applied as:

$$f_i^V(\hat{s}) = \frac{f_{i,0}^V}{(1+\hat{s}/\Lambda)^n} \tag{2.7}$$

where $i = 4, 5$, $V = Z, \gamma$ and Λ is taken to be the scale at which the new physics becomes directly observable. n gives the power of the form-factor, and is generally taken to be $n = 3$ [40]. For limits derived at a fixed $\hat{s}$ it is trivial to convert between coupling parameters derived with different choices of Λ and n and at different values of $\hat{s}$. Unfortunately at hadron colliders limits arise from integration of a range of $\hat{s}$, so it is not possible to compare limits derived at different Λ, n or for different ranges of $\hat{s}$. Limits are therefore often also derived without a form-factor (or equivalently, taking $\Lambda = \infty$) to allow comparison between the results of different experiments.

2.4.1 Origin of nTGCs

The simplest model for generating anomalous nTGCs is from heavy fermion loops arising from a new generation of fermions; this is shown in Figure 2.10. New heavy fermions arise in many models beyond the SM, such as SUSY, GUTs and Technicolor. Such loops can only generate the CP-conserving couplings f_5^V; higher-order processes are needed to generate CP-violating couplings f_4^V. A heavy fermion with Standard Model couplings to the Z and γ, would give couplings [41]:

$$f_5^V \propto \frac{\alpha}{4\pi}\frac{m_Z^2}{M_F^2} \tag{2.8}$$

where M_F is the heavy fermion mass. If the new family of heavy fermions were exactly degenerate in mass, the couplings would vanish as the combination of heavy fermion contributions would exactly cancel. If there was a mass splitting between doublets in the new family of order m_Z the couplings could be restored, but would be proportional to m_Z^4/M_F^4 and thus heavily suppressed. In a more experimentally favourable scenario, if one particle of the family had a mass far lower than the rest of the family, the coupling would be restored with a strength similar to that given in Equation 2.8. This is still suppressed by the loop $\alpha/4\pi$

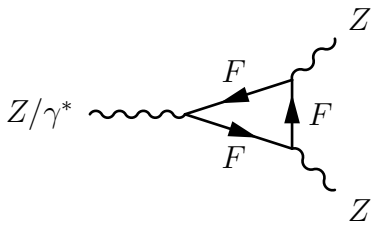

Figure 2.10: Production of a ZZV vertex through a heavy fermion loop.

factor, and yields anomalous couplings of order 10^{-3} for M_F in the 100 GeV range. Contributions from loops of SM particles generate couplings at the level of $\mathcal{O}(10^{-4})$ [2].

One concrete example of a new physics model giving rise to anomalous nTGCs is supersymmetry [41]. In the MSSM, the additional fermion loop diagrams would arise from charginos and neutralinos. The charginos couple to the gauge bosons through their gaugino and higgsino components, and so contribute to the f_5^Z and f_5^γ couplings. The neutralinos contribute only through the higgsino coupling, so contribute only to the f_5^Z coupling.

2.4.2 Signatures at Hadron Colliders

Non-zero nTGCs would manifest themselves as an increased ZZ production cross section, particularly at high $\sqrt{\hat{s}}$. This means that the enhancement of the cross section is most apparent at high ZZ invariant mass and high Z transverse momentum [40], and at large scattering angles. Figure 2.11 shows the $m(ZZ)$ and p_{T} of the leading Z boson in Standard Model $ZZ \to \ell^-\ell^+\ell^-\ell^+$ decays, as well as in $ZZ \to \ell^-\ell^+\ell^-\ell^+$ decays in four samples generated with anomalous nTGCs included in the simulation. The nTGC samples are generated with couplings close to the limits derived from previous experiments (see Section 2.5), and with $\Lambda = 3$ TeV and $n = 3$. As expected, the presence of nTGCs manifests itself as enhanced event counts at high $m(ZZ)$ and leading Z p_{T}.

[2] This is smaller than the maximal 10^{-3} stated for a new heavy fermion as in that case it was assumed one multiplet in the family was far lighter than the rest, which is not the case in the SM.

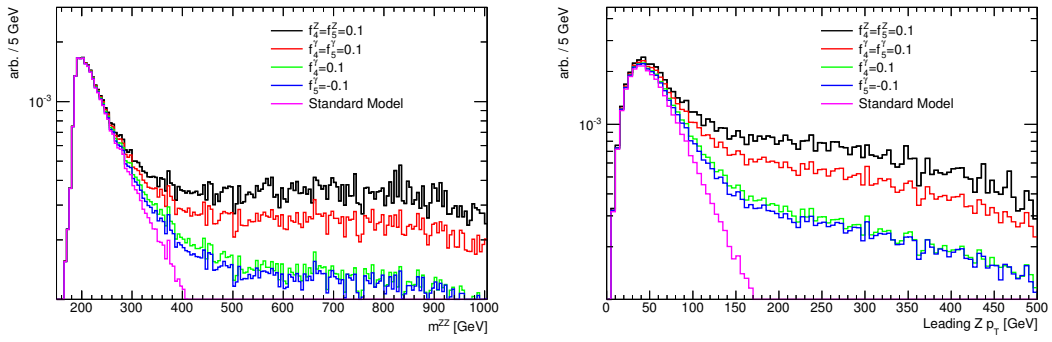

(a) (b)

Figure 2.11: (a) $m(ZZ)$ and (b) p_{T} of the leading Z boson in Standard Model $ZZ \to \ell^-\ell^+\ell^-\ell^+$ decays, as well as $ZZ \to \ell^-\ell^+\ell^-\ell^+$ decays in four samples generated with anomalous nTGCs included in the simulation. The nTGC samples are generated with $\Lambda = 3$ TeV and $n = 3$.

2.5 Previous Experimental Results

Diboson ZZ production was first observed in e^+e^- collisions at LEP in 1997 when the centre of mass energy of the collider first reached 183 GeV, the threshold for producing two on-shell Z bosons. The L3 experiment published the first observation and cross section measurement of on-shell ZZ production [42], based on 55.3 pb^{-1} of data collected at an average centre-of-mass energy of 182.7 GeV. All visible decay-channels were used in the measurement. Whilst no events were observed in the $\ell^-\ell^+\ell^-\ell^+$ final state, a total of 63 were observed in the other visible final states. The majority (47) of these were in the all-hadronic channel, which suffered from high backgrounds from $e^+e^- \to qq\gamma$ and $e^+e^- \to WW$. In this channel a neural network method was used to distinguish the signal events from the background. A log-likelihood fit of the neural network output and the observed mass spectra in the other channels was used to combine the channels, and gave a cross section of $\sigma_{ZZ} = 0.30\ ^{+0.22}_{-0.16}\ ^{+0.07}_{-0.03}$ pb, in very good agreement with the Standard Model prediction.

Measurements of the ZZ production cross section in e^+e^- collisions were later made by all four LEP experiments at centre of mass energies between 183 GeV and 209 GeV [43–46]. These have been combined at each centre of mass energy using a χ^2 minimisation technique, taking into account correlations between the systematic uncertainties [47]. The resulting combined cross sections as a function of centre of mass energy, shown in Figure 2.12, are in good agreement with theoretical predictions.

Each of the LEP experiments also set limits on the ZZZ and $ZZ\gamma$ anomalous triple gauge couplings f_i^V. The limits were set using the measured total ZZ

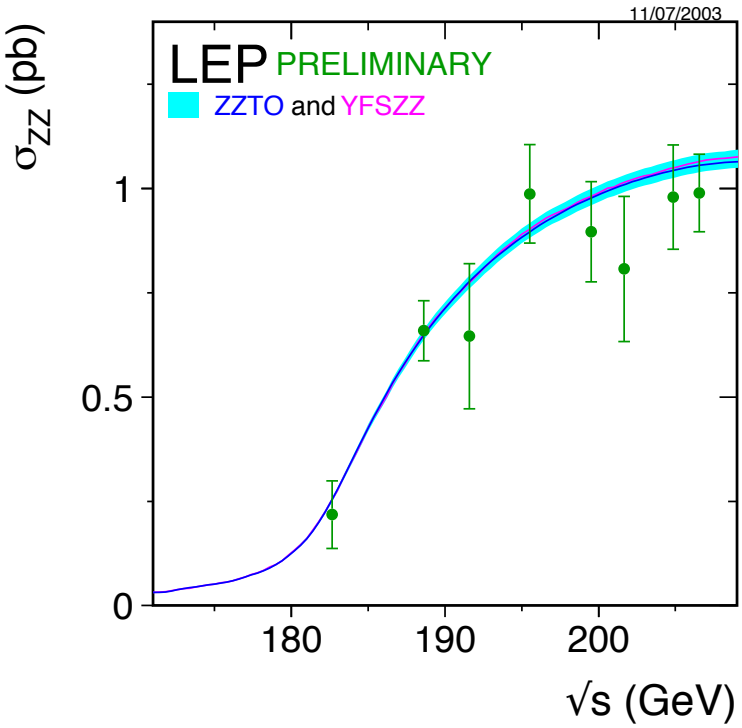

Figure 2.12: Measurements of the ZZ production cross section in e^+e^- collisions as a function of centre of mass energy $\sqrt{s}$. The measurements are a combination of measurements from the four LEP experiments. Figure from [47].

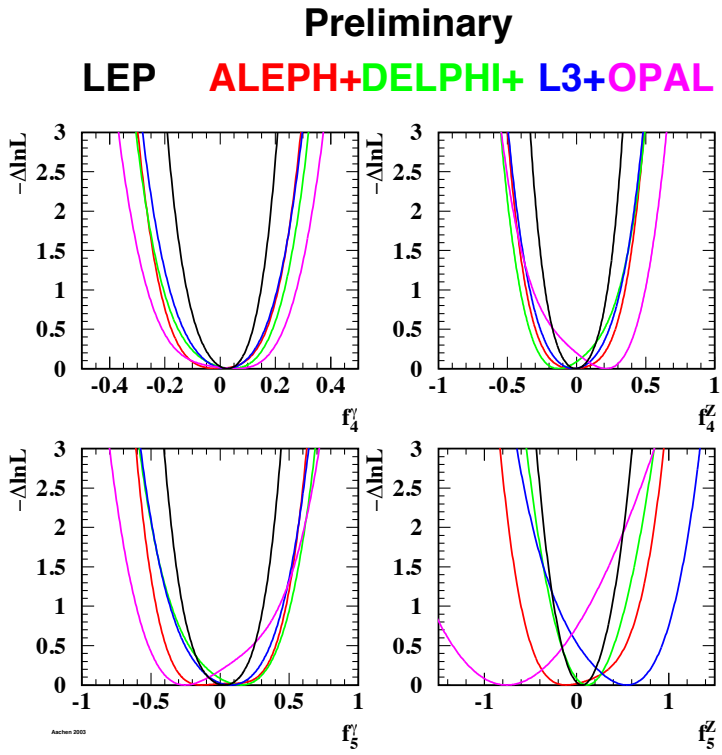

Figure 2.13: Negative log-likelihood curves for nTGC couplings from the four LEP experiments (coloured bands) and their combination (black band). No form-factor is applied. Figure from [47].

cross section, as well as kinematic distributions sensitive to aTGCs. ALEPH [46], DELPHI [48] and OPAL [49] used the $\cos(\theta_Z)$ distribution, where θ_Z is the production angle of the Z boson with respect to the beam axis. L3 [45] used fits to different kinematic variables in each decay channel. Each experiment first combined its limits across the different decay channels and centre of mass energies, and provided the negative log-likelihood as a function of the parameter to be combined. Limits were set varying each parameter independently, holding the other parameters at their standard model value of zero. Two parameter fits were also carried out. No deviations from the Standard Model were observed. The negative log-likelihood distributions from each of the experiments, as well as the combined negative log-likelihood, are shown in Figure 2.13, and the single parameter limits are given in Table 2.4.

Measurements of the ZZ production cross section in $p\bar{p}$ collisions at a centre of mass energy of $\sqrt{s} = 1.96$ TeV have been made at the Tevatron by both the D0 and the CDF experiments. D0 measured the ZZ cross section in 6.4 fb^{-1} of integrated luminosity using the $ZZ \to \ell^-\ell^+\ell^-\ell^+$ channel [50] and in 8.6 fb^{-1}

using the $ZZ \to \ell^-\ell^+\nu\bar{\nu}$ channel [51]. In the $ZZ \to \ell^-\ell^+\ell^-\ell^+$ channel 10 events were observed with the requirement that both dilepton pairs have mass above 30 GeV, with an expected background of 0.37 ± 0.13 events. Combining the two channels, the measured cross section for ZZ production with the requirement of $60 < m_Z < 120$ GeV was $\sigma(p\bar{p} \to ZZ) = 1.44\,^{+0.31}_{-0.28}\,(\text{stat})\,^{+0.17}_{-0.19}\,(\text{syst})$ pb, in agreement with the Standard Model prediction of $\sigma(p\bar{p} \to ZZ) = 1.3 \pm 0.1\,\text{pb}$. The observed kinematic distributions were also in good agreement with the Standard Model predictions.

CDF [52] measured the ZZ cross section using both the $ZZ \to \ell^-\ell^+\nu\bar{\nu}$ and $ZZ \to \ell^-\ell^+\ell^-\ell^+$ channels in 6 fb^{-1} of integrated luminosity. In the $ZZ \to \ell^-\ell^+\ell^-\ell^+$ channel, events were required to have two opposite-sign same-flavour lepton pairs, with one pair required to have invariant mass within ± 25 GeV of the Z mass, and the other in the range $40 < m_{\ell^-\ell^+} < 140$ GeV. 14 such events were observed, with an expected background of $0.26^{+0.53}_{-0.15}$ events. The measured cross section, combining the two channels and correcting to the zero-width approximation, was $\sigma(p\bar{p} \to ZZ) = 1.64\,^{+0.44}_{-0.38}\,(\text{stat} + \text{syst})\,\text{pb}$, again in agreement with the Standard Model prediction of $\sigma(p\bar{p} \to ZZ) = 1.4 \pm 0.1\,\text{pb}$.

D0 set limits on nTGCs using $ZZ \to \ell^-\ell^+\ell^-\ell^+$ decays in 1 fb^{-1} of data [53], requiring that both dilepton pairs had an invariant mass > 50 (70) GeV for di-muon (di-electron) pairs. No events were observed passing this selection. Limits were set by comparing observed number of events with the yields predicted in samples simulated with different values of the anomalous couplings. The resulting 95% confidence limits obtained by varying one parameter at a time and holding the rest at zero are shown in Table 2.4. Two-dimensional limits were also set.

The CMS experiment have measured the ZZ production cross section in pp collisions at 7 TeV [54] using $ZZ \to \ell^-\ell^+\ell^-\ell^+$ decays. In a dataset of 5 fb^{-1}, events with two opposite-sign same-flavour dilepton pairs were selected, with the requirement that the first di-lepton pair must be composed of electrons or muons and have a mass $60 < m_{\ell^-\ell^+} < 120$ GeV, and the second pair be composed of either electrons, muons or taus. In the case of the second pair being e^+e^- or $\mu^+\mu^-$ the same mass cut is applied as for the first pair. In the case of $\tau^+\tau^-$, the visible mass is required to satisfy $30 < m^{\text{vis}}_{\tau\tau} < 80$ GeV. In the $4e$,4μ and $2e2\mu$ channels they observed 54 events, with a Standard Model prediction of 54.5 ±0.3 (stat) ±4.8 (syst) (including a small background component). In the $2\ell2\tau$ channels, 11 events were observed, with a Standard Model prediction of 11.7 ± 0.8 (stat) ± 1.0 (syst) (including 4.4 events from background processes). Combining all final states, the measured cross section, requiring both Z bosons to be in the range $60 < m_Z < 120$

GeV, was found to be $\sigma(pp \to ZZ) = 6.24\,^{+0.86}_{-0.80}\,(\text{stat})\,^{+0.41}_{-0.32}\,(\text{syst}) \pm 0.14\,(\text{lumi})$ pb, in excellent agreement with the Standard Model prediction of 6.3 ± 0.4 pb. Limits were set on nTGCs using the observed four-lepton mass distribution for the $4e$,4μ and $2e2\mu$ channels combined. CMS recently also published a measurement of the ZZ production cross section at $\sqrt{s} = 8$ TeV in a dataset of 5.3 fb^{-1} [55], using a similar analysis to the $\sqrt{s} = 7$ TeV measurement. They measured the cross section to be $\sigma(pp \to ZZ) = 8.4 \pm 1.0\,(\text{stat}) \pm 0.7\,(\text{syst}) \pm 0.4\,(\text{lumi})$ pb, consistent with the Standard Model prediction of 7.7 ± 0.4 pb.

The observed 95% confidence limits on nTGCs from LEP, D0 and CMS are given in Table 2.4.

Experiment	Λ, n	f_4^Z	f_5^Z	f_4^γ	f_5^γ
LEP	∞, –	[-0.30, 0.30]	[-0.34, 0.38]	[-0.17, 0.19]	[-0.32, 0.36]
D0	1.2 GeV, 3	[-0.28, 0.28]	[-0.31, 0.29]	[-0.26, 0.26]	[-0.30, 0.28]
CMS	∞, –	[-0.011, 0.012]	[-0.012, 0.012]	[-0.013, 0.015]	[-0.014, 0.014]

Table 2.4: 95 % confidence level limits on anomalous triple gauge coupling parameters obtained from LEP [47], D0 [53] and CMS [54]. In each case the cutoff scale Λ and form factor n is indicated.

Part II

Experimental Description

Chapter 3

The ATLAS Detector at the LHC

3.1 The Large Hadron Collider

The Large Hadron Collider (LHC) is a particle accelerator located at CERN, the European Organisation for Nuclear Research, on the French-Swiss border near Geneva. The LHC is the world's most powerful particle accelerator, colliding beams of protons together at centre of mass energies of up to 8 TeV, with the aim of better understanding the workings of our Universe. It is installed in a tunnel of circumference 26.7 km, which previously held the Large Electron-Positron Collider (LEP), and is between 45 and 170 m below the ground. The beams are brought to collision at four points around the ring, at each of which a different experiment is located. The machine is also capable of colliding heavy ions, providing a complementary heavy-ion physics program.

The design of the LHC is described in detail in [56] and [57]. A brief summary is given in 3.1.1, and details of LHC operations in 2011 and 2012 are given in 3.1.2.

3.1.1 Machine Design

In normal operating mode, the LHC contains two counter-circulating beams of protons. Since the beams are of similarly charged particles orbiting in opposite directions, they require opposite bending fields, thus need to be in separate beam-pipes. Due to space and cost constraints, the two beam-pipes are contained within a single structure incorporating a twin bore superconducting magnet. Superconducting dipole magnets are used to bend the beams and keep them in orbit and superconducting quadrupole magnets are used to keep the beams focussed. The magnets must be cooled to 2K to retain their superconducting properties; this is achieved with a helium-based cooling system.

Protons are injected into the LHC from the SPS (Super Proton Synchrotron)

in bunches, at an energy of 450 GeV. They are then accelerated to the desired collision energy by means of superconducting Radio Frequency (RF) cavities. Once the particles are accelerated to full energy, the RF cavities are used to keep the particles in their bunches. The bunches are brought to collision at four points around the ring, at each of which a different experiment is located. The ATLAS experiment at Point 1 and the CMS experiment at Point 5 are general purpose detectors, and the LHCb experiment at Point 8 and ALICE at Point 2 are specialised detectors studying heavy-flavour physics and heavy-ion collisions respectively.

The rate at which collisions occur depends on the instantaneous luminosity $\mathcal{L}$ and the collision cross section σ, related by:

$$\frac{dN}{dt} = \mathcal{L} \cdot \sigma \tag{3.1}$$

The total cross section for proton-proton collisions at the LHC has been measured to be $98.3 \pm 0.2\,(\text{stat}) \pm 2.8\,(\text{syst})$ mb[1] at a centre of mass energy of 7 TeV [58], thus at the LHC design luminosity of 1×10^{34} cm^{-2}s^{-1} collisions occur at a rate of approximately 100 MHz.

The rate at which a particular physics process occurs depends on the cross section for the process in question. Since many of the physics processes under study at the LHC are very rare and have small cross sections, it is important to maximise the luminosity as much as possible. The instantaneous luminosity is given by:

$$\mathcal{L} = \frac{N_{\text{b}}^2 n_{\text{b}} f_{\text{rev}} F \gamma_{\text{r}}}{4\pi \epsilon_n \beta^*} \tag{3.2}$$

where:

- N_{b} is the number of particles per bunch,
- n_{b} is the number of bunches per beam,
- f_{rev} is the revolution frequency,
- F is a geometric function to account for the crossing angle between the beams (since they are generally not collided head on),
- γ_r is the relativistic Lorentz factor $(1 - v^2/c^2)^{-\frac{1}{2}}$.
- ϵ_n is the beam emittance, a measure of how uniform the momentum of particles in the beam is or how small the beam can be 'squeezed',

[1] $1\text{b} = 10^{-28}\text{m}^2$

- β^* is a measure of how narrow the beam is at the interaction point, or how 'squeezed' it is,

The geometrical cross section of the beam at the interaction point is proportional to $\epsilon_n \cdot \beta^*$. The instantaneous luminosity can be maximised by increasing the number of particles per bunch, decreasing the bunch spacing (or equivalently increasing the number of bunches per beam) or decreasing the size of the bunch at the interaction point by decreasing ϵ_n and β^*.

A measure of how many collisions have occurred is the integrated luminosity:

$$L = \int \mathcal{L}\, dt \tag{3.3}$$

The number of events occurring for a given process with cross section σ_{process} in a data sample corresponding to an integrated luminosity L is given by:

$$N_{\text{process}} = L \cdot \sigma_{\text{process}} \tag{3.4}$$

3.1.2 LHC Operation in 2011 and 2012

The LHC began operation in November 2009 with collisions at a centre of mass energy of 900 GeV, with the centre of mass energy rising to a world record 2.36 TeV by the end of the year. In 2010 the centre of mass energy was successfully increased to 7 TeV. Over 2010 and 2011 the LHC continued to run at $\sqrt{s} = 7$ TeV, with the instantaneous luminosity steadily increasing. In 2010 the LHC delivered 48.1 pb^{-1} of integrated luminosity to ATLAS and delivered 5.43 fb^{-1} in 2011. In 2012 the centre of mass energy was increased to 8 TeV, and the instantaneous luminosity further increased by increasing the number of particles per bunch slightly and decreasing ϵ_n and β^*, leading to a total integrated luminosity delivered to ATLAS in 2012 of 22.8 fb^{-1}.

Figure 3.1 shows the instantaneous luminosity as measured by ATLAS as a function of time between 2010 and 2012. Figure 3.2 shows the cumulative integrated luminosity delivered to ATLAS in 2011 and 2012. Details of the LHC operational parameters in 2011 and 2012, together with the nominal design values, are given in Table 3.1.

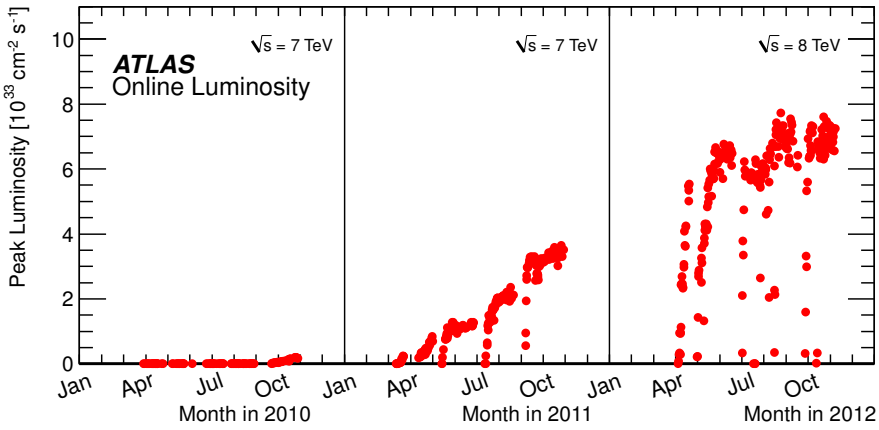

Figure 3.1: Peak instantaneous luminosity delivered by the LHC per run as a function of time from 2010 to 2012. Figure from [59].

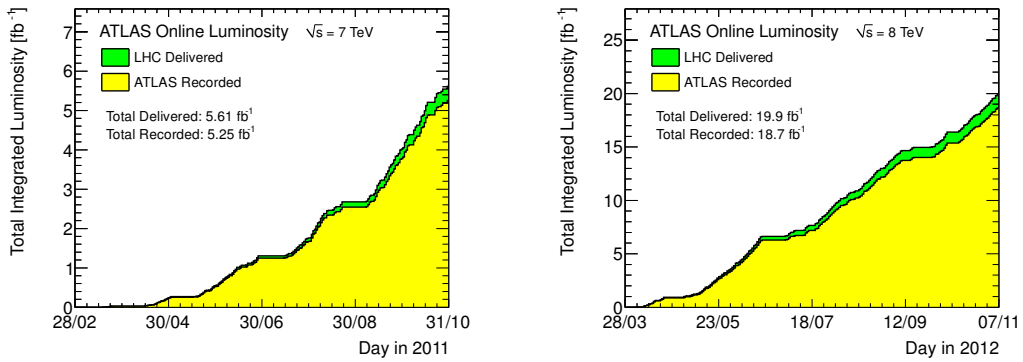

(a) (b)

Figure 3.2: Cumulative integrated luminosity as a function of time in (a) 2011 and (b) 2012. The totals for the two years are separate. Figures from [59].

Parameter	Nominal	2011 Operation	2012 Operation
Proton Energy	7 TeV	3.5 TeV	4 TeV
N_b	1.15×10^{11}	1.5×10^{11}	1.6×10^{11}
n_b	2808	1380	1380
Bunch spacing (ns)	25	50	50
β^* (m)	0.55	1.0	0.6
ϵ_n (μm)	3.75	1.9 - 2.3	1.7 - 3.0
Peak $\mathcal{L}$ (cm^{-2}s^{-1})	1.0×10^{34}	3.6×10^{33}	7.7×10^{33}

Table 3.1: LHC operational parameters. A comparison is made of the nominal design parameters [57], and those used in 2011 operation and in 2012 operation [60] [61].

3.2 The ATLAS Detector

ATLAS (A Toroidal LHC ApparatuS) is one of two general purpose particle-physics detectors at the LHC, built to study both proton-proton and ion-ion interactions. The high centre of mass energy and high luminosity of LHC proton-proton collisions allows the study of physics at the TeV scale for the first time, as well as precision measurements of the Standard Model. ATLAS has been designed to be capable of a wide range of measurements, including (but by no means limited to): high precision tests of QCD, electroweak interactions, and flavour physics; searching for and measuring the properties of the Higgs Boson; searches for supersymmetery; measurements of the properties of the top quark; searches for new vector bosons and searches for extra-dimensions.

The extremely high luminosity presents challenges which the detector has been designed to overcome. At design luminosity, 10^9 inelastic collisions occur per second, which results in multiple interactions - up to 35 in 2012 running - occurring simultaneously. The detector has been designed to cope with these high 'pile-up' conditions, as well as be capable of operating in the high radiation environment arising from the high luminosity. Many of the physics processes of interest occur at very small rates with respect to extremely high QCD background rates. The detector must therefore be capable of distinguishing processes of interest from the background.

To meet these challenges, ATLAS was designed with the following criteria in mind:

- High granularity to cope with high particle fluxes and overlapping events.
- Full azimuthal coverage to allow for missing transverse energy measurement, and large acceptance in pseudo-rapidity.
- Precision tracking to provide high charged particle momentum resolution and reconstruction efficiency, and to allow observation of secondary vertices to identify b-hadrons and τ-leptons.
- Precise electromagnetic calorimetry for electron and photon identification.
- Full-coverage hadronic calorimetry for accurate jet and missing transverse energy measurements.
- High muon identification efficiency, momentum resolution and charge determination over a wide range of momentum.

- Efficient triggering on low transverse-momentum objects.

The main performance goals are given in Table 3.2.

Detector Component	Design Resolution	η coverage	
		Measurement	Level 1 Trigger
Tracking	$\sigma_{p_T}/p_T = 0.05\% \, p_T \oplus 1\%$	± 2.5	None
EM Calorimetry	$\sigma_E/E = 10\%/\sqrt{E} \oplus 0.7\%$	± 3.2	± 2.5
Hadronic Calorimetry			
Barrel and End-Cap	$\sigma_E/E = 50\%/\sqrt{E} \oplus 3\%$	± 3.2	± 3.2
Forward	$\sigma_E/E = 100\%/\sqrt{E} \oplus 10\%$	$3.1 < \|\eta\| < 4.9$	$3.1 < \|\eta\| < 4.9$
Muon Spectrometer	$\sigma_{p_T}/p_T = 10\%$ at $p_T = 1$ TeV	± 2.7	± 2.4

Table 3.2: Performance goals of the ATLAS detector. Units of p_T and E are GeV.

A cut-away view of the ATLAS detector [62] is shown in Figure 3.3. The detector consists of an inner tracking detector, which is surrounded by electromagnetic and hadronic calorimeters and finally a muon spectrometer. The inner detector is immersed in a 2 T solenoidal field to allow for momentum measurement. The muon spectrometer is also immersed in a magnetic field, provided by an air-core toroid system which generates strong bending power over a large volume with a minimum of material, thus minimising multiple-scattering effects. A three-level trigger system is used to select events to read out. The various sub-systems are described in more detail in the following sections.

3.2.1 ATLAS Co-ordinate System

ATLAS uses a right-handed coordinate system with an origin at the nominal interaction point in the centre of the detector. The z-axis points along the beam-pipe, the x-axis towards the centre of the LHC ring, and the y-axis upwards. Particle directions and detector element positions are generally described by their azimuthal angle ϕ and their pseudorapidity η. The azimuthal angle describes the angle in the x-y plane, with $\phi = 0$ along the x axis, increasing clockwise around the beam-pipe. The pseudorapidity η is defined in terms of the polar angle θ (the angle in the $x - z$ plane) as $\eta = -\ln[\tan(\theta/2)]$, and is an approximation to rapidity in the high energy limit. The radial co-ordinate R measures the radial distance from the interaction point.

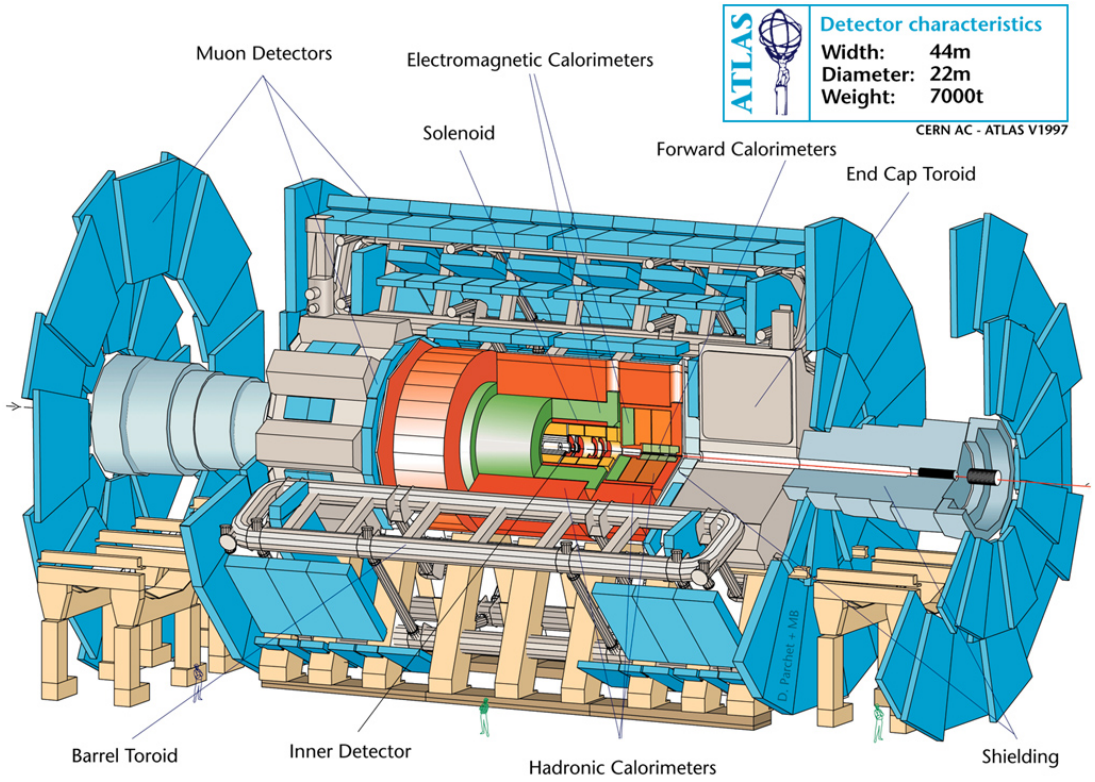

Figure 3.3: Cut-away view of the ATLAS detector [63]. The various detector sub-systems are labelled.

3.2.2 Inner Detector

The ATLAS inner detector (ID) is located closest to the beam pipe. It is a tracking detector designed to provide hermetic coverage and robust pattern recognition, locate interaction vertices, including displaced secondary vertices from long-lived particles, and provide a precise measurement of the transverse momenta of charged particles with a nominal p_{T} threshold of 0.5 GeV. It consists of a silicon pixel detector (the *Pixel Detector*), a silicon strip detector (the *Semiconductor Tracker* or SCT) and a transition radiation tracker (the TRT), located within a 2 T magnetic field provided by a solenoidal superconducting magnet.

A cut-away diagram of the inner detector is shown in Figure 3.4. The sub-detectors all consist of concentric cylindrical layers surrounding the beam pipe, referred to as 'barrels', with disks referred to as 'end caps' covering each end of the barrels. A plan view of a quarter of the inner detector is shown in Figure 3.5. The Pixel and SCT detectors provide coverage for $|\eta| < 2.5$, with the TRT enhancing pattern recognition and track momentum resolution for $|\eta| < 2.0$.

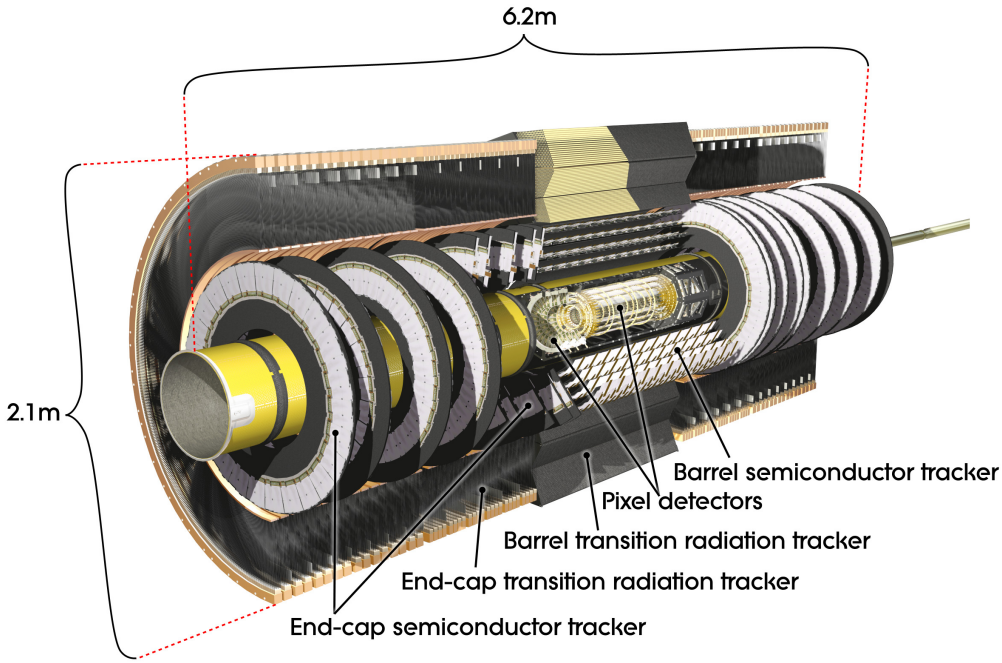

Figure 3.4: Cut-away view of the inner detector, taken from [64].

Pixel Detector

The pixel detector is the detector component closest to the beam. It is formed of layers of silicon semiconducting pixels, and is designed to have a very high granularity for resolving primary and secondary interaction vertices. There are three barrel layers closed by an endcap consisting of three disks at each end. The barrels are numbered from 0 to 2. The closest layer to the beam pipe, termed the b-layer (due to its important role in detecting secondary vertices for b physics), is positioned at a radius of 50.5 mm. Due to the high radiation dose that it will receive at this position, it will need to be replaced after three years of operation at design luminosity.

The detector layers are formed of silicon sensor modules, each consisting of 46,080 active pixels with nominal dimensions of 50×400 μm^2. In total there are approximately 80.4×10^6 readout channels.

Particles with $|\eta| < 2.0$ will traverse three layers of the detector; in most case producing three space-points. The intrinsic accuracy of the position measurement is 10 μm in (R $-$ ϕ) and 115 μm in z (R) in the barrel (endcaps).

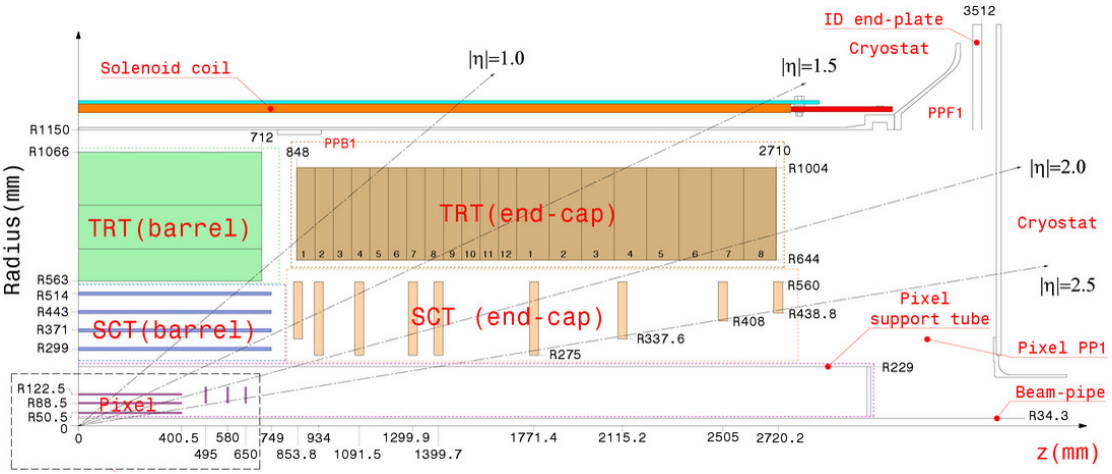

Figure 3.5: Plan view of a quarter section of the inner detector showing the positions and pseudo-rapidity coverage of the various subdetectors. Figure taken from [64].

Semiconductor Tracker (SCT)

The SCT is a silicon strip detector, consisting of four barrel layers and two end-caps consisting of nine disks each. The barrel layers consist of 2112 separate modules and are numbered from 3 to 6. Each endcap consists of 988 modules, arranged in such a way that a particle must pass through four layers of the detector.

SCT modules are made from two layers of single sided p-in-n silicon chips biased at 150V (this voltage will increase as the detector become radiation damaged). Charged particles passing through the depletion region at the centre of the junction produce electron hole pairs, which are swept apart by the bias voltage. The electrons are then collected on the top of the chip, producing a signal which can be read out. A photo of an SCT barrel module is shown in Figure 3.6.

Each side of the module consists of 768 strips of length 6.4 cm, with a pitch of 80 μm for barrel modules, and an average pitch of 80 μm for endcap modules. The strips on one layer of the module run parallel to the beam axis on the barrel, and along the R direction on the endcap. The other layer is placed at a stereo angle of 40 mrad to form a two-sided module. In total there are approximately 6.3×10^6 readout channels.

The readout is of a binary form, with a charge collection threshold of 1 fC (chosen to maximise efficiency and minimise noise). To form a space-point, a coincidence of hits on either side of the module is required. The stereo angle gives the ability to determine where along the strip the hit occurred, giving resolution

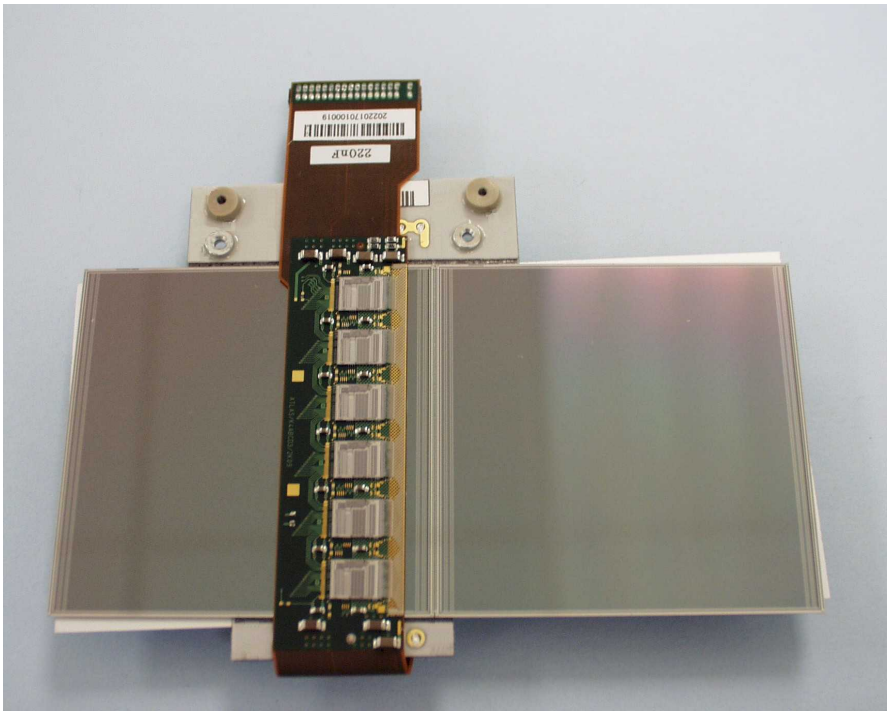

Figure 3.6: Photograph of an SCT barrel module. Figure from [62]

in z (R) in the barrels (endcaps). A small angle is used to prevent ambiguities in the presence of multiple nearby hits (so called 'ghost hits'). The spatial resolution of the detector is 17 μm in (R $-$ ϕ) and 580 μm in z (R) in the barrel (endcaps).

Transition Radiation Tracker (TRT)

The Transition Radiation Tracker is a straw drift tube tracker, with additional particle identification capabilities from transition radiation. It consists of modules formed from bundles of 4 mm diameter straws, filled with a gas mixture consisting of 70% Xe, 27% CO_2 and 3% O_2. A tungsten wire runs down the centre of the tube to collect charge. In the barrel the straws run parallel with the beam axis and are electrically divided into two halves at $|\eta| = 0$ and read out at either end (this subdivision leads to an inefficiency along a length of approximately 2 cm at the centre of the TRT). In the endcaps the straws run radially. In total there are 351,000 readout channels.

All charged tracks with $p_{\mathrm{T}} > 0.5$ GeV and $|\eta| < 2.0$ will traverse at least 36 straws, except in the barrel to endcap transition region ($0.8 < |\eta| < 1.0$) where only 22 straws will be traversed. The ($R - \phi$) resolution is 130 μm. Despite the low resolution compared to the silicon trackers, and the lack of a measurement in the z direction, the hits in the TRT contribute significantly to the pattern

recognition and momentum resolution due to the large number of measurements and longer measured track length.

The barrel straws are embedded in a matrix of polypropylene fibres, and the endcap disk layers are sandwiched between polypropylene foils. When charged particles cross the boundary between the straw and the fibre they emit transition radiation photons. These photons are then absorbed by the Xenon gas mixture, and produce much larger signals than minimum-ionising charged particles. The energy of the transition radiation photons depends heavily on particle type, and is approximately 200 keV for a 20 GeV electron and 1 keV for a 20 GeV pion. This difference can be exploited for particle identification, by counting the number of hits over a higher energy threshold. Electrons with $p_{\mathrm{T}} > 2$ GeV typically produce 7 - 10 high threshold hits, whereas pions and other charged particles will produce far fewer.

3.2.3 Calorimetry

The ATLAS calorimeter systems sit outside the inner detector and its magnetic field. The purpose of the calorimeter is to measure the energy and position of particles. A particle entering the calorimeter produces a 'shower' of secondary particles; the energy of this shower is then measured. ATLAS uses sampling calorimeters, in which different materials sandwiched together in layers are used to initiate the shower development (absorption) and to measure the energy of its constituents. This allows for a more compact design and hence better shower containment. Position measurement is obtained by segmenting the calorimeter in the z and ϕ directions.

Different absorbers are required depending on whether the particle interacts via the electromagnetic or the strong force, and the properties of the showers that develop are different. The ATLAS calorimeters are divided into two distinct subsystems, the electromagnetic calorimeter and the hadronic calorimeter. An electromagnetic shower consists of electrons, positrons and photons, and is normally fully contained in the calorimeter; thus it can be fully detected. Hadronic showers involve many more particle types, including neutrons, muons, and neutrinos which escape detection, and tend to be longer and wider, often spilling out of the calorimeter. The full energy of the shower is thus not fully detected, and so a calibration of the energy response is required. It is important for the calorimeter to provide good containment of electromagnetic and hadronic showers, not only for the purposes of energy measurement, but also to allow a good missing transverse

energy requirement, and to prevent punch-through into the muon system.

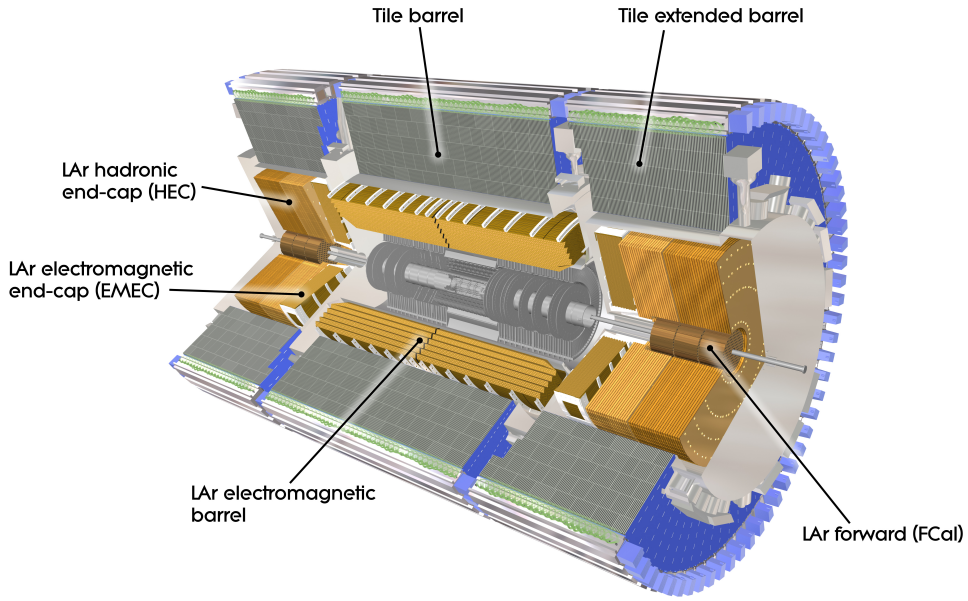

Figure 3.7: Cut-away view of the ATLAS calorimeter system. Image taken from [62].

A cutaway view showing the location of the various calorimeter elements is shown in Figure 3.7. The calorimeters cover the range $|\eta| < 4.9$. Over the η range of the inner-detector, the electromagnetic calorimeter gives fine granularity to allow precise measurement of electrons and photons. The hadronic calorimeter is more coarsely segmented, but is sufficient to meet the requirements of jet and missing transverse energy measurement.

Electromagnetic Calorimeters

The electromagnetic (EM) calorimeter (also referred to as the *LAr*) uses liquid argon as the active detector material, and lead as an absorber. Charged particles in the shower ionise the liquid argon, where the electrons drift to copper electrodes in the presence of an electric field.

The LAr consists of two half barrels extending to $|\eta| < 1.475$ (with a 4 mm gap at $z = 0$), and two coaxial wheels on each side (named the *EMEC*), the first covering $1.375 < |\eta| < 2.5$ and the second covering $2.5 < |\eta| < 3.2$. Additional material needed to instrument and cool the detector creates a 'crack' region at $1.375 < |\eta| < 1.52$, where the energy resolution is significantly degraded.

The barrel calorimeter has an accordion structure in order to avoid azimuthal cracks and to provide full ϕ symmetry, as shown in Figure 3.8. The accordion structure is made of the lead absorber, with the liquid argon filling the 2.11 mm gaps between the absorbers. The barrel of the LAr calorimeter is divided into three layers, with different cell granularity. The first layer is divided into cells of $\Delta\eta \times \Delta\phi = 0.0031 \times 0.098$. The fine granularity in η of this layer is used to determine the pseudo-rapidity of the particle, and for measurements of the shower shape, an important input to particle identification. The second layer has cell size $\Delta\eta \times \Delta\phi = 0.025 \times 0.0245$ and contains the largest energy fraction of the shower, measuring approximately 16 radiation lengths. The third layer, with cell size $\Delta\eta \times \Delta\phi = 0.05 \times 0.0245$, collects the tail of the shower. The first wheel of the LAr calorimeter is also segmented into three layers with the same granularity as the barrel. The second wheel has a coarser granularity that varies as a function of pseudorapidity. A liquid argon pre-sampler exists for $|\eta| < 1.8$ to correct for energy lost by incident particles traversing material before the calorimeters, and to aid with discriminating between $\pi^0 \to \gamma\gamma$ decays and prompt photons.

Hadronic Calorimeters

The hadronic calorimeter consists of a plastic scintillator tile calorimeter (referred to as the *tile* calorimeter) covering $|\eta| < 1.7$ and a liquid argon endcap calorimeter (referred to as the *HEC*) covering $1.5 < |\eta| < 3.2$.

The tile calorimeter consists of a barrel covering $|\eta| < 0.8$ and two extended barrels covering $0.8 < |\eta| < 1.7$, and is located immediately behind the EM calorimeter. The active material consists of 3 mm thick layers of the plastic scintillator placed perpendicular to the beam direction, sandwiched between steel absorbers. The scintillators are connected at each end to readout photomultiplier tubes by wavelength-shifting fibres. The fibres are grouped together to form readout cells, giving projective towers in η. There are three layers of cells, with a granularity of $\Delta\eta \times \Delta\phi = 0.1 \times 0.1$ in the first two layers, and $\Delta\eta \times \Delta\phi = 0.2 \times 0.1$ in the third.

The HEC consists of two wheels per endcap, HEC1 and HEC2, located directly behind the EMEC and sharing the same cryostat. Each wheel has two layers of cells. The HEC covers $1.5 < |\eta| < 3.2$ and so overlaps with the tile calorimeter on one side and the FCAL on the other, thus avoiding cracks in the transition regions. HEC1 (HEC2) is built from 25 mm (50 mm) copper plate absorbers interleaved with 8.5 mm gaps containing liquid argon. The liquid argon gaps are

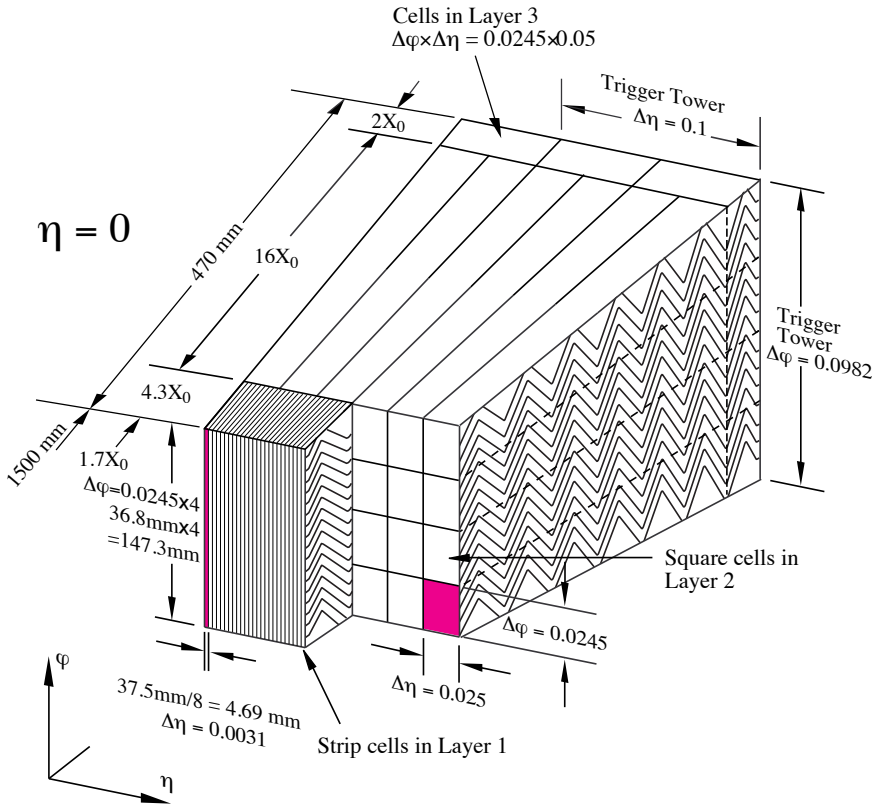

Figure 3.8: Diagram of the ATLAS liquid argon calorimeter, showing the accordion structure and the different granularity in the different layers. Diagram taken from [62].

split into four drift spaces of roughly 1.8 mm by three electrodes. This is to avoid ion build-up due to the higher particles fluxes and energies in the forward region, and also allows a lower high voltage than a single electrode design.

3.2.4 Forward Calorimeter

The forward calorimeter (*FCAL*) covers $3.1 < |\eta| < 4.9$. To reduce the neutron flux, the FCAL begins 1.2 m away from the EM calorimeter front face. Due to the high particle fluxes and energies in the forward region, the calorimeter must contain relatively long showers in the small volume allowed by design constraints, and thus must be very dense. The FCAL is divided into three compartments. The first, FCAL1, is designed for electromagnetic measurements, and uses copper as an active material with liquid argon as a passive material. The second two compartments, FCAL2 and FCAL3, are designed for hadronic measurements, and use tungsten as a passive material, chosen for its high density to provide

containment and minimise the lateral spread of hadronic showers. An additional copper alloy shielding plate is placed behind FCAL3 to reduce background to the muon endcap system.

3.2.5 Muon Spectrometer

The muon spectrometer (MS) sits outside of the calorimeter system, and is designed to provide precision muon momentum measurements over a momentum range of 3 GeV to 3 TeV as well as to provide triggering on bunch crossings containing muons. An overview of the MS is given in Figure 3.9. The system sits inside a giant air coil toroidal magnet system, producing a magnetic field orthogonal to the muon momentum to provide deflection of the muons for momentum measurement. The use of an air coil reduces multiple scattering which degrades the momentum resolution, and allows a greater tracking volume within cost constraints.

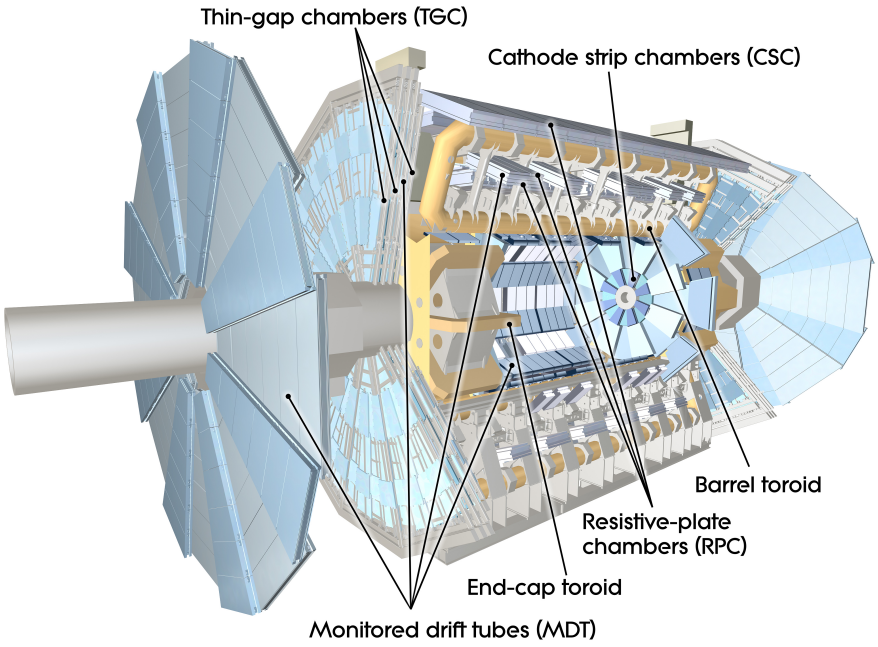

Figure 3.9: Cut away view showing the various components of the ATLAS muon spectrometer. Figure taken from [62].

Resistive Plate Chambers (RPCs) and Thin Gap Chambers (TGCs) provide triggering for $|\eta| < 2.4$ and a measurement in the $x - y$ (ϕ) plane for $|\eta| < 2.7$. The RPCs cover $|\eta| < 1.05$ and the TGCs cover $1.05 < |\eta| < 2.7$. The muon trigger has a time resolution of between 1.5 ns and 4 ns.

Precision measurements in the bending ($R-z$) plane are obtained from Monitored Drift Tubes (MDTs) and Cathode Strip Chambers (CSCs). The MDTs cover $|\eta| < 2.7$ and consist of three layers, referred to as *stations*. Each station consists of two *mulitlayers* formed of three or four layers of tubes, sandwiched between layers of RPCs or TGCs. In the innermost layer, for $2.0 < |\eta| < 2.7$ the MDTs are replaced by CSCs due to the higher rates and higher backgrounds in this region. The CSCs are multiwire proportional chambers, and so give a higher granularity than the MDTs, and are better able to cope with high rates and fluxes.

3.3 Trigger

ATLAS uses a three-level trigger system to decide when to read out the detector and to reduce the event rate to a manageable level by identifying interesting events. The collision rate of approximately 20 MHz has to be reduced to a rate of between 200 and 1000 Hz for offline reconstruction, storage and analysis. An overview of the ATLAS trigger system is shown in Figure 3.10.

The first level, L1, uses fast custom electronics to identify the presence of signals from a hard scattering such as high p_{T} electrons, muons or jets, or a large amount of missing transverse energy. The L1 trigger has a maximum latency of 2.5 μs, and must reduce the rate to approximately 60 kHz (the design L1 rate was 75 kHz, however significant detector dead-time has been observed above 65 kHz). To meet this tight time constraint, only low-granularity signals from the calorimeters and dedicated muon trigger chambers are used. The L1 trigger also identifies 'Regions of Interest' (RoI) surrounding the signature that caused the trigger to be fired, for use in later levels of the trigger.

The second (L2) and third level (the *Event Filter* or EF) trigger are software based, and are collectively known as the 'High Level Trigger' (HLT). At each level, the decision of the previous level is refined by using more detector information and allowing a longer time for the decision to be made and thus more complicated algorithms to be run, as well as tightening the selection requirements to further reduce the rate. At L2 the full readout from the RoIs identified at L1 is available. L2 uses dedicated algorithms to return a decision based on the RoI information within 100 ms. The EF has access to the full event readout, although typically only information inside or just outside the RoI is used. The EF algorithms are based on the offline object reconstruction algorithms, and may take up to 1 s to make a decision.

The trigger is organised into 'chains' with an L1 trigger seeding a chain of algorithms in the HLT. Each chain is responsible for selecting a specific trigger signature. The 'trigger menu' is the collection of chains used to select data during a run. It typically consists of about 200 primary chains for selecting data for physics analysis and about 300 supporting chains for selecting data for background and performance studies. The design of the trigger menu involves balancing between the sensitivity for physics analysis resulting from the trigger, and the need to reduce the rate to a level dictated by the available resources for reconstruction and storage. The offline computing processing power limits the EF trigger rate to about 400 Hz. The trigger menu had to evolve throughout 2011 and 2012 to meet challenges posed by the constant increase in instantaneous luminosity, and the increase of pileup to almost double the design value. The measurements described in this thesis use single electron and muon triggers. These triggers account for the largest slice of the trigger bandwidth, with rates of approximately 50 Hz each. They are described in more detail in Sections 5.3.1 and 5.4.1.

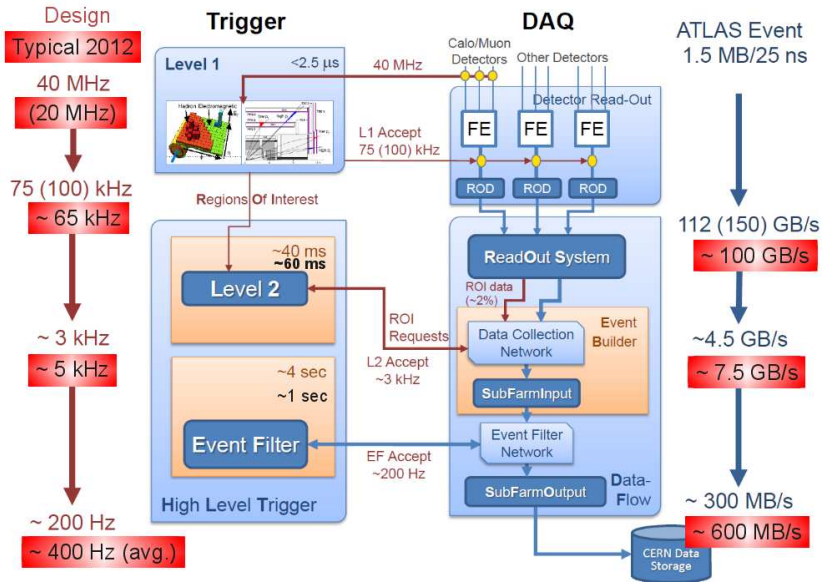

Figure 3.10: An overview of the ATLAS trigger and DAQ system. The design and 2012 typical trigger rates at each level are shown on the left, and the design and 2012 typical output bandwidths are shown on the right. Figure taken from [65].

3.4 Detector Simulation

Simulation of the detector response to various physics processes is a vital ingredient to making a physics measurement. It is important for understanding and calibrating the detector response to different signatures, for estimation of acceptances and efficiencies, and also to be able to compare experimental results with theoretical models. A custom detector simulator, which uses the GEANT4 [66] toolkit, is used to simulate interactions between particles and matter in the ATLAS detector. It takes as input the output of Monte-Carlo generators as described in Section 1.3 in HepMC format, with all particles with a lifetime less than $c\tau = 10$ mm decayed by the generator. The simulator then propagates the particles through the ATLAS detector, using GEANT4 to simulate their interaction with the material of the detector.

The response of the detector components to the particles produced is also simulated, and simulated output signals are produced in the same format as the real detector output. These are then reconstructed in the same way as for real data (as described in Chapter 5). To simulate the effect of pileup, minimum bias events generated with the PYTHIA generator are overlaid with the hard event.

3.5 Luminosity Measurement

An accurate measurement of the delivered luminosity is an essential ingredient to any physics analysis, for example to enable the measurement of a cross section or to allow the correct normalisation of simulated backgrounds. The instantaneous luminosity can be expressed as:

$$\mathcal{L} = \frac{\mu n_{\mathrm{b}} f_{\mathrm{r}}}{\sigma_{\mathrm{inel}}} \tag{3.5}$$

where μ is the number of interactions per bunch crossing, n_{b} is the number of colliding bunch pairs, f_{r} is the bunch crossing frequency, and σ_{inel} is the inelastic cross section. The instantaneous luminosity is measured during data taking by measuring the observed interaction rate per bunch crossing μ_{vis} [67, 68]. Equation 3.5 can be rewritten in term of this quantity:

$$\mathcal{L} = \frac{\mu_{\mathrm{vis}} n_{\mathrm{b}} f_{\mathrm{r}}}{\sigma_{\mathrm{vis}}} \tag{3.6}$$

where $\sigma_{\text{vis}} = \epsilon\sigma_{\text{inel}}$ is the total inelastic cross section multiplied by the efficiency of the method used to measure μ_{vis}. The parameters n_{b} and f_{r} are known machine parameters, and so a measurement of μ_{vis} gives a measurement of the relative luminosity; this must be calibrated by measuring σ_{vis} in order to give an absolute luminosity measurement.

Two primary detectors are used for the measurement of μ_{vis}: LUCID [69] and the BCM [70]. LUCID is specifically designed for measuring the luminosity delivered to ATLAS, and is a Cerenkov detector consisting of sixteen aluminium tubes filled with C_4F_{10} gas, surrounding the beampipe each side of the interaction point at a distance of 17 m. The Cerenkov photons are reflected down the tubes to photomultipliers (PMTs); if one of the PMTs records a signal over threshold the tube records a 'hit' for that event. LUCID receives signals directly from the LHC clock, allowing it to record event rates separately for each bunch crossing, and is separate from the main ATLAS DAQ enabling luminosity measurement even when the detector is not in data-taking mode. The BCM (Beam Conditions Monitor) is primarily designed to measure beam-induced backgrounds and issue a beam-abort request in case of dangerous levels of background that would be damaging to ATLAS. It consists of four diamond sensors located on each side of the interaction point at a distance of 1.8 m; diamond sensors are chosen for their radiation hardness and fast readout. The fast readout means it also provides a bunch-by-bunch signal which can be used as a measure of μ_{vis}. Since the efficiencies of the BCM and LUCID are different, they will measure a different μ_{vis} and hence need to be calibrated separately.

The calibration of σ_{vis} is done using dedicated *van Der Meer (vdM) scans*, where the absolute luminosity is measured directly from machine parameters. The delivered luminosity can be written as:

$$\mathcal{L} = \frac{n_{\text{b}} f_r n_1 n_2}{2\pi \Sigma_x \Sigma_y} \cdot F \tag{3.7}$$

where n_1, n_2 are the bunch charges in each beam, and Σ_x, Σ_y are the vertical and horizontal width of the beam. In a vdM scan, the beams are separated in steps of known distance, and the change in event rates measured. From this the beam widths Σ_x, Σ_y can be deduced. The bunch charge product $n_1 \cdot n_2$ is measured by two DC current transformers, which have high accuracy but are unable to resolve individual bunch charges, and two fast beam current transformers (FBCT) which have lower accuracy but are able to resolve each bunch [71]. Combining these two measurements, a direct measurement of the luminosity is made. By compar-

ing the peak luminosity (when the beam separation is at a minimum) with the peak interaction rate measured by LUCID or the BCM, and using Equations 3.6 and 3.7, a measurement of σ_{vis} is obtained, enabling absolute normalisation of the luminosity.

The luminosity measurement is cross-checked using an independent measurement of the luminosity using information from the ATLAS calorimeters. The PMT current from the tile calorimeter and the total ionisation current in the liquid argon of the FCal are related to the mean number of particles interacting in the calorimeter, and so are sensitive to the luminosity.

3.6 Data Samples

The measurements described in this thesis use data collected in 2011 and 2012, and correspond to the full proton-proton datasets collected by ATLAS in each of those two years. The dataset is broken down into *runs*, continuous periods of data-taking typically corresponding to one fill of the LHC. Each run is further broken down into *luminosity blocks* consisting of roughly two or three minutes-worth of data-taking. Runs are grouped together into *periods*, with the accelerator, detector and trigger conditions being similar in each period. The periods within each year are labelled A to M.

Luminosity blocks where there were problems with the detector (for example a HV trip in the LAr) which would affect the reconstruction of electrons, muons, jets or other physics objects are removed using a "Good Runs List" which records which luminosity blocks have such defects. After removing these luminosity blocks the integrated luminosity of 2011 dataset is 4.6 fb^{-1} and the integrated luminosity of the 2012 dataset is 20 fb^{-1}. The uncertainty on the luminosity measurement is 3.9% for 2011 data and 2.8% for 2012 data.

Chapter 4

SCT Temperature Monitoring

4.1 Introduction

In order to mitigate the effects of radiation damage and to prevent damage caused by excessive heat, it is important to keep the Semiconductor Tracker modules cool, maintaining the silicon sensors at temperatures of approximately $-7°$C. The SCT and Pixel sub-detectors use a common evaporative cooling system to remove heat from their modules. Monitoring of the module temperature is important to ensure that the cooling system is functioning as designed, and that the modules remain coupled to the cooling structures. Additionally, monitoring of the temperature difference between the front and the back of barrel modules provides a check of the mechanical integrity of the modules. This chapter describes tools developed to monitor variables associated with the temperatures of SCT modules, and presents results for thirty-two months of operation between January 2010 and October 2012.

4.1.1 Effects of Radiation Damage on Semiconductor Detectors

Given the LHC design luminosity of 10^{34} cm^{-2}s^{-1}, the inner layers of the SCT are expected to receive a radiation dose of up to 2×10^{14} n_{eq}/cm^2 [72] over the course of its design lifetime of 10 years. Exposure to such high radiation doses causes damage to the silicon detectors.

The primary method of radiation damage is interactions with irradiating particles displacing nuclei from their lattice position, damaging the structure of the material. Displaced nuclei can form stable defects in the material, which change the effective doping. Exposure to radiation will cause an n-type semi-conductor to become more p-type, and will eventually change the material from n-type to

p-type, in an effect known as *type-inversion*. The change in effective doping has two effects: a loss of mobility of drifting electrons and ions due to recombination, and an increase in the leakage current across the p-n junction. This leads to lower charge collection efficiency and increased noise. Charge collection efficiency can be maintained by increasing the displacement voltage applied to the junction, though for sufficiently high radiation doses it becomes impossible to fully deplete the sensors. It is therefore essential to reduce the effects of radiation damage as much as possible.

It is found that for temperatures of approximately -7°C the effects of radiation damage are greatly reduced [73], so it is important to maintain the silicon at these low temperatures. After type-inversion occurs, a process known as reverse-annealing occurs, whereby the radiation damage continues to occur even after exposure to the radiation has ceased. After type-inversion, it will therefore be necessary to run the detector cooling even when there are no beams in the LHC.

The leakage current is induced by thermal creation of electron-hole pairs from shallow donors arising from defects in the material, and increases the signal to noise ratio of the sensor. The size of the leakage current is dependent on the temperature of the sensor, and so reducing the temperature decreases the noise due to leakage currents.

4.1.2 SCT Module Design

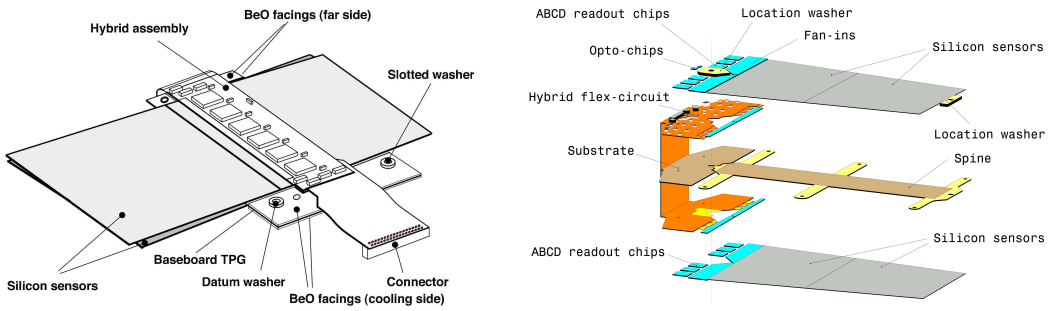

(a) (b)

Figure 4.1: Diagram of (a) an SCT barrel module and (b) an SCT endcap module, showing the location of the different components. Figure from [62]

SCT modules consist of two layers of silicon sensors, bonded together at a small stereo angle as described in Section 3.2.2. Figure 4.1 shows a diagram of the layout of barrel and endcap modules. Barrel modules are constructed by gluing

the sensors either side of a graphite base-board which provides the module's mechanical structure. The read-out chips are located on a polyimide hybrid wrapped around the outside of the module. The HV is applied to the sensors via the base board. Endcap modules are constructed in a similar fashion, gluing the sensors either side of a base-board spine, with the hybrid located at one end of the module. Heat from the sensors and from the read-out electronics on the hybrid is conducted by the base-board to the cooling pipe, which is connected at one edge of the module via a layer of thermal grease and an aluminium cooling block.

4.1.3 The Inner Detector Cooling System

Each SCT module produces between 5.5W and 6W of heat when the "High Voltage (HV)" biasing voltage is applied. This is expected to increase to around 8W as the detector suffers the effects of radiation damage and the bias voltage must be increased to compensate. An active cooling system based upon evaporative cooling is used to remove this heat from the SCT modules [74] and hold them at the low temperatures necessary to mitigate the effects of radiation damage. The system is common to the SCT and the Pixel detector.

An evaporative cooling system was chosen over a mono-phase system as it has a larger cooling capacity per unit volume due to utilisation of the latent heat of vaporisation rather than a liquid's heat capacity. This allows the resulting system to be smaller and with a lower mass, thus resulting in less material in the inner-detector. Additionally, an evaporative system has smaller temperature gradients along long cooling tubes, allowing for more uniform module temperatures.

Figure 4.2 shows a schematic of the cooling system. The system uses the fluorocarbon refrigerant C_3F_8 as a cooling fluid, chosen since it is stable against irradiation, non-flammable, non-toxic, electrically neutral, and has the highest heat transfer coefficients of similar fluorocarbon refrigerants. The cooling fluid is delivered at room temperature in saturated liquid phase to capillaries located immediately before the detector structure. The fluid expands through the capillaries and passes along the cooling pipe at boiling point. The modules are coupled to the pipe by means of cooling blocks and heat is absorbed from the modules by the passing fluid causing it to evaporate. At the end of the cooling pipe a heater evaporates any residual liquid and heats the vapour to above the cavern dew point to avoid condensation in the return pipes. The exhaust gas is piped to the ATLAS service cavern where it is compressed and condensed, and then returned to the cooling loop. Recuperative heat exchangers are used to transfer heat between

the cold return vapour and the warm inlet liquid, increasing the efficiency of the thermodynamic cycle by decreasing the vapour quality[1] of the fluid at the inlet to the cooling structure. The temperature to which the modules are cooled depends on the boiling pressure of the fluid, which is controlled by backpressure regulators (BPR) located at the end of the return tubes.

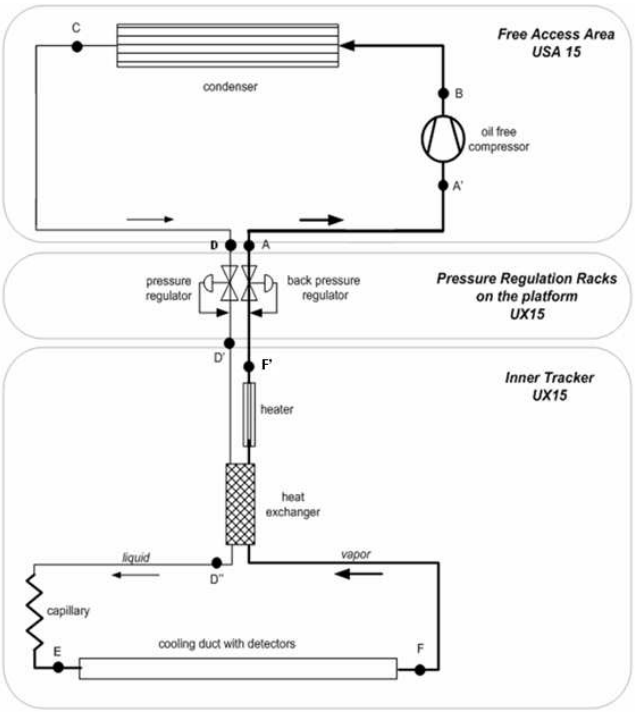

Figure 4.2: Schematic of the SCT evaporative cooling system. Figure from [75]

The cooling system consists of 204 independent cooling circuits or 'loops', of which 44 cool modules on the SCT barrels, 72 cool modules on the SCT endcaps and the remaining 88 cool modules on the Pixel detector.

4.2 Methodology

The temperatures of SCT modules are monitored by thermistors mounted on the module hybrids on the front side of the module (the side furthest from the interaction point). Barrel modules have an additional thermistor mounted on the back side of the module. The temperatures recorded by the module thermistors are read out by the ATLAS detector control system, *PVSS* [76]. A data point is written to the Oracle database every 12 hours for offline analysis. In addition,

[1]The *vapour quality* of a saturated fluid is the mass-fraction that is vapour.

whenever a module temperature changes above a deadband of 0.4°C, the new value is written to the database.

It is important to monitor the module temperatures only during periods of stable running, as the temperatures will vary as the detector is cooled down or warmed up, or when calibration work is in progress. Stable periods are found by requiring that the number of cooling loops turned on is constant and greater than zero. Stable periods are required to be at least 6 hours long, to veto periods where the detector is being turned on and off, and stable periods longer than 24 hours are broken down into 24 hour blocks.

For each module, a number of monitoring variables are calculated; these are described below. The distributions of these variables are plotted for each of the barrel layers and endcap disks. Modules which fall in the tails regions of the distributions are identified as 'problem' modules. A list of problem modules is maintained, and these modules are monitored. The monitoring plots are produced automatically on a daily basis by scripts running on one of the SCT monitoring computers and are made available as part of the 'SCT Calibration Monitoring' website at https://pc-sct-www01.cern.ch/CalibMonitor/ (ATLAS login required).

4.3 Monitoring Variables

4.3.1 Front-Back Temperature Difference - ΔT

The difference in temperature between the front and the back of a module should be very small and any large temperature difference would indicate defective thermal coupling between the two sides. This would suggest that the front and the back of the module had lost mechanical integrity and were coming apart from one another. It is therefore useful to monitor modules ΔT, the front-back temperature difference, defined as:

$$\Delta T = T_{\text{front}} - T_{\text{back}} \tag{4.1}$$

where T_{front} and T_{back} are the temperatures recorded at the front and the back of the module respectively.

For each period of stable operation the distribution of ΔT is plotted, for all barrels together as well as for each barrel separately. Example plots for 01:20 22/9/2012 to 01:20 23/9/2012 are shown in Figure 4.3 (separately for each barrel).

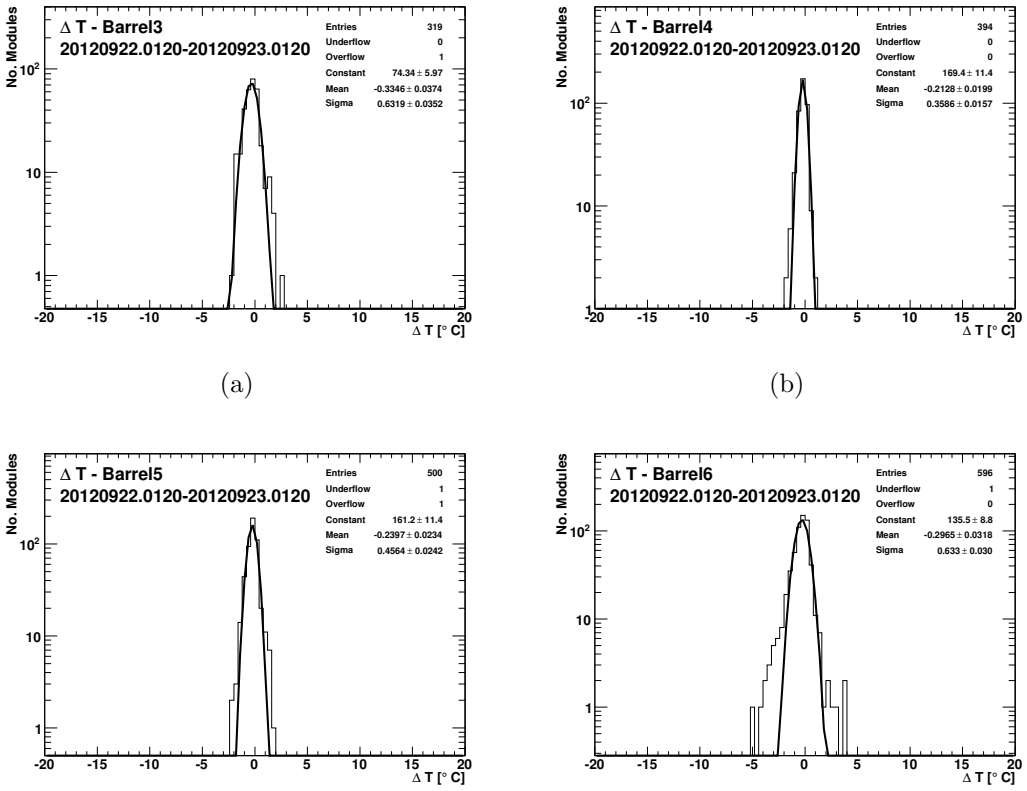

Figure 4.3: ΔT distributions for the SCT Barrel 3 (a), Barrel 4 (b), Barrel 5 (c) and Barrel 6 (d) for 01:20 22/9/2012 to 01:20 23/9/2012. The distributions are fitted to a Gaussian; the mean and width of the Gaussian is indicated on the plot.

The distributions are fitted with a Gaussian and the mean and width of the Gaussian are obtained. These are listed in Table 4.1 for each of the barrel layers, averaged over 5 months of data between 20/1/2010 and 20/6/2010.

In order to identify modules with a high value of ΔT, a threshold of 5 times the width of the Gaussian is set, separately for each barrel. Modules with a value of ΔT greater than this threshold are identified as 'problem modules'. Table 4.2 gives the number and percentage of modules with front-back temperature difference greater than the threshold at least five times during the period 20/1/2010 to 19/6/2010, for each barrel layer. The width of the distribution is greatest for Barrel 3, and so the thresholds for identifying high ΔT modules is highest for this barrel. The width of the distribution for Barrel 6 is the second widest, however the distribution is observed to have large non-Gaussian tails, leading to a larger fraction of problematic modules on Barrel 6 than other modules. This is attributed to the fact that for Barrels 3, 4 and 5 only modules with $|\Delta T| < 2°$C

Barrel	$\sqrt{\langle\sigma^2\rangle}$	$5\sqrt{\langle\sigma^2\rangle}$	χ^2 / ndf	$\langle\Delta T_{\text{mean}}\rangle$
All barrels	0.52	2.61	132.64	-0.25
Barrel 3	0.64	3.21	19.44	-0.36
Barrel 4	0.39	1.96	8.22	-0.21
Barrel 5	0.48	2.38	36.06	-0.23
Barrel 6	0.60	3.02	59.06	-0.26

Table 4.1: The width, goodness of fit and mean of a Gaussian fit to the ΔT distribution averaged over stable periods between 20/1/2010 and 20/6/2010.

Component	# Problem Modules	% Modules Problematic
Barrel 3	1	0.3
Barrel 4	1	0.2
Barrel 5	7	1.2
Barrel 6	17	2.5

Table 4.2: Number and percentage of modules with $|\Delta T|$ greater than the threshold for identifying problem modules at least 5 times during the period 20/1/2010 - 19/6/2010 for each barrel.

measured on production were accepted, whereas for Barrel 6 this was relaxed to $|\Delta T| < 4°\text{C}$ [75].

The mean value of the ΔT distributions tend to be negative, implying that on average the back side of the modules (the side facing into the carbon fibre barrel) tends to be warmer than the front. This effect was also observed in tests carried out on the modules reception at CERN in 2006 [75], and in tests carried out in 2008 [77]. Investigations suggested that this bias is a property of the module itself, rather than an effect due to the module's environment. A possible explanation is the way that the hybrid was glued to the substrate, whereby the top wing of the hybrid was first glued to the front of the module, then the bend made, then the bottom wing glued. It is possible that following the bend the quality of the glue joint decreased, increasing thermal impedance between the back of the hybrid and the base-board.

4.3.2 Difference In Temperature To Local Average - T_{diff}

Modules with a bad thermal coupling to the cooling pipe can be identified by looking for modules with a temperature significantly different from other modules on the same cooling structure. The monitoring variable T_{diff} is defined as:

$$T_{\text{diff}} = \bar{T}_{\text{struct}} - T_{\text{module}} \tag{4.2}$$

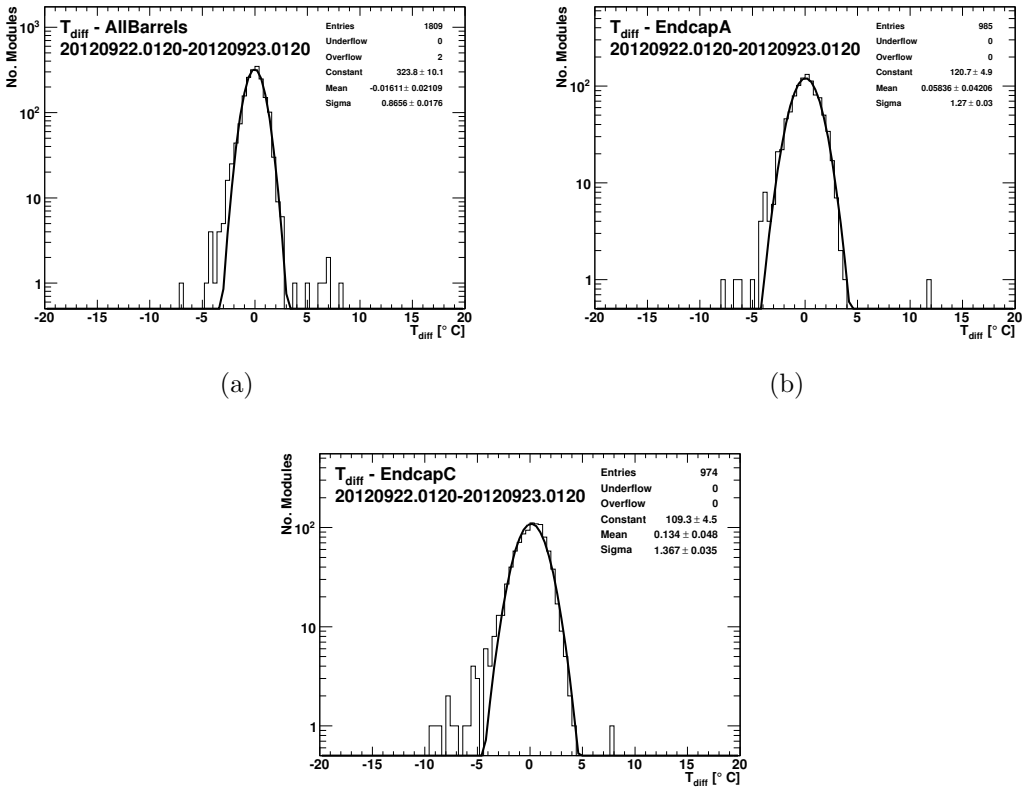

Figure 4.4: T_{diff} distributions for the SCT barrel and endcaps for 01:20 22/9/2012 to 01:20 23/9/2012

where:

$$\bar{T}_{\text{struct}} = \frac{\Sigma_1^N T_{\text{i}}}{N} \tag{4.3}$$

is the average temperature of modules on the cooling structure. For the SCT barrels a cooling structure is defined as a stave (consisting of two loops) and for the endcaps it is defined as a single cooling loop. Any module warmer than its neighbours gives a negative value of T_{diff}, whilst modules cooler than their neighbours give a positive value.

Figure 4.4 shows the distributions of T_{diff} for the barrel and for each of the endcaps for 01:20 22/9/2012 to 01:20 23/9/2012. As expected the mean of the distribution is consistent with zero. Endcap C shows a large tail to low T_{diff}, indicating there are a large number of modules warmer than other modules on their cooling loop. Examination of the distributions for each disk suggest that this effect is observed on disks 1-5, but not on disks 6-9. The cause of this effect is unknown.

Barrel	$\sqrt{\langle\sigma^2\rangle}$	$5\sqrt{\langle\sigma^2\rangle}$	χ^2 / ndf
All Barrels	0.81	4.03	48.82
Barrel3	0.87	4.33	12.66
Barrel4	0.71	3.56	13.88
Barrel5	0.82	4.09	18.5
Barrel6	0.77	3.84	35.44
EndcapA All Disks	1.31	6.53	28.68
EndcapA Disk1	1.33	6.67	11.17
EndcapA Disk2	1.38	6.89	14.93
EndcapA Disk3	1.26	6.31	15.21
EndcapA Disk4	1.28	6.42	11.04
EndcapA Disk5	1.49	7.43	19.32
EndcapA Disk6	1.45	7.27	15.54
EndcapA Disk7	1.81	9.05	13.96
EndcapA Disk8	1.39	6.95	10.05
EndcapA Disk9	1.96	9.8	9.05
EndcapC All Disks	1.31	6.57	44.63
EndcapC Disk1	1.24	6.21	17.52
EndcapC Disk2	1.41	7.03	14.18
EndcapC Disk3	1.26	6.28	19.22
EndcapC Disk4	1.41	7.07	18.36
EndcapC Disk5	1.19	5.96	19.22
EndcapC Disk6	1.64	8.22	11.29
EndcapC Disk7	1.25	6.27	11.17
EndcapC Disk8	1.29	6.47	13.39
EndcapC Disk9	1.72	8.58	9.38

Table 4.3: The first column shows the width of a Gaussian fitted to the T_{diff} distribution for each stable period between 20/1/2010 and 20/6/2010. The threshold used for identifying high T_{diff} modules is set as 5 times this value; this is shown in the second column. The third column shows the χ^2 goodness of fit parameter.

As with the ΔT monitoring variable, five times the average width of the Gaussian fit is used as a threshold for identifying problem modules. The threshold is set separately for each SCT barrel layer and endcap disk. The thresholds are given in Table 4.3. The endcaps tend to have much wider distributions than the barrels, indicating that the module temperature is less uniform on endcap cooling loops. This is consistent with the findings of the 2008 study [77]. The number and percentage of modules with $|\ T_{\text{diff}}|$ greater than threshold at least 5 times during the period 20/1/2010 - 19/6/2010 is shown in Table 4.4.

The majority of the modules above threshold had negative values of T_{diff}, indicating that they are warmer than their neighbours. This is generally caused

Component	# Problem Modules	% Modules Problematic
Barrel 3	3	0.8
Barrel 4	1	0.2
Barrel 5	3	0.5
Barrel 6	6	0.9
Endcap A	4	0.4
Endcap C	9	0.9

Table 4.4: Number and percentage of modules with $|T_{\text{diff}}|$ greater than the threshold for identifying problem modules at least 5 times during the period 20/1/2010 - 19/6/2010 for each barrel and for each of the endcaps.

by the modules not being in complete contact with their cooling block. A small number of modules had very large positive values of T_{diff}, indicating that they are cooler than their neighbours. This indicates a lower power dissipation through the module which is either due to the module being disabled and thus not receiving the high voltage current, or due to incorrect chip settings.

4.4 Time Evolution of Monitoring Variables

In order to track problematic modules, plots are produced each month showing the problem modules and on which days they were problematic. An example of such a plot is shown in Figure 4.5. These plots are available on the calibration monitoring website.

4.4.1 Number of Problem Modules

Of obvious concern is whether the number of problematic modules is increasing. Figure 4.6 shows the number of problem modules above the problem threshold

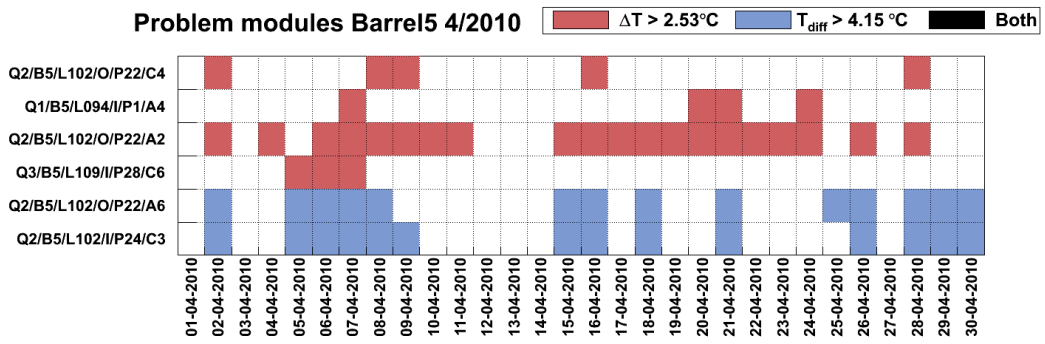

Figure 4.5: Problem modules on barrel 5 in April 2010.

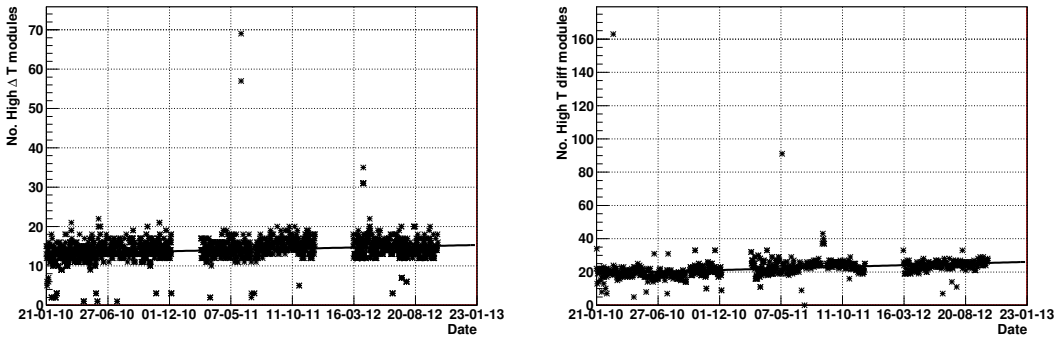

(a) (b)

Figure 4.6: The number of 'problematic' modules with (a) ΔT and (b) T_{diff} of greater magnitude than the problem threshold per day as a function of time between 20/01/2010 to 16/10/2012. The number of 'problematic' modules is not seen to increase significantly as a function of time.

on a given day as a function of time between 20/01/2010 to 16/10/2012 for the ΔT and T_{diff} monitoring variables. For both monitoring variables, there is no significant increase in the number of problematic variables observed as a function of time. Fitting the distributions to a linear function, the average number of T_{diff} modules above the problem threshold is found to increase at a rate of 0.74 ± 0.05 per year. The average number of ΔT modules above the problem threshold is found to increase at a rate of 2.54 ± 0.15 per year.

4.5 Behaviour of Problematic Modules

For each of the modules identified as problematic at least five times, the value of the problematic monitoring variable has been plotted as a function of time for the first six months of 2010 in order to identify any trends. For most of the problematic modules the magnitude of the monitoring variable does not increase over the period, aside from small fluctuations. However, one module has been identified with a high ΔT of increasing magnitude, and four modules with a T_{diff} of increasing magnitude. A further two show unusual behaviour.

The plot on the left of 4.7 shows the only module with a ΔT of increasing magnitude. The temperature difference between the front and back of the module has increased by about 1.5°C in six months, with back of the module warmer than the front, suggesting worsening thermal coupling across the module. The plot on the right of 4.7 shows a module for which ΔT jumps between 0°C and

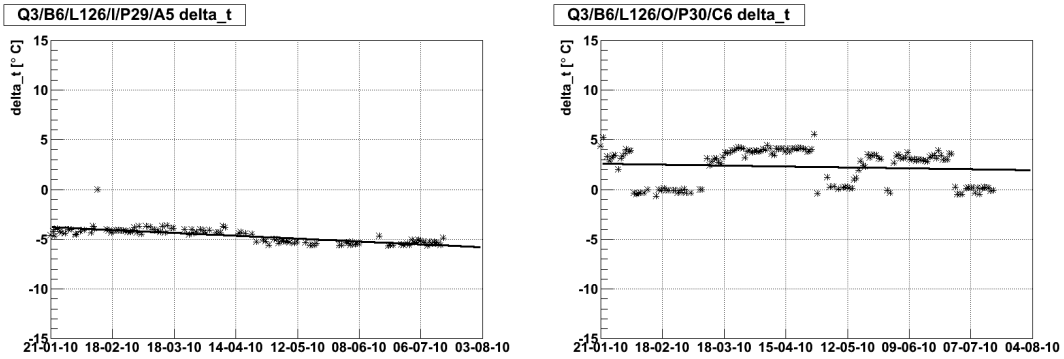

(a) (b)

Figure 4.7: The temperature difference between the front and back of the module (ΔT) for (a) barrel module Q3/B6/L126/I/P29/A5 and (b) barrel module Q3/B6/L126/O/P30/C6 as a function of time between 20/1/2010 to 18/7/2010.

3-4°C every 1 or 2 months. This suggests an intermittent failure in the integrity of the module. No other problems with this module have been recorded.

Three modules were observed to have a T_{diff} becoming more negative with time, indicating that they are becoming warmer relative to their neighbours by about 1°C over six months. This suggests a failure in coupling to the cooling pipe that is getting worse with time. One of these modules is shown on the left of Figure 4.8. The right hand plot of Figure 4.8 shows a module with T_{diff} becoming more positive over time, and also showing sharp jumps in the variable. An increasing positive T_{diff} means the module is cooler than its neighbours, and becoming even more cooler. This would suggest that the module is running at a lower power, although it is unclear why this would cause the T_{diff} to increase over time, nor explain the sudden jumps. Generally modules running at lower power are detected with the DAQ (Data Acquisition) software, but no problem has been reported for this module. A further seven modules with a T_{diff} which jumps between 0°C and around +7°C have been observed. All seven of these modules have other known problems; either the modules do not receive the high voltage, or there is a problem with the module communication. These modules are out of configuration, and data sent from these modules is not used for physics.

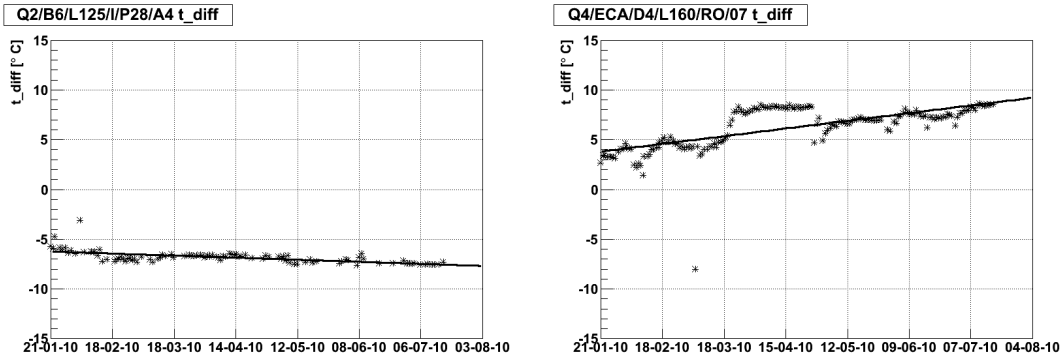

(a) (b)

Figure 4.8: The difference in temperature between the module and the average temperature of modules on the same cooling structure (T_{diff}) as a function of time for (a) module Q2/B5/L102/I/P24/C3 and (b) Q4/ECA/D4/L160/RO/07 between 20/1/2010 and 18/7/2010.

4.6 Long Term Trends in Monitoring Variables

To evaluate the long term performance of the SCT cooling, plots of the mean and width of the distributions of the monitoring variables as a function of time were produced. Such plots allow identification of trends common to all modules, which would not be identified by the procedure of identifying 'problematic' outliers as described in the previous sections.

Figure 4.9 shows the width and mean of the ΔT distributions as a function of time. For the widths, each point on the graph corresponds to the width of the Gaussian fit to the ΔT distribution for one stable period (such as the distribution shown in Figure 4.3); similarly for the means, each point corresponds to the mean of the Gaussian fit for one stable period. The mean and width of the distributions are seen to be stable as a function of time, indicating that there is no long term shift in the front-back temperature difference common to all barrel modules.

Figure 4.10 shows the width and mean of the module temperature distributions as a function of time. Similarly to the ΔT plots, each point on the graph corresponds to the width or mean of the Gaussian fit to the module temperature distributions for one stable period. For barrel modules, the temperature is taken as the average of the front and back thermistor temperatures. The means of the temperature distributions are observed to increase slightly as a function of time; this is attributed to increasing occupancy as the instantaneous luminosity increased, which causes increased power dissipation in the readout chips. The slight decrease in temperature at the start of the 2012 run is attributed to calibration

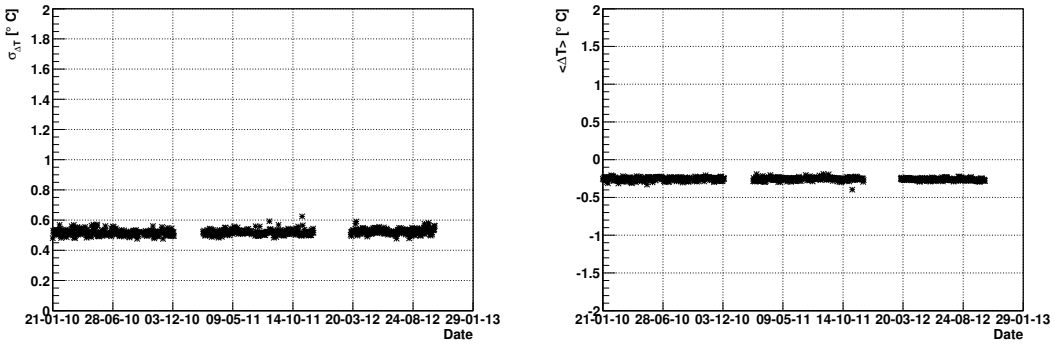

(a) (b)

Figure 4.9: The (a) width and (b) mean of the module ΔT distribution for SCT barrel modules as a function of time.

work occurring during the recommissioning, and the sudden jump in the average endcap module temperature near the start of 2010 is due to the changing of one of the compressors. The width of the temperature distributions are observed to be stable as a function of time.

Figure 4.11 shows the width of the T_{diff} distributions as a function of time; the means are not shown as they are identically zero by construction. The widths are observed to be stable, indicating that there is no long term increase in the spread of module temperatures for modules along a cooling pipe.

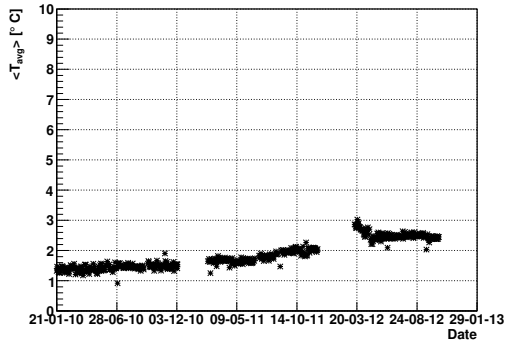

(a) Barrels

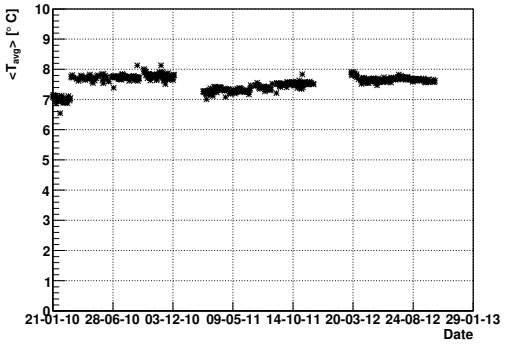

(b) Endcaps

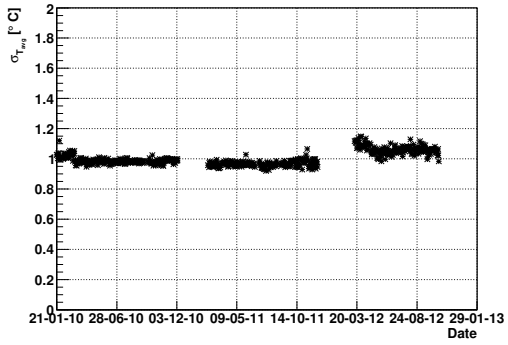

(c) Barrels

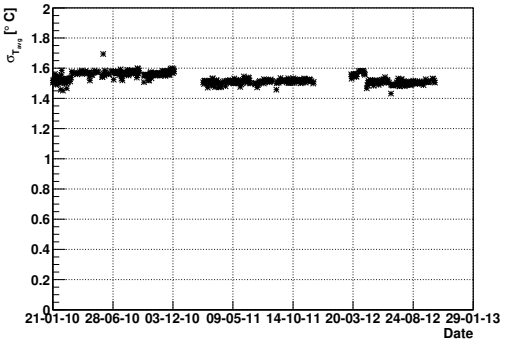

(d) Endcaps

Figure 4.10: The mean and width of the module temperature distribution as a function of time. Figures (a) and (b) show the mean of the module temperature distribution as a function of time for the SCT barrels and endcaps, respectively. Figures (c) and (d) show the width of the module temperature distribution as a function of time, again for the barrels and endcaps respectively.

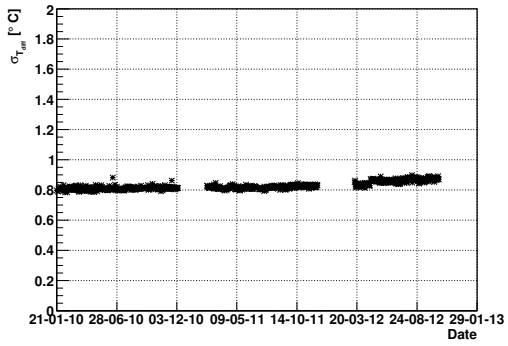

(a) Barrels

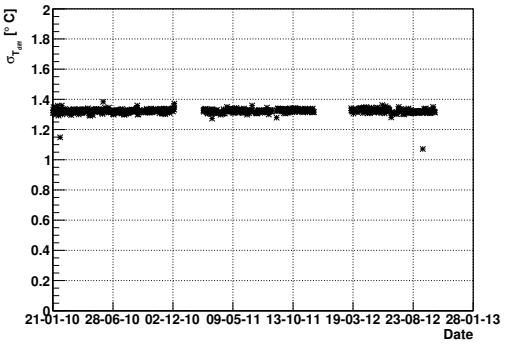

(b) Endcaps

Figure 4.11: The width of the T_{diff} distribution as a function of time for (a) the barrels and (b) the endcaps.

4.7 Conclusions

Studies of the performance of the SCT cooling system have been performed. Variables for identifying modules losing coupling to the cooling pipe and for identifying modules losing mechanical integrity have been defined, and an automated monitoring set up to produce plots of the distributions of these variables and to identify 'problematic' modules. Only a small fraction of the modules are found to be problematic, and in most cases these problematic modules are known to have other problems and their readout is not used for physics analysis. Over almost three years of running the number of problematic modules is not seen to increase significantly, and the mean and width of the distributions of the monitoring variables remain stable.

Chapter 5

Particle Reconstruction

In this chapter the software algorithms used to reconstruct and identify different particles are described. The first step in particle reconstruction involves reconstructing tracks in the inner detector and the muon spectrometer, identifying interaction vertices, and identifying clusters of energy deposits in the calorimeter systems. These are then combined to reconstruct particles such as electrons, muons, jets, photons, and tau leptons, as well as to measure properties of the event such as missing transverse energy. Since triggering on electrons and muons is a crucial component of the measurements described in this thesis, this is also described in more detail here.

Figure 5.1 shows schematically how different types of particle interact with the different detector components. Muons leave a track in the inner detector, typically deposit little energy in the calorimeters and then leave a track in the Muon Spectrometer. Photons leave no track in the inner detector, and will typically deposit all of their energy in the EM calorimeter, leaving an electromagnetic shower. Electrons also typically deposit all of their energy in the EM calorimeter, but will also leave a track in the inner detector. Charged hadrons such as protons leave a track in the inner detector, deposit minimal amounts of energy in the EM calorimeter, and then deposit most of their energy in the hadronic calorimeter, leaving a long wide shower. Neutral hadrons such as neutrons behave in a similar manner to charged hadrons, but do not leave an inner detector track. Neutrinos completely escape the detector leaving no trace in any of the detectors systems.

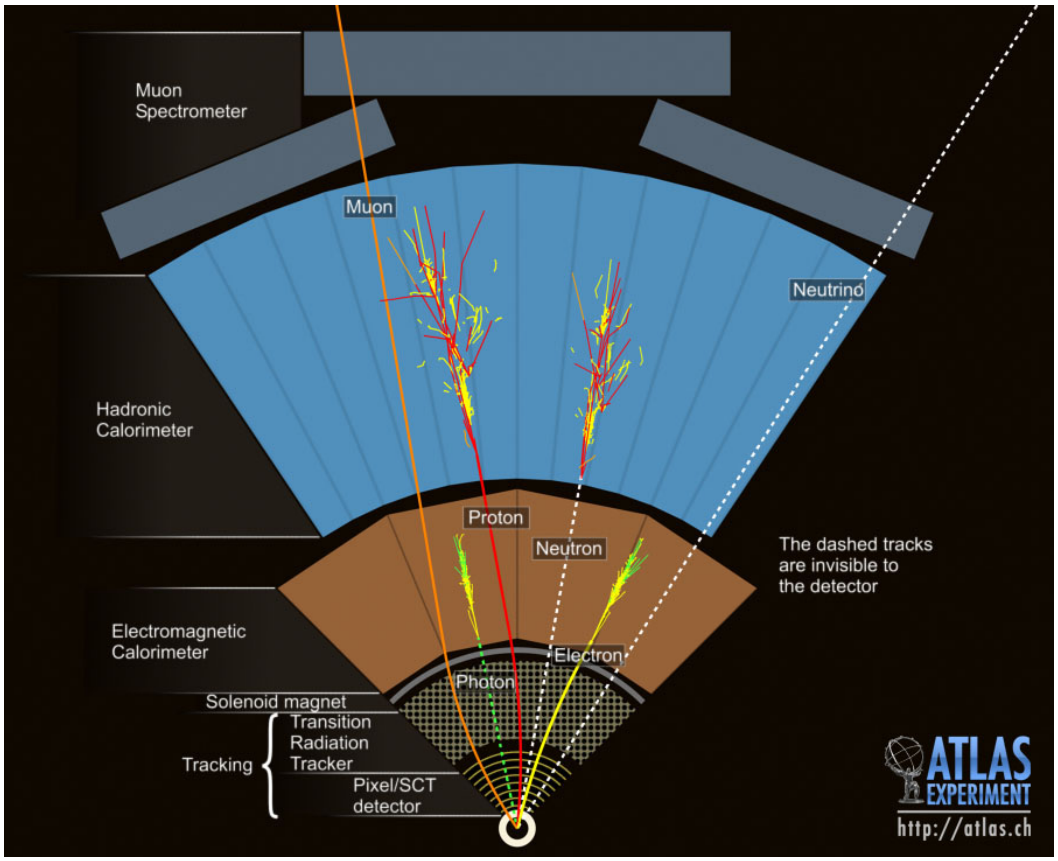

Figure 5.1: Schematic view of the progression of different types of particle through the ATLAS detector. Figure from [78].

5.1 Tracking

Particles traversing the inner detector travel in an approximately helical path under the influence of the magnetic field, leaving hits in the various detector components that they traverse. In order to use these hits to identify and measure particles, it is necessary to reconstruct particle tracks from these hits, in a process known as tracking. At the collision energies and levels of pileup at the LHC, there will typically be hundreds of hits in the Inner Detector. The tracking algorithm must be able to correctly associate hits with tracks, as well as reconstruct the track parameters. As well as interacting with the active elements of the detector, particles will also interact with the dead material in the inner detector, leading to multiple scatterings, ionisation energy loss and, especially for electrons, radiation energy loss from bremsstrahlung. A detailed description of the ATLAS tracking is given in [79].

A particle's trajectory can be described by five parameters, $\mathbf{x_i}$. In ATLAS,

the parameters are chosen to be:

$$\mathbf{x_i} = (l_1, l_2, \phi, \theta, q/p) \tag{5.1}$$

where l_1, l_2 are two co-ordinates in the frame of the detector surface in which a measurement is made, and the other three parameters describe the momentum of the track in the global frame.

5.1.1 Inside-Out Tracking

In ATLAS, the main tracking algorithm is known as 'inside-out' tracking, as it begins in the inner layers of the detector and works outwards. The first step is the formation of space-points from the measurements in the silicon detectors. In the Pixel detector a space-point corresponds simply to a hit in the detector. In the SCT space-points are required to have hits in both sides of the module in order to give a measurement in z (due to the stereo-angle). Track seeds are then formed from combinations of space-points in the three Pixel detector layers and the first layer of the SCT.

These seeds are used to build roads through the rest of the detector elements. A Kalman fitter-smoother [80] is used to follow the trajectory, successively adding hits to the track fit. From a given layer, the Kalman filter will predict the track parameters on the next detector layer, then update the track parameters and covariances taking into account the measurements found on the next layer (filtering), as well as refining the estimates for the track parameters on the previous layers based on the new measurement. The Kalman filter takes into account linear distortions to the track from multiple scattering and from ionisation energy loss. Energy loss through bremsstrahlung is, however, highly non-gaussian, and is not modelled well in this approach. Roughly 10% of seeds will lead to track candidates.

The next step in the procedure is ambiguity resolution; many of the track candidates found in the track finding will share hits, or will be as a result of fakes, or will erroneously incorporate outliers. At this stage the track is refitted with a global χ^2 fit [81], using a refined reconstruction geometry with more detailed material description and omitting outliers. A score is assigned to each track, based upon the fit quality χ^2/N_{dof}, the number of hits on the track, the presence of overlapping hits on a layer, and with penalties for 'holes' (missing hits). The scores for different detector elements are weighted giving greater weight to more precise detector elements. Ambiguities are resolved by choosing the track with

the greater score; tracks with a score below a certain threshold are discarded.

The track is then extended into the TRT, associating drift circles from the straw tubes with the track. The extended tracks are refitted once again, using the full information of all three detectors. The quality of the extended track is compared to the quality of the silicon only track; the track extension is kept only if it improves the quality of the fit.

5.1.2 Outside-In Tracking

The inside-out tracking procedure will fail to find tracks from photon conversions or decays of long lived particles in the inner detector, as these particles will not produce hits in the inner layers of the detector and so will not produce seeds. Additionally, inside-out tracking will sometimes fail due to ambiguous hits shadowing the track seed in the densely populated inner layers of the silicon detectors. Further, high energy loss at the outer radii of the SCT may cause the track to change direction in the bending plane and the extension search to go in the wrong direction.

A complementary tracking procedure called 'outside-in' tracking attempts to solve these problems by starting from the TRT and working inwards. It begins by searching for track segments in the TRT using hits not already associated with a silicon track extension, using a Hough transform to identify tracks [82]. These track segments are fitted using a Kalman filter to take into account the drift-time measurements. They are then extended back into the SCT and Pixel detectors, where hits not already associated to tracks are associated to them.

5.2 Vertex Finding

Location of interaction vertices is important in order to know which particles are associated with the primary interaction vertex, and to construct parameters such as the longitudinal and transverse impact parameters, which can be used to distinguish leptons from conversions or from secondary decays in jets. In the ATLAS reconstruction process vertex-finding occurs after reconstruction of inner detector tracks, as described in Section 5.1. The vertex-finding algorithm must associate tracks with vertices, and obtain a best fit for the vertex positions and the associated uncertainties.

The default ATLAS approach to vertex finding is called 'finding-through-fitting' [83]. Tracks are preselected by consistency with the interaction region,

and a single seed vertex is formed from all of the preselected tracks. This is fitted using an 'Adaptive Vertex Finding' [84] algorithm, which uses a Kalman filter to minimise the least squares distances of the tracks from the vertex position. After a preliminary fit, tracks are assigned a weight depending on their compatibility with the vertex, with outlier tracks being down-weighted so as to have less of a pull on the vertex position. The process is iterated until convergence. Following the fit, tracks identified as outliers are used to create a second vertex seed. A simultaneous fit is then carried out of the two vertices, and again outlier tracks are used to create a new primary vertex. The procedure is iterated until none of the remaining outliers fits with any vertex with a χ^2 probability of more than 1%.

5.3 Electron Reconstruction and Identification

5.3.1 Electron Triggers

Events containing electrons are triggered on using ATLAS's three level trigger system as described in Section 3.3. They are triggered on at L1 by requiring that two adjacent towers of calorimeter cells of size $\Delta\eta \times \Delta\phi = 0.1 \times 0.1$ have an energy above a certain threshold. The towers are used to identify a RoI for use at L2. At L2 fast calorimeter clustering and ID tracking algorithms are used. Basic shower-shape cuts on the width of the shower in η and the ratio of energy deposits in the different calorimeter layers are used to reject backgrounds. The EF uses the offline reconstruction and identification algorithms described in Section 5.3.2 and Section 5.3.3, although slightly looser cuts are applied to remain fully efficient offline.

The bandwidth dedicated to electron and photon triggers is approximately 30% of the total EF bandwidth. As the instantaneous luminosity increased throughout 2011 and 2012 it was necessary to regularly tighten the triggers to keep the bandwidth at an acceptable level [85]. At the start of 2011 the primary single electron trigger had a threshold at EF level of 20 GeV. When the instantaneous luminosity exceeded 2×10^{33} cm^{2}s^{-1} the threshold was increased to 22 GeV, and as the luminosity further increased to 3×10^{33} cm^{2}s^{-1}, the identification requirements used at L2 and EF were tightened. The L1 thresholds were also brought closer to the EF threshold, and varying L1 thresholds with η were introduced to account for varying material before the calorimeter. A hadronic leakage cut was also introduced to further reduce the L1 rate. In 2012 the EF threshold was

further raised to 24 GeV, and a track isolation cut introduced at EF, requiring the total p_{T} of tracks surrounding the electron's track in a cone of $\Delta R < 0.2$ to have less than 10% of the p_{T} of the electron.

5.3.2 Electron Reconstruction

Electrons are reconstructed in the central region ($|\eta| < 2.5$) by searching for clusters of energy deposits in the EM calorimeter (referred to henceforth simply as 'clusters') and matching them to inner detector tracks [86, 87]; this is referred to as the *standard* electron algorithm and is described below. In the forward regions ($2.5 < |\eta| < 4.9$) there is no inner detector tracking, and electrons are reconstructed solely from calorimeter clusters; this is also described below.

Standard Electron Reconstruction

Reconstruction begins with the construction of seed clusters in the EM calorimeter. These are formed from calorimeter towers of size $\Delta\eta \times \Delta\phi = 0.025 \times 0.025$, corresponding to the size of cells in the second layer of the EM calorimeter. This results in a grid of 200×256 towers. The energy of the tower is the sum of the cells in all three calorimeter layers falling within the tower. Where cells are shared between more than one tower, the energy is shared according to the fractional overlap of the cell with each tower. The seed cells are formed by sliding a window of size $\Delta\eta \times \Delta\phi = 0.075 \times 0.125$ (3×5 towers) over the grid of towers and identifying local maxima with $E_{\mathrm{T}} > 2.5$ GeV. The position of the cluster is taken to be the energy weighted η, ϕ barycentre of cells in a window around the centre of the cluster. If two seeds are closer than $\Delta\eta \times \Delta\phi = 0.050 \times 0.050$, then only the one with higher E_{T} is kept.

Electron candidates are then formed by matching inner detector tracks to the seed clusters. If there is a reasonable agreement ($\Delta\eta < 0.2$ and $\Delta\phi < 0.1$) between a track's co-ordinates (measured at the origin of the track) and a cluster seed, the track is extrapolated from its last measurement point to the middle layer of the EM calorimeter (TRT-only tracks are all extrapolated). In η, the cluster is required to be within $\Delta\eta < 0.05$ of the track. In ϕ, the cluster must be within $\Delta\phi < 0.1$ of the track if it falls on the side towards which the track bends, or $\Delta\phi < 0.05$ if it is on the opposite side. This asymmetry in the ϕ requirement is to account for the fact that the electrons undergo heavy energy losses from bremsstrahlung due to the large amount of material in the inner detector, which will tend to increase their bending, particularly at high η. If a seed cluster matches to at least one

track, an electron candidate is formed. Seed clusters with no track matches are considered as photon candidates. If several tracks match, tracks with silicon hits are preferred, and the one closest to the cluster in ΔR is chosen. In the case of TRT-only tracks, only a matching in ϕ is required, due to the limited η resolution in the TRT.

The clusters for electron candidates are then rebuilt, using a fixed rectangle of size $\Delta\eta \times \Delta\phi = 0.075 \times 0.175$ (0.125×0.125) in the barrel (endcap), again using a sliding window to find the local maximum. The cluster energy is the sum of four components: the estimated energy deposits before the calorimeter, the measured energy in the cluster, the estimated leakage laterally into other calorimeter cells and the estimated longitudinal leakage behind the EM calorimeter. The four terms are parameterised as a function of the measured cluster energy in the pre-sampler (where it exists) and the measured energy in each of the three calorimeter layers, based on detailed simulations of energy depositions in the calorimeters and the dead material. Additional calibrations are applied to the electron energy based on measurements of $Z \to ee$ and $J/\psi \to e^-e^+$ [87]. The energy of the electron is taken as the cluster energy, and the direction as the track η and ϕ, providing the track has sufficient silicon hits.

Forward Electron Reconstruction

Forward electrons are reconstructed solely from energy deposits in the calorimeter. *Topological clusters* [88] are formed by grouping neighbouring cells in three dimensions. The topological clusters have variable size, depending on the energy deposit and the clustering criteria used. Cells with a signal versus noise significance above a high threshold t_{seed} are used as seeds. Neighbouring cells with a signal significance above a lower threshold t_{cell} are added to the cluster. The neighbours may act as secondary seeds if they have signal significance above an intermediate threshold $t_{\text{neighbour}}$. For electron topological clusters t_{seed} is set equal to $t_{\text{neighbour}}$. The lower threshold at the cell perimeter ensures that tails of showers are not discarded, while the higher thresholds for seeds and neighbours suppress electronics and pile-up noise. The cells are split if they contain more than one local maxima above a certain energy threshold.

An electron candidate is constructed if the cluster has $E_{\text{T}} > 5$ GeV and only a small hadronic energy component. The energy of the electron is taken as the sum of the energy of all cells belonging to the cluster, corrected for energy loss before the calorimeter and lateral and for longitudinal leakages. The direction

of the forward electron is defined by the barycentre of the cells belonging to the cluster, assuming that the electron originated from the origin.

Improvements to electron reconstruction in 2011 and 2012

By default the ATLAS track fitting assumes a pion hypothesis for the modelling of material effects. This does not account well for energy losses via bremsstrahlung. Due to their small mass, these losses are most substantial for electrons, and can have significant effects on their trajectories through the magnetic field. The amount of material in the inner detector in terms of radiation lengths X_0 is shown in Figure 5.2. It is highly non uniform with high concentrations of material at high η and at certain radii. This leads to large variations of the reconstruction efficiency as a function of η, and degradations in estimates of the track parameters. To this end the default ATLAS reconstruction was progressively improved in 2011 and 2012 to better account for energy losses due to bremsstrahlung in the inner detector.

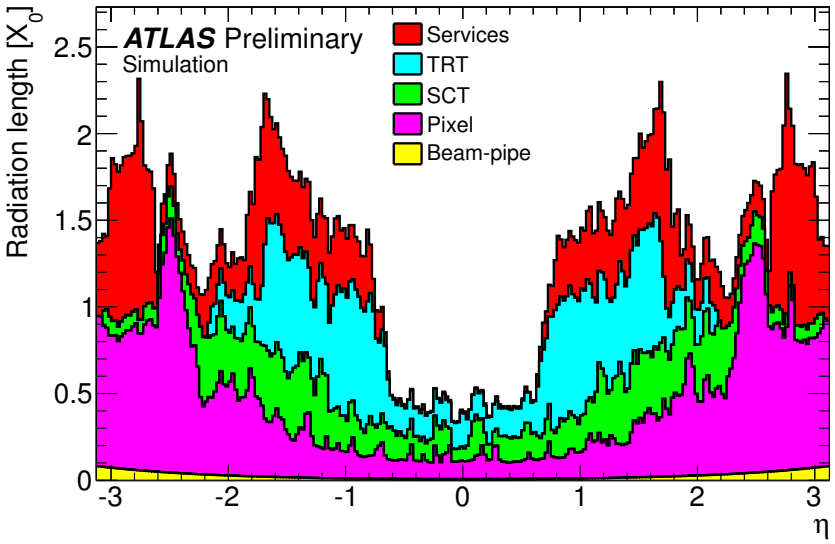

Figure 5.2: Distribution of the inner detector material for each sub-detector as a function of the pseudorapidity. The material of the Pixel and SCT detectors includes passive material arising from electronics, cabling, cooling and mechanical support. Figure from [89].

The radiative loss of energy via bremsstrahlung is highly non-Gaussian, and so is not well modelled by the standard Kalman Filter, which can only incorporate Gaussian noise terms. A non-linear extension of the Kalman filter, the *Gaussian*

Sum Filter (GSF), has been developed [90, 91]. It approximates the probability distribution function (pdf) for energy loss from bremsstrahlung as a weighted sum of Gaussian components, and uses a separate Kalman Filter to process each one. For example, one can consider the extrapolation of a measurement from a surface $k-1$ with state described by n_{k-1} components to surface k, where ϵ_k Gaussians are used to describe the energy losses due to bremsstrahlung between surfaces $k-1$ and k. A separate Kalman Filter is then applied to each of the n_{k-1} components, for each of the ϵ_k noise terms, resulting in the state at surface k being described by $n_k = n_{k-1} \cdot \epsilon_k$ components. At each layer the number of components is artificially reduced to a fixed number by merging similar components, in order to make the extrapolation computationally feasible. Using the GSF allows for better pattern recognition by picking up hits occurring after kinks in tracks caused by bremsstrahlung, as well as improving the resolution of the track parameters.

For 2011 data taking, 'brem-refitting' was applied to reconstructed electron candidates [89]. For technical reasons, it was not possible to include the bremsstrahlung recovery from the beginning of electron reconstruction. Instead, electrons were reconstructed using the standard pion-hypothesis tracking and track cluster matching as described above. The tracks of these candidates were then refitted using the GSF algorithm, and the rest of the electron reconstruction chain re-run using these refitted candidates. This led to the best matches between cluster and track changing in approximately 5% of cases at high pseudo-rapidity (0.8 % overall). However, since it was only possible to run the refitting on tracks already associated to electron clusters using the standard tracking, the full benefit of using GSF was not gained as many tracks with significant energy loss from bremsstrahlung would not be reconstructed successfully by the standard tracking and thus could not be re-fitted. For this reason the brem-refitting did not significantly improve the reconstruction efficiency, but did significantly improve the resolution of track parameters in the bending plane such as d_0, $d_0/\sigma(d_0)$, ϕ and q/p. For example, Figure 5.3 shows the impact parameter significance ($d_0/\sigma(d_0)$) distribution with and without the GSF refit.

In 2012, improvements were made to all stages of the electron reconstruction chain, from the initial tracking pattern recognition through to the track cluster matching [92].

Since the GSF tracking takes approximately 10 times more time to run than the standard Kalman filter, it is not feasible to fit all tracks using the GSF when doing the initial pattern recognition and track finding (see Section 5.1.1). Additionally, the use of such a filter with electron hypothesis would adversely affect

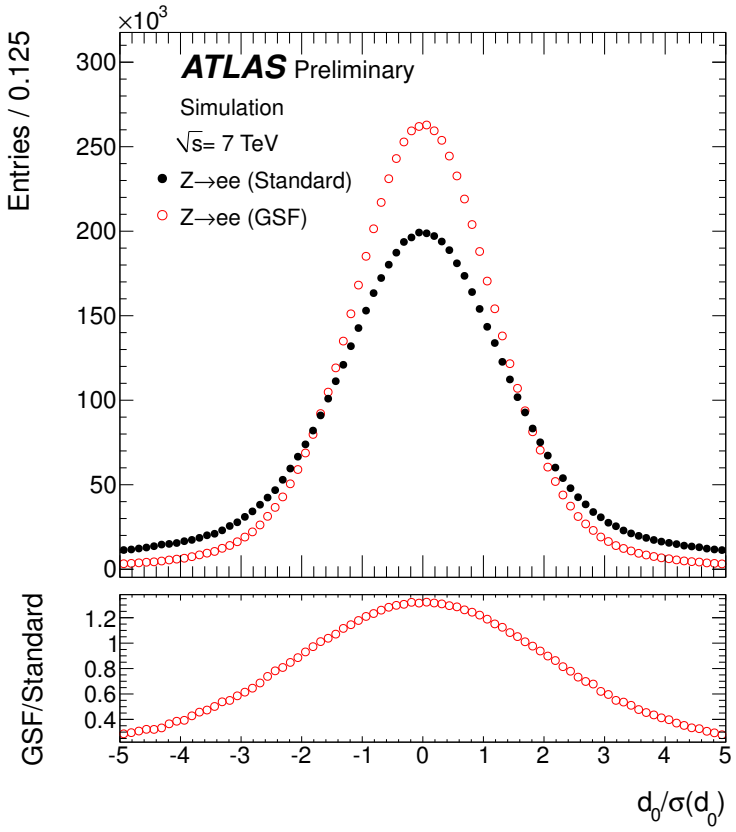

Figure 5.3: Distribution of the simulated transverse impact parameter significance for GSF (open red) and standard (solid black) electrons from Z-boson decays. Figure from [89].

non-electron tracks. Instead, the effects of bremsstrahlung on electron tracks are crudely modelled at the initial pattern recognition by allowing for 30% energy loss at each surface for tracks with momentum above 1 GeV. In order to avoid degrading non-electron tracks, this allowance is made only in regions of interest in a cone of $\Delta R < 0.3$ around EM calorimeter clusters.

The global χ^2 fitter was also improved to allow for electron hypothesis tracks by refitting tracks with a low χ^2 with an energy loss term for the most significant bremsstrahlung energy loss. The modified χ^2 fitter gives a significant improvement in the track parameter resolution, giving an improvement almost as great as using the more sophisticated GSF algorithm, but running in approximately one tenth of the time.

At this stage, there will still be a number of tracks which had large energy

losses from bremsstrahlung and were consequentially badly fitted. A refit using the GSF fitter described above is thus carried out for all tracks loosely matched to an EM calorimeter cluster. This two-step procedure is carried out so that only tracks which have a chance of forming an electron candidate are fitted with the time-consuming GSF fitter. The final matching of the refitted tracks to the clusters and the selection of the best match is also improved by scaling the track momentum to the cluster energy before extrapolating the track to the cluster barycentre.

Overall, these improvements increase the electron reconstruction efficiency by $\sim 2\%$ in the calorimeter barrel and $\sim 5\%$ in the calorimeter endcaps. For low E_{T} electrons ($E_{\mathrm{T}} < 20$ GeV) the improvement is up to 6%.

Electron Reconstruction Efficiencies

Figure 5.4 shows the electron reconstruction efficiency in 2011 and 2012 as a function of the pseudo-rapidity and the transverse energy of the electron cluster. These are measured in the data with a tag-and-probe technique using $Z \to ee$, $W \to e\nu$ and $J/\psi \to e^{-}e^{+}$ decays [87]; the efficiencies predicted by Monte Carlo are also shown. The reconstruction efficiency in 2011 drops by approximately 4% between central and forward pseudo-rapidities. In 2012 the overall reconstruction efficiency improves by approximately 2% at central pseudo-rapidity, and the drop-off in efficiency at high pseudo-rapidity is reduced to roughly 1%. Similarly, the reconstruction efficiency at low E_{T} improves by roughly 6% in 2012 with respect to 2011. Good agreement is observed between the reconstruction efficiency observed in data and the efficiency predicted by simulation. Scale-factors, parameterised as a function of η and E_{T}, are applied to the Monte Carlo to correct the reconstruction efficiency to that observed in data.

The charge mis-identification rate is also measured using a tag-and-probe technique, and is found to be about 0.5% in the barrel and up to 8% at the limit of the Inner Detector tracker. The rates are observed to be well simulated in the Monte Carlo [87].

Electron Energy Calibration

A first measurement of the EM calorimeter energy scale is derived from test beam measurements, however there are large uncertainties in the transfer of the measurement from the test-beam to the actual ATLAS environment. Further, the calorimeter energy response needs to be calibrated to account for the varying

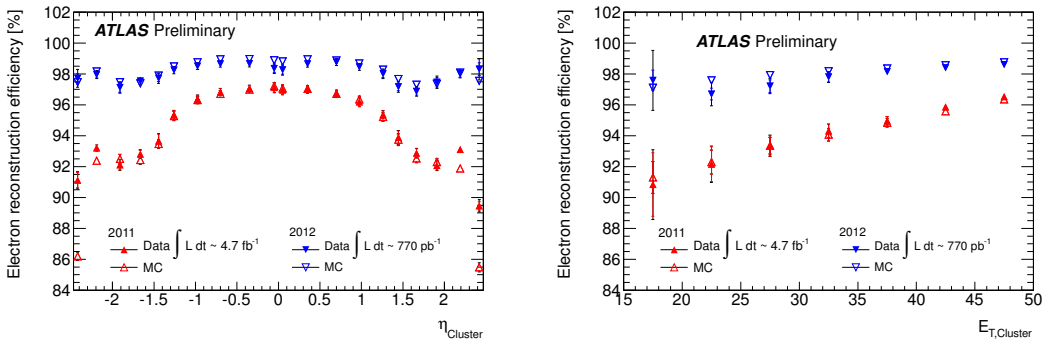

(a) (b)

Figure 5.4: Electron reconstruction efficiency in 2011 and 2012 as a function of (a) the cluster η and (b) the cluster E_{T}. The solid coloured points show the efficiency observed in data whilst the open points show the simulated efficiency in Monte Carlo. Figures from [93].

amount of dead material before the calorimeters as a function of pseudo-rapidity. Monte Carlo-derived calibrations are applied to the clusters to correct for dead material and leakage outside the calorimeter. The energy response is further calibrated in-situ using $Z \to ee$ decays. This also allows the inter-calibration of different regions of the calorimeters in η. The measured energy of an electron candidate in region i can be related to its true energy by:

$$E^{\mathrm{meas}} = E^{\mathrm{true}}(1 + \alpha_i) \tag{5.2}$$

where E^{true} is the true electron energy, E^{meas} is the measured energy after applying the Monte Carlo based energy-scale correction and α_i measures the residual mis-calibration. The residual calibrations are determined by selecting pairs of opposite-sign high p_{T} electrons with a di-electron invariant mass near to the Z peak. The α parameters are obtained by performing an unbinned fit minimising the log-likelihood function:

$$-\ln L_{\mathrm{tot}} = \sum_{i,j} \sum_{k}^{N_{ij}^{\mathrm{events}}} \left[-\ln L_{ij} \left(\frac{m_k}{1 + \frac{\alpha_i + \alpha_j}{2}} \right) \right] \tag{5.3}$$

where i, j label the η regions of the two electrons from the $Z \to ee$ decay, m_k is the measured di-electron mass (after applying the test-beam and Monte Carlo calibrations) in event k and $L_{ij}(m)$ is a probability density function describing the likelihood of observing a $Z \to ee$ decay with mass m. The pdf is taken from Monte Carlo simulation. The resulting calibration parameters α_i, measured in

2010 data, are shown in Figure 5.5(a). Figures 5.5(b) and 5.5(c) show the calibration parameters measured as a function of time in 2011 and 2012 respectively, and Figures 5.5(d) and 5.5(e) show the parameters as a function of the average number of interactions per bunch crossing due to pileup for 2011 and 2012 data respectively. The calibration is found to be constant in time, and insensitive to pileup. The linearity of the response with respect to electron energy is checked by applying a similar procedure to electrons from $J/\psi \to e^- e^+$ decays (for which the sample is much more statistically limited). The results are found to be in good agreement with the results from $Z \to ee$ decays, and the resulting difference is assigned as an energy scale systematic at low E_{T}.

The electron energy resolution is also measured in data. The fractional energy resolution is parameterised as:

$$\frac{\sigma(E)}{E} = \frac{a}{\sqrt{E}} \oplus \frac{b}{E} \oplus c \tag{5.4}$$

where a is the sampling term, b is the noise term and c is the constant term. Due to limited statistics, only the constant term is measured in data, and the description of the sampling and noise terms is taken from simulation. Figure 5.6 shows the observed di-electron mass distribution for all η bins for data taken in 2011 after applying the energy calibration described above. The distribution is fitted to a Breit-Wigner to model the Z lineshape convolved with a Crystal-Ball function to model the detector resolution and effects of FSR. The constant term is extracted by comparing the width of the Crystal-Ball functions in the data and in the simulation. Since the resolution observed in data is slightly worse than the simulated resolution, a Gaussian smearing is applied to electron energies in the simulation to reproduce the resolution observed in the data.

5.3.3 Electron Identification

The electron candidates reconstructed as described in the previous section will contain a high contamination from jets faking electrons, non-isolated electrons from decays in jets, and electrons from photon conversions. In order to identify prompt electrons, a cut-based identification is used. Cuts are made on variables relating to the shape of the electromagnetic shower in the calorimeter, the quality of the inner detector track, the track-calorimeter matching and particle identification information from the TRT. The cuts were optimised using a multivariate analysis program (TMVA), in 10 bins of cluster η and 11 bins of cluster E_{T} from

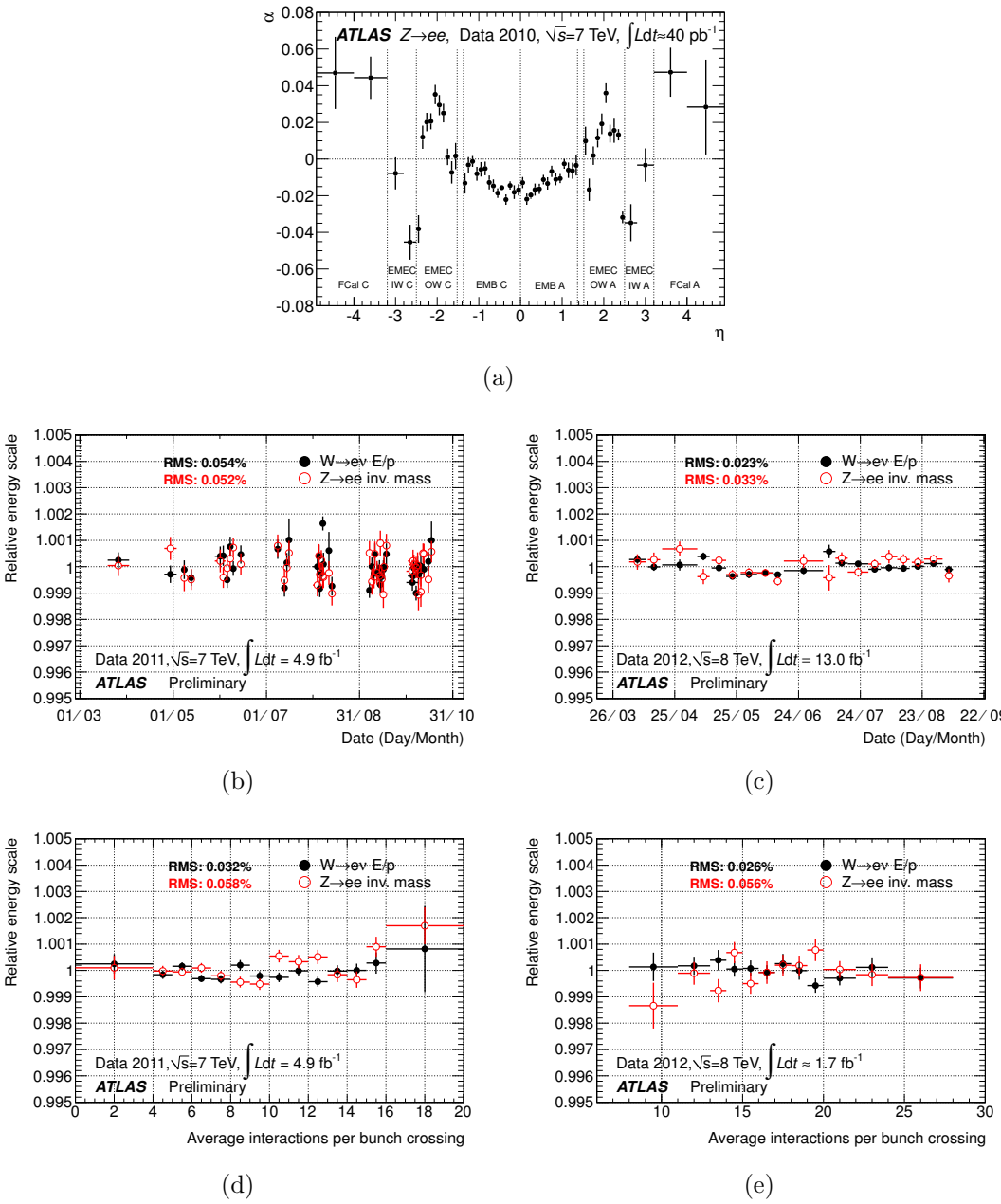

Figure 5.5: Figure (a) shows the energy-scale correction factor α as a function of the pseudorapidity of the electron cluster derived from fits to $Z \to ee$ in 2010 [87]. The errors shown are statistical only. Figures (b) and (c) show the stability of the energy-scale correction factor α (integrated over all η) in 2011 [94] and 2012 [95] respectively. Figures (d) and (e) show the stability with respect to pile-up in 2011 [94] and 2012 [96] respectively.

5 GeV to $>$ 80 GeV. Three reference sets of cuts are used, denoted `Loose++`, `Medium++` and `Tight++`, designed to give progressively greater background rejection, at the cost of signal efficiency. The expected jet rejections (from simulation)

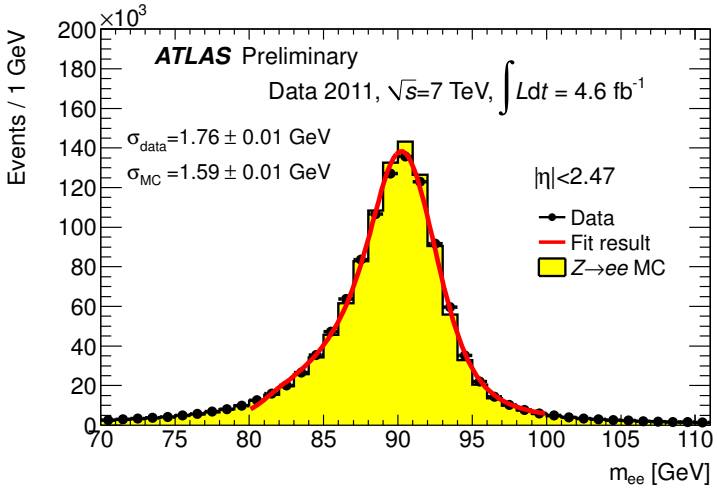

Figure 5.6: Di-electron mass distribution after applying the energy scale calibration. The points show the distribution observed in data whilst the histogram shows the prediction from simulation. The red line shows a fit to the data using a Breit-Wigner convolved with a Crystal-Ball function in order to determine the resolution. Figure from [97].

of the three points are 500, 5000 and 50000 respectively [86]. In 2012, the identification selections were re-optimised with respect to the 2011 selections to prevent drops in efficiency of up to 20% in events with high pileup .

The variables cut on at the different working points are described below. Simulated distributions for these variables in the 2012 reconstruction for prompt electrons from Z boson decays and from hadrons reconstructed as electrons are shown in Figures 5.7 and 5.8. Typical values of the cuts in 2012 for the bin with $0.1 < |\eta| < 0.6$ and 20 GeV$< p_{\mathrm{T}} <$ 30 GeV are also indicated on the plots; these are the cuts made in the `Loose++` selection, so long as the variable in question is cut on in `Loose++`, otherwise the cut value for the loosest selection at which the variable is cut on is shown.

`Loose++` Requirements

In both 2011 and 2012 the `Loose++` selection makes cuts on shower-shape variables in the first and second layers of the EM calorimeter, leakage into the hadronic calorimeter, track quality in the silicon detectors, and loose track cluster matching. The variables cut on are as follows:

- **Shower Shapes:** cuts are made on the following shower-shape variables which distinguish between electromagnetic showers originating from electrons or photons and hadronic showers originating from particles in jets:

  - Hadronic leakage, R_{had}, the ratio of E_{T} in the first layer of the hadronic calorimeter to the E_{T} of the EM cluster. In the range $0.8 < |\eta| < 1.37$ the E_{T} of the full hadronic calorimeter is used, to compensate for the crack between the barrel and extended barrel of the tile calorimeter.
  - R_{η}, the ratio of the energy in the middle layer of the calorimeter in 3×7 cells to the energy in 7×7 cells centered at the electron cluster position.
  - $w_{\eta 2}$, the lateral width of the shower in the second layer of the EM calorimeter.
  - E_{ratio}, the ratio of the energy difference between the largest and second largest energy deposit in the first layer of the EM calorimeter to the sum of their energies.
  - w_{stot}, the total width of the shower in the first layer of the EM calorimeter.

- **Silicon Hits:** at least 7 hits in the silicon detectors, of which at least one must be in the pixel detector. This ensures good track quality and rejects backgrounds from conversions or decays such as $\pi^0 \to e^+e^-$.
- **Track-Cluster matching:** a loose matching in η is applied, requiring $\Delta\eta < 0.015$; this ensures that the track and the cluster originate from the same physical particle and rejects backgrounds from combinatoric fakes.

The shower-shape variables R_{η} and R_{had} are particularly susceptible to pileup since they sample a large area of the calorimeter. Cuts on these variables were therefore loosened in 2012 with respect to 2011, reducing the rejection power of `Loose++` by about 20%.

`Medium++` Requirements

All `Loose++` cuts are required to be passed, and in addition:

- **Shower Shapes:** the shower-shape cuts made in `Loose++` (R_{η}, R_{had}, $w_{\eta 2}$, E_{ratio}, w_{stot}) are made tighter. For 2012, the cuts on R_{η} and R_{had} were loosened with respect to 2011, and made at the same value as for `Loose++`, whilst the cuts on $w_{\eta 2}$, E_{ratio} and w_{stot} were tightened with respect to 2011.
- **Track-Cluster matching:** a tighter matching in η is applied, requiring $\Delta\eta < 0.005$.

- **Impact Parameter:** require that the electron's track has a transverse impact parameter $|d_0| < 5$ mm; this rejects backgrounds from electrons originating from decays of hadrons in jets.
- **Silicon Hits:** stricter requirements are made on hits in the silicon detectors. It is required that there is at least one hit in the b-layer for $|\eta| < 2.01$ ($|\eta| < 2.37$ in 2012). In 2011, at least 1 Pixel hit is required for $|\eta| < 2.01$ and at least two for $|\eta| > 2.01$. For 2012, two Pixel hits are required in all bins.
- **Fraction in third calorimeter layer f_3:** for 2012 a cut on the fraction of the shower energy deposited in the third layer of the EM calorimeter was added to compensate for the loosening of the cuts in the first layer of the calorimeter. This cut is only applied for $E_{\mathrm{T}} < 80$ GeV, since the depth of the EM shower and hence leakage into the third layer increases with energy.
- **TRT High Threshold Hits** A loose requirement is made on the fraction of high-threshold (HT) hits from transition radiation photons in the TRT detector (see Section 3.2.2).

`Tight++` Requirements

All `Medium++` cuts are required to be passed, and in addition:

- **Shower Shapes:** cuts on shower-shape variables are made at equal or tighter values to those for `Medium++`. As for `Medium++`, the cuts on R_η and R_{had} were loosened in 2012 with respect to 2011, whilst the cuts on $w_{\eta 2}$, E_{ratio} and w_{stot} were tightened.
- **Track-Cluster matching:** a cluster matching in ϕ is added, requiring $\Delta\phi < 0.02$, and cuts are made on the ratio of the cluster energy to the track momentum, E/p.
- **Impact Parameter:** the transverse impact parameter cut is tightened to $|d_0| < 1$ mm.
- **Silicon Hits:** stricter requirements are made on hits in the silicon detectors, requiring that there is at least one hit in the b-layer for all η, and, in 2012, at least 2 hits in the Pixel detector for all η.
- **Conversion Rejection:** candidates matched to reconstructed photon conversions are rejected.

Forward Electron Identification

Since in the forward region there is no tracking from the inner detector, identification must rely on calorimeter shower-shape variables alone. A good discrimination between electrons and hadrons may be made due to the fine transverse and longitudinal segmentation of the calorimeter, but it is not possible to distinguish electrons and photons in the forward region. Two selections are defined for forward electrons: `Loose` and `Tight`. The cuts are optimised in two bins of η for 2011 running (one for the EMEC and one for the FCAL) and in two bins of η and four bins of number of primary vertices in the event (n_{PV}) for 2012.

The variables cut on at the two working points are described below. Expected distributions from simulation for these variables in 2012 data for prompt electrons from Z boson decays and from hadrons reconstructed as electrons are shown in Figure 5.9. Typical values of the cuts in 2012 for the lowest n_{PV} EMEC bin are also indicated on the plots.

Forward `Loose` Requirements

Cuts are made on the following variables:

- **Shower depth, λ_{centre}:** the distance of the shower barycentre from the front face of the calorimeter along its axis.
- **Longitudinal Second Moment,** $\langle\lambda^2\rangle$ the second moment[1] of the distance of each cell to the shower barycentre in the longitudinal direction.
- **Transverse Second Moment,** $\langle r^2\rangle$ the second moment of the distance of each cell to the shower barycentre in the transverse direction.

Forward `Tight` Requirements

All of the `Loose` cuts are required to be passed, and in addition cuts are made on the following variables:

- **Fraction of cluster energy in the most energetic cell, f_{max}.**
- **Normalised lateral moment,** $\frac{w_2}{w_2+w_{\text{max}}}$ where w_2 is the second moment of r_i setting $r_i = 0$ for the two most energetic cells and w_{max} is the second moment of r_i setting $r_i = 4$ cm for the two most energetic cells and $r_i = 0$ for the remaining cells.

[1] The n^{th} moment is defined as $\langle x^n\rangle = \frac{\sum_i E_i x_i^n}{\sum_i E_i}$ where i runs over all cells in the cluster.

- **Normalised longitudinal moment,** $\frac{l_2}{l_2+l_{\max}}$ where, similarly to the normalised longitudinal moment, l_2 is the second moment of λ_i setting $\lambda_i = 0$ for the two most energetic cells and $l_{\max}$ is the second moment of λ_i setting $\lambda_i = 10$ cm for the two most energetic cells and $\lambda_i = 0$ for the remaining cells.

Electron Identification Efficiencies

Figure 5.10 shows the electron identification efficiency in 2011 and 2012, measured in a similar fashion to the reconstruction efficiency described above, as a function of the number of reconstructed primary vertices in the event. Using the 2011 identification requirements, the efficiency can drop by over 5% in events with 18 reconstructed primary vertices with respect to the efficiency in events with a single primary vertex. Figure 5.11 shows the `Loose++` identification efficiency as a function of E_{T}, using the 2011 requirements. Differences at the level of a few percent are observed between the efficiency measured in data and the efficiency measured in Monte Carlo simulation. This is mainly attributed to mis-modelling of the shower-shape variables in the Monte Carlo. Scale-factors, parameterised as a function of η and E_{T}, are applied to the Monte Carlo to correct the reconstruction efficiency to that observed in data.

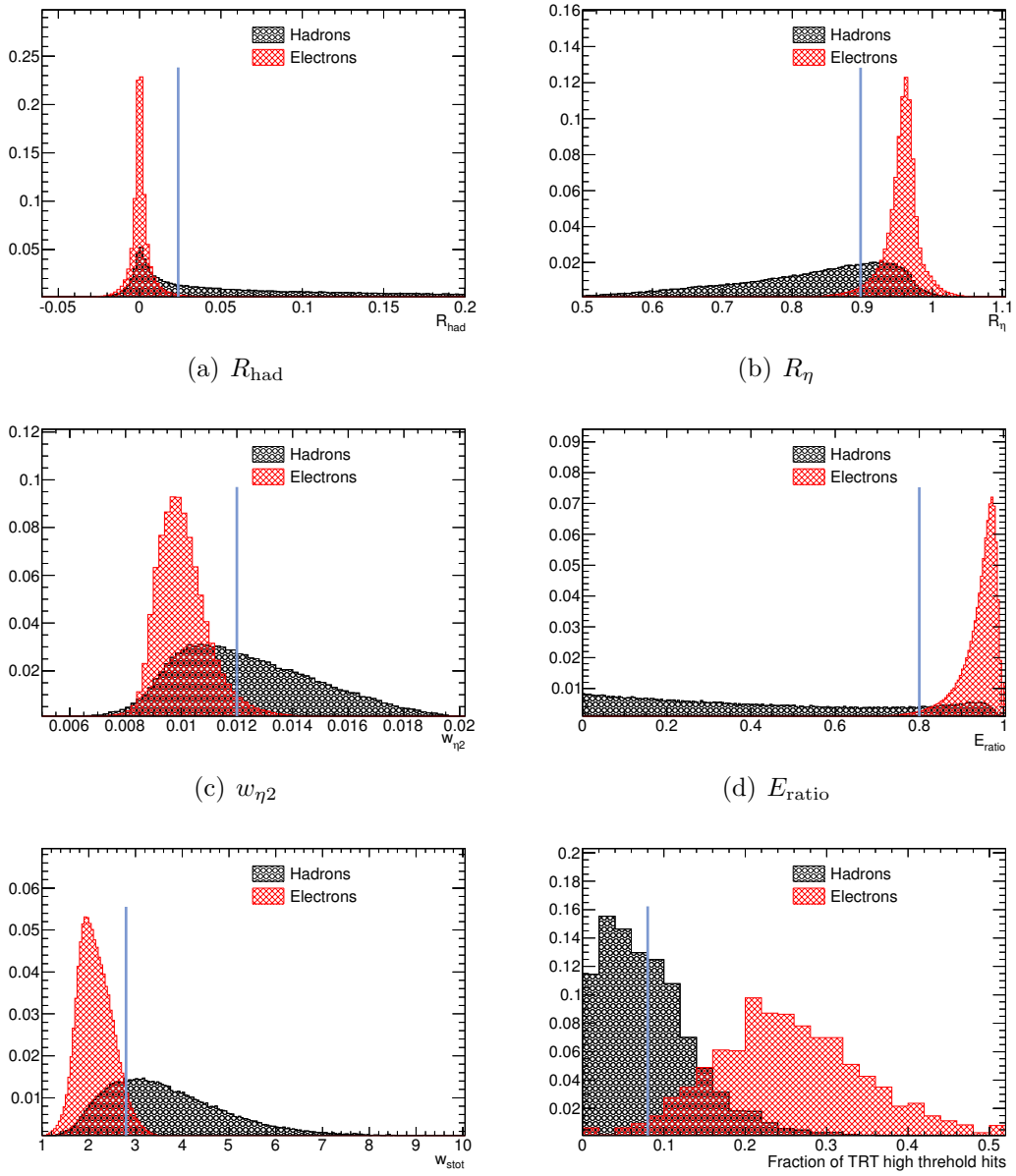

(a) R_{had} (b) R_{η}

(c) $w_{\eta 2}$ (d) E_{ratio}

(e) w_{stot} (f) TRT High Threshold Hits Fraction

Figure 5.7: Simulated distributions of variables used in central electron identification. The black histogram shows the distributions for prompt electrons from decays of Z bosons, whilst the red histogram shows the distributions for hadrons reconstructed as electrons. Since the shapes of the distributions are different in the different regions of the calorimeter, only electrons and hadrons in the LAr barrel region ($|\eta| < 1.47$) are shown. The blue lines indicate typical values of the cuts, which are optimised in 50 bins of p_{T} and η. See the text for a description of the variables.

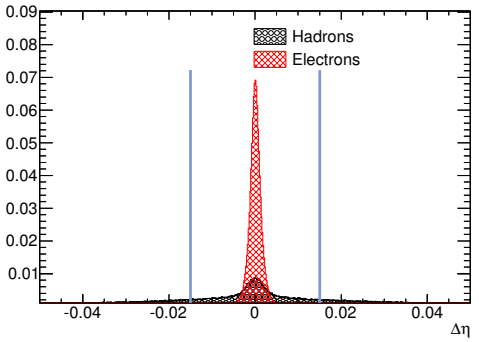

(a) $\Delta\eta$

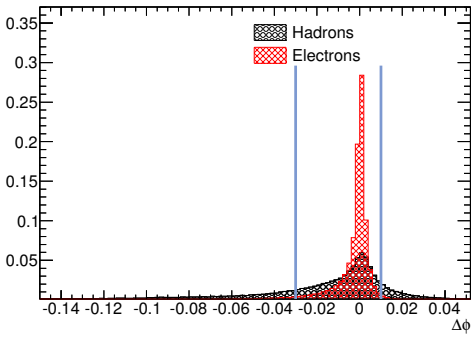

(b) $\Delta\phi$

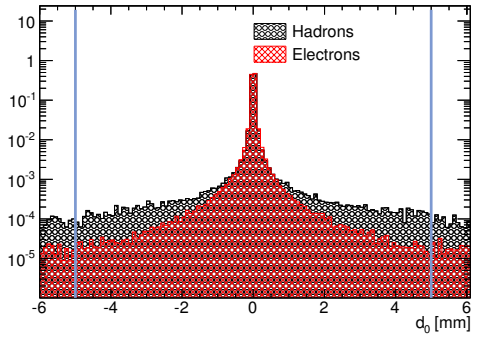

(c) d_0

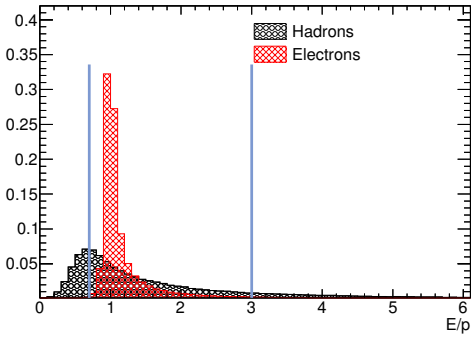

(d) E/p

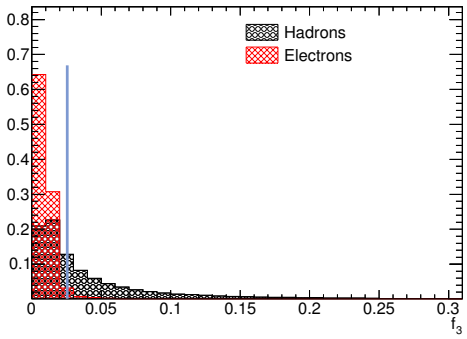

(e) f_3

Figure 5.8: Simulated distributions of variables used in central electron identification. The black histogram shows the distributions for prompt electrons from decays of Z bosons, whilst the red histogram shows the distributions for hadrons reconstructed as electrons. Since the shapes of the distributions are different in the different regions of the calorimeter, only electrons and hadrons in the LAr barrel region ($|\eta| < 1.47$) are shown. The blue lines indicate typical values of the cuts, which are optimised in 50 bins of p_{T} and η. See the text for a description of the variables.

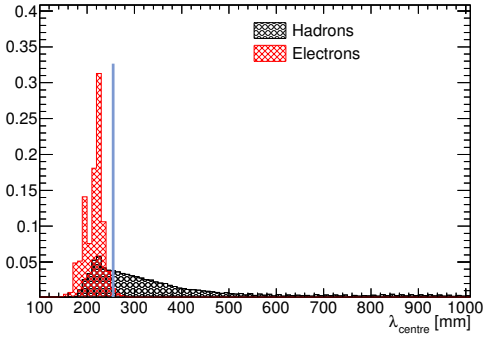

(a) λ_{centre}

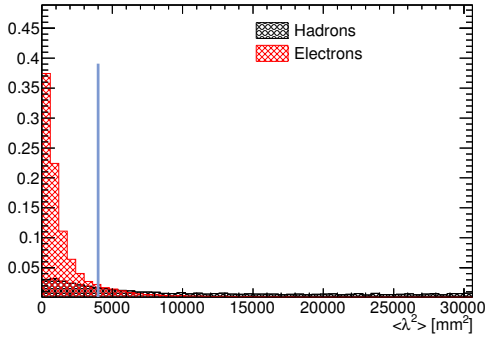

(b) $\langle\lambda^2\rangle$

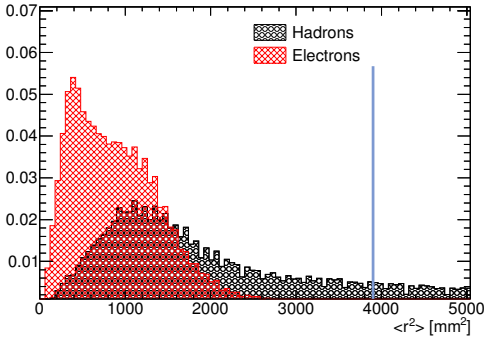

(c) $\langle r^2\rangle$

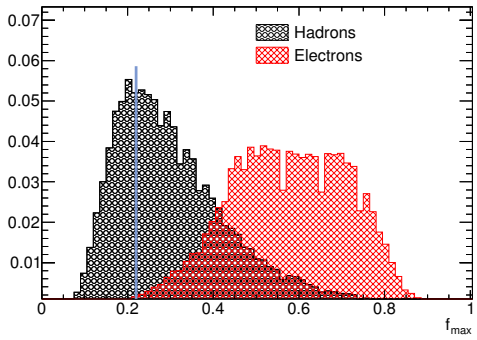

(d) f_{max}

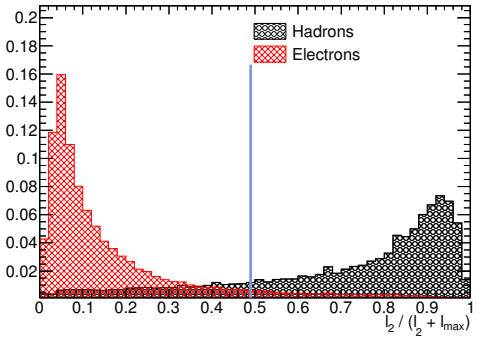

(e) Normalised longitudinal moment

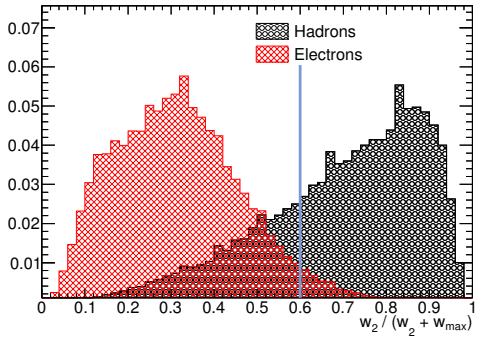

(f) Normalised lateral moment

Figure 5.9: Simulated distributions of variables used in forward electron identification. The black histogram shows the distributions for prompt electrons from decays of Z bosons, whilst the red histogram shows the distributions for hadrons reconstructed as electrons. The blue lines indicate the cut values for $2.47 < |\eta| < 3.16$. See the text for a description of the variables.

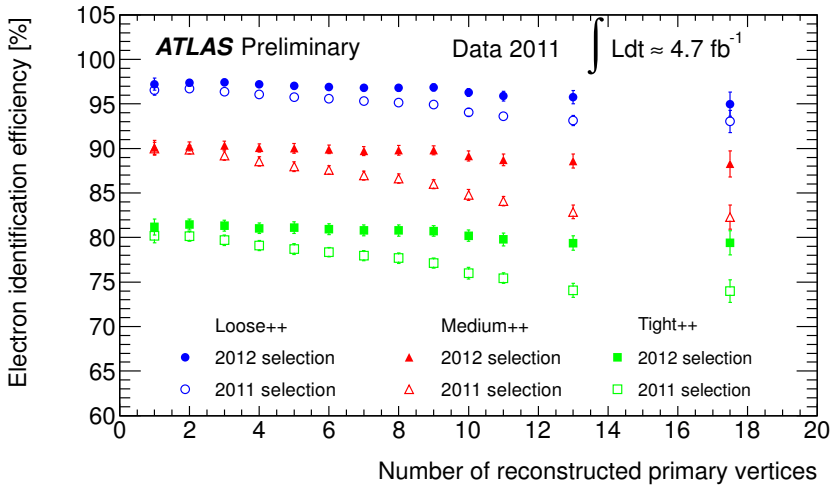

Figure 5.10: Electron identification efficiency in 2011 (open markers) and 2012 (solid markers) as a function of the number of reconstructed primary vertices in the event. The blue circles show the efficiency for the `Loose++` selection, the red triangles for the `Medium++` and the green squares for the `Tight++`. Figure from [98].

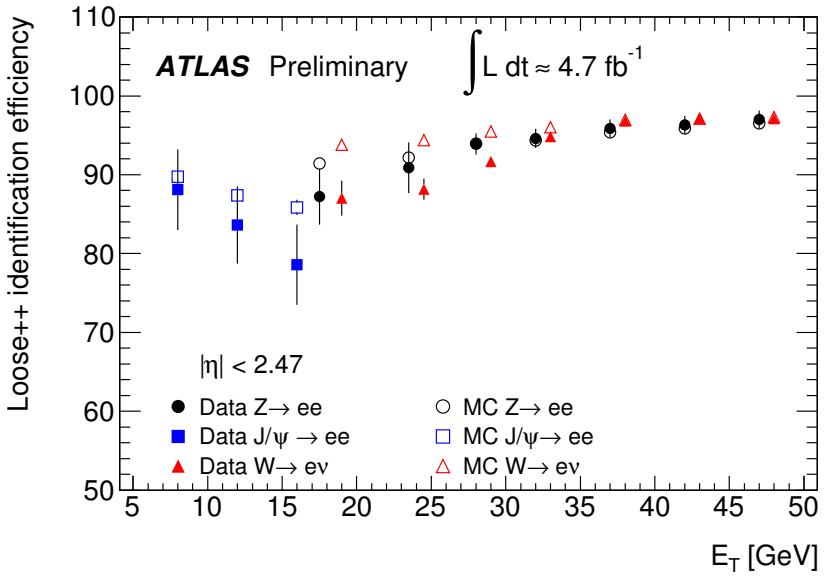

Figure 5.11: Efficiency of the `Loose++` identification requirements as a function of the cluster transverse energy. The solid points indicate data based measurements whilst the open points indicate predictions from Monte Carlo. The different markers indicate the method used to measure the efficiency: results from $Z \to ee$ tag and probe are shown as black circles, results from $J/\psi \to ee$ as blue squares and results from $W \to e\nu$ as red triangles. Figure from [99].

5.4 Muon Reconstruction and Identification

5.4.1 Muon triggers

Muons are triggered on at L1 using the RPC in the barrel ($|\eta| < 1.05$) and the TGC in the endcaps ($|\eta| < 2.4$). As shown in Figure 5.12, the muon trigger chambers are arranged in three planes of two to four layers; the L1 trigger fires on coincident hits in different planes. The coverage is ∼99% in the endcaps but only ∼80% in the barrel due to gaps for services and the detector feet. The RPC planes consist of doublets of independent layers, and for low p_{T} triggers a coincidence in three out of the four layers of the two inner planes is required. The high p_{T} triggers start from the low p_{T} triggers, and look for hits in one of the two layers of the third plane (referred to as the high p_{T} confirmation plane). Similarly, the two outermost planes of the TGC consist of doublets of independent detectors and low p_{T} triggers again require the coincident hits in three out of four layers. The TGC inner plane has three layers; high p_{T} triggers require coincidences in at least two out of the three layers of this plane, in addition to the coincidences of a low p_{T} trigger. Coincidences are generated separately for η and ϕ; a coincidence is required in both co-ordinates for the trigger to be fired. To apply a p_{T} threshold to the trigger the coincidences are required to fall inside *roads*: parameterised geometrical regions corresponding to muons of either charge with momentum above a given p_{T} threshold. In 2011 the L1 p_{T} threshold for the primary single muon trigger was 15 GeV; in 2012 it was 20 GeV.

The muon HLT uses similar algorithms to the online muon reconstruction described below. At L2, each L1 muon candidate is refined by including precision hit data from the MDT and CSC in a RoI defined by the L1 candidate. Muon spectrometer (MS) tracks are built by opening narrow roads around the L1 trigger chamber hits and associating hits from other chambers with the track. A rough p_{T} measurement is obtained using a lookup table. The MS tracks are then combined with ID tracks, reconstructed using the same fast L2 ID tracking as the electron L2 trigger. The muon EF uses the full offline algorithms, running in RoIs determined by the L2 trigger. There are two reconstruction strategies used at EF level: *outside-in* (starting from the reconstructed MS tracks, extrapolating to the beamline and attempting to combine with an ID track) and *inside-out* (starting from ID tracks and attempting to extrapolate to the MS). In 2011, both strategies were run in parallel to maximise efficiency. In 2012, to reduce processing time, the outside-in algorithm is run first, and only in events failing the trigger at this

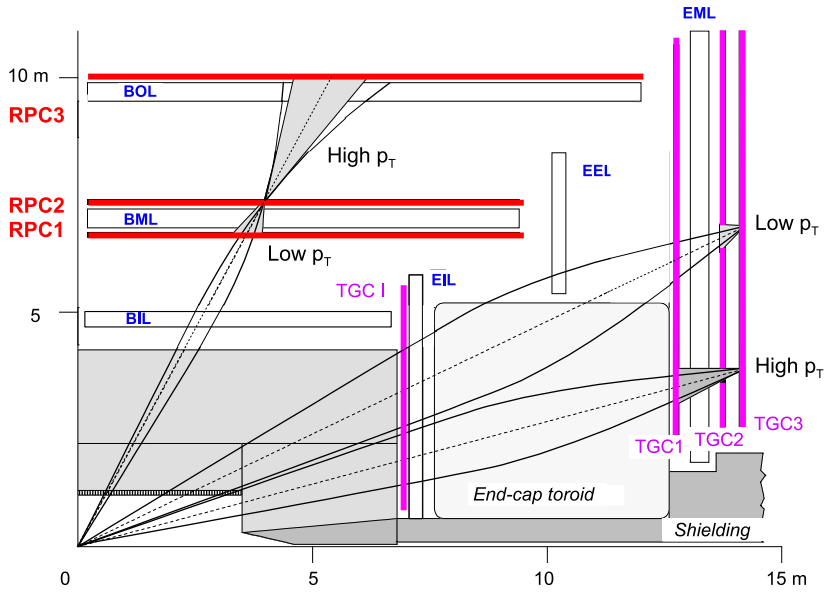

Figure 5.12: Cross sectional view of the muon trigger chambers. Figure from [100].

stage is the inside-out algorithm run. In 2011 the HLT threshold used for the primary single muon trigger was 18 GeV; in 2012 it was raised to 24 GeV. The muon trigger is not sensitive to pile-up, but modifications were required in 2012 in order to keep the rate at an acceptable level in the higher luminosity conditions. To achieve this an ID track based isolation cut was applied at EF level, requiring that the sum of the p_{T} of tracks in a cone of $\Delta R < 0.2$ around the muon track be less than 12% of the muon's p_{T}. Only tracks with $p_{\mathrm{T}} > 1$ GeV enter the calculation, and to reduce pileup dependency, must have $|\Delta z_0| < 6$mm, where Δz_0 is the difference in longitudinal impact parameter between the track and the muon track.

5.4.2 Reconstruction and Identification

Muon reconstruction is in general based on combinations of accurate measurements in the muon spectrometer and the inner detector [101, 102]. There are four categories of muons:

- **Combined:** combination of an MS track with an ID track. In general limited by the acceptance of the ID, $|\eta| < 2.5$, but due to the complicated nature of the magnetic field it is possible to form Combined muons beyond this.

- **Segment-Tagged:** combination of an ID track with an MS track segment. An MS track segment is a straight line track segment reconstructed in a single MS station (as defined in Section 3.2.5) where the segment did not form a full MS track. The track parameters of the reconstructed muon are taken solely from the ID track.

- **Stand-Alone:** a muon track reconstruction based solely on MS measurements. Possible over the full acceptance of the MS, $|\eta| < 2.7$.

- **Calorimeter-Tagged:** ID tracks are tagged as originating from muons by matching them to calorimeter deposits consistent with a minimum ionising muon. No MS information is used.

Since Combined muons have a fully reconstructed track in both the ID and the MS, they are the preferred muon type and will have the best track parameter resolution. The ID provides the best momentum measurement at low to intermediate momenta, whereas the MS provides the better measurement at higher p_{T} (roughly for $p_{\mathrm{T}} > 100$ GeV). Combination with an ID track improves the momentum resolution over the range $4 < p_T < 100$ GeV. Segment-Tagged muons are useful to recover efficiency at low p_{T} where muons may only reach the inner layer of the muon chamber and in regions of limited detector acceptance. Stand-Alone muons are useful to extend coverage beyond the coverage of the ID. Calorimeter-Tagged muons suffer large fake rates from jets and electrons, but can be used to recover acceptance at $|\eta| < 0.1$ where there are gaps in the muon chambers to provide space for services to the ID, the solenoid magnet and the calorimeters.

There are two parallel muon reconstruction chains in use in ATLAS, `STACO`[103] and `MUID`. Each uses slightly different track finding algorithms, and approach the combination of ID and MS tracks in different ways. `MUID` performs a global refit of hits in the MS and the ID, whereas `STACO` attempts a statistical combination of the two track measurements, weighting the relative contributions according to their covariance matrices. The two chains are found to give similar performance. The measurements in this thesis all use muons reconstructed with the `STACO` chain, so this chain is described in detail here.

The `STACO` chain begins with the reconstruction of MS tracks using the `MuonBoy` algorithm. First, the muon trigger chambers are used to identify Regions of Activity (RoA). The RoA are areas of size $\Delta\eta \times \Delta\phi = 0.4 \times 0.4$ where there is at least one RPC or TGC hit in both co-ordinates. Local straight track segments are then reconstructed within the RoA by attempting to combine each MDT hit in

a multilayer[2] with each MDT hit in the other multilayer of the same or adjacent station. This gives four possible track segments. Each of these segments is extrapolated to the rest of the MDT tubes in the station and matched with hits. The segment candidates are required to point loosely towards the interaction point, and cuts are applied on the χ^2 of the track segment, with penalties for missing hits.

Track candidates are then formed by combining at least two segments from different stations to form track candidates, as follows. The tracks are seeded from track segments that have at least one hit from a trigger-chamber to provide a measurement in the non-bending plane. A first rough estimate of the momentum is deduced from the position and direction of the segment. Each of these segments is then extrapolated to the other stations, and matches in position and direction are found. Since the track momentum is not well known at this point, a 'momentum-scan' of several possible momentum values is performed. The best match (if any) is chosen, and the track segments are combined and refitted to obtain a more accurate momentum measurement. A second, finer momentum scan is performed around the improved momentum estimate, extrapolating to all other stations, and segments which match to the track are added to it. The track is then refitted (still using the track segments as inputs) to more accurately determine the momentum, position and direction.

Next a global fit is performed on the candidate tracks, starting from the best results of the previous fit, but using the full raw hit information rather than the track segments. This gives a better estimate of the likelihood of the track and gives a better discrimination of outlier hits from 'good' hits. Finally, a last fit including a detailed description of the material traversed by the tracks is performed. This fit properly takes into account multiple scattering effects, by including the scattering angles at a set of discretised scattering centres in the fit. The energy loss due to interactions is also taken into account by parametrising the most probable energy loss as a function of the track momentum and the amount of material crossed. The selection of reconstructed muons is made based on the χ^2 quality of this final fit.

Selected muon tracks are then extrapolated back to the interaction point, correcting for energy loss and multiple scattering in the calorimeters and the material of the ID [3]. MS tracks are combined with ID tracks by selecting tracks to be paired on the basis of a match χ^2, defined from the difference between the

[2]Each station consists of two *multilayers* of MDT sandwiched between RPC chambers

[3]The typical energy loss in the calorimeter is ~ 3 GeV.

two sets of track parameters weighted by their combined covariance matrix. The track parameters are combined, weighting the relative contributions according to their covariance matrix.

The efficiency of the muon reconstruction in the MS decreases very rapidly with decreasing p_{T} because accurate tracking of low p_{T} muons in the highly inhomogeneous magnetic field is very complicated. Furthermore as p_{T} decreases, the energy lost by the muons inside the calorimeters becomes comparable to their energy, especially in the barrel region. The `MuTag` algorithm is used to recover efficiency at low p_{T} by starting from ID tracks, extrapolating them to the inner station of the MS and attempting to match them with MS track segments not yet associated to Combined tracks, yielding Segment-Tagged muons.

Calorimeter-Tagged Muons

It is also possible to reconstruct muons independently of the MS by using the calorimeter to tag inner-detector tracks originating from muons. A muon with sufficient momentum will traverse all layers of the calorimeter, leaving a small energy deposit in each layer. It is possible to distinguish this pattern of energy deposition from that of other particles. A low-momentum hadron will deposit most of its energy in the first layers of the calorimeter, leaving no signal in the last layers. High-momentum hadrons will deposit most of their energy in the core cells, and electrons will deposit most of their energy in the EM calorimeter. The `CaloTrkMuID` algorithm identifies muon candidates by requiring an ID track matched to a signal consistent with a minimum-ionising particle in each layer of the calorimeter. Both a cut-based quality selection and a likelihood ratio based quality selection are used, and muon candidates passing either are accepted. Calorimeter tagged muons are used to recover efficiency at $|\eta| < 0.1$ where there is a gap in the muon-spectrometer.

Reconstruction Efficiencies

Figure 5.13 shows the observed reconstruction efficiency for muons reconstructed as either Combined or Segment-Tagged in the 2011 data, measured using a tag and probe technique on Z boson decays [102], as well as the efficiency predicted by the Monte Carlo simulation. The efficiency is seen to drop significantly for $|\eta| < 0.1$ for reasons explained above. The efficiency for calorimeter tagged muons is also shown, and it is seen that they effectively recover the loss in efficiency at $|\eta| < 0.1$. The muon reconstruction efficiency is seen to be almost constant as

a function of p_{T}. In both p_{T} and η good agreement is seen between the Monte Carlo simulation and the data, but as with the electrons, scale-factors are applied to the Monte Carlo to reproduce the efficiency observed in data. The muon charge mis-identification rate is found to be negligible.

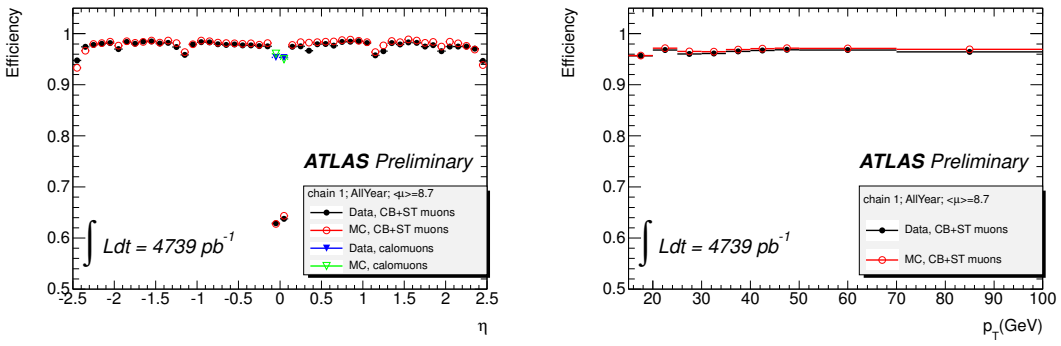

(a) (b)

Figure 5.13: Muon reconstruction efficiency in 2011 as a function of (a) the pseudo-rapidity and (b) the transverse momentum of the muon for muons reconstructed as either Combined or Segment-Tagged using the `STACO` algorithm. The solid black points show the efficiency observed in data, and the open red circles show the efficiency predicted by Monte Carlo simulation. In figure (a) the efficiencies for calorimeter tagged muons are also shown for $|\eta| < 0.1$ (solid blue triangles for data and open green triangles for Monte Carlo). Figures from [104].

Muon Momentum Resolution

The muon momentum resolution in the MS can be parameterised as:

$$\frac{\sigma(p)}{p} = \frac{p_0^{MS}}{p_T} \oplus p_1^{MS} \oplus p_2^{MS} \cdot p_T \tag{5.5}$$

where p_0^{MS}, p_1^{MS} and p_2^{MS} are coefficients related to the energy loss in the calorimeters, multiple scattering and intrinsic resolution, respectively. For the ID, the momentum resolution depends on the track length measured in the active elements, which is reduced at the edges of the detector where particles will not traverse all layers of the TRT. The ID muon momentum resolution can thus be parameterised as:

$$\frac{\sigma(p)}{p} = \begin{cases} p_1^{ID} \oplus p_2^{ID} \cdot p_T & \text{for } |\eta| < 1.9 \\ p_1^{ID} \oplus p_2^{ID} \cdot p_T \cdot \frac{1}{\tan^2(\theta)} & \text{for } |\eta| > 1.9 \end{cases} \tag{5.6}$$

The muon momentum resolution is measured in data using $Z \to \mu\mu$ decays.

The width of the reconstructed di-muon invariant mass peak at the Z pole is fitted to a convolution of a Breit-Wigner modelling the natural width of the Z boson, and a Gaussian modelling the muon momentum measurement resolution. The distributions measured in the ID and the MS are fitted independently to obtain separate measurements of the di-muon mass resolution in the two sub-detectors. An iterative fitting procedure is then carried out to obtain the single muon resolution parameters p_2^{ID}, p_1^{MS} and p_2^{MS}. A series of simulated di-muon mass distributions are produced for various momentum resolution values and then matched to the one observed in data. The difference between the independent momentum measurements in the ID and MS is included in the fit. The inner detector multiple scattering term p_2^{ID} is determined separately using the reconstructed K_s^0 mass and the observed J/ψ width. A smearing is applied to the simulated muon momentum in order to reproduce the resolution observed in data.

Figure 5.14 shows the observed di-muon mass resolution. For Combined muons, the resolution is of order 2-3 GeV across the full pseudo-rapidity range. Also shown in Figure 5.14 is the simulated di-muon resolution before and after correcting the resolution to that observed in the data as described in the last paragraph.

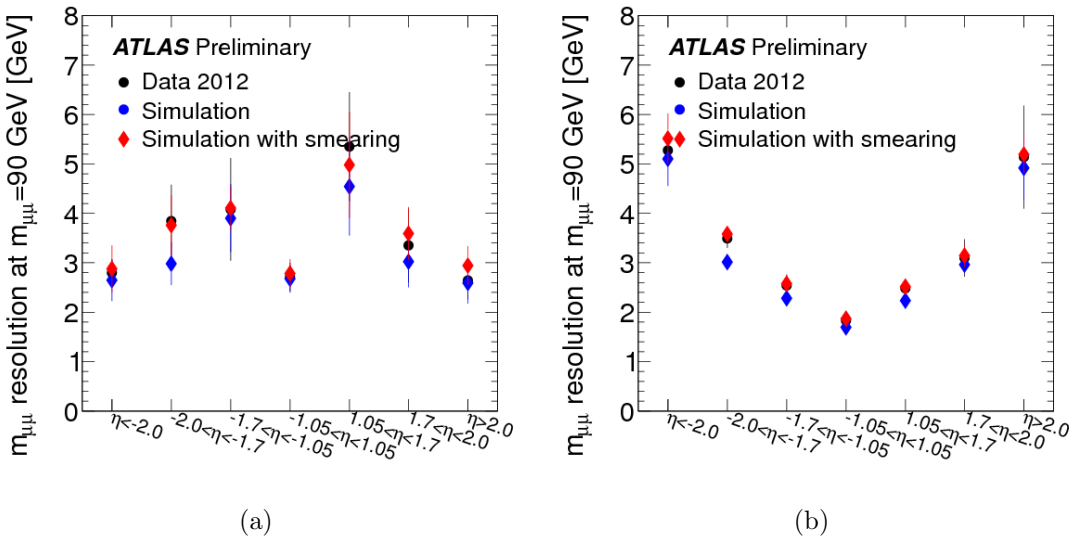

(a)

(b)

(c)

Figure 5.14: Di-muon mass resolutions for (a) muon tracks measured in the muon spectrometer, (b) muon tracks measured in the inner detector, and (c) Combined muon tracks. The solid points show the measured values in selected $Z \to \mu\mu$ events in data collected in 2012. The blue points show the resolution in simulated $Z \to \mu\mu$ decays, and the red diamonds show the simulated resolution after applying muon momentum resolution corrections to the simulation. Figures from [105].

5.5 Jet Reconstruction

Partons produced in particle interactions are not physically observable since they hadronise and produce a collimated shower of particles known as a jet. In order to reconstruct the jet in a physically meaningful way, it is necessary to specify an algorithm to associate multiple energy deposits in the calorimeters to a single jet (*clustering*) and a recombination scheme for how to combine their four-momentum.

Jet algorithms need to be theoretically well behaved with respect to QCD divergences. In particular, it is important that the jets produced are not affected by soft emissions (the algorithm must be *infrared safe*) and are not affected if a parton splits into two collinear partons (the algorithm must be *collinear safe*). Additionally, the algorithm must give the same physics results regardless of whether the input is partons or particles from Monte Carlo simulation or calorimeter clusters. There are two main classes of jet clustering algorithm: cone algorithms and successive combination algorithms. Cone algorithms start from seed objects and add in all other objects within a cone of a specified size in ΔR, where $\Delta R = \sqrt{(\Delta\eta)^2 + (\Delta\phi)^2}$. Cone algorithms are generally theoretically unsafe as soft or collinear emissions can affect the choice of seeds. Successive combination algorithms iteratively merge pairs of objects according to a definition of distance that generally involves the distance between the objects and their transverse momentum.

In ATLAS, the default jet clustering algorithm is a successive combination algorithm called anti-k_t [106]. This combines objects according to the distance parameters $d_{i,j} = \min(p_{T,i}^{-2}, p_{T,j}^{-2}) \cdot \frac{\Delta R}{R}$ and $d_{i,\text{beam}} = p_{T,i}^{-2}$ where $p_{T,i}$ is the transverse momentum of object i and ΔR is the distance between objects i, j in η, ϕ as defined above. The parameter R is a parameter controlling the size of the jet, and is analagous to the cone size in a cone based jet algorithm. The algorithm starts with a list of all objects, and calculates $d_{i,j}$ for all pairs of objects and $d_{i,\text{beam}}$ for all objects. If the minimum of all $\{d_{i,j}, d_{i,\text{beam}}\}$ is a $d_{i,j}$ the objects will be merged; if it is a $d_{i,\text{beam}}$ the object will be considered a jet and removed from the list. This process is repeated until there are no objects remaining. This algorithm is collinear and infrared safe as soft radiation is clustered to harder objects. It results in regular conical jets, which is experimentally desirable since it gives a well defined jet area that can be used for pileup supression. Where jets are used in this thesis, the R parameter is set to be 0.4.

The four-momentum of the jet is obtained simply by summing the four-momentua of the constituent objects. This scheme conserves energy and momentum, and al-

lows a meaningful definition for the jet mass.

Jets in the calorimeter are reconstructed from three-dimensional topological clusters of hadronic calorimeter cells, as described in Section 5.3.2. When constructing the jets, the topoclusters are considered as massless pseudo-particles, with an energy equal to the sum of the energy of the constituent cells and with a direction defined by a vector pointing from the origin of the ATLAS co-ordinate system to the energy weighted cluster barycentre.

The ATLAS hadronic calorimeters are non-compensating, so do not compensate for the different energy response of electromagnetically interacting particles and hadronically interacting particles, and do not account for energy lost from the hadronic shower due to production of secondary particles such as neutrons, neutrinos and muons that escape from the calorimeter or due to leakage of the shower out of the calorimeter. An important aspect of jet mesurements therefore is the calibration of the hadronic calorimeter response [107]. First, the topological clusters are corrected to the *EM scale*, correcting their energy such that the response to purely electromagnetic showers would be correct. To achieve this, a p_{T} and η dependant correction is applied, derived from a combination of Monte Carlo simulation, test-beam measurements and measurements of $Z \rightarrow ee$ decays in data. Further corrections are applied to the clusters to correct for the effects of pile-up, derived from minimum-bias data as a function of the number of primary vertices in the event. The cluster four momentum is is also modified so that the cluster points to the primary vertex with the highest sum of track transverse momentum.

The *Jet Energy Scale (JES)* correction is applied to jets constructed from the EM scale clusters in order to correct for the non compensating nature of the calorimeters, and also corrects for the effects of dead material, leakage outside of the calorimeters and energy lost due to particles being deflected out of the jet by the magnetic fields. The corection is parameterised by the jet p_{T} and η and is primarily derived from Monte Carlo simulation by comparing the energy of reconstructed jets with the energy of a 'truth' jet constructed from the final state particles that make up the jet. In-situ measurements such as Z+jet balance [108] and $Z + \gamma$ balance [109] are used to validate the Monte Carlo based corrections.

Part III

Analysis

Chapter 6

Object and Event Selection

In this chapter the electron, muon, and event-level selection requirements used to select ZZ events are described. The requirements are slightly different for the analysis of 7 TeV data (collected in 2011) and for the analysis of 8 TeV data (collected in 2012), reflecting the different experimental conditions, such as higher pile-up in 2012, as well as optimisations made for the analysis of the 2012 data. After describing the selection requirements, the efficiency and acceptance of the selection are discussed, and expected event yields are given. Finally, systematic uncertainties associated with the reconstruction acceptance are considered.

6.1 Electron Selection

Electron reconstruction and identification was described in Section 5.3. Both central electrons (with $|\eta| < 2.47$) and forward electrons are used for the 7 TeV analysis; for the 8 TeV analysis, measurements of the forward electron reconstruction efficiency in data were not available, and so the forward electrons are not used. In addition to the identification requirements described in Section 5.3, additional selection requirements are imposed to select electrons likely to have originated from Z boson decays and to reject backgrounds. The electron selection requirements are summarised in Table 6.1 and are described in more detail below.

6.1.1 Central Electron Selection

Central electrons, with $|\eta_{\text{cluster}}| < 2.47$, are reconstructed using the 'standard' electron algorithm as described in Section 5.3.2. For the 7 TeV data, the algorithm used was slightly different to the 'standard' ATLAS electron reconstruction as tracks were refitted using a Gaussian-sum filter (GSF) to account for the effect of bremsstrahlung in the inner detector. For the 8 TeV data, this became the default

Requirement	7 TeV	8 TeV
Central Electron Selection		
Algorithm	Standard (with GSF refit)	Standard
Quality	Good Data Quality	*Same*
ID Selection	`Loose++`	*Same*
η	$\lvert\eta_{\text{cluster}}\rvert < 2.47$	*Same*
E_T	$E_T > 7$ GeV	*Same*
z_0	$\lvert z_0\rvert < 2$ mm	$\lvert z_0 \sin(\theta)\rvert < 0.5$ mm
$d_0/\sigma(d_0)$	$\lvert d_0/\sigma(d_0)\rvert < 6$	*Same*
Track isolation	$\Sigma p_{\text{T}}(\Delta R < 0.2)/p_{\text{T}} < 0.15$	*Same*
Calorimeter isolation	$\Sigma E_{\text{T}}^{\text{calo}}(\Delta R < 0.2)/p_{\text{T}} < 0.3$	*Not Applied*
Overlap removal	a) Remove e if $\Delta R < 0.1$ from μ	*Same*
	b) Remove lowest E_T e in $\Delta R < 0.1$ from another e	*Same*
Forward Electron Selection:		
Algorithm	Forward	*Not Used*
Quality	Good Data Quality	
ID Selection	Tight	
η	$2.5 < \lvert\eta_{\text{cluster}}\rvert < 3.16$	
E_T	$E_T > 20$ GeV	
Overlap removal	Remove if overlaps with central electron or any muon in $\Delta R < 0.1$	

Table 6.1: Electron selection requirements.

reconstruction algorithm. Central electrons are required to pass the `Loose++` identification requirements.

For electron candidates with 4 or more silicon (SCT and Pixel) hits, the energy of the electron is taken from the cluster measurement, and the η and ϕ are taken from the track measurement (this requirement is automatically satisfied for electrons passing the `Loose++` identification requirements). For electron candidates with fewer than 4 silicon hits, all electron parameters are taken directly from the cluster. In both cases, the cluster η and ϕ are used for the η requirement and for overlap removal. Using the energy and direction defined in this way, the electron candidates are required to have $E_{\text{T}} > 7$ GeV, where E_{T} is defined as $E\sin(\theta) = E/\cosh(\eta)$.

A small number of the Front-End Boards (FEBs) of the LAr calorimeter were inactive for the 7 TeV data taking in 2011; the exact number varied with time as some were repaired whilst other developed faults. Additionally, for both 7 and 8 TeV data taking, a number of individual cells were masked in the readout (i.e. had their energy set to zero) due to frequently producing high noise or failing to give a readout. There were also regions where the High-Voltage supply to the LAr

was faulty. Electrons are rejected if they fall into a region of η, ϕ space consistent with the presence of a dead FEB in the first or second sampling layer, the presence of a dead HV region affecting all three samplings, or the presence of a masked cell in the core of the cluster.

To ensure that the candidates come from the primary vertex (defined as the vertex that has the highest $\sum p_{\mathrm{T}}^2$ of associated tracks), requirements are applied to the longitudinal impact parameter z_0 of the electron track with respect to the primary vertex. For 7 TeV data, the requirement is $|z_0| < 2$ mm; for 8 TeV data, the requirement is $|z_0 \sin(\theta)| < 0.5$ mm. The *unbiased* impact parameter is used, obtained by refitting the vertex without the track in question, then calculating the impact parameter with respect to this refitted vertex, thus removing the pull of the track from the vertex fit. The transverse impact parameter d_0 must have a significance (d_0 divided by the error on its measurement, $d_0/\sigma(d_0)$) of magnitude less than 6. This helps reduce backgrounds, particularly from decays of pions and kaons in jets to electrons, since these decays occur further from the interaction point giving larger impact parameters.

Isolation requirements are applied to reduce the backgrounds from jets misidentified as electrons, or from electrons from decays in jets. The tracks of such objects will typically be surrounded by many other tracks, and they will be surrounded by large energy deposits in the calorimeter from other particles in the jet. *Track Isolation* requirements are imposed, requiring that the sum of the p_{T} of tracks surrounding the electron's track in a cone of $\Delta R < 0.2$[1] be less than 15% of the electron's p_{T}, i.e. $\Sigma p_{\mathrm{T}}(\Delta R < 0.2)/p_{\mathrm{T}} < 0.15$. Tracks included in the calculation are required to have $p_{\mathrm{T}} > 0.4$ GeV, have impact parameters consistent with the same vertex as the electron and have at least 9 silicon hits, thus ensuring good track quality and purity. The impact parameter requirement means that this variable is insensitive to pileup as most tracks from other (pileup) vertices are excluded.

Additionally, for the 7 TeV data, a calorimeter isolation requirement is imposed. This is defined as the sum of calorimeter cell energies in a cone of $\Delta R < 0.2$ around the barycentre of the electron cluster, excluding a 5x7 grid of cells in the centre of the cone (which are assumed to be due to the electron). Cells from both the EM and hadronic calorimeters are included. The requirement is that the sum of such energies be less than 30% of electron E_{T}, i.e. $\Sigma E_{\mathrm{T}}^{\mathrm{calo}}(\Delta R < 0.2)/p_{\mathrm{T}} < 0.3$. This variable is particularly sensitive to pileup, as pileup events tend to deposit

[1] where $\Delta R = \sqrt{(\Delta\eta)^2 + (\Delta\phi)^2}$

additional energy isotropically throughout the detector, thus increasing the energy in the isolation cone. A correction, parameterised by the number of vertices reconstructed in the event, is applied to correct the isolation variable for extra energy due to pileup. Additional corrections are applied to correct for leakage of the electron's energy out of the core cells of the cone, which tends to increase with p_{T}. Calorimeter isolation requirements were not applied to electrons in the 8 TeV data.

Electrons closer than $\Delta R < 0.1$ to a muon which passes all of the muon selection requirements (see Section 6.2) are rejected. If two selected electrons overlap within $\Delta R < 0.1$, the lower-E_{T} electron is removed, although in the case of a central electron overlapping with a forward electron, which could occur near the edge of the tracker, the central electron takes precedence.

The estimated efficiencies of the electron selection requirements for electrons in ZZ events are shown in Table 6.2.

	7 TeV		8 TeV	
Requirement	$N_{\mathrm{cut}}/N_{\mathrm{all}}$	$N_{\mathrm{cut}}/N_{\mathrm{cut}-1}$	$N_{\mathrm{cut}}/N_{\mathrm{all}}$	$N_{\mathrm{cut}}/N_{\mathrm{cut}-1}$
Object Quality	$99.2 \pm 0.1\%$	$99.2 \pm 0.1\%$	$99.7 \pm 0.0\%$	$99.7 \pm 0.1\%$
$E_T > 7$ GeV	$98.7 \pm 0.1\%$	$99.5 \pm 0.1\%$	$99.4 \pm 0.0\%$	$99.7 \pm 0.1\%$
Overlap Removal	$98.6 \pm 0.1\%$	$99.9 \pm 0.1\%$	$99.3 \pm 0.0\%$	$99.8 \pm 0.1\%$
`Loose++`	$91.7 \pm 0.1\%$	$93.0 \pm 0.1\%$	$94.5 \pm 0.1\%$	$95.2 \pm 0.1\%$
z_0	$91.4 \pm 0.1\%$	$99.7 \pm 0.1\%$	$94.2 \pm 0.1\%$	$99.7 \pm 0.1\%$
d_0 Significance	$90.8 \pm 0.1\%$	$99.3 \pm 0.1\%$	$93.3 \pm 0.1\%$	$99.1 \pm 0.1\%$
Track Isolation	$90.4 \pm 0.1\%$	$99.6 \pm 0.1\%$	$92.2 \pm 0.1\%$	$98.8 \pm 0.1\%$
Calorimeter Isolation	$90.1 \pm 0.1\%$	$99.6 \pm 0.1\%$	*Not Applied*	

Table 6.2: Efficiency of the central electron selection requirements. The efficiencies are estimated from Monte Carlo after applying correction factors to correct the efficiencies to those observed in data. The efficiencies shown are for single electrons, matched to a generator-level electron from a Z decay within $\Delta R < 0.2$, in events which fall in the ZZ fiducial volume at generator level. The first and third columns show cumulative efficiencies with respect to the number of reconstructed electrons within the η acceptance ($|\eta| < 2.46$), for the 7 TeV and 8 TeV analyses respectively. The second and fourth columns show the efficiency with respect to the previous requirement.

6.1.2 Forward Electron Selection

Electrons reconstructed using the forward electron reconstruction algorithm are used to extend the pseudo-rapidity coverage beyond the limit of the tracker, $|\eta| < 2.5$. Only electrons falling in the EMEC region are used, with pseudo-rapidity $2.5 < |\eta_{\mathrm{cluster}}| < 3.16$. Since the lack of tracking makes it harder to reject

hadronic and photon fakes, these electrons are required to pass tighter identification requirements: "Forward Tight". Since forward electrons lack a track measurement, it is impossible to determine their charge, and of course impossible to apply track isolation and track parameter cuts. Forward electrons are required to have $E_{\mathrm{T}} > 20$ GeV; this higher energy requirement is motivated by the difficulty of measuring reconstruction and identification efficiencies in data below this energy and by the higher hadronic and photonic backgrounds at low energy. Forward electrons are not used in the 8 TeV analysis.

The estimated efficiencies of the forward electron selection requirements for forward electrons in ZZ events are shown in Table 6.3.

	7 TeV	
Requirement	$N_{\mathrm{cut}}/N_{\mathrm{all}}$	$N_{\mathrm{cut}}/N_{\mathrm{cut}-1}$
Object Quality	$99.9 \pm 0.1\%$	$99.9 \pm 0.1\%$
$E_T > 20$ GeV	$80.0 \pm 0.5\%$	$80.1 \pm 0.5\%$
Overlap Removal	$80.0 \pm 0.5\%$	$100.0 \pm 0.0\%$
`Tight` ID	$46.8 \pm 0.7\%$	$58.5 \pm 0.7\%$

Table 6.3: Efficiency of the forward electron selection requirements. The efficiencies are estimated from Monte Carlo after applying correction factors to correct the efficiencies to those observed in data. The efficiencies shown are for single electrons, matched to a generator-level electron from a Z decay within $\Delta R < 0.2$, in events which fall in the ZZ fiducial volume at generator level. The first column shows the cumulative efficiencies with respect to the number of reconstructed electrons within the η acceptance ($2.47 < |\eta| < 3.16$). The second columns shows the efficiency with respect to the previous requirement.

6.1.3 Electron Distributions

To motivate the isolation, $d_0/\sigma(d_0)$ and z_0 requirements described above, Figure 6.1 shows the distribution of these variables for additional electron candidates in events with an opposite-sign same-flavour di-lepton pair in the 7 TeV data. The leptons forming the di-lepton pair are required to pass all of the selection requirements described above, one must match to the triggering object within $\Delta R < 0.1$ and have $p_{\mathrm{T}} > 25$ GeV, and they must have invariant mass satisfying $66 < m_{\ell^-\ell^+} < 116$ GeV. Any additional electrons in the event are required to pass the kinematic (p_{T}, η) requirements and the `Loose++` identification requirements; the distributions of the isolation, $d_0/\sigma(d_0)$ and z_0 variables for these additional electrons are shown in the plots.

The dominant physics processes contributing to this selection are $Z \to \ell\ell$

produced in association with jets or photons, $t\bar{t}$ and diboson W^+W^-, $W^\pm Z$ and ZZ. In the $W^\pm Z$ and ZZ processes, the additional electrons entering the plot are mainly prompt isolated leptons from $W^\pm$ or Z decays. In the $Z \to \ell\ell$, $t\bar{t}$ and W^+W^- processes, the additional electron candidates mainly arise from jets faking leptons, electrons from hadronic decays in jets, or from photon conversions. These 'background' electrons tend to be less isolated, and have broader $d_0/\sigma(d_0)$ and z_0 distributions.

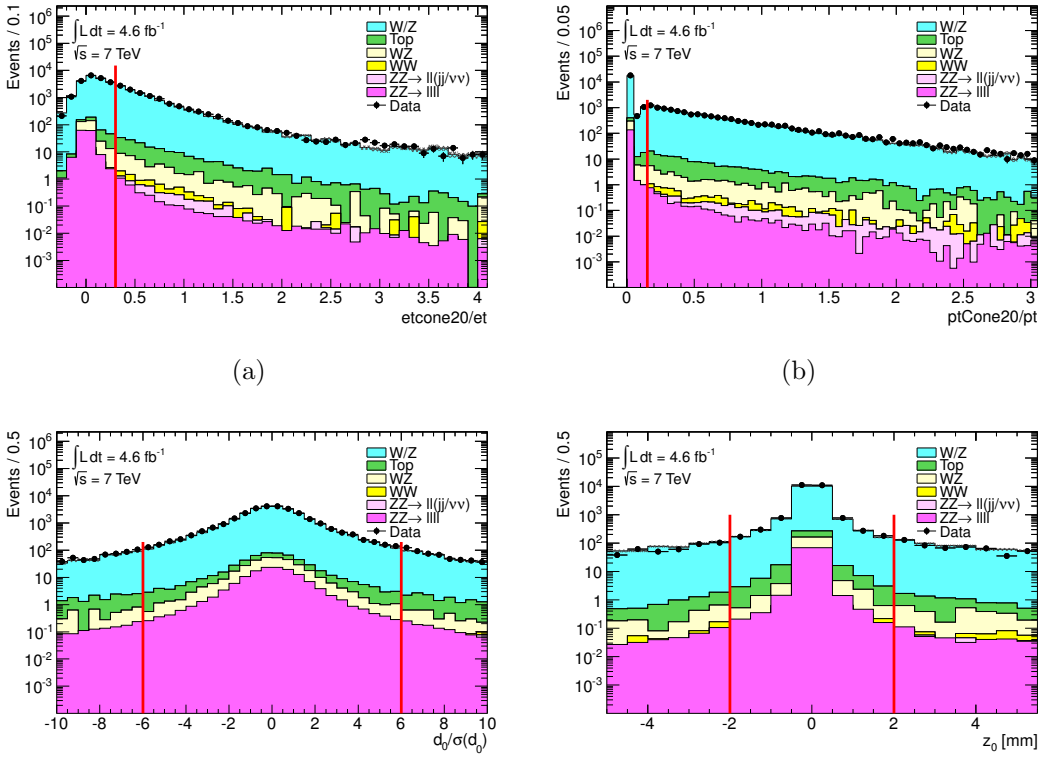

Figure 6.1: Distributions of (a) relative calorimeter isolation, (b) relative track isolation, (c) impact parameter significance $d_0/\sigma(d_0)$, and (d) longitudinal impact parameter z_0 for additional electron candidates in events containing an opposite-sign same-flavour di-lepton pair with invariant mass $66 < m_{\ell^-\ell^+} < 116$ GeV in 7 TeV data. The leptons forming the di-lepton pair are required to pass all of the selection requirements described above, and one must match to the triggering object within $\Delta R < 0.1$ and have $p_{\mathrm{T}} > 25$ GeV. Additional electron candidates other than those forming the di-lepton pair are required to pass the kinematic selection requirements and the `Loose++` identification requirements; only these additional candidates are included in the plots.

6.2 Muon Selection

Muon reconstruction was described in Section 5.4. Three distinct categories of muons are used in this analysis: 'central' muons with $|\eta| < 2.5$, and 'forward' muons with $2.5 < |\eta| < 2.7$, both reconstructed with the `STACO` algorithm; and calorimeter tagged muons with $|\eta| < 0.1$, reconstructed without using the muon spectrometer. As for electrons, additional selection requirements are applied to select muons likely to have originated from Z boson decays and to reject backgrounds. The muon selection requirements are summarised in Table 6.4 and are described in more detail below.

6.2.1 Central Muon Selection

Central muons may be either Combined (with a full MS and ID track) or Segment-Tagged (with a full ID track but only track segment in the MS), and have $p_{\mathrm{T}} > 7$ GeV and $|\eta| < 2.47$.

As for electrons, track and calorimeter isolation requirements are imposed to reject backgrounds. In the case of muons this is mainly from heavy flavour decays in jets and 'punch-through' of hadrons into the muon spectrometer. The track isolation is defined in the same way as for electrons, and as for electrons the requirement is $\Sigma p_{\mathrm{T}}(\Delta R < 0.2)/p_{\mathrm{T}} < 0.15$. The calorimeter isolation variable is defined in a similar way to that for electrons, however the size of the 'core' deposit of energy attributed to the muon is smaller than in the case of electron isolation, and varies by calorimeter component depending on the expected muon energy deposition pattern (e.g. a single cell in the EM pre-sampler, but a 3x3 grid of cells in the second layer of the EM calorimeter). The calorimeter isolation requirement is $\Sigma E_{\mathrm{T}}^{\mathrm{calo}}(\Delta R < 0.2)/p_{\mathrm{T}} < 0.3$, and as for electrons is only applied to the 7 TeV data.

To ensure that the candidates come from the primary vertex, the magnitude of the longitudinal impact parameter with respect to the primary vertex, $|z_0|$ must be less than 2 mm for the 7 TeV data. For the 8 TeV data, the requirement is $|z_0 \sin(\theta)| < 0.5$ mm. The magnitude of the transverse impact parameter significance, $|d_0/\sigma(d_0)|$ is required to be less than 3.5(3) in the 7(8) TeV analysis. The $d_0/\sigma(d_0)$ requirement for muons is tighter than for electrons, since because muons do not emit bremsstrahlung to the same extent as electrons, the track fit and thus the resolution of the impact parameter is improved, so tighter requirements can be made whilst maintaining high signal efficiency.

Requirement	7 TeV	8 TeV
Central Muons		
Algorithm	`STACO`	*Same*
Type	Combined or Segment-Tagged	*Same*
η	$\lvert\eta\rvert < 2.5$	*Same*
p_T	$p_T > 7$ GeV	*Same*
ID Track Quality		
- B Layer Hits	≥ 1	*Same*
- Pixel Hits	≥ 2	≥ 1
- SCT Hits	≥ 6	≥ 5
- Silicon 'Holes'	< 3	*Same*
- TRT	**If** $\lvert\eta\rvert < 1.9$**:** Require $n_{hits} + n_{outliers} > 5$ and $n_{outliers}/(n_{hits} + n_{outliers}) < 0.9$	**If** $0.1 < \lvert\eta\rvert < 1.9$**:** Require $n_{hits} + n_{outliers} > 5$ and $n_{outliers}/(n_{hits} + n_{outliers}) < 0.9$
	If $\lvert\eta\rvert > 1.9$**:** If $n_{hits} + n_{outliers} > 5$ require $n_{outliers}/(n_{hits} + n_{outliers}) < 0.9$	**If** $\lvert\eta\rvert > 1.9$ **or** $\lvert\eta\rvert < 0.1$**:** If $n_{hits} + n_{outliers} > 5$ require $n_{outliers}/(n_{hits} + n_{outliers}) < 0.9$
z_0	$\lvert z_0\rvert < 2$ mm	$\lvert z_0 \sin(\theta)\rvert < 0.5$ mm
$d_0/\sigma(d_0)$	$\lvert d_0/\sigma(d_0)\rvert < 3.5$	$\lvert d_0/\sigma(d_0)\rvert < 3$
Track isolation	$\Sigma p_{\mathrm{T}}(\Delta R < 0.2)/p_{\mathrm{T}} < 0.15$	*Same*
Calorimeter isolation	$\Sigma E_{\mathrm{T}}^{\mathrm{calo}}(\Delta R < 0.2)/p_{\mathrm{T}} < 0.3$	*Not Applied*
Forward Muons		
Algorithm	`STACO`	*Same*
Type	Combined or Stand-Alone	*Same*
η	$2.5 < \lvert\eta\rvert < 2.7$	*Same*
p_T	$p_T > 10$ GeV	*Same*
Calorimeter isolation	$\Sigma E_{\mathrm{T}}^{\mathrm{calo}}(\Delta R < 0.2)/p_{\mathrm{T}} < 0.15$	*Same*
	Additional requirements for Combined Muons	
ID Track Quality		
- B Layer Hits	≥ 1	*Same*
- Pixel Hits	≥ 2	≥ 1
- SCT Hits	≥ 4	≥ 3
- Silicon 'Holes'	< 3	*Same*
z_0	$\lvert z_0\rvert < 2$ mm	$\lvert z_0 \sin(\theta)\rvert < 0.5$ mm
$d_0/\sigma(d_0)$	$\lvert d_0/\sigma(d_0)\rvert < 3.5$	$\lvert d_0/\sigma(d_0)\rvert < 3$
Calorimeter Tagged Muons		
Type	Calorimeter Tagged	*Same*
η	$\lvert\eta\rvert < 0.1$	*Same*
p_T	$p_T > 20$ GeV	*Same*
Quality	Calorimeter Muon ID Cuts	*Same*
Overlap removal	Remove if overlaps with a central muon in $\Delta R < 0.1$	*Same*
ID Track Quality, Track Isolation, Calorimeter Isolation, z_0, $d_0/\sigma(d_0)$ as central muons		

Table 6.4: Muon selection requirements.

	7 TeV		8 TeV	
Requirement	$N_{\text{cut}}/N_{\text{all}}$	$N_{\text{cut}}/N_{\text{cut}-1}$	$N_{\text{cut}}/N_{\text{all}}$	$N_{\text{cut}}/N_{\text{cut}-1}$
$p_T > 7$ GeV	$99.9 \pm 0.1\%$	$99.9 \pm 0.1\%$	$99.9 \pm 0.1\%$	$99.9 \pm 0.1\%$
Track Hits	$98.6 \pm 0.1\%$	$98.8 \pm 0.1\%$	$99.2 \pm 0.1\%$	$99.2 \pm 0.1\%$
z_0	$98.6 \pm 0.1\%$	$100.0 \pm 0.1\%$	$99.1 \pm 0.1\%$	$99.9 \pm 0.1\%$
d_0 Significance	$98.3 \pm 0.1\%$	$99.7 \pm 0.1\%$	$98.5 \pm 0.1\%$	$99.4 \pm 0.1\%$
Track Isolation	$97.6 \pm 0.1\%$	$99.3 \pm 0.1\%$	$97.3 \pm 0.1\%$	$98.8 \pm 0.1\%$
Calorimeter Isolation	$97.0 \pm 0.1\%$	$99.5 \pm 0.1\%$	*Not Applied*	

Table 6.5: Efficiency of the central muon selection requirements. The efficiencies are estimated from Monte Carlo after applying correction factors to correct the efficiencies to those observed in data. The efficiencies shown are for single muons, matched to a generator-level muon from a Z decay within $\Delta R < 0.2$, in events which fall in the ZZ fiducial volume at generator level. The first and third columns show cumulative efficiencies with respect to the number of reconstructed muons within the η acceptance ($|\eta| < 2.5$), for the 7 TeV and 8 TeV analyses respectively. The second and fourth columns show the efficiency with respect to the previous requirement.

The inner detector tracks associated with central muons must have a minimum number of hits in each silicon sub-detector to ensure good track quality. For 7 TeV data the requirements are: at least 1 hit in the b-layer, 2 hits in all Pixel layers, 6 hits in the SCT, and less than 3 holes (no hit in a layer crossed by the track) in all silicon layers. For all silicon hit conditions, dead sensors count as hits observed, not as holes. Finally, a pseudo rapidity-dependent condition on TRT hits and outliers is applied to ensure that the TRT extension of the track is successful within the η acceptance of the TRT (TRT hits can be associated as outliers when the extension is not successful): for $|\eta| < 1.9$, require hits + outliers > 6 and outliers $< 0.9 \times$ (outliers + hits); for $|\eta| > 1.9$, if hits + outliers > 6, require outliers $< 0.9 \times$ (outliers + hits). For 8 TeV data, the requirements are slightly loosened in order to recover efficiency losses arising from higher pileup in 2012; this was not found to increase the misidentification rate significantly; see Table 6.4 for details of the changes.

The estimated efficiencies of the muon selection requirements for muons in ZZ events are shown in Table 6.5.

6.2.2 Forward Muon Selection

Muons in the region $2.5 < |\eta| < 2.7$ are required to have a full muon spectrometer track with hits in each station of the spectrometer and must have $p_{\text{T}} > 10$ GeV. Although the inner detector only extends to $|\eta| = 2.5$, the complicated nature of the magnetic field makes it possible for some muons up to $|\eta| < 2.6$ to be

combined with an ID track, forming Combined muons; those that do not have an ID track are termed 'Stand-Alone'. Figure 6.2 shows the fraction of forward muons which are Combined as a function of η. In data reconstructed in 2012, muons without a full ID track may be combined with pixel detector 'tracklets' up to $|\eta| < 2.65$. Such 'Silicon Associated' muons benefit from improved vertex parameter estimation, but are otherwise treated as Stand-Alone.

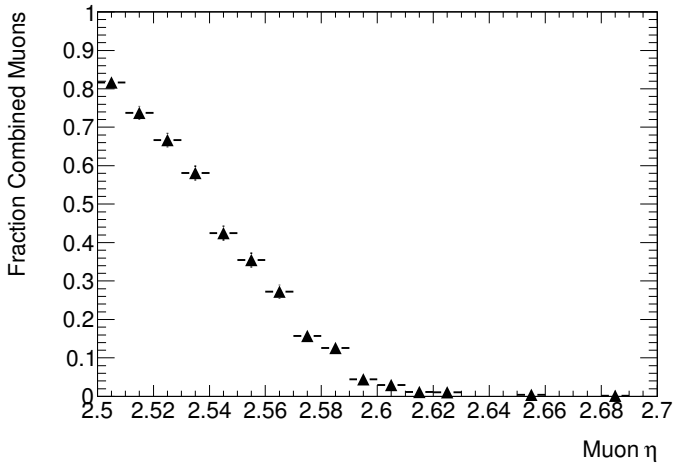

Figure 6.2: Fraction of forward muons which have an ID track and are Combined muons, as a function of η. The fractions are estimated from Monte Carlo simulation; the error bars show statistical uncertainties.

Since not all forward muons have tracks, a track isolation requirement is not applied; instead a tighter calorimeter isolation requirement is applied to forward muons: $\Sigma E_{\mathrm{T}}^{\mathrm{calo}}(\Delta R < 0.2)/p_{\mathrm{T}} < 0.15$. This is applied to both the 7 TeV and the 8 TeV data.

For forward muons with an ID track, quality cuts are applied to the number of hits in the silicon detectors, similar to the cuts for central muons but slightly looser. For 7 TeV data, the requirements are: at least 1 hit in the b-layer, 2 in all Pixel layers, 4 in the SCT, and less than 3 holes in all silicon layers. No cut is applied to the number of TRT hits, as forward muon tracks are generally outside the acceptance of the TRT. As for central muons, the requirements were relaxed slightly for 2012 data. Forward muons with an ID track are required to satisfy the same z_0 and $d_0/\sigma(d_0)$ requirements as central muons.

The estimated efficiencies of the forward muons selection requirements for forward muons in ZZ events are shown in Table 6.6.

	7 TeV		8 TeV	
Requirement	$N_{\text{cut}}/N_{\text{all}}$	$N_{\text{cut}}/N_{\text{cut}-1}$	$N_{\text{cut}}/N_{\text{all}}$	$N_{\text{cut}}/N_{\text{cut}-1}$
$p_T > 10$ GeV	$97.1 \pm 0.7\%$	$97.1 \pm 0.7\%$	$97.6 \pm 0.5\%$	$97.6 \pm 0.5\%$
Track Hits	$91.8 \pm 1.1\%$	$94.6 \pm 1.0\%$	$94.1 \pm 0.8\%$	$96.4 \pm 0.6\%$
z_0	$91.8 \pm 1.1\%$	$99.9 \pm 0.1\%$	$93.8 \pm 0.8\%$	$99.7 \pm 0.2\%$
d_0 Significance	$91.4 \pm 1.1\%$	$99.6 \pm 0.2\%$	$92.8 \pm 0.9\%$	$98.9 \pm 0.5\%$
Calorimeter Isolation	$90.0 \pm 1.2\%$	$98.5 \pm 0.5\%$	$90.9 \pm 1.0\%$	$98.0 \pm 0.5\%$

Table 6.6: Efficiency of the forward muon selection requirements. The efficiencies are estimated from Monte Carlo after applying correction factors to correct the efficiencies to those observed in data. The efficiencies shown are for single muons, matched to a generator-level muon from a Z decay within $\Delta R < 0.2$, in events which fall in the ZZ fiducial volume at generator level. The first and third columns show cumulative efficiencies with respect to the number of reconstructed muons within the η acceptance ($2.5 < |\eta| < 2.7$), for the 7 TeV and 8 TeV analyses respectively. The second and fourth columns show the efficiency with respect to the previous requirement.

6.2.3 Calorimeter Tagged Muon Selection

Calorimeter tagged muons are used to recover efficiency at $|\eta| < 0.1$ where there is a gap in the muon-spectrometer. Due to the higher level of fakes from jets and electrons at low p_{T}, and the difficulty of measuring the identification efficiency at low p_{T}, the p_{T} requirement for calorimeter tagged muons is $p_{\text{T}} > 20$ GeV. They are required to pass either the cut or the likelihood based calorimeter tagged muon identification requirements described in Section 5.4.2, and are not selected if they overlap with a selected central muon within $\Delta R < 0.1$. Calorimeter tagged muons must satisfy the same track and calorimeter isolation, ID track quality, z_0 and $d_0/\sigma(d_0)$ requirements as central muons.

The estimated efficiencies of the calorimeter tagged muon selection requirements for calorimeter tagged muons in ZZ events are shown in Table 6.7.

6.2.4 Muon Distributions

To motivate the muon isolation, $d_0/\sigma(d_0)$ and z_0 requirements described above, Figure 6.3 shows the distribution of these variables in 7 TeV data for additional muon candidates in events with an opposite-sign same-flavour di-lepton pair with invariant mass $66 < m_{\ell^-\ell^+} < 116$ GeV. Similarly to the electron distributions, the leptons forming the di-lepton pair are required to pass all of the selection requirements described above, and one must match to the triggering object within $\Delta R < 0.1$ and have $p_{\text{T}} > 25$ GeV. Any additional muon candidates in the event are required to pass the kinematic (p_{T},η) selection requirements, and the distributions

	7 TeV		8 TeV	
Requirement	$N_{\text{cut}}/N_{\text{all}}$	$N_{\text{cut}}/N_{\text{cut}-1}$	$N_{\text{cut}}/N_{\text{all}}$	$N_{\text{cut}}/N_{\text{cut}-1}$
$p_T > 7$ GeV	$93.1 \pm 0.6\%$	$93.1 \pm 0.6\%$	$94.5 \pm 0.5\%$	$94.5 \pm 0.5\%$
Quality	$92.7 \pm 0.7\%$	$99.6 \pm 0.2\%$	$94.0 \pm 0.5\%$	$99.4 \pm 0.2\%$
Track Hits	$87.6 \pm 0.9\%$	$94.5 \pm 0.6\%$	$89.6 \pm 0.6\%$	$95.4 \pm 0.4\%$
z_0	$87.6 \pm 0.9\%$	$100.0 \pm 0.0\%$	$89.1 \pm 0.6\%$	$99.4 \pm 0.1\%$
d_0 Significance	$86.8 \pm 0.9\%$	$99.1 \pm 0.3\%$	$88.2 \pm 0.6\%$	$98.9 \pm 0.2\%$
Track Isolation	$86.1 \pm 0.9\%$	$99.2 \pm 0.2\%$	$87.1 \pm 0.7\%$	$98.8 \pm 0.2\%$
Calorimeter Isolation	$85.6 \pm 0.9\%$	$99.5 \pm 0.2\%$	*Not Applied*	

Table 6.7: Efficiency of the calorimeter-tagged muon selection requirements. The efficiencies are estimated from Monte Carlo after applying correction factors to correct the efficiencies to those observed in data. The efficiencies shown are for single muons, matched to a generator-level muon from a Z decay within $\Delta R < 0.2$, in events which fall in the ZZ fiducial volume at generator level. The first and third columns show cumulative efficiencies with respect to the number of reconstructed muons within the η acceptance ($|\eta| < 0.1$), for the 7 TeV and 8 TeV analyses respectively. The second and fourth columns show the efficiency with respect to the previous requirement.

of the isolation, $d_0/\sigma(d_0)$ and z_0 variables for these additional candidates are shown in the plots.

As for electrons, in the $W^{\pm}Z$ and ZZ processes the additional muon candidates are mainly prompt isolated leptons from $W^{\pm}$ or Z decays. In the $Z \to \ell\ell$, $t\bar{t}$ and $W^{+}W^{-}$ processes, the additional candidates mainly arise from muons from hadronic decays in jets or 'punch-through' of hadrons to the muon spectrometer. These 'background' muon candidates tend to be less isolated, and have broader $d_0/\sigma(d_0)$ and z_0 distributions. Whilst the Monte Carlo simulation models the shape of the distribution fairly well, the number of additional muon candidates observed in data is much higher than predicted by the simulation.

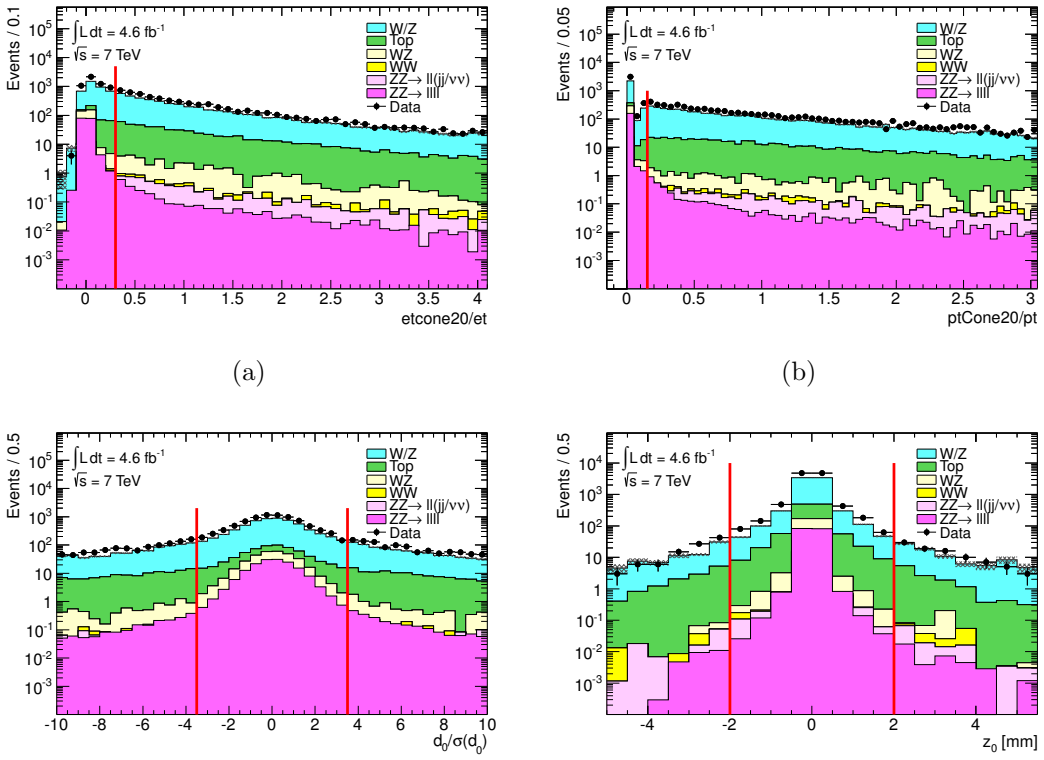

Figure 6.3: Distributions of (a) relative calorimeter isolation, (b) relative track isolation, (c) impact parameter significance $d_0/\sigma(d_0)$ and (d) longitudinal impact parameter z_0 for additional muon candidates in events containing an opposite-sign same-flavour di-lepton pair with invariant mass $66 < m_{\ell^-\ell^+} < 116$ GeV in the 7 TeV data. The leptons forming the di-lepton pair are required to pass all of the selection requirements described above, and one must match to the triggering object within $\Delta R < 0.1$ and have $p_{\mathrm{T}} > 25$ GeV. Any additional muon candidates, other than those forming the di-lepton pair, are required to pass the kinematic selection requirements; only these additional candidates are included in the plots.

6.3 Trigger Selection

Candidate ZZ events are triggered on using the lowest threshold un-prescaled single-electron or single-muon triggers, as described in Section 5.3.1 and 5.4.1. For the $e^-e^+\mu^-\mu^+$ final state, the event may be selected using either the electron or the muon trigger. The triggers used in the different data taking periods and the associated integrated luminosities are shown in Table 6.8 for the electron triggers and Table 6.9 for the muon triggers.

At least one of the selected leptons in triggered events must match to the object that caused the trigger to fire with $\Delta R < 0.1$. Such leptons are referred

Period	E_{T} Threshold (GeV)	Isolation Requirement	Int. Luminosity (fb^{-1})
2011 (7 TeV data)			
B - I	20	None	1.65
J - K	22	None	0.91
L - M	22	None	2.76
2012 (8 TeV data)			
A - M	24	$\Sigma p_{\mathrm{T}}(\Delta R < 0.2)/p_{\mathrm{T}} < 0.10$	22.3

Table 6.8: Electron triggers used in the different data taking periods.

Period	p_{T} Threshold (GeV)	Isolation Requirement	Int. Luminosity (fb^{-1})
2011 (7 TeV data)			
B - I	18	None	1.65
J - M	18	None	3.67
2012 (8 TeV data)			
A - M	24	$\Sigma p_{\mathrm{T}}(\Delta R < 0.2)/p_{\mathrm{T}} < 0.12$	22.3

Table 6.9: Muon triggers used in the different data taking periods.

to as *trigger-matched* leptons. To reduce uncertainties associated with the trigger efficiency measurement, to be considered trigger matched, a lepton must have a p_{T} such that it is on the efficiency plateau of the trigger, and must also satisfy the same identification requirements as used in the trigger. Trigger-matched electrons in both the 7 TeV and the 8 TeV data are required to have $p_{\mathrm{T}} > 25$ GeV, cluster $|\eta| < 2.47$, and to pass the `Medium++` requirements. Trigger matched muons are required to be Combined muons, have $|\eta| < 2.4$ and have $p_{\mathrm{T}} > 20(25)$ GeV in the 7(8) TeV data.

6.3.1 Trigger Efficiencies

The efficiency for a single lepton to fire the trigger is measured in data using $Z \to \ell\ell$ events. Events are triggered on by a 'tag' lepton; the efficiency for the second 'probe' lepton to fire the trigger is then measured. By comparing the efficiencies in data and in Monte Carlo simulation, scale-factors are derived to correct the single lepton trigger efficiencies in the simulation to those observed in data. This is translated to an event-level trigger efficiency scale-factor using the

following formula:

$$SF = \frac{1 - \prod_{n=1}^{N_l}(1 - \epsilon_{Data,l_n})}{1 - \prod_{n=1}^{N_l}(1 - \epsilon_{MC,l_n})} \tag{6.1}$$

where N_l is the number of leptons passing the trigger-matching kinematic and identification requirements given above (not necessarily equal to the number of trigger-matched leptons), ϵ_{Data,l_n} is the observed single-lepton trigger efficiency in data for a lepton of flavour flavor l_n, and ϵ_{MC,l_n} is the corresponding efficiency simulated in the MC.

Event-level trigger efficiencies for ZZ events passing the full event selection described in the next section are listed in Table 6.10. They are derived from simulation after applying the trigger efficiency scale-factors described above.

Channel	Trigger Efficiency [%]		
	ZZ Selection (7 TeV)	ZZ^* Selection (7 TeV)	ZZ Selection (8 TeV)
$e^-e^+e^-e^+$	99.69 ± 0.08 ± 0.02	99.38 ± 0.10 ± 0.03	99.89 ± 0.02 ± 0.03
$\mu^-\mu^+\mu^-\mu^+$	98.50 ± 0.15 ± 0.14	97.68 ± 0.17 ± 0.18	98.10 ± 0.10 ± 0.20
$e^-e^+\mu^-\mu^+$	99.52 ± 0.07 ± 0.06	99.06 ± 0.08 ± 0.08	99.49 ± 0.05 ± 0.09
$\ell^-\ell^+\ell^-\ell^+$	99.23 ± 0.06 ± 0.08	98.67 ± 0.07 ± 0.10	99.14 ± 0.04 ± 0.11

Table 6.10: Trigger efficiencies for ZZ events passing the full event selection excluding the trigger requirement and the requirement for a reconstructed lepton to match to the triggering object. The trigger efficiencies are estimated using ZZ Monte Carlo, applying scale-factors to correct the single lepton trigger-efficiency to that observed in data. The first error is due to Monte Carlo statistics, and the second is due uncertainties on the measurement of the trigger efficiencies in data.

6.4 Dilepton Control Plots

To demonstrate reconstruction performance and the performance of modelling in the Monte Carlo compared to the data, a high statistics sample of inclusive $Z \to \ell\ell$ decays is used. $Z \to ee$ and $Z \to \mu\mu$ events are selected by requiring that events have at least two electrons or muons passing all of the lepton selection requirements described above. The events must fire either the single electron or the single muon trigger, and have at least one lepton matched to the triggering object as described above. Two of the selected leptons must form an opposite-sign same-flavour pair, with invariant mass $66 < m_{\ell^-\ell^+} < 116$ GeV. In events where there is more than one pair satisfying this requirement, the pair with invariant

mass closest to the Z mass is chosen. Figure 6.4 shows the di-lepton invariant mass and the di-lepton transverse momentum for the 7 TeV data; Figure 6.5 shows the same distributions for the 8 TeV data. Figures 6.6 and 6.7 show the lepton p_{T}, η and ϕ for the 7 TeV and 8 TeV data, respectively. The Monte Carlo samples used to describe the various processes are as listed in Table 7.1, except that the $W^{\pm}Z$ process is modelled using HERWIG as $W^{\pm}Z$ the samples listed in Table 7.1 do not include hadronic decays of the $W^{\pm}$ boson. Good agreement is seen between the data and the Monte Carlo simulation. A slight excess in the data for the di-electron distributions at low invariant mass and low lepton p_{T} is attributed to QCD dijet events, which are not simulated in the Monte Carlo.

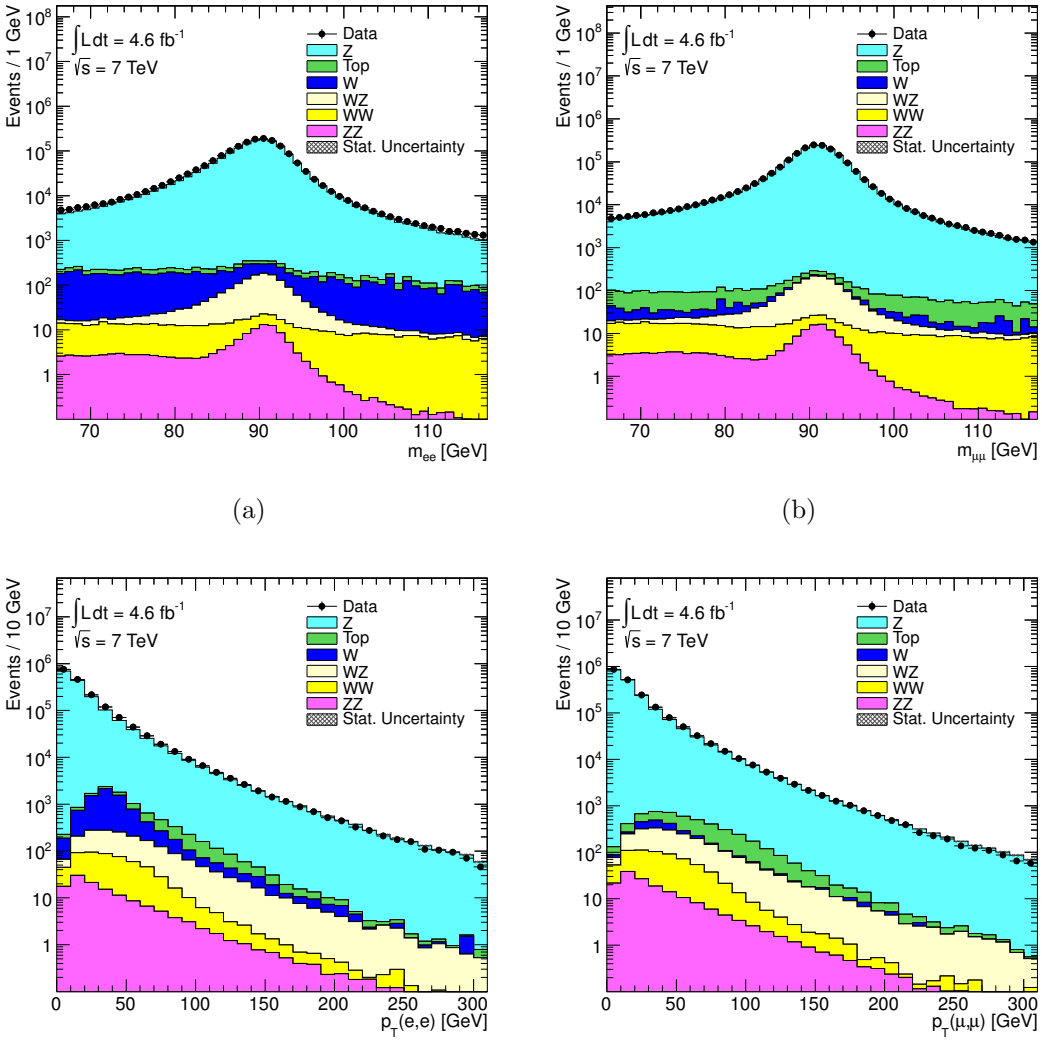

Figure 6.4: Figures (a) and (b) show distributions of the di-lepton invariant mass for di-electron and di-muon pairs, respectively, in events in the 7 TeV data containing a pair of opposite-sign same-flavour leptons passing all of the lepton selection criteria described in Sections 6.1 and 6.2. Figures (c) and (d) show the di-lepton transverse momentum for events passing the same criteria, with the additional requirement that the di-lepton pair have $66 < m_{\ell^-\ell^+} < 116$ GeV.

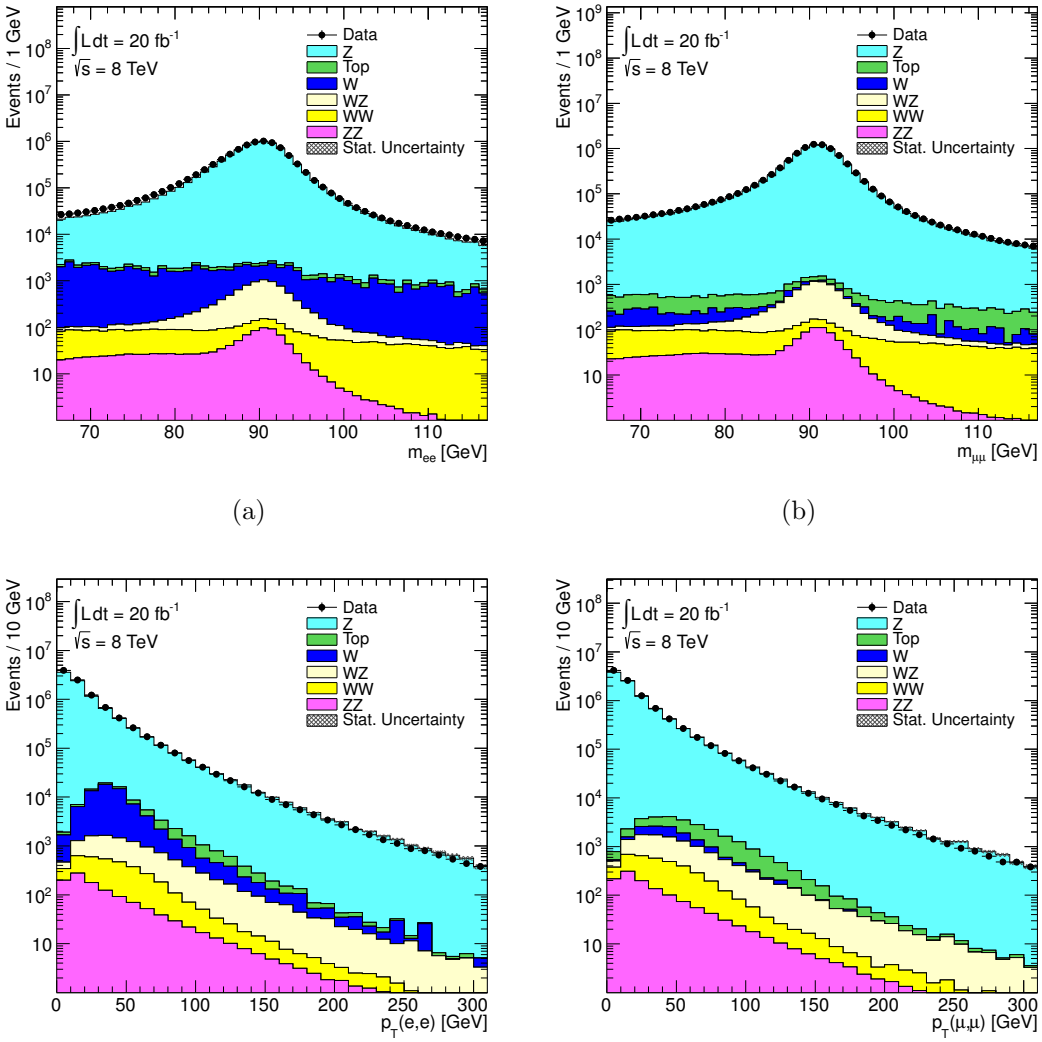

(a) (b)

(c) (d)

Figure 6.5: Figures (a) and (b) show distributions of the di-lepton invariant mass for di-electron and di-muon pairs, respectively, in events in the 8 TeV data containing a pair of opposite-sign same-flavour leptons passing all of the lepton selection criteria described in Sections 6.1 and 6.2. Figures (c) and (d) show the di-lepton transverse momentum for events passing the same criteria, with the additional requirement that the di-lepton pair have $66 < m_{\ell^-\ell^+} < 116$ GeV.

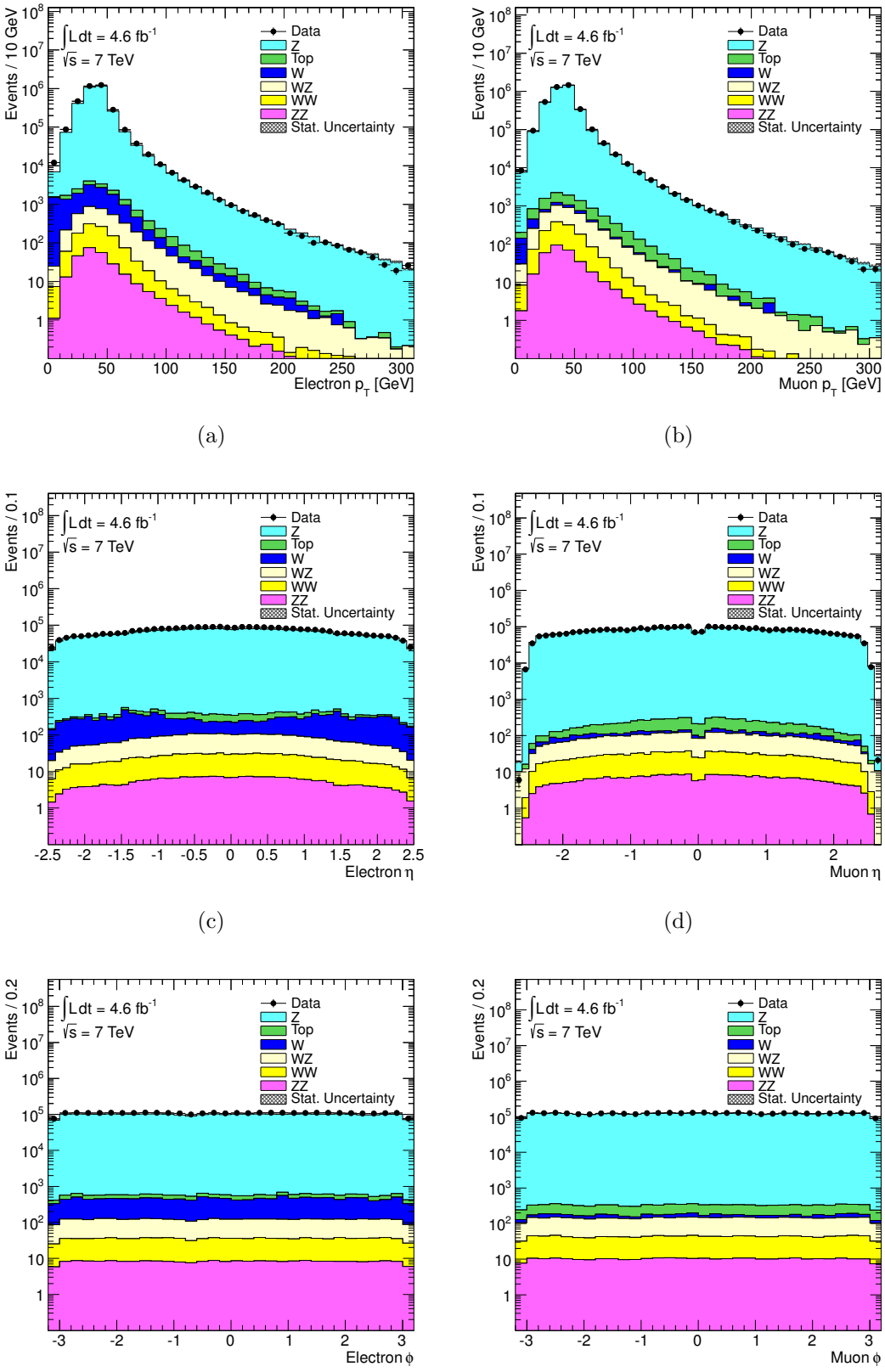

(a) (b)

(c) (d)

(e) (f)

Figure 6.6: Kinematic distributions for leptons in events in the 7 TeV data containing an opposite-sign same-flavour lepton pair. The leptons are required to pass all of the selection requirements described in Sections 6.1 and 6.2 and the pair must have $66 < m_{\ell^-\ell^+} < 116$ GeV. Figures (a) and (b) show the lepton p_{T} for electrons and muons respectively, figures (c) and (d) the lepton η and figures (d) and (e) the lepton ϕ.

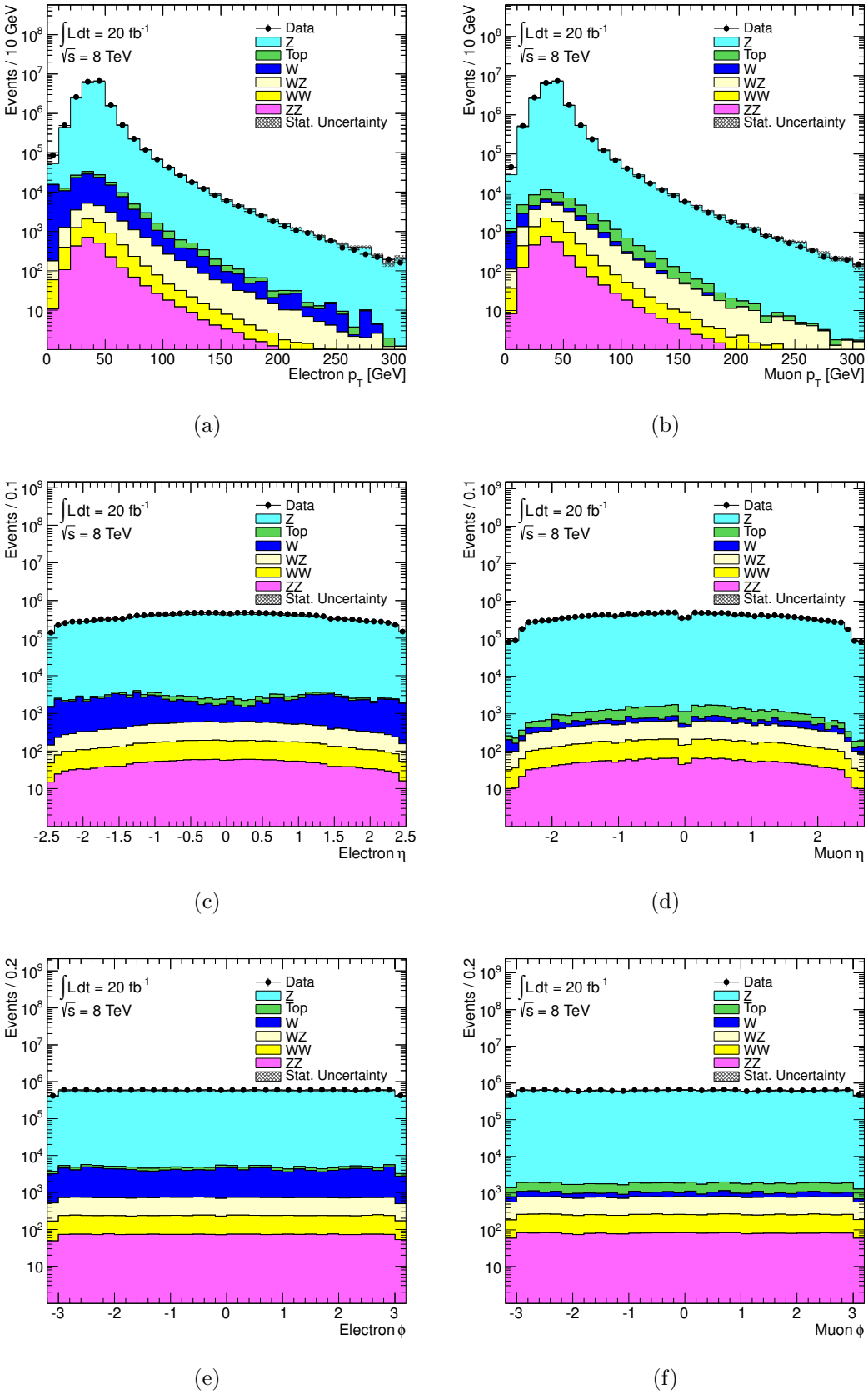

(a) (b)

(c) (d)

(e) (f)

Figure 6.7: Kinematic distributions for leptons in events in the 8 TeV data containing an opposite-sign same-flavour lepton pair. The leptons are required to pass all of the selection requirements described in Sections 6.1 and 6.2 and the pair must have $66 < m_{\ell^-\ell^+} < 116$ GeV. Figures (a) and (b) show the lepton p_{T} for electrons and muons respectively, figures (c) and (d) the lepton η and figures (d) and (e) the lepton ϕ.

6.5 ZZ Event Selection

6.5.1 Z Candidate Definitions

In referring to Z candidate di-lepton pairs in the diboson ZZ selection, the following definitions are used:

- **Leading and Subleading:** The Z candidate with the larger p_{T} of the two is referred to as the *leading* Z; the Z candidate with the lower p_{T} is referred to as the *subleading* Z.
- **Primary and Secondary:** The Z candidate closer to the Z boson mass (from [10]) is referred to as the *primary* Z; the other candidate is referred to as the *secondary* Z.

6.5.2 Event Selection Requirements

Candidate ZZ events are selected by imposing the following requirements:

1. **Data Quality:** Events are required to pass a 'Good Run List' to remove events occurring in a lumiblock where there were defects affecting the quality of the data; for example a ROD (Read Out Device) going 'busy', meaning data from a large fraction of a sub-detector was missing.
2. **Trigger:** The event must pass a high p_{T} single electron or single muon trigger as described in Section 6.3.
3. **Four Leptons:** The event must have exactly four electrons or muons passing the selection requirements described in Sections 6.1 and 6.2. The requirement of exactly four leptons, rather than at least four leptons, greatly simplifies the background estimate. MC simulation predicts that only 1.3% of signal events fail this cut. In 7 TeV data, no events with more than four fully selected leptons were observed. In 8 TeV data, 11 events with more than four leptons passing all of the selection requirements were observed (without applying any mass requirements), compared to 1682 events with exactly four leptons.
4. **Lepton Separation:** The leptons are required to be spatially separated by $\Delta R(\ell, \ell) > 0.2$. This requirement is automatically satisfied after applying the lepton isolation requirements (applied to all leptons except forward

electrons). It is made here explicitly, to highlight the fact that there is no analysis sensitivity to events with leptons separated by $\Delta R < 0.2$, which is of importance when performing searches for nTGCs, where the Z bosons are expected to be heavily boosted and thus the leptons produced at small opening angle in the detector frame. The limits to sensitivity to events with high ZZ mass or high Z p_{T} resulting from this requirement are discussed below.

5. **Trigger Match:** At least one selected lepton must match to the object that caused the trigger to fire within $\Delta R < 0.1$, and pass the same kinematic and identification requirements applied in the trigger, as described in Section 6.3.

6. **Quadruplet Formation:** There must be two same-flavour (SF), oppositely-signed (OS) lepton pairs. In $eeee$ and $\mu\mu\mu\mu$ events there are two possible ways of pairing the four leptons into OS pairs. The pairing which minimises the quantity $|m_{12} - m_Z| + |m_{34} - m_Z|$ is chosen, where m_{12}, m_{34} are the invariant masses of the two lepton pairs in a certain pairing and m_Z is the Z boson mass, taken from [10].

7. **"Primary" Z Candidate:** The primary Z candidate must satisfy the mass cut $66 < m_{12} < 116$ GeV.

8. **"Secondary" Z Candidate:** Two non-exclusive mass cuts are applied to the secondary Z candidate, one to select the event as a ZZ event and the other to select the event as a ZZ^* event:

   (a) To be classified as a ZZ event, the secondary Z candidate must satisfy the mass cut $66 < m_{34} < 116$ GeV.

   (b) To be classified as a ZZ^* event, the secondary Z candidate must satisfy the mass cut $m_{34} > 20$ GeV.

   For the 8 TeV data, only the ZZ selection (selection (a)) is used.

9. J/ψ **Veto:** For the 8 TeV data, any events which have any combination of oppositely charged, same flavor lepton pairs with invariant mass below 5 GeV are rejected, in order to reject J/ψ events. This requirement was not applied for the 7 TeV data. The efficiency of this cut is estimated from Monte Carlo to be 99.6%. No events failing this cut were observed in either the 7 TeV or the 8 TeV data.

The expected number of events in 4.6 fb^{-1} of 7 TeV data after various stages of the selection is shown in Table 6.11. The corresponding numbers for 20 fb^{-1} of 8 TeV data are shown in Table 6.12. The numbers are obtained from the nominal PowhegBox+gg2zz samples, described in Section 2.3.

N_{ZZ} (7 TeV, 4.6 fb^{-1})	$e^-e^+e^-e^+$	$\mu^-\mu^+\mu^-\mu^+$	$e^-e^+\mu^-\mu^+$	$\ell^-\ell^+\ell^-\ell^+$
Four Leptons	18.08 ± 0.19	34.33 ± 0.27	49.09 ± 0.32	101.49 ± 0.46
Quadruplet	17.20 ± 0.19	34.31 ± 0.27	47.84 ± 0.32	99.35 ± 0.46
66< M_{12} <166 GeV	14.36 ± 0.17	25.87 ± 0.24	38.22 ± 0.28	78.44 ± 0.41
M_{34} >20 GeV	13.14 ± 0.16	21.96 ± 0.22	32.61 ± 0.26	67.71 ± 0.38
66< M_{34} <116 GeV	10.80 ± 0.15	17.45 ± 0.19	27.12 ± 0.24	55.38 ± 0.34

Table 6.11: Expected number of events in the 7 TeV data by cut for 4.6 fb^{-1}. The errors are statistical only. The contribution from $ZZ \to \tau + X$ where the tau decays into an electron or a muon is included; the estimated contribution is given in Table 6.14.

N_{ZZ} (8 TeV, 20 fb^{-1})	$e^-e^+e^-e^+$	$\mu^-\mu^+\mu^-\mu^+$	$e^-e^+\mu^-\mu^+$	$\ell^-\ell^+\ell^-\ell^+$
Four Leptons	106.95 ± 0.62	167.39 ± 0.80	266.62 ± 1.42	540.97 ± 1.75
Quadruplet	102.43 ± 0.61	167.27 ± 0.80	260.76 ± 1.41	530.47 ± 1.73
66< M_{12} <166	82.65 ± 0.55	132.07 ± 0.71	205.55 ± 1.25	420.27 ± 1.54
66< M_{34} <116	59.63 ± 0.46	90.97 ± 0.59	143.02 ± 1.05	293.62 ± 1.29
J/ψ Veto	59.53 ± 0.46	90.23 ± 0.59	142.71 ± 1.04	292.47 ± 1.28

Table 6.12: Expected number of events in the 8 TeV data by cut for 20 fb^{-1}. The errors are statistical only. The contribution from $ZZ \to \tau + X$ where the tau decays into an electron or a muon is included; the estimated contribution is given in Table 6.15.

6.6 Selection Efficiencies

6.6.1 Mis-pairing Rates

As described above, in $e^-e^+e^-e^+$ and $\mu^-\mu^+\mu^-\mu^+$ final states there are two possible ways of pairing the four leptons to give two oppositely signed pairs. There are a number of different ways of resolving this ambiguity, using different pairing algorithms. All pairing algorithms will have some rate of failure, so it is important to find the algorithm with the lowest mis-pairing rate.

The mis-pairing rates of four algorithms were compared. The four algorithms considered were:

1. **Sum Of Distances:** Choose the pairing minimising the quantity $|m_{12} - m_Z| + |m_{34} - m_Z|$.

2. **Sum Of Distances Squared:** Choose the pairing minimising the quantity $(m_{12} - m_Z)^2 + (m_{34} - m_Z)^2$.

3. **Closest to the pole:** Choose the pairing which has the di-lepton mass closest to the Z mass.

4. **Breit-Wigner Probability:** For each pairing calculate the product of the values of two Breit-Wigner probability distributions centred at the Z mass with width equal to the Z width evaluated at the masses of the two di-lepton pairs and choose the pairing with the highest probability.

The mis-pairing rates of each algorithm are estimated using $ZZ \to e^-e^+\mu^-\mu^+$ events, by assigning di-lepton pairs using the algorithm in question ignoring lepton flavour, then checking whether the pairing chosen by the algorithm is the correct one by examining the flavour matching of the pairs. The mis-pairing rates estimated in this way are given in Table 6.13. The rates are calculated after applying the Z mass cuts based on the correct pairing. For ZZ events, the 'Sum Of Distances' algorithm has the lowest mis-pairing rate of 1.1%. For ZZ^* events that are not ZZ events (i.e. one of the di-lepton pairs is outside $66 < m_{\ell^-\ell^+} < 116$ GeV), the mis-pairing rates are significantly higher, and for these events the 'Sum Of Distances' algorithm has a mis-pairing rate of 22.5%. In this case the 'Closest to the pole' algorithm gives the lowest mis-pairing rate. Considering the full ZZ^* selection, the 'Breit-Wigner' algorithm gives the lowest mis-pairing rate, with the 'Sum Of Distances' coming second.

Algorithm	ZZ (%)	ZZ^* (%)	ZZ^* not ZZ(%)
Sum Of Distances	1.1 ± 0.1	4.7 ± 0.2	22.5 ± 0.8
Sum Of Distances Squared	1.3 ± 0.1	6.6 ± 0.2	33.6 ± 1.0
Closest to Pole	5.1 ± 0.2	5.5 ± 0.2	7.7 ± 0.5
Breit Wigner Probability	1.4 ± 0.1	2.9 ± 0.1	10.7 ± 0.6

Table 6.13: Mis-pairing rates in percent for different algorithms for choosing the di-lepton pairs in four-lepton events. The errors shown are due to Monte Carlo statistics.

In practice, it is not possible to apply different algorithms to the ZZ and ZZ^* selections, since until one has chosen a pairing it is not possible to apply mass cuts and thus not possible to decide whether the event is ZZ or ZZ^*. The

'Sum of Distances' algorithm is thus applied to all events, since it gives the lowest mis-pairing for ZZ events.

6.6.2 Effect of Minimum ΔR Requirement

As discussed above, the lepton isolation requirements prevent any event with leptons overlapping with $\Delta R < 0.2$ from passing the selection, since the lower p_{T} lepton would be vetoed by the energy of the higher p_{T} lepton in its isolation cone, and the event would fail the selection as it would not have four selected leptons. In events with low p_{T} Z boson candidates this does not affect the efficiency significantly since in the Z boson rest frame the leptons are produced 'back-to-back'. In events with highly boosted Z bosons the leptons are produced with small opening angle in the detector frame, and so the ΔR requirement imposes an upper threshold on the centre of mass energy to which the analysis is sensitive.

Figure 6.8 shows the minimum ΔR between any two leptons at generator level in four-lepton events as a function of the mass of the four-lepton system and as a function of the transverse momentum of the leading Z. A $ZZ \to \ell^-\ell^+\ell^-\ell^+$ Monte Carlo sample generated with nTGCs is used, with the anomalous coupling f_4^γ set to 0.1 and no form-factor applied, in order to give statistics at high centre of mass energies. The plots show that the $\Delta R < 0.2$ cut limits sensitivity to events where the four-lepton system has invariant mass $m(ZZ) > 2$ TeV and to events where the leading Z boson has high p_{T}, $p_{\mathrm{T}}(Z1) > 900$ GeV. This is in the tails of the distributions expected with nTGC couplings set near previous experimental limits, so this cutoff is not expected to adversely affect the sensitivity of the nTGC limits.

6.6.3 Reconstruction Acceptance C_{ZZ}

In order to extrapolate from the number of observed events to a cross section or similar measurement, it is necessary to know the acceptance of the selection requirements. This is described by the *reconstruction acceptance factor*, C_{ZZ}, which is used to extrapolate from the number of observed events to the true number of events in the fiducial phase-space. The definition of the fiducial phase-space was given in Section 2.1.2. Formally, C_{ZZ} is defined as:

$$C_{ZZ} = \epsilon_{trig} \times \epsilon_{event} \times \epsilon_{lep} \times \alpha_{reco} \tag{6.2}$$

where ϵ_{trig} is the trigger efficiency, ϵ_{event} is the efficiency of the event level cuts, and $\epsilon_{lep} = \epsilon_{lep1}\epsilon_{lep2}\epsilon_{lep3}\epsilon_{lep4}$ is the product of the individual reconstruction and selection efficiencies for the four leptons. α_{reco} corrects for small differences between the regions of phase space covered by detector acceptance and the definition of the fiducial phase space; it also accounts for the effects of detector resolution and contamination from $ZZ \to \tau\tau\ell\ell$ decays.

In practice, C_{ZZ} is estimated from Monte Carlo by dividing the number of events in a $ZZ \to \ell^-\ell^+\ell^-\ell^+$ sample which pass the selection requirements by the number of those events which were generated inside the fiducial phase space (as given in Section 2.1.2):

$$C_{ZZ} = \frac{N^{\text{MC Pass All Cuts}}_{\text{Reconstructed } ZZ} \times SF}{N^{\text{MC Fiducial Volume}}_{\text{Generated } ZZ}} \tag{6.3}$$

where SF is the event level scale factor applied to the Monte Carlo to correct the lepton selection efficiencies and trigger efficiencies to those observed in data. The numerator includes contributions from $ZZ \to \tau\tau\ell\ell$ decays (and to a smaller extent $ZZ \to \tau\tau\tau\tau$), where the taus decay leptonically. The numerator also includes a contribution from events which are generated outside the fiducial volume but pass all of the cuts at reconstruction level; for example an event with a generated lepton with p_{T} just lower than the lepton p_{T} threshold which is reconstructed with p_{T} just above the threshold. Since the numerator is not a subset of the denominator due to these two contaminations, C_{ZZ} is not a true efficiency.

C_{ZZ} is calculated separately for each of the three final states ($e^-e^+e^-e^+$, $\mu^-\mu^+\mu^-\mu^+$ and $e^-e^+\mu^-\mu^+$), and separately for the ZZ and ZZ^* selection and for the 7 TeV and 8 TeV analysis. In calculating the number of generated events falling inside the fiducial volume it is necessary to assign the four generator-level leptons into pairs in order to apply the mass cuts. There is no ambiguity in doing this in the $e^-e^+\mu^-\mu^+$ channel as one simply pairs the two electrons and the two muons, however as when dealing with events observed in data or reconstructed MC, there is an ambiguity in assigning the pairs in the $e^-e^+e^-e^+$ and $\mu^-\mu^+\mu^-\mu^+$ channels. One could use the generator documentation to determine which leptons came from which Z, but this is discouraged as it makes use of internal details of the generator's calculation, which do not have a well defined physical meaning and may vary from generator to generator. Instead, the same algorithm is used as in the data and the reconstructed MC; that is, picking the pairing that minimises the sum of the distances of the pairs from the PDG Z boson mass. It is found from applying this algorithm to the $e^-e^+\mu^-\mu^+$ sample, ignoring lepton-

flavour, that the number of events falling in the fiducial volume is over-estimated by the algorithm with respect to the number obtained by choosing the correct pair based on lepton-flavour by $2.84 \pm 0.03\%$ for the 7 TeV analysis with the ZZ selection, by $7.16 \pm 0.08\%$ for the 7 TeV analysis with the ZZ^* selection and by $2.66 \pm 0.01\%$ for the 8 TeV analysis. This leads to the C_{ZZ} factors in the $e^-e^+e^-e^+$ and $\mu^-\mu^+\mu^-\mu^+$ channels being *too low* by the corresponding percentage. The $e^-e^+e^-e^+$ and $\mu^-\mu^+\mu^-\mu^+$ reconstruction factors are therefore increased by the corresponding percentage to compensate. The statistical uncertainties on these percentages are taken as an additional uncertainty on C_{ZZ}. These percentages are higher than the mis-pairing rates given in Section 6.6.1, as those rates were calculated after applying the ZZ or ZZ^* mass cut; these percentages include also a contribution from events that would otherwise fail the mass cuts, but pass as a result of mis-pairing.

Values for C_{ZZ} are given in Tables 6.14 and 6.15, as well as the estimated contribution from tau decays and from events generated outside the fiducial volume (including the contribution from mis-pairing described in the previous paragraph). These are obtained from the POWHEGBOX and GG2ZZ generators, as described in Section 2.2.4, with the relative contributions from the two generators combined according to their cross section. Also given is the true selection efficiency, defined analogously to C_{ZZ}, but with only events generated in the fiducial phase space included in the numerator such that the numerator is a subset of the denominator.

The reconstruction efficiency in the $e^-e^+e^-e^+$ final state is significantly lower than in the $\mu^-\mu^+\mu^-\mu^+$ final state: as much as to 40% lower for the ZZ^* selection at 7 TeV. This is attributed to the lower reconstruction and identification efficiencies for electrons compared to muons. Since in a four-lepton final state the average event level selection efficiency is the average single lepton selection efficiency to the fourth power, differences in efficiency between electrons and muons get significantly amplified. The reconstruction efficiency is slightly lower for the ZZ^* selection than for the ZZ selection, particularly in final states with electrons; as much as 6% lower in the $e^-e^+e^-e^+$ final state at 7 TeV. This is attributed to the higher proportion of leptons at low p_{T} in the ZZ^* selection, and the fact that the electron reconstruction and identification efficiency drops off significantly below 20 GeV (see Figure 5.11). The contamination from events outside the fiducial volume is smaller for the $e^-e^+\mu^-\mu^+$ final state as there is no contribution from events generated outside the fiducial volume incorrectly passing the di-lepton mass cuts as a result of mis-pairing, since there is no mis-pairing in in $e^-e^+\mu^-\mu^+$ decays.

ZZ, 7 TeV	$e^-e^+e^-e^+$	$\mu^-\mu^+\mu^-\mu^+$	$e^-e^+\mu^-\mu^+$	$\ell^-\ell^+\ell^-\ell^+$
Reconstruction acceptance C_{ZZ}	0.440 ± 0.005	0.707 ± 0.004	0.546 ± 0.003	0.560 ± 0.002
Contamination from $ZZ \to \tau + X$ (%)	0.37 ± 0.04	0.25 ± 0.03	0.18 ± 0.02	0.24 ± 0.01
Contamination from events outside fiducial region(%)	3.88 ± 0.17	3.46 ± 0.12	0.81 ± 0.08	2.24 ± 0.08
True reconstruction efficiency	0.422 ± 0.005	0.681 ± 0.004	0.541 ± 0.003	0.546 ± 0.002

ZZ^*, 7 TeV	$e^-e^+e^-e^+$	$\mu^-\mu^+\mu^-\mu^+$	$e^-e^+\mu^-\mu^+$	$\ell^-\ell^+\ell^-\ell^+$
Reconstruction acceptance C_{ZZ}	0.439 ± 0.004	0.727 ± 0.004	0.540 ± 0.003	0.562 ± 0.002
Contamination from $ZZ \to \tau + X$ (%)	2.16 ± 0.09	1.53 ± 0.06	1.70 ± 0.05	1.73 ± 0.04
Contamination from events outside fiducial region(%)	8.24 ± 0.21	7.69 ± 0.15	0.76 ± 0.07	4.36 ± 0.17
True reconstruction efficiency	0.398 ± 0.004	0.665 ± 0.004	0.527 ± 0.003	0.529 ± 0.002

Table 6.14: Details of the acceptance and selection efficiencies and contaminations, estimated from Monte Carlo, for the 7 TeV analysis. The first row shows the reconstruction factor C_{ZZ}, defined as the ratio of the number of events passing the selection requirements (including contributions from $ZZ \to \tau + X$ and events outside the fiducial region) to the number of generated events in the fiducial region. The second row shows the percentage contamination from $\to \tau + X$ events, and the third the percentage contamination from events falling outside the fiducial region at generator level, but passing the selection due to the energy, momentum or track direction being mis-reconstructed, or due to mis-pairing. The final row shows the "true" reconstruction efficiency, with the contribution from $ZZ \to \tau + X$ and events outside the fiducial region removed from the numerator. All errors shown are statistical only.

ZZ, 8 TeV	$e^-e^+e^-e^+$	$\mu^-\mu^+\mu^-\mu^+$	$e^-e^+\mu^-\mu^+$	$\ell^-\ell^+\ell^-\ell^+$
Reconstruction acceptance C_{ZZ}	0.553 ± 0.003	0.831 ± 0.002	0.658 ± 0.003	0.675 ± 0.002
Contamination from $ZZ \to \tau + X$ (%)	0.40 ± 0.06	0.44 ± 0.05	0.19 ± 0.03	0.31 ± 0.02
Contamination from events outside fiducial region(%)	3.29 ± 0.07	3.14 ± 0.06	0.54 ± 0.05	1.94 ± 0.02
True reconstruction efficiency	0.532 ± 0.003	0.800 ± 0.002	0.653 ± 0.003	0.660 ± 0.002

Table 6.15: Details of the acceptance and selection efficiencies and contaminations, estimated from Monte Carlo, for the 8 TeV analysis. The first row shows the reconstruction factor C_{ZZ}, defined as the ratio of the number of events passing the selection requirements (including contributions from $ZZ \to \tau + X$ and events outside the fiducial region) to the number of generated events in the fiducial region. The second row shows the percentage contamination from $\to \tau + X$ events, and the third the percentage contamination from events falling outside the fiducial region at generator level, but passing the selection due to the energy, momentum or track direction being mis-reconstructed, or due to mis-pairing. The final row shows the "true" reconstruction efficiency, with the contribution from $ZZ \to \tau + X$ and events outside the fiducial region removed from the numerator. All errors shown are statistical only.

6.6.4 Comparison of Reconstruction Acceptances at 7 TeV and 8 TeV

The reconstruction acceptances given in Tables 6.14 and 6.15 are not directly comparable, due to the different fiducial volume definitions used in the 7 TeV analysis and the 8 TeV analysis. In order to compare the acceptance between the two analyses, the C_{ZZ} are re-calculated using a common fiducial volume, defined identically to the 7 TeV fiducial volume, but with the lepton pseudo-rapidity requirements set to $|\eta| < 2.5$. Only central electrons and muons are included. The resulting C_{ZZ} are shown in Table 6.16. The acceptance in the 8 TeV analysis is significantly greater compared to the 7 TeV analysis, particularly in channels involving electrons. This can be attributed in part to the improvements in the electron reconstruction algorithms in 2012, but also to the relaxing of the `Loose++` identification requirements in 2012, as well as to the removal of the calorimeter isolation requirement in the 8 TeV analysis.

	$e^-e^+e^-e^+$	$\mu^-\mu^+\mu^-\mu^+$	$e^-e^+\mu^-\mu^+$	$\ell^-\ell^+\ell^-\ell^+$
7 TeV	0.482± 0.005	0.736 ± 0.004	0.577 ± 0.004	0.593 ± 0.003
8 TeV	0.619± 0.003	0.792 ± 0.002	0.675 ± 0.003	0.690 ± 0.002
Increase (%)	28.4%	7.6%	17.0%	16.4%

Table 6.16: Comparison of the fiducial acceptance C_{ZZ} between the 7 TeV analysis and the 8 TeV analysis. The acceptances given here are calculated in a restricted fiducial volume, common between the two analyses. It is defined identically to the 7 TeV fiducial volume, but with the lepton pseudo-rapidity requirements set to $|\eta| < 2.5$; only central electrons and muons are included.

6.6.5 Contribution from $ZZ \to \tau\tau\ell\ell$ and $ZZ \to \tau\tau\tau\tau$

The percentage of tau events passing the selection requirements is approximately 0.5% for the ZZ selection and $\sim 2\%$ for the ZZ^* selection. This higher contamination in the ZZ^* selection can be accounted for by the fact that di-electron or di-muon pairs from decays of a di-tau pair with an invariant mass near the Z mass will have a lower invariant mass due to the energy carried away by the neutrinos. There is therefore a higher chance of their passing the looser mass cut applied in the ZZ^* selection than passing the $66 < m_{\ell^-\ell^+} < 116$ GeV mass cut applied in the ZZ selection. The contamination from events outside the fiducial phase space is similar in the ZZ and ZZ^* selections, at a level of $\sim 1\%$.

6.6.6 Contribution from $H \to ZZ \to \ell^-\ell^+\ell^-\ell^+$

The ATLAS [14] and CMS [13] experiments recently observed a new neutral boson with a mass of around 126 GeV with properties consistent with the Higgs boson. A Standard Model Higgs boson with such a mass will decay to pairs of Z bosons, but only when at least one of the bosons is off shell. The contribution to the event selection described here from a SM Higgs boson with a mass of 126 GeV was estimated from Monte Carlo. For the on-shell ZZ selection, the contribution is found to be negligible. For the ZZ^* selection at 7 TeV, the contribution is found to be $1.7 \pm 0.03\,(\text{stat})$ events, corresponding to a contribution of less than 3%. No correction is made to the observed events to account for this contribution.

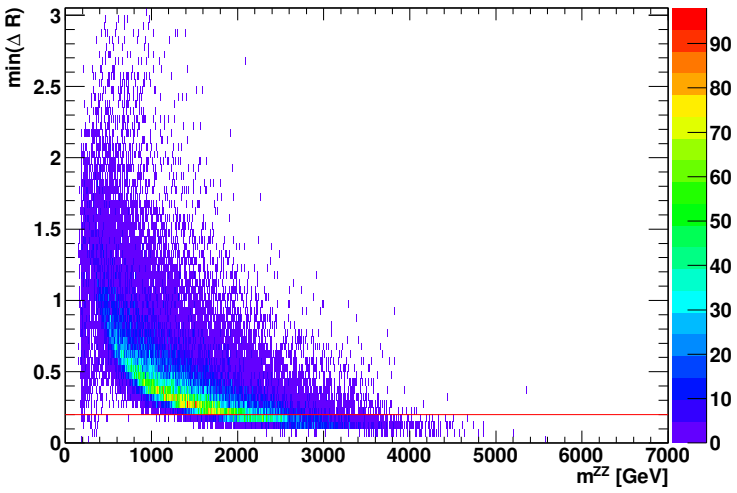

(a)

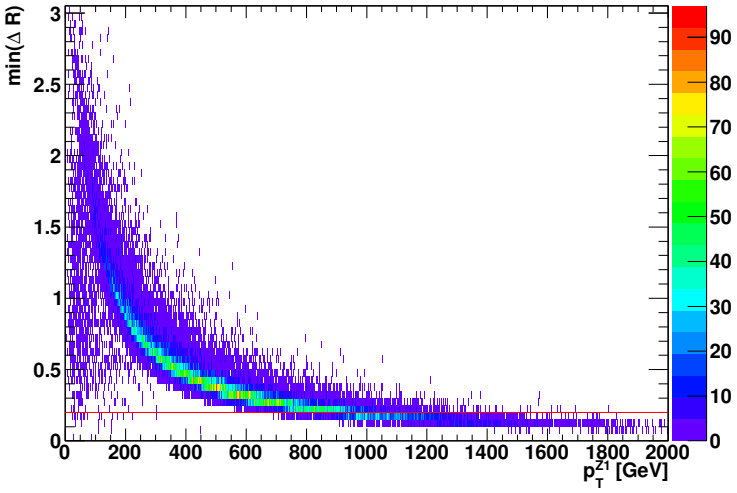

(b)

Figure 6.8: The minimum ΔR between any two leptons at generator level in a four-lepton Monte Carlo sample as a function of (a) mass of the four-lepton system and (b) transverse momentum of the leading Z. A $ZZ \to \ell^-\ell^+\ell^-\ell^+$ sample generated with aTGCs is used, with $f_4^\gamma = 0.4$ and no form-factor applied, in order to give statistics at high centre of mass energies. The horizontal red line shows the $\Delta R < 0.2$ cut.

6.7 Systematic Uncertainties

In this section, the systematic uncertainties associated with the reconstruction acceptance C_{ZZ} and the expected signal yield are discussed and estimated.

6.7.1 Sources of Systematic Uncertainty

Uncertainties arise due to the determination of electron and muon reconstruction and identification efficiencies, the electron and muon energy scales and resolutions, and the trigger efficiency, as well as theoretical uncertainties associated with the Monte Carlo simulation used to estimate C_{ZZ}. Each of these sources of uncertainty is discussed in more detail below, and the estimated size of the uncertainty given in Section 6.7.2.

Electron Systematic Uncertainties

- **Reconstruction and Identification Efficiency:** Uncertainties arise from the measurement of the electron reconstruction and identification efficiencies. The efficiencies are measured using a 'Tag and Probe' technique using decays of $W^{\pm}$, Z and J/ψ. Uncertainties arise due to the methods used to subtract the background, possible biases of the methodology, the definition of the tag electron and differences between the results from different decays, as well as due to the limited statistics in the data and Monte Carlo samples. These uncertainties are propagated to C_{ZZ} by varying the scale-factor applied to the electrons up and down by the estimated 1-sigma uncertainty; this is carried out separately for the reconstruction and identification efficiency, assuming the uncertainties to be uncorrelated.

- **Energy Scale:** Uncertainties arise on the calibration of the electron energy scale due to: the different method used to measure the energy scale; the choice of Monte Carlo generator used; the uncertainty on the pre-sampler energy scale; uncertainty on the amount of dead material; differences between results from $Z \to ee$ and from $J/\psi \to e^{-}e^{+}$ at low E_{T}; and from statistical uncertainties on the measurements. Whilst the energy scale calibration is applied to data, the systematic is estimated by varying the energy scale in the Monte Carlo up and down by the uncertainty. For the 7 TeV analysis, all energy scale uncertainties are considered at once by summing in quadrature the uncertainties on the scale parameter α then propagating

the uncertainty to the uncertainty on C_{ZZ} by varying α up and down by the combined uncertainty; for the 8 TeV analysis each source of uncertainty listed above is considered separately, then the resulting changes in C_{ZZ} are summed in quadrature.

- **Energy Resolution:** Uncertainties arise on the measurement of the energy resolution in data, mainly from uncertainty on the sampling term (as the constant term is extracted assuming that the sampling term is correctly reproduced by the simulation, as discussed in Section 5.3.2), uncertainty on the background subtraction and from statistics. The uncertainty is propagated to C_{ZZ} by varying the amount of energy smearing applied to the Monte Carlo up and down.

- **Isolation/z_0/d_0Efficiency:** The efficiency of the additional electron selection requirements (isolation, z_0, $d_0/\sigma(d_0)$) is estimated from data using a tag and probe technique on $Z \to ee$ decays. For the 7 TeV analysis, the efficiency observed in the data is consistent with that estimated by Monte Carlo within the uncertainties of the efficiency measurement. No correction is made to the central value of the Monte Carlo, but the uncertainties on the measurement of the efficiency in data, arising from uncertainties on the background subtraction and biases in the methodology as well as limited statistics, are propagated to the uncertainty on C_{ZZ}. For the 8 TeV analysis, scale-factors are applied to correct the efficiency of the Monte Carlo to the efficiencies observed in the data, and the uncertainty on the scale-factor is taken as a systematic. The scale-factors applied at 8 TeV, and their uncertainty, are shown in Figure 6.9.

- **Impact Parameter Resolution:** The impact parameter resolution is observed to be slightly wider in data than in Monte Carlo. Whilst no correction is applied to the central value of the Monte Carlo, the impact of this effect is estimated by applying a smearing to the Monte Carlo to match the impact parameter resolution observed in data, and taking the difference in C_{ZZ} with and without the smearing as an additional systematic. This is done for both electrons and muons simultaneously.

Muon Systematic Uncertainties

- **Reconstruction Efficiency:** Similarly to the electrons, uncertainties arise from the measurement of the muon reconstruction efficiency in data.

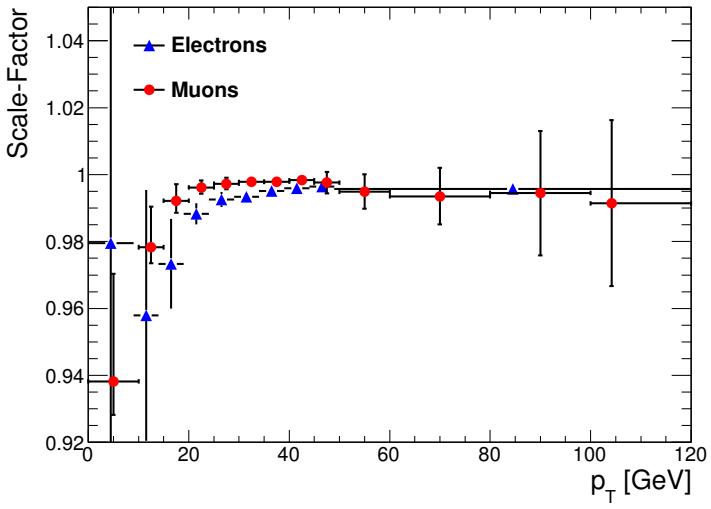

(a)

Figure 6.9: Efficiency-correction scale-factors for the d_0 significance, $z_0 \cdot sin(\theta)$ and track isolation cuts for electrons and muons in the 8 TeV data, as a function p_T of the lepton. The errors shown are a combination of the statistical and systematical uncertainties.

- **Energy Scale:** For the 7 TeV analysis, uncertainties on the muon energy scale are conservatively estimated by taking the difference between the values of C_{ZZ} obtained with and without the muon energy scale correction applied. For the 8 TeV analysis, the systematic is estimated by varying the muon energy scale correction applied to the Monte Carlo up and down by the 1-sigma uncertainty on the correction.

- **Energy Resolution:** The energy resolution is measured separately for the muon's inner detector and muon spectrometer track. Uncertainties are estimated by varying the amount of smearing applied to the muon ID and MS measurements separately.

- **Isolation/z_0/d_0 Efficiency:** Similarly to the electron case, the efficiency of the additional muon selection cuts (isolation, z_0, $d_0/\sigma(d_0)$) is estimated from data using a tag and probe technique on $Z \to \mu\mu$ decays. As for electrons, the 7 TeV data and Monte Carlo are found to be in agreement with the uncertainty of the scale-factor measurement, so no correction is made to the central value of the Monte Carlo and uncertainties on the efficiency are propagated to the uncertainty on C_{ZZ}. For the 8 TeV analysis, scale-factors are applied to correct the efficiency of the Monte Carlo and the uncertainty on the scale-factor is taken as a systematic. The scale-factors applied at

8 TeV, and their uncertainty, are shown in Figure 6.9.

Trigger Systematic Uncertainty

Uncertainties arise on the measurement of the single-lepton trigger efficiency in data. These are propagated to C_{ZZ} by varying the single-lepton trigger efficiencies in Equation 6.1 up and down by their 1-sigma uncertainties.

Theoretical Systematic Uncertainty

Theoretical uncertainties on C_{ZZ} arise due to the choice of factorisation and renormalisation scale, the choice of PDF set, and from differences arising due to different kinematic distributions obtained from different from Monte Carlo generators, due to, for example, different parton shower models and different models for QED radiation.

The effect of the scale and PDF set are assessed by reweighting the POWHEG-BOX sample to a scale of $\frac{1}{4}m(ZZ)$ and to a scale of $m(ZZ)$ from its default scale of $\frac{1}{2}m(ZZ)$, and by reweighting to the MSTW08 PDF set. The reweighting is done by assigning an weight to each event, which is the fractional difference in fiducial cross section predicted by MCFM at the two-scales or PDF sets, binned in terms of the p_{T} of the leading Z boson. This is done for the 8 TeV analysis; the resulting variations on C_{ZZ} are small, and are much smaller than the systematic from comparing different generators, so for the 7 TeV analysis the systematic from generator comparisons is taken to cover differences arising from PDF set and scale choice.

The systematic uncertainty due to the Monte Carlo generator is evaluated by comparing different $qq \to ZZ$ Monte Carlo samples produced using different generators. A comparison is made between the default POWHEGBOX and SHERPA, which uses a different model for the parton shower, and a different model for QED radiation, as described in Section 2.2.4. Table 6.17 compares the C_{ZZ} for the $qq \to ZZ$ process obtained from POWHEGBOX and SHERPA as well as from the LO generator PYTHIA. Also shown is the C_{ZZ} for the $gg \to ZZ$ process obtained from GG2ZZ, as well the combination of the C_{ZZ} from POWHEGBOX and GG2ZZ, weighted by the relative contributions of the qq and gg processes to the fiducial cross section; this final number is the one used in the cross section calculation. The largest difference between POWHEGBOX and SHERPA is taken as the systematic uncertainty; the number from PYTHIA is not considered, although is seen to be in good agreement with POWHEGBOX.

ZZ, 7 TeV	$e^-e^+e^-e^+$	$\mu^-\mu^+\mu^-\mu^+$	$e^-e^+\mu^-\mu^+$	$\ell^-\ell^+\ell^-\ell^+$
qq **Processes**				
PowhegBox	0.438 ± 0.005	0.701 ± 0.004	0.543 ± 0.003	0.556 ± 0.002
Sherpa	0.449 ± 0.004	0.709 ± 0.004	0.550 ± 0.003	0.564 ± 0.002
Pythia	0.437 ± 0.004	0.715 ± 0.004	0.549 ± 0.003	0.562 ± 0.002
gg **Processes**				
gg2zz	0.479 ± 0.002	0.787 ± 0.002	0.596 ± 0.002	0.614 ± 0.001
Combined				
PowhegBox+gg2zz	0.440 ± 0.005	0.707 ± 0.004	0.546 ± 0.003	0.560 ± 0.002

ZZ^*, 7 TeV	$e^-e^+e^-e^+$	$\mu^-\mu^+\mu^-\mu^+$	$e^-e^+\mu^-\mu^+$	$\ell^-\ell^+\ell^-\ell^+$
qq **Processes**				
PowhegBox	0.437 ± 0.004	0.722 ± 0.004	0.537 ± 0.003	0.558 ± 0.002
Sherpa	0.450 ± 0.004	0.731 ± 0.004	0.536 ± 0.003	0.563 ± 0.002
Pythia	0.443 ± 0.004	0.738 ± 0.004	0.543 ± 0.003	0.567 ± 0.002
gg **Processes**				
gg2zz	0.490 ± 0.002	0.815 ± 0.002	0.589 ± 0.002	0.621 ± 0.001
Combined				
PowhegBox+gg2zz	0.439 ± 0.004	0.727 ± 0.004	0.540 ± 0.003	0.562 ± 0.002

Table 6.17: Reconstruction Acceptance C_{ZZ}, compared between different MC generators for the 7 TeV analysis. The C_{ZZ} used in the cross section extraction is the weighted average of the C_{ZZ} from PowhegBox and gg2zz generators, weighting by the relative contribution to the fiducial cross section, as show in Table 2.3. The difference between PowhegBox and Sherpa is taken as an additional systematic uncertainty. Only the statistical uncertainty is shown.

ZZ, 8 TeV	$e^-e^+e^-e^+$	$\mu^-\mu^+\mu^-\mu^+$	$e^-e^+\mu^-\mu^+$	$\ell^-\ell^+\ell^-\ell^+$
qq **Processes**				
PowhegBox	0.551 ± 0.003	0.832 ± 0.002	0.657 ± 0.003	0.674 ± 0.002
Sherpa	0.561 ± 0.009	0.840 ± 0.006	0.670 ± 0.006	0.685 ± 0.004
Pythia	0.544 ± 0.007	0.832 ± 0.004	0.653 ± 0.004	0.671 ± 0.003
gg **Processes**				
gg2zz	0.576 ± 0.003	0.827 ± 0.002	0.668 ± 0.002	0.685 ± 0.001
Combined				
PowhegBox+gg2zz	0.553 ± 0.003	0.831 ± 0.002	0.658 ± 0.003	0.675 ± 0.002

Table 6.18: Reconstruction Acceptance C_{ZZ}, compared between different MC generators for the 8 TeV analysis. The C_{ZZ} used in the cross section extraction is the weighted average of the C_{ZZ} from PowhegBox and gg2zz generators, weighting by the relative contribution to the fiducial cross section as show in Table 2.3. The difference between PowhegBox and Sherpa is taken as an additional systematic uncertainty. Only the statistical uncertainty is shown.

6.7.2 Estimates of Systematic Uncertainties on C_{ZZ}

The effect of each of the systematic uncertainties described above on C_{ZZ} is estimated using the PowhegBox and $gg \to ZZ$ Monte Carlo. The resulting shifts in the value of C_{ZZ} in percent are shown in Table 6.19 for the 7 TeV analysis and in Table 6.20 for the 8 TeV analysis, as well as the total uncertainty obtained by summing each source in quadrature. The dominant sources of systematic uncertainty are the electron and muon reconstruction, identification and isolation/z_0/d_0-Significance efficiencies. The uncertainty in the $e^-e^+e^-e^+$ final state is over twice as large as for the $\mu^-\mu^+\mu^-\mu^+$ final state, due to the larger reconstruction and identification uncertainties for electrons.

6.7.3 Estimates of Systematic Uncertainties on Expected Signal

The systematic uncertainty on the expected signal yield is slightly larger than the systematic uncertainty on the reconstruction acceptance as theoretical uncertainties affecting the fiducial cross section will tend to cancel out between the numerator and denominator of C_{ZZ}, but not when considering the absolute number of expected events. Table 6.21 gives the systematic uncertainties on the expected yields. The reconstruction uncertainties to the expected yield are identical to the reconstruction uncertainties on C_{ZZ}, so the contribution of each individual source is not shown in this table.

ZZ Selection, 7 TeV	$e^-e^+e^-e^+$	$\mu^-\mu^+\mu^-\mu^+$	$e^-e^+\mu^-\mu^+$	$\ell^-\ell^+\ell^-\ell^+$
Reconstruction Uncertainties (%)				
e energy scale	0.5	-	0.1	0.1
e energy resolution	< 0.1	-	< 0.1	< 0.1
e reconstruction efficiency	3.9	-	1.9	1.7
e identification efficiency	5.5	-	2.7	2.4
e isolation/z_0/d_0/$\sigma(d_0)$efficiency	3.3	-	1.6	1.4
μ momentum scale	-	< 0.1	< 0.1	< 0.1
μ momentum resolution	-	< 0.1	< 0.1	< 0.1
μ reconstruction efficiency	-	1.2	0.6	0.7
μ isolation/z_0/d_0/$\sigma(d_0)$efficiency	-	2.2	1.1	1.3
IP Resolution	< 0.1	0.4	0.3	0.3
Trigger	< 0.1	0.1	0.1	0.1
Total Reconstruction	7.5	2.6	3.9	3.5
Theoretical Uncertainties (%)				
MC Generator Difference	1.6	1.6	1.6	1.6
Total C_{ZZ} Uncertainty (%)	7.7	3.0	4.2	3.9

ZZ^* Selection, 7 TeV	$e^-e^+e^-e^+$	$\mu^-\mu^+\mu^-\mu^+$	$e^-e^+\mu^-\mu^+$	$\ell^-\ell^+\ell^-\ell^+$
Reconstruction Uncertainties (%)				
e energy scale	0.5	-	0.1	0.2
e energy resolution	< 0.1	-	< 0.1	< 0.1
e reconstruction efficiency	4.0	-	2.0	1.7
e identification efficiency	6.0	-	2.8	2.5
e isolation/z_0/d_0/$\sigma(d_0)$efficiency	3.6	-	1.7	1.5
μ momentum scale	-	< 0.1	< 0.1	< 0.1
μ momentum resolution	-	< 0.1	< 0.1	< 0.1
μ reconstruction efficiency	-	1.2	0.6	0.7
μ isolation/z_0/d_0/$\sigma(d_0)$efficiency	-	2.4	1.2	1.3
IP Resolution	< 0.1	0.4	0.3	0.3
Trigger	< 0.1	0.2	0.1	0.1
Total Reconstruction	8.1	2.7	4.1	3.7
Theoretical Uncertainties (%)				
MC Generator Difference	1.5	1.5	1.5	1.5
Total C_{ZZ} Uncertainty (%)	8.3	3.1	4.3	4.0

Table 6.19: Summary of systematic uncertainties on the reconstruction acceptance C_{ZZ} in percent, by ZZ final state, for the 7 TeV analysis. The top table gives uncertainties on the ZZ selection, the bottom on the ZZ^* selection. The fourth column gives the weighted average of the three final states. The total uncertainty is also given, which is the sum in quadrature of the individual uncertainties.

ZZ Selection, 8 TeV	$e^-e^+e^-e^+$	$\mu^-\mu^+\mu^-\mu^+$	$e^-e^+\mu^-\mu^+$	$\ell^-\ell^+\ell^-\ell^+$
Reconstruction Uncertainties (%)				
e energy scale	0.4	-	0.1	0.1
e energy resolution	< 0.1	-	< 0.1	< 0.1
e reconstruction efficiency	3.1	-	1.5	1.4
e identification efficiency	5.3	-	2.6	2.4
e isolation/z_0/d_0/$\sigma(d_0)$efficiency	1.8	-	0.8	0.8
μ momentum scale	-	< 0.1	< 0.1	< 0.1
μ momentum resolution	-	< 0.1	< 0.1	< 0.1
μ reconstruction efficiency	-	1.2	0.6	0.6
μ isolation/z_0/$d_0$efficiency	-	2.6	1.3	1.5
Trigger	-	0.2	0.1	0.1
Total Reconstruction	6.4	2.8	3.4	3.3
Theoretical Uncertainties (%)				
MC Generator Difference	1.7	0.9	1.8	1.5
Total C_{ZZ} Uncertainty (%)	6.6	3.0	3.9	3.6

Table 6.20: Summary of systematic uncertainties on the reconstruction acceptance C_{ZZ} in percent, by ZZ final state, for the 8 TeV analysis. The fourth column gives the weighted average of the three final states. The total uncertainty is also given, which is the sum in quadrature of the individual uncertainties.

ZZ Selection, 7 TeV	$e^-e^+e^-e^+$	$\mu^-\mu^+\mu^-\mu^+$	$e^-e^+\mu^-\mu^+$	$\ell^-\ell^+\ell^-\ell^+$
Reconstruction Uncertainties	7.5	2.6	3.9	3.5
MC Generator Difference	1.6	1.6	1.6	1.6
PDF	3.5	3.5	3.5	3.5
Scale	3.3	3.3	3.3	3.3
Total Yield Uncertainty (%)	9.1	5.7	6.4	6.2

ZZ^* Selection, 7 TeV	$e^-e^+e^-e^+$	$\mu^-\mu^+\mu^-\mu^+$	$e^-e^+\mu^-\mu^+$	$\ell^-\ell^+\ell^-\ell^+$
Reconstruction Uncertainties	8.1	2.7	4.1	3.7
MC Generator Difference	1.5	1.5	1.5	1.5
PDF	3.2	3.2	3.2	3.2
Scale	4.4	4.4	4.4	4.4
Total Yield Uncertainty (%)	9.9	6.3	7.0	6.7

ZZ Selection, 8 TeV	$e^-e^+e^-e^+$	$\mu^-\mu^+\mu^-\mu^+$	$e^-e^+\mu^-\mu^+$	$\ell^-\ell^+\ell^-\ell^+$
Reconstruction Uncertainties	6.4	2.8	3.4	3.3
MC Generator Difference	1.7	0.9	1.8	1.5
PDF	3.4	3.4	3.4	3.4
Scale	3.8	3.8	3.8	3.8
Total Yield Uncertainty (%)	8.4	5.9	6.4	6.3

Table 6.21: Summary of systematic uncertainties on the expected signal yield in percent, by ZZ final state,. The fourth column gives the weighted average of the three final states. The total uncertainty is also given, which is the sum in quadrature of the individual uncertainties. For a breakdown of the reconstruction uncertainties, see Tables 6.19 and 6.20.

Chapter 7

Background Estimate

The four-lepton final state is expected to be very clean with little background, since few other Standard Model interactions produce four high-p_{T} isolated leptons in the final state. Almost all of the sources of background include one or more *background leptons*, where a background lepton is defined as either a fake-lepton arising due to jets or photons mis-identified as a lepton, or a real lepton from decays within jets or from photon conversions. The dominant background contribution is expected to arise from the production of a Z boson in association with jets and or photons (collectively termed Z+X). Other contributions arise from top-quark production ($t\bar{t}$ and single-t) and from the other diboson processes W^+W^- and $W^{\pm}Z$, where the bosons are produced in association with jets or photons.

An additional background arises from triboson ZZZ and WZZ production, and from $t\bar{t}$+V where $V = W^{\pm}, Z$. In these backgrounds there are four leptons from $W^{\pm}$ or Z boson decays, so they will tend to be isolated and have small impact parameters, making these irreducible sources of background. The cross sections for these processes are, however, very small, so they contribute only a small fraction of the overall background.

Monte Carlo simulation can be used to estimate the size of the background, however this relies on accurate modelling of particle production within jets. Accurate modelling is important so that the rate of lepton production from hadronic decays within jets is represented correctly, and so that the shower shapes of jets in the calorimeters are well described, in order for the rate at which jets fake the electron identification is well predicted. In order for leptons or fakes to pass the analysis selection requirements they must the isolation requirement; background leptons will therefore tend to be in the tails of the jet distribution where the energy density due to other particles in the jet is lower. The Monte Carlo simulation is not expected to perform well in this area, as it relies heavily on the

model used for hadronisation and on details of the parton shower. A data-driven method is therefore used to estimate the background from events with one or two background leptons. This method estimates the expected combined background from Z+X, $Z+\gamma$, W^+W^-, $W^\pm Z$, $t\bar{t}$, and single-t. Monte Carlo simulation is used to estimate the irreducible backgrounds, and as a cross-check to the data-driven estimate.

Monte Carlo based background estimates are described in Section 7.1, and the data-driven estimate is described in Section 7.2.

7.1 Monte Carlo Background Estimates

The Monte Carlo generators used to model the different sources of background are listed in Table 7.1. In a few cases different generators were used for the 8 TeV analysis with respect to the 7 TeV analysis, owing to developments in the available Monte Carlo generators. The Z+X samples generated with ALPGEN are normalised to the inclusive NNLO cross section prediction of the FEWZ program [110]; these include the contribution from a Z boson produced in association with a hard photon. The $t\bar{t}$ samples are normalised to the approximate NNLO calculation of HATHOR [111]. Other samples are normalised to the cross section predictions of the generator used to produce them.

The Monte Carlo estimated background for the 7 TeV analysis is shown in Table 7.2, separately for each source of background and for each final state. The background estimates are all statistically limited, with typically only one or two events passing all of the selections for each source of background. In the $e^-e^+e^-e^+$ final-state, the background is seen to arise mainly from Z+X, with a smaller contribution from $W^\pm Z$ and W^+W^-. The background to the ZZ^* selection is significantly larger than the background to the ZZ selection, as the tighter mass cut applied in the ZZ selection rejects backgrounds where the second Z boson

Process	Generator 7 TeV	Generator 8 TeV
Z+X	ALPGEN +JIMMY	ALPGEN +JIMMY
$t\bar{t}$	MC@NLO +JIMMY	MC@NLO +JIMMY
single-t	ACERMC+JIMMY	ACERMC+PYTHIA
$W^\pm Z$	MC@NLO +JIMMY	POWHEGBOX+PYTHIA
W^+W^-	MC@NLO +JIMMY, GG2WW	POWHEGBOX+PYTHIA, GG2WW
ZZZ/WWZ	Not Used	MADGRAPH+PYTHIA
$t\bar{t}+V$	Not Used	MADGRAPH+PYTHIA

Table 7.1: Monte Carlo generators used to model background processes.

candidate is formed from background leptons. The background to the $\mu^-\mu^+\mu^-\mu^+$ final-state is estimated to be much smaller, with the only contribution in the Monte Carlo simulation arising from $W^{\pm}Z$ events. For the 7 TeV analysis, no Monte Carlo samples were available to model the ZZZ/WWZ background. In order to estimate the size of the background from these processes, the 8 TeV samples are used, applying the 7 TeV selection and normalising to the 7 TeV cross section and luminosity. For the 7 TeV analysis, the total estimated background to the ZZ selection due to fakes is 1.5 ± 0.4; the estimated background to the ZZ^* selection is 8.3 ± 1.3. The estimated irreducible background is 0.4 ± 0.1 for the ZZ selection and 1.2 ± 0.1 for the ZZ^* selection. The Monte Carlo estimated backgrounds to the 8 TeV analysis are shown in Table 7.3. For the 8 TeV analysis, the estimated background from reducible sources is 3.9 ± 2.6 and the estimated irreducible background is 1.6 ± 0.1.

$e^-e^+e^-e^+$	Z+X	WZ/WW	Top	ZZZ/ZWW	$t\bar{t}+V$
Four Leptons	12.2 ± 1.8	0.8 ± 0.4	0.2 ± 0.2	0.09 ± 0.01	0.24 ± 0.03
2 OS-SF Pairs	7.0 ± 1.5	0.6 ± 0.2	0.2 ± 0.2	0.08 ± 0.01	0.20 ± 0.03
66<M_{Z1}<116 GeV	5.1 ± 1.2	0.5 ± 0.2	< 0.04	0.08 ± 0.01	0.20 ± 0.03
M_{Z2} >20 GeV	3.5 ± 0.9	0.3 ± 0.1	< 0.04	0.07 ± 0.01	0.18 ± 0.03
66<M_{Z2}<116 GeV	0.6 ± 0.2	0.1 ± 0.1	< 0.04	0.02 ± 0.01	0.07 ± 0.02

$\mu^-\mu^+\mu^-\mu^+$	Z+X	WZ/WW	Top	ZZZ/ZWW	$t\bar{t}+V$
Four Leptons	0.3 ± 0.3	0.1 ± 0.1	< 0.04	0.09 ± 0.01	0.30 ± 0.04
2 OS-SF Pairs	0.3 ± 0.3	0.1 ± 0.1	< 0.04	0.09 ± 0.01	0.29 ± 0.04
66<M_{Z1}<116 GeV	< 0.6	0.1 ± 0.1	< 0.04	0.09 ± 0.01	0.29 ± 0.04
M_{Z2} > 20 GeV	< 0.6	0.1 ± 0.1	< 0.04	0.08 ± 0.01	0.26 ± 0.04
66<M_{Z2}<116 GeV	< 0.6	< 0.1	< 0.04	0.03 ± 0.01	0.11 ± 0.02

$e^-e^+\mu^-\mu^+$	Z+X	WZ/WW	Top	ZZZ/ZWW	$t\bar{t}+V$
Four Leptons	21.2 ± 2.9	1.2 ± 0.2	0.1 ± 0.1	0.19 ± 0.01	0.57 ± 0.05
2 OS-SF Pairs	7.0 ± 1.2	0.7 ± 0.2	< 0.04	0.18 ± 0.01	0.48 ± 0.05
66<M_{Z1}<116 GeV	4.9 ± 1.0	0.6 ± 0.2	< 0.04	0.17 ± 0.01	0.47 ± 0.05
M_{Z2}>20 GeV	4.0 ± 0.9	0.5 ± 0.1	< 0.04	0.14 ± 0.01	0.44 ± 0.05
66<M_{Z2}<116 GeV	0.7 ± 0.3	0.1 ± 0.1	< 0.04	0.05 ± 0.01	0.15 ± 0.03

$\ell^-\ell^+\ell^-\ell^+$	Z+X	WZ/WW	Top	ZZZ/ZWW	$t\bar{t}+V$
Four Leptons	34.5 ± 3.4	2.0 ± 0.4	0.3 ± 0.2	0.38 ± 0.01	1.11 ± 0.07
2 OS-SF Pairs	14.3 ± 1.9	1.3 ± 0.3	0.2 ± 0.2	0.35 ± 0.01	0.97 ± 0.07
66<M_{Z1}<116 GeV	10.0 ± 1.6	1.2 ± 0.3	< 0.04	0.34 ± 0.01	0.96 ± 0.07
M_{Z2}>20 GeV	7.4 ± 1.3	0.8 ± 0.2	< 0.04	0.28 ± 0.01	0.89 ± 0.06
66<M_{Z2}<116 GeV	1.2 ± 0.4	0.3 ± 0.1	< 0.04	0.11 ± 0.01	0.33 ± 0.04

Table 7.2: MC predicted number of events passing various levels of selection for the Z+X, $W^{\pm}Z/W^+W^-$, top quark, ZZZ/WWZ and $t\bar{t}+V$ backgrounds for the 7 TeV analysis. The top table shows the estimated background to the $e^-e^+e^-e^+$ final state, the second to $\mu^-\mu^+\mu^-\mu^+$, the third to $e^-e^+\mu^-\mu^+$ and the final table shows the combined background estimate for all $\ell^-\ell^+\ell^-\ell^+$ final states. The Z+X background includes contributions from both light and heavy flavour jets and from photons. The top quark background includes contributions from $t\bar{t}$ and single top. Only statistical uncertainties are sown. The yields are normalised to 4.6 fb^{-1}.

$e^-e^+e^-e^+$	Z+X	WZ/WW	Top	ZZZ/ZWW	$t\bar{t}+V$
Four Leptons	123.6 ± 25.0	5.4 ± 0.5	4.0 ± 0.7	0.39 ± 0.02	0.96 ± 0.08
Quadruplet	40.0 ± 13.5	3.4 ± 0.4	2.4 ± 0.5	0.37 ± 0.02	0.78 ± 0.07
$66<M_{Z1}<166$ GeV	40.0 ± 13.5	2.9 ± 0.4	1.4 ± 0.4	0.33 ± 0.02	0.74 ± 0.07
$66<M_{Z2}<116$ GeV	2.6 ± 2.6	0.4 ± 0.2	0.1 ± 0.1	0.11 ± 0.01	0.29 ± 0.04
J/ψ veto	2.6 ± 2.6	0.4 ± 0.2	0.1 ± 0.1	0.11 ± 0.01	0.29 ± 0.04

$\mu^-\mu^+\mu^-\mu^+$	Z+X	WZ/WW	Top	ZZZ/ZWW	$t\bar{t}+V$
Four Leptons	< 4.5	0.5 ± 0.2	0.7 ± 0.3	0.49 ± 0.02	0.97 ± 0.08
Quadruplet	< 4.5	0.3 ± 0.1	0.8 ± 0.3	0.49 ± 0.02	0.90 ± 0.08
$66<M_{Z1}<166$ GeV	< 4.5	0.2 ± 0.1	0.4 ± 0.2	0.44 ± 0.02	0.86 ± 0.07
$66<M_{Z2}<116$ GeV	< 4.5	0.0 ± 0.0	< 0.9	0.18 ± 0.01	0.30 ± 0.04
J/ψVeto	< 4.5	< 0.1	< 0.9	0.18 ± 0.01	0.30 ± 0.04

$e^-e^+\mu^-\mu^+$	Z+X	WZ/WW	Top	ZZZ/ZWW	$t\bar{t}+V$
Four Leptons	110.5 ± 21.7	7.5 ± 0.6	11.4 ± 1.3	0.93 ± 0.03	2.27 ± 0.12
Quadruplet	43.7 ± 13.6	4.7 ± 0.5	3.9 ± 0.8	0.88 ± 0.03	1.83 ± 0.11
$66<M_{Z1}<166$ GeV	34.3 ± 12.7	3.4 ± 0.4	1.6 ± 0.5	0.76 ± 0.03	1.69 ± 0.10
$66<M_{Z2}<116$ GeV	< 4.5	0.7 ± 0.2	0.1 ± 0.1	0.26 ± 0.01	0.44 ± 0.05
J/ψVeto	< 4.5	0.7 ± 0.2	0.1 ± 0.1	0.26 ± 0.01	0.44 ± 0.05

$\ell^-\ell^+\ell^-\ell^+$	Z+X	WZ/WW	Top	ZZZ/ZWW	$t\bar{t}+V$
Four Leptons	234.1 ± 33.1	13.5 ± 0.8	16.2 ± 1.5	1.81 ± 0.04	4.19 ± 0.16
Quadruplet	83.7 ± 19.1	8.3 ± 0.6	7.1 ± 1.0	1.75 ± 0.04	3.50 ± 0.15
$66<M_{Z1}<166$ GeV	74.3 ± 18.5	6.6 ± 0.6	3.4 ± 0.7	1.53 ± 0.04	3.28 ± 0.14
$66<M_{Z2}<116$ GeV	2.6 ± 2.6	1.1 ± 0.2	0.2 ± 0.1	0.55 ± 0.02	1.03 ± 0.08
J/ψVeto	2.6 ± 2.6	1.1 ± 0.2	0.2 ± 0.1	0.55 ± 0.02	1.03 ± 0.08

Table 7.3: MC estimated number of events passing various levels of selection for the Z+X, $W^{\pm}Z/W^+W^-$, top quark, ZZZ/WWZ and $t\bar{t}+V$ backgrounds for the 8 TeV analysis. The top table shows the estimated background to the $e^-e^+e^-e^+$ final state, the second to $\mu^-\mu^+\mu^-\mu^+$, the third to $e^-e^+\mu^-\mu^+$ and the final table shows the combined background estimate for all $\ell^-\ell^+\ell^-\ell^+$ final states. The Z+X background includes contributions from light and heavy flavour jets and from photons; the top quark background includes contributions from $t\bar{t}$ and single top. Only statistical uncertainties are sown. The yields are normalised to 20 fb^{-1}.

7.2 Data Driven Background Estimates

7.2.1 Methodology

The reducible background sources fall into two categories:

- Backgrounds with two prompt isolated leptons and two 'background' leptons. Such background include Z+X, $Z+\gamma$, W^+W^-+jets, $t\bar{t}$ and single-t (in the s and t channels).
- Backgrounds with three prompt isolated leptons and one 'background' lepton. Such backgrounds include $W^{\pm}Z$+jets and single-t production in the $W^{\pm}t$ channel.

Denoting true leptons passing all of the selection requirements as T and background leptons as B, the total background due to background leptons can be expressed as:

$$N_{4l}^{\text{fake}} = N_{TTTB} \times f + N_{TTBB} \times f^2 \tag{7.1}$$

where f is the fake rate, the fraction of background leptons that pass the full lepton selection requirements. Of course, given a selected lepton in data it is impossible to know whether it is a true lepton or a background lepton (if it were, background rejection would be trivial). Instead, in order to estimate the background two new definitions are introduced: *selected-leptons*, denoted L, that pass all of the lepton selection requirements; and *lepton-like-jets*, denoted J, which pass most of the selection requirements, but fail a few selected requirements. The background is estimated by extrapolating from control regions containing two or three selected-leptons and one or two lepton-like-jet(s) using the *fake-factor*, FF, defined as the ratio of the probability for a background lepton to be classified as a selected-lepton to the probability for it to be classified as a lepton-like-jet. In a sample containing only background leptons, the fake rate and fake-factor are given by:

$$f = \frac{N_L}{N_L + N_J}, \; FF = \frac{N_L}{N_J} \tag{7.2}$$

where N_L and N_J are the number of selected-leptons and lepton-like-jets in the sample, respectively. FF and f are thus related by:

$$f = \frac{FF}{1 + FF}, \; FF = \frac{f}{1 - f} \tag{7.3}$$

The number of events observed with three L and one J, denoted N_{LLLJ}, is related to the true composition by:

$$\begin{aligned} N_{LLLJ} = N_{TTTB} \times (1-f) \; + \; N_{TTBB} \times 2f(1-f) \\ + N_{TBBB} \times 3f^2(1-f) \; + \; N_{BBBB} \times 4f^3(1-f) \end{aligned} \tag{7.4}$$

where the numerical factors arise due to combinatorics. Similarly, the number of events with two L and two J, denoted N_{LLJJ}, is related to the true composition by:

$$N_{LLJJ} = N_{TTBB} \times (1-f)^2 + N_{TBBB} \times 3f(1-f)^2 + N_{BBBB} \times 6f^2(1-f)^2 \tag{7.5}$$

Since f is small, terms of order f^3 or higher are neglected.

The background to the four-lepton selection given in Equation 7.1 can be rewritten in terms of the number of events in the $LLLJ$ and $LLJJ$ control regions as:

$$\begin{aligned} N_{4l}^{\text{fake}} &= N_{TTTB} \times f + N_{TTBB} \times f^2 \\ &= N_{TTTB} \times f + N_{TTBB} \times 2f^2 - N_{TTBB} \times f^2 \\ &= N_{TTTB} \times (1-f)FF + N_{TTBB} \times 2f(1-f)FF \\ &\quad - N_{TTBB} \times (1-f)^2 FF^2 \\ &= N_{LLLJ} \times FF - N_{LLJJ} \times FF^2 \end{aligned} \tag{7.6}$$

where use has been made of Equation 7.3. In reality, observed $LLJJ$ and $LLLJ$ events will include some contribution from $ZZ \to \ell^-\ell^+\ell^-\ell^+$ events where one or two leptons fail the selection requirements and are classified as J. The background estimate is thus:

$$N_{4l}^{\text{fake}} = (N_{LLLJ}^{obs} - N_{LLLJ}^{ZZ}) \times FF - (N_{LLJJ}^{obs} - N_{LLJJ}^{ZZ}) \times FF^2 \tag{7.7}$$

where N_{LLLJ}^{ZZ} and N_{LLJJ}^{ZZ} are the number of ZZ events with one or two leptons being classified as J; these must be estimated from Monte Carlo simulation.

7.2.2 Lepton-Like-Jet Definitions

A *pre-lepton* is defined as a reconstructed lepton object that passes all of the selection requirements, apart from the isolation and d_0-significance requirements (for muons) or the isolation and `Loose++` identification requirements (for electrons).

The pre-leptons may than be classified as either lepton-like-jets or selected-leptons. Pre-muons that fail *either* the isolation *or* the d_0-significance requirement are classified as J. Those that pass both requirements are classified as L; those that fail both are discarded. Similarly, pre-electrons that fail *either* the isolation *or* the `Loose++` significance requirement are classified as J; those that fail both are discarded. For the 7 TeV analysis where both calorimeter and track isolation requirements are used, a lepton may fail either the track or calorimeter requirement to be considered a J. For forward electrons, for which no isolation requirements are applied, pre-leptons are classified as J if they fail the `Tight` ID requirement. For forward Stand-Alone muons which have no track, pre-leptons are classified as J if they fail the isolation requirements. A summary of the J definitions is given in Table 7.4.

Lepton	Selected Leptons L	Lepton Like Jets J
Muon	Pass Isolation AND Pass d_0-significance	(Fail Isolation AND Pass d_0-significance) OR (Fail Isolation AND Pass d_0-significance)
Electron	Pass Isolation AND Pass `Loose++`	(Fail Isolation AND Pass `Loose++`) OR (Fail Isolation AND Pass `Loose++`)
Forward Electron	Pass `Tight`	Fail `Tight`

Table 7.4: Definition of selected-leptons L and lepton-like-jets J. The full lepton selection requirements, with the exception of those listed in the table, are applied to both L and J.

7.2.3 Fake-Factor Measurement

In order to measure the fake-factor, a sample of background leptons must be identified, with a similar composition in terms of the different sources of background leptons as the signal sample. This is done using a *Z-tag* sample, selecting events containing an opposite-sign same-flavour di-lepton pair passing all of the lepton selection requirements. The pair must have invariant mass $|m_{\ell^+\ell^-} - m_Z| < 20$ GeV, in order to be consistent with a Z boson. It is then required that the event contain at least one additional pre-lepton. The sample will be dominated by Z+X, $W^{\pm}Z$ and ZZ events. The additional pre-leptons in Z+X events are all background electrons; in $W^{\pm}Z$ and ZZ events there will be one or two additional true leptons. The $W^{\pm}Z$ component is suppressed by rejecting events with large missing transverse energy (requiring $E_{\mathrm{T}}^{\mathrm{miss}}$<25 GeV). The ZZ component and any remaining $W^{\pm}Z$ is subtracted using Monte Carlo. The Z-tag sample selection is

summarised Table 7.5

Criteria	Requirement
Trigger	Single electron and muon triggers as described in Section 6.3.
Leptons	An opposite-sign same-flavour pair of selected leptons.
	≥ 1 trigger matched.
Z-tag	$\lvert m_{\ell^+\ell^-} - m_Z \rvert < 20$ GeV
$E_{\mathrm{T}}^{\mathrm{miss}}$	$E_{\mathrm{T}}^{\mathrm{miss}}$<25 GeV

Table 7.5: Event selection requirements for the Z-tag sample used to measure the fake-factor.

The pre-leptons are then identified as either L or J (or neither), and the fake-factors are obtained by dividing the distributions of the selected-leptons by the distributions of the lepton-like-jets. In this way, fake-factors parameterised in p_{T} and in η are obtained. For a given bin of p_{T} or η, the fake-factor is given by:

$$FF = \frac{N_L^{\mathrm{data}} - N_L^{\mathrm{MC}\,WZ,ZZ}}{N_J^{\mathrm{data}} - N_J^{\mathrm{MC}\,WZ,ZZ}} \tag{7.8}$$

The fake-factor for a given p_{T} and η is applied as:

$$FF(p_{\mathrm{T}}, \eta) = \frac{FF(p_{\mathrm{T}}) \times FF(\eta)}{< FF >} \tag{7.9}$$

where $< FF >$ is the unparameterised (average) fake-factor.

The resulting distributions of p_{T} and η for the selected-lepton and lepton-like-jets for electrons are shown in Figure 7.1 for the 7 TeV analysis and in Figure 7.2 for the 8 TeV analysis. Figures 7.3 and 7.4 show the equivalent distributions for muons.

The resulting fake-factors for electrons are shown in Figure 7.5 for the 7 TeV analysis and in Figure 7.6 for the 8 TeV analysis; the fake-factors for muons are shown in Figure 7.7 for the 7 TeV analysis and in Figure 7.8 for the 8 TeV analysis. The fake-factor estimated from Monte Carlo simulation (blue triangles) is in reasonable agreement with the fake-factor measured in data (black points). For the calculation of the background, no use is made of the fake-factor estimated from Monte Carlo simulation. The unparameterised FFs, used as the numerator in Equation 7.9, are given in Table 7.6.

The large FF values for central and forward muons arise due to the fact that objects reaching the muon spectrometer are already very similar to signal muons. The assumption in Equation 7.6 that terms proportional to f^3 and f^4 are small and may be ignored is nevertheless still justified, due to the low number of N_{LJJJ}

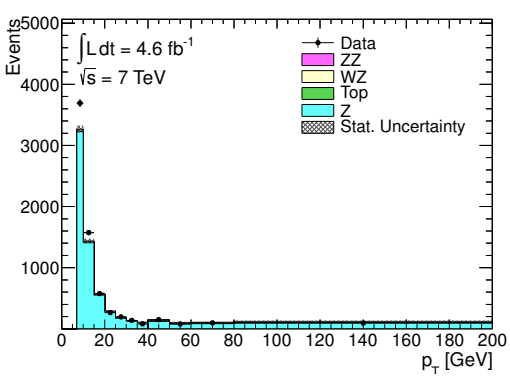

(a) Selected Central Electrons

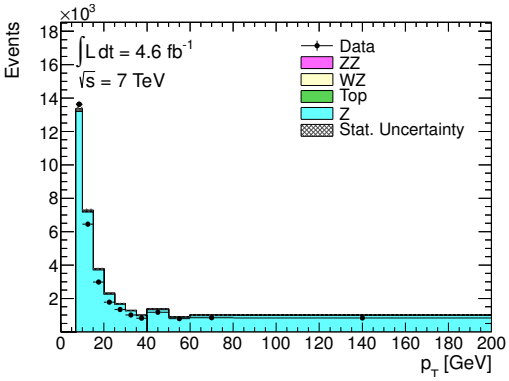

(b) Central Electron-Like-Jets

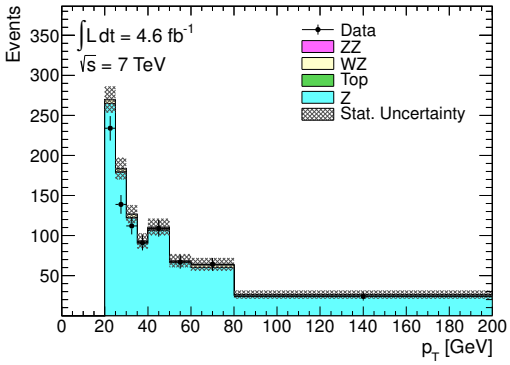

(c) Selected Forward Electrons

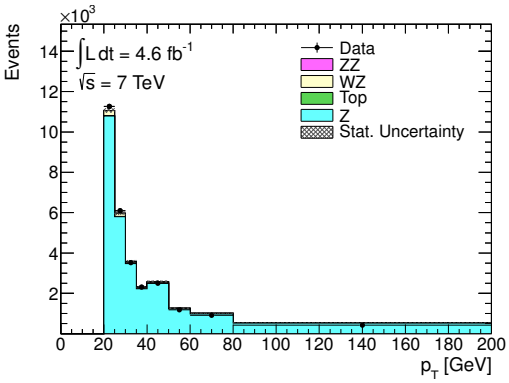

(d) Forward Electron-Like-Jets

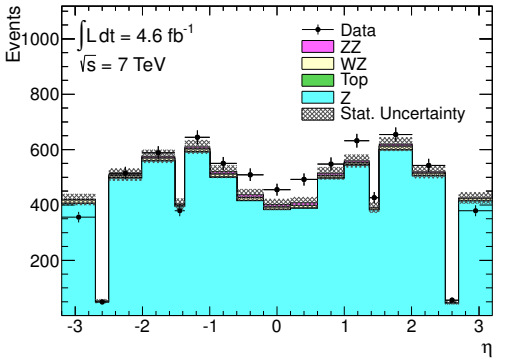

(e) Selected Electrons

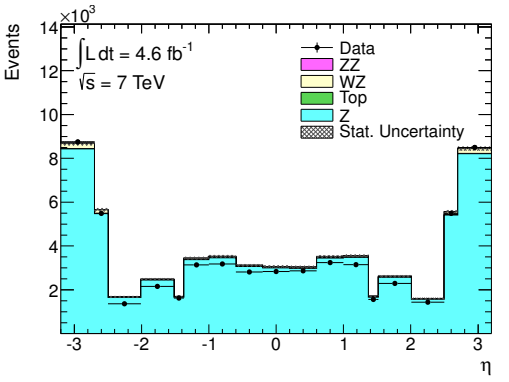

(f) Electron-Like-Jets

Figure 7.1: p_{T} and η distributions for selected electrons L and lepton-like-electrons J in the Z-tag sample for 7 TeV data. For the p_{T} distributions, central and forward electrons are shown separately; for the η distributions central and forward electrons are shown in the same plot.

and N_{JJJJ} events composed of muon-like jets. In the 8 TeV data, just one N_{JJJJ} event and no N_{LJJJ} events were observed in the $\mu^-\mu^+\mu^-\mu^+$ final state. Scaling the one N_{JJJJ} event by the average fake-factor for central muons gives an additional background contribution of 0.02 events; this is neglected.

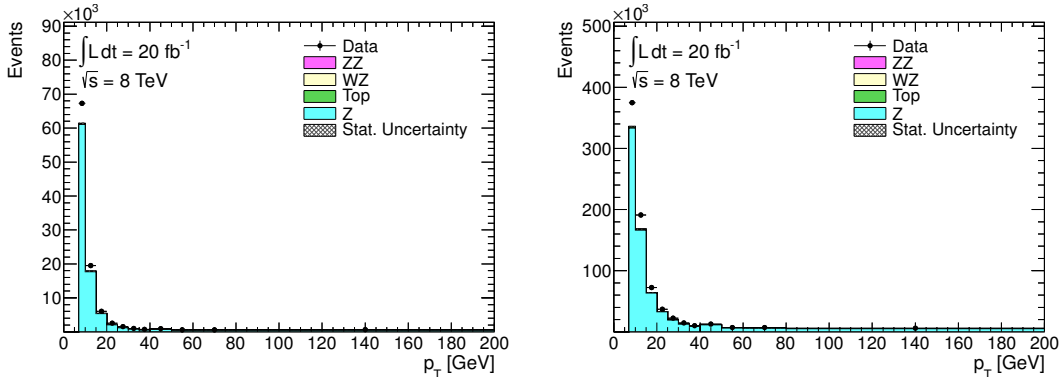

(a) Selected Central Electrons

(b) Central Electron-Like-Jets

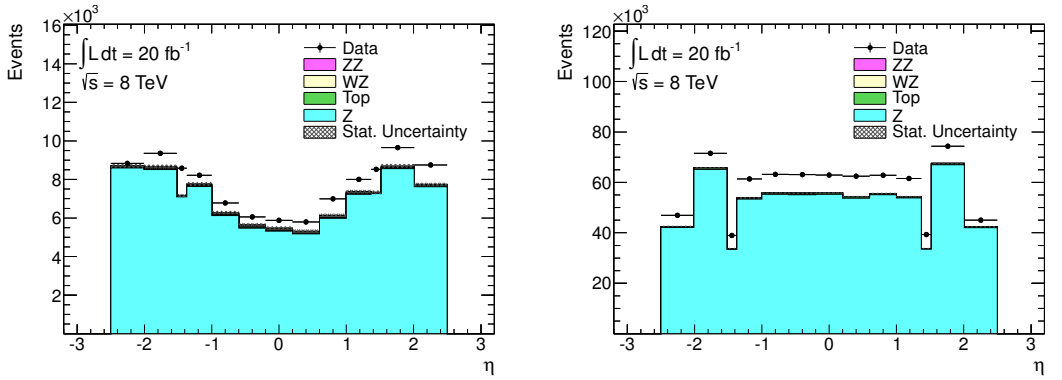

(c) Selected Central Electrons

(d) Central Electron-Like-Jets

Figure 7.2: p_{T} and η distributions for selected electrons L and lepton-like-electrons J in the Z-tag sample for 8 TeV data.

Lepton	$< FF >$ 7 TeV	$< FF >$ 8 TeV
Central Electron	0.215 ± 0.003 (stat)	0.133 ± 0.001 (stat)
Forward Electron	0.030 ± 0.001 (stat)	-
Central Muon	0.250 ± 0.010 (stat)	0.395 ± 0.005 (stat)
Forward Muon	0.782 ± 0.199 (stat)	1.212 ± 0.128 (stat)
Calorimeter-Tagged Muon	0.123 ± 0.024 (stat)	0.098 ± 0.007 (stat)

Table 7.6: Unparameterised (average) fake-factors for different lepton types.

7.2.4 Statistical and Systematic Uncertainties

The statistical error from the fake-factor measurement is propagated to the background estimate by repeating the calculation with the fake-factor shifted up and down by their one-sigma statistical uncertainties. The variation of the predicted background is then added in quadrature with the statistical uncertainty due to limited numbers of observed $LLLJ$ and $LLJJ$ events.

Systematic uncertainties are estimated by varying the criteria used to define the lepton-like-jets as follows:

- Increasing the inverted isolation requirement to >20%, >30%, and >40%. For the 7 TeV data, where both track and calorimeter isolation are used, the requirements on the two isolations are varied simultaneously.

- Increasing the inverted d_0-significance requirement to > 3.5 (8 TeV only), $> 4.0, > 4.5, > 5.0$.

The variations are designed to vary the composition of the different regions in terms of the different sources of background leptons. Stability under these variations indicates that the method is not highly sensitive to the composition of the control region relative to the composition of the signal region. The final background estimate is taken as the mean of the nominal background estimate and the estimate obtained under each of these variations. The statistical uncertainty is taken as the mean of the statistical uncertainties from each variation and the systematic is taken as the RMS spread of the estimates obtained from different variations.

7.2.5 Monte Carlo Closure Test

To demonstrate the validity of the background estimate method, a Monte Carlo closure test is performed. The entire background estimate methodology described above is applied to a Monte Carlo sample modelling the Z+X, $t\bar{t}$, single-t, $W^{\pm}Z$ and $W^{+}W^{-}$ backgrounds, to give a 'background estimate' according to the Monte Carlo. The fake-factors are derived from the Monte Carlo, and are then applied to $LLJJ$ and $LLLJ$ events from the Monte Carlo samples. The resulting 'background estimate' should then be in agreement with the number of $LLLL$ events passing the full selection in the background Monte Carlo sample.

The results of the closure test are shown in Table 7.7. The statistical uncertainties on the 8 TeV estimates are much larger, owing to the size of the available Monte Carlo samples at 8 TeV being far smaller. In all cases, the background estimate from Monte Carlo obtained using the fake-factor method is in good agreement with the number of $LLLL$ events in the Monte Carlo.

7.2.6 Results

The number of observed $LLLJ$ and $LLJJ$ events, these quantities multiplied by the fake-factor (squared in the latter case), the estimated correction due to contamination from ZZ events, and the resulting background estimate for the

	$e^-e^+e^-e^+$	$\mu^-\mu^+\mu^-\mu^+$	$e^-e^+\mu^-\mu^+$	$\ell^-\ell^+\ell^-\ell^+$
7 TeV, ZZ Selection				
N_{BG} (Fake-Factor method)	0.83 ± 0.29	0.04 ± 0.02	0.94 ± 0.36	1.81 ± 0.46
N_{LLLL}	0.69 ± 0.25	0.01 ± 0.01	0.79 ± 0.28	1.49 ± 0.37
7 TeV, ZZ^* Selection				
N_{BG}	4.22 ± 0.81	-0.01 ± 0.07	4.54 ± 0.83	8.75 ± 1.17
N_{LLLL}	3.80 ± 0.92	0.06 ± 0.05	4.41 ± 0.92	8.26 ± 1.30
8 TeV, ZZ Selection				
N_{BG}	2.40 ± 2.01	0.19 ± 0.05	2.16 ± 1.95	4.74 ± 2.80
N_{LLLL}	2.99 ± 2.58	0.04 ± 0.04	0.62 ± 0.17	3.66 ± 2.58

Table 7.7: Results of the Monte Carlo closure test for the data driven background estimate.

'nominal' J definition are shown in Table 7.8 for the 7 TeV data and in Table 7.9 for the 8 TeV data. The fake-factor is applied individually to each J, parameterised by the p_{T} and η of the J. The background estimates under each of the systematic variations described in the previous section are shown in Tables 7.10 and 7.11. The results are observed to be rather stable under the systematic variations, within the large statistical uncertainties.

In the $\mu^-\mu^+\mu^-\mu^+$ channel the number of observed $LLLJ$ and $LLJJ$ events is small, and so the final background estimate is negative due to N_{LLJJ} being larger than N_{LLLJ}. In this case, the final result is quoted as a truncated Gaussian, with mean at zero and sigma equal to the estimated uncertainty. This procedure gives a conservative upper limit for the background in that channel. The final data-driven background estimates are shown in Table 7.12.

7.2.7 Cross-Check with Same-Sign Events

An additional cross-check of the background estimate is performed by estimating the background using a data sample composed of events passing the full event selection, but with one opposite-signed di-lepton pair and one same-signed di-lepton pair (termed OS-SS). The majority of the reducible backgrounds, those due to $Z+\gamma$, Z+light-jets, $t\bar{t}$, W^+W^- and $W^\pm Z$ events will contribute to the OS-SS selection at the same rate as to the signal selection with two oppositely-signed pairs (SS-SS). The exception to this is $Z+b\bar{b}$, where leptons from heavy flavour decay will tend to be oppositely-charged in the two jets. There will be significant contamination to this control region from ZZ events where one lepton has its charged misidentified. This is estimated from Monte Carlo, and subtracted from the observed OS-SS events to give the background estimate by this method.

7 TeV, ZZ	$e^-e^+e^-e^+$	$\mu^-\mu^+\mu^-\mu^+$	$e^-e^+\mu^-\mu^+$	$\ell^-\ell^+\ell^-\ell^+$
N_{LLLJ}	23.00 ± 4.80	1.00 ± 1.00	22.00 ± 4.69	46.00 ± 6.78
(+) $N_{LLLJ} \times FF$	1.75 ± 0.49	0.19 ± 0.19	2.17 ± 0.76	4.11 ± 0.92
(−) $N_{LLLJ}^{ZZ,MC} \times FF$	0.35 ± 0.01	0.35 ± 0.02	0.72 ± 0.02	1.42 ± 0.04
N_{LLJJ}	101.00 ± 10.05	4.00 ± 2.00	87.00 ± 9.33	192.00 ± 13.86
(−) $N_{LLJJ} \times FF^2$	1.07 ± 0.19	0.42 ± 0.23	0.94 ± 0.20	2.43 ± 0.36
(+) $N_{LLJJ}^{ZZ,MC} \times FF^2$	0.00 ± 0.00	0.00 ± 0.00	0.01 ± 0.00	0.01 ± 0.00
N_{BG}	0.33 ± 0.53 $^{+0.33}_{-0.04}$	-0.58 ± 0.30 $^{+0.38}_{-0.08}$	0.52 ± 0.78 $^{+0.93}_{-0.04}$	0.27 ± 0.99 $^{+1.34}_{-0.38}$

7 TeV, ZZ^*	$e^-e^+e^-e^+$	$\mu^-\mu^+\mu^-\mu^+$	$e^-e^+\mu^-\mu^+$	$\ell^-\ell^+\ell^-\ell^+$
N_{LLLJ}	75.00 ± 8.66	4.00 ± 2.00	95.00 ± 9.75	174.00 ± 13.19
(+) $N_{LLLJ} \times FF$	9.87 ± 1.42	0.86 ± 0.44	16.31 ± 2.72	27.04 ± 3.10
(−) $N_{LLLJ}^{ZZ,MC} \times FF$	0.63 ± 0.01	0.64 ± 0.03	1.16 ± 0.03	2.43 ± 0.04
N_{LLJJ}	297.00 ± 17.23	15.00 ± 3.87	240.00 ± 15.49	552.00 ± 23.49
(−) $N_{LLJJ} \times FF^2$	5.84 ± 0.53	1.43 ± 0.46	5.71 ± 0.58	12.98 ± 0.91
(+) $N_{LLJJ}^{ZZ,MC} \times FF^2$	0.01 ± 0.00	0.01 ± 0.00	0.02 ± 0.00	0.04 ± 0.00
N_{BG}	3.42 ± 1.52 $^{+0.47}_{-0.13}$	-1.21 ± 0.64 $^{+0.89}_{-0.24}$	9.47 ± 2.78 $^{+3.42}_{-1.96}$	11.67 ± 3.23 $^{+3.65}_{-0.94}$

Table 7.8: Details of the background estimate for 4.6 fb^{-1} of 7 TeV data. The top table shows the background estimate for the ZZ selection and the bottom for the ZZ^* selection. In each table, first row shows the number of observed $LLLJ$ events. The second row shows this quantity scaled by the fake-factor (applied on an event by event basis), and the third row the MC estimated number of ZZ events identified as $LLJJ$, scaled by the fake-factor. The fourth and fifth rows show the number of observed $LLJJ$ events, and the number of $LLJJ$ events scaled by the fake-factor, and the sixth row the estimated number of ZZ events identified as $LLLJ$, scaled by the fake-factor. The resulting background estimate is shown in the last row, and is the sum of the rows indicated with '(+)', minus the sum of the rows indicated with '(−)'. The first error is due to statistical uncertainty on the number of observed $LLLJ$ and $LLJJ$ events, while the second error is due to statistical uncertainty on the fake-factor.

8 TeV, ZZ	$e^-e^+e^-e^+$	$\mu^-\mu^+\mu^-\mu^+$	$e^-e^+\mu^-\mu^+$	$\ell^-\ell^+\ell^-\ell^+$
N_{LLLJ}	166.00 ± 12.88	9.00 ± 3.00	114.00 ± 10.68	289.00 ± 17.00
(+) $N_{LLLJ} \times FF$	17.71 ± 1.60	5.60 ± 2.30	17.52 ± 2.95	40.83 ± 4.07
(−) $N_{LLLJ}^{ZZ,MC} \times FF$	0.80 ± 0.02	1.90 ± 0.07	3.09 ± 0.12	5.79 ± 0.15
N_{LLJJ}	661.00 ± 25.71	11.00 ± 3.32	443.00 ± 21.05	1115.00 ± 33.39
(−) $N_{LLJJ} \times FF^2$	7.05 ± 0.36	1.58 ± 0.54	5.77 ± 0.53	14.39 ± 0.84
(+) $N_{LLJJ}^{ZZ,MC} \times FF^2$	0.01 ± 0.00	0.02 ± 0.01	0.02 ± 0.00	0.05 ± 0.01
N_{BG}	$9.88 \pm 1.64\ ^{+0.86}_{-0.05}$	$2.14 \pm 2.37\ ^{+2.79}_{-0.49}$	$8.68 \pm 3.00\ ^{+4.83}_{-1.18}$	$20.70 \pm 4.16\ ^{+8.48}_{-1.72}$

Table 7.9: Details of the background estimate for 20 fb^{-1} of 8 TeV data. The first row shows the number of observed $LLLJ$ events. The second row shows this quantity scaled by the fake-factor (applied on an event by event basis), and the third row the MC estimated number of ZZ events identified as $LLJJ$, scaled by the fake-factor. The fourth and fifth rows show the number of observed $LLJJ$ events, and the number of $LLJJ$ events scaled by the fake-factor, and the sixth row the estimated number of ZZ events identified as $LLLJ$, scaled by the fake-factor. The resulting background estimate is shown in the last row, and is the sum of the rows indicated with '(+)', minus the sum of the rows indicated with '(−)'. The first error is due to statistical uncertainty on the number of observed $LLLJ$ and $LLJJ$ events, while the second error is due to statistical uncertainty on the fake-factor.

7 TeV, ZZ	$e^-e^+e^-e^+$	$\mu^-\mu^+\mu^-\mu^+$	$e^-e^+\mu^-\mu^+$	$\ell^-\ell^+\ell^-\ell^+$
Nominal$J$	$0.33 \pm 0.53\ ^{+0.33}_{-0.04}$	$-0.63 \pm 0.32\ ^{+0.52}_{-0.50}$	$0.51 \pm 0.77\ ^{+0.90}_{-0.02}$	$0.20 \pm 0.99\ ^{+0.73}_{-0.54}$
$\lvert d_0/\sigma(d_0)\rvert > 0.40$	$0.33 \pm 0.53\ ^{+0.33}_{-0.04}$	$-0.68 \pm 0.36\ ^{+0.58}_{-0.68}$	$0.63 \pm 0.76\ ^{+0.94}_{-0.09}$	$0.27 \pm 1.00\ ^{+0.59}_{-0.53}$
$\lvert d_0/\sigma(d_0)\rvert > 0.45$	$0.33 \pm 0.53\ ^{+0.33}_{-0.04}$	$-0.67 \pm 0.36\ ^{+0.57}_{-0.68}$	$0.65 \pm 0.76\ ^{+0.92}_{-0.10}$	$0.31 \pm 1.00\ ^{+0.57}_{-0.51}$
$\lvert d_0/\sigma(d_0)\rvert > 0.50$	$0.33 \pm 0.53\ ^{+0.33}_{-0.04}$	$-0.41 \pm 0.27\ ^{+0.32}_{-0.11}$	$0.66 \pm 0.76\ ^{+0.91}_{-0.11}$	$0.58 \pm 0.97\ ^{+1.13}_{-0.25}$
Isolation>0.2	$0.35 \pm 0.54\ ^{+0.32}_{-0.03}$	$-0.69 \pm 0.37\ ^{+0.60}_{-0.74}$	$0.48 \pm 0.75\ ^{+0.89}_{-0.04}$	$0.14 \pm 1.00\ ^{+0.60}_{-0.47}$
Isolation>0.3	$0.37 \pm 0.55\ ^{+0.32}_{-0.03}$	$-0.72 \pm 0.42\ ^{+0.47}_{-0.42}$	$0.62 \pm 0.79\ ^{+0.89}_{-0.09}$	$0.27 \pm 1.01\ ^{+0.79}_{-0.41}$
Isolation>0.4	$0.39 \pm 0.57\ ^{+0.31}_{-0.04}$	$-0.99 \pm 0.60\ ^{+0.73}_{-0.97}$	$0.75 \pm 0.88\ ^{+0.95}_{-0.13}$	$0.16 \pm 1.16\ ^{+0.63}_{-0.29}$
Isolation>0.5	$0.19 \pm 0.56\ ^{+0.29}_{-0.05}$	$-0.82 \pm 0.61\ ^{+0.67}_{-1.01}$	$-0.09 \pm 0.60\ ^{+0.57}_{-0.23}$	$-0.72 \pm 0.97\ ^{+0.95}_{-0.15}$

7 TeV, ZZ^*	$e^-e^+e^-e^+$	$\mu^-\mu^+\mu^-\mu^+$	$e^-e^+\mu^-\mu^+$	$\ell^-\ell^+\ell^-\ell^+$
Nominal$J$	$3.42 \pm 1.52\ ^{+0.47}_{-0.13}$	$-1.27 \pm 0.63\ ^{+1.02}_{-0.79}$	$8.10 \pm 2.13\ ^{+1.80}_{-0.55}$	$10.25 \pm 2.68\ ^{+1.48}_{-0.60}$
$\lvert d_0/\sigma(d_0)\rvert > 0.40$	$3.42 \pm 1.52\ ^{+0.47}_{-0.13}$	$-1.03 \pm 0.58\ ^{+0.90}_{-0.75}$	$8.32 \pm 2.13\ ^{+1.90}_{-0.67}$	$10.70 \pm 2.67\ ^{+1.62}_{-0.36}$
$\lvert d_0/\sigma(d_0)\rvert > 0.45$	$3.42 \pm 1.52\ ^{+0.47}_{-0.13}$	$-1.24 \pm 0.53\ ^{+0.95}_{-0.83}$	$8.39 \pm 2.13\ ^{+1.90}_{-0.70}$	$10.57 \pm 2.67\ ^{+1.54}_{-0.38}$
$\lvert d_0/\sigma(d_0)\rvert > 0.50$	$3.42 \pm 1.52\ ^{+0.47}_{-0.13}$	$-0.92 \pm 0.47\ ^{+0.67}_{-0.23}$	$8.41 \pm 2.13\ ^{+1.88}_{-0.71}$	$10.90 \pm 2.66\ ^{+2.12}_{-0.10}$
Isolation>0.2	$3.17 \pm 1.52\ ^{+0.43}_{-0.16}$	$-1.32 \pm 0.68\ ^{+1.11}_{-1.10}$	$7.82 \pm 2.16\ ^{+1.86}_{-0.64}$	$9.67 \pm 2.73\ ^{+1.19}_{-0.63}$
Isolation>0.3	$3.28 \pm 1.54\ ^{+0.44}_{-0.15}$	$-1.55 \pm 0.66\ ^{+1.01}_{-0.81}$	$8.16 \pm 2.26\ ^{+1.90}_{-0.74}$	$9.89 \pm 2.82\ ^{+1.53}_{-0.41}$
Isolation>0.4	$3.78 \pm 1.60\ ^{+0.47}_{-0.10}$	$-1.77 \pm 0.85\ ^{+1.25}_{-1.31}$	$9.01 \pm 2.58\ ^{+2.37}_{-1.18}$	$11.02 \pm 3.15\ ^{+1.54}_{-0.17}$
Isolation>0.5	$3.69 \pm 1.64\ ^{+0.45}_{-0.11}$	$-1.56 \pm 0.96\ ^{+1.19}_{-1.36}$	$6.96 \pm 2.23\ ^{+1.09}_{-0.12}$	$9.08 \pm 2.93\ ^{+1.42}_{-0.18}$

Table 7.10: Comparison of background estimates for the 7 TeV analysis, using different criteria to define the lepton-like-jets J. The first column indicates the variation made to J from the nominal definition given in Table 7.4. The top table shows estimates for the ZZ selection, the bottom for the ZZ^*.

8 TeV, ZZ	$e^-e^+e^-e^+$	$\mu^-\mu^+\mu^-\mu^+$	$e^-e^+\mu^-\mu^+$	$\ell^-\ell^+\ell^-\ell^+$
Nominal J	$9.01 \pm 1.56\ ^{+0.85}_{-0.05}$	$1.98 \pm 2.32\ ^{+2.82}_{-0.49}$	$8.35 \pm 2.99\ ^{+4.84}_{-1.18}$	$19.34 \pm 4.10\ ^{+8.51}_{-1.72}$
$\lvert d_0/\sigma(d_0)\rvert > 0.35$	$9.01 \pm 1.56\ ^{+0.85}_{-0.05}$	$0.70 \pm 1.81\ ^{+1.93}_{-0.07}$	$5.31 \pm 2.17\ ^{+3.11}_{-0.20}$	$15.02 \pm 3.23\ ^{+5.89}_{-0.32}$
$\lvert d_0/\sigma(d_0)\rvert > 0.40$	$9.01 \pm 1.56\ ^{+0.85}_{-0.05}$	$0.83 \pm 1.84\ ^{+1.83}_{-0.09}$	$3.55 \pm 1.55\ ^{+2.06}_{-0.37}$	$13.39 \pm 2.87\ ^{+4.74}_{-0.24}$
$\lvert d_0/\sigma(d_0)\rvert > 0.45$	$9.01 \pm 1.56\ ^{+0.85}_{-0.05}$	$0.93 \pm 1.88\ ^{+1.77}_{-0.12}$	$3.64 \pm 1.56\ ^{+1.98}_{-0.35}$	$13.58 \pm 2.90\ ^{+4.60}_{-0.18}$
$\lvert d_0/\sigma(d_0)\rvert > 0.50$	$9.01 \pm 1.56\ ^{+0.85}_{-0.05}$	$1.06 \pm 1.98\ ^{+1.78}_{-0.16}$	$3.37 \pm 1.53\ ^{+1.88}_{-0.37}$	$13.44 \pm 2.96\ ^{+4.52}_{-0.17}$
Isolation>0.2	$9.29 \pm 1.58\ ^{+0.83}_{-0.06}$	$2.36 \pm 2.44\ ^{+2.58}_{-0.58}$	$8.20 \pm 3.00\ ^{+4.67}_{-1.23}$	$19.85 \pm 4.18\ ^{+8.07}_{-1.87}$
Isolation>0.3	$9.40 \pm 1.61\ ^{+0.80}_{-0.06}$	$2.23 \pm 2.59\ ^{+2.24}_{-0.56}$	$8.21 \pm 3.04\ ^{+4.45}_{-1.28}$	$19.84 \pm 4.31\ ^{+7.49}_{-1.90}$
Isolation>0.4	$9.69 \pm 1.64\ ^{+0.80}_{-0.07}$	$2.74 \pm 3.12\ ^{+2.49}_{-0.76}$	$9.12 \pm 3.56\ ^{+4.89}_{-1.64}$	$21.55 \pm 5.01\ ^{+8.18}_{-2.47}$
Isolation>0.5	$9.89 \pm 1.64\ ^{+0.80}_{-0.07}$	$0.71 \pm 2.53\ ^{+1.93}_{-0.04}$	$10.03 \pm 4.09\ ^{+5.51}_{-1.96}$	$20.63 \pm 5.08\ ^{+8.25}_{-2.08}$

Table 7.11: Comparison of background estimates for the 8 TeV analysis, using different criteria to define the lepton-like-jets J. The first column indicates the variation made to J from the nominal definition given in Table 7.4.

	4e	4mu	2e2mu	4l
ZZ, 7 TeV	$0.33\ ^{+0.63}_{-0.54} \pm 0.06$	$< 0.71\ [^{+0.69}_{-0.00}\ ^{+0.15}_{-0.00}]$	$0.53\ ^{+1.16}_{-0.77} \pm 0.25$	$0.15\ ^{+1.26}_{-1.08} \pm 0.35$
ZZ^*, 8 TeV	$3.45\ ^{+1.61}_{-1.55} \pm 0.19$	$< 1.25\ [^{+1.21}_{-0.00}\ ^{+0.27}_{-0.00}]$	$8.15\ ^{+2.88}_{-2.31} \pm 0.55$	$10.26\ ^{+3.19}_{-2.81} \pm 0.63$
ZZ, 8 TeV	$9.26\ ^{+1.79}_{-1.59} \pm 0.32$	$1.50\ ^{+3.14}_{-1.50} \pm 0.77$	$6.64\ ^{+4.54}_{-2.78} \pm 2.51$	$17.41\ ^{+7.72}_{-4.04} \pm 3.25$

Table 7.12: Final data-driven fake background estimates. The first error is statistical, the second is systematic.

	$e^-e^+e^-e^+$	$\mu^-\mu^+\mu^-\mu^+$	$e^-e^+\mu^-\mu^+$	$\ell^-\ell^+\ell^-\ell^+$
Observed OS-SS Events	8	0	16	24
Expected ZZ OS-SS	2.65 ± 0.10	0.03 ± 0.01	3.19 ± 0.16	5.95 ± 0.19
Bkg. Estimate (OS-SS)	5.35 ± 2.83	< 1.27	12.81 ± 4.00	18.05 ± 2.83
Bkg. Estimate (fake-factor)	$9.3^{+1.8}_{-1.6} \pm 0.3$	$1.5^{+3.1}_{-1.5} \pm 0.8$	$6.6^{+4.5}_{-2.8} \pm 2.5$	$17.4^{+7.7}_{-4.0} \pm 3.3$

Table 7.13: Background estimate cross-check to the 8 TeV ZZ analysis using same-sign events.

The number of observed events passing the OS-SS selection, the estimated ZZ contamination and the resulting background estimate are shown in Table 7.13 for the 8 TeV analysis (this cross-check was not performed for the 7 TeV data). The results are in good agreement with the fake-factor method.

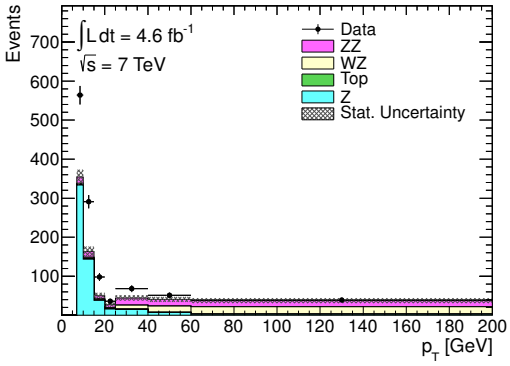

(a) Selected Central Muons

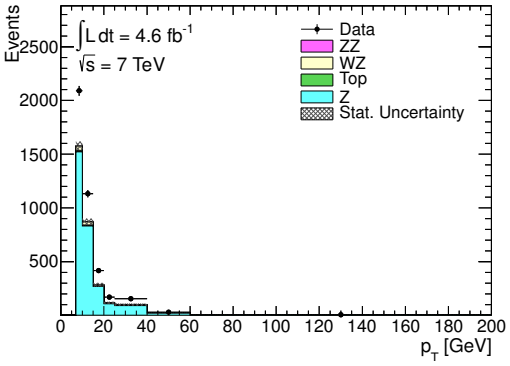

(b) Central Muon-Like-Jets

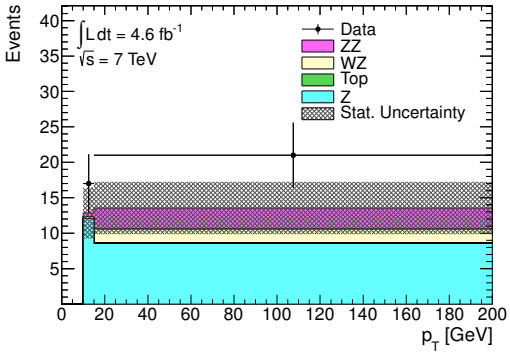

(c) Selected Forward Muons

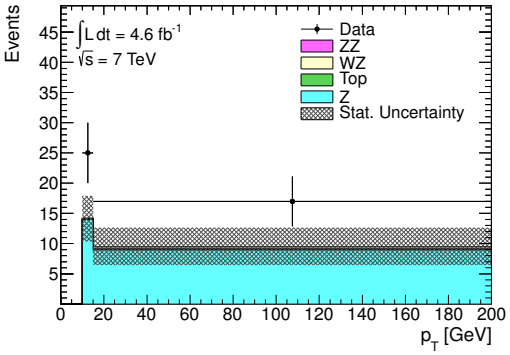

(d) Forward Muon-Like-Jets

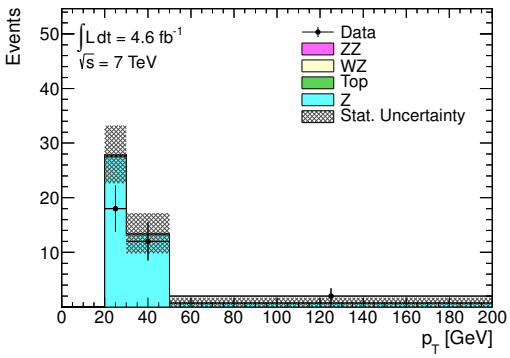

(e) Selected Calorimeter-Tagged Muons

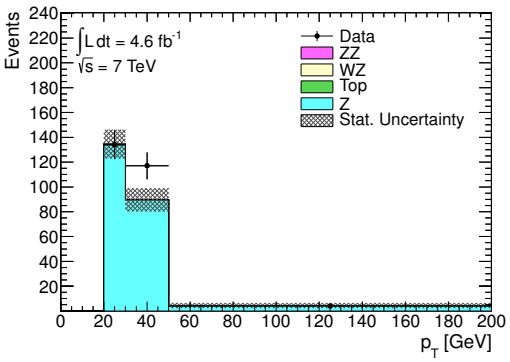

(f) Calorimeter-Tagged Muon-Like-Jets

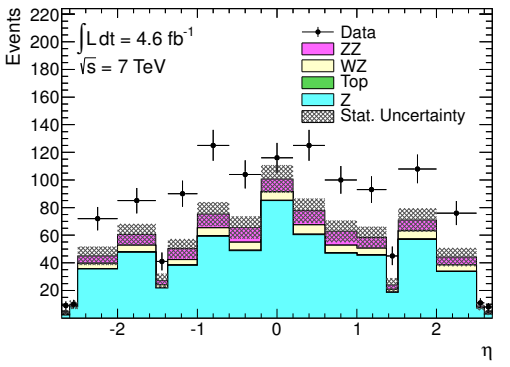

(g) Selected Muons

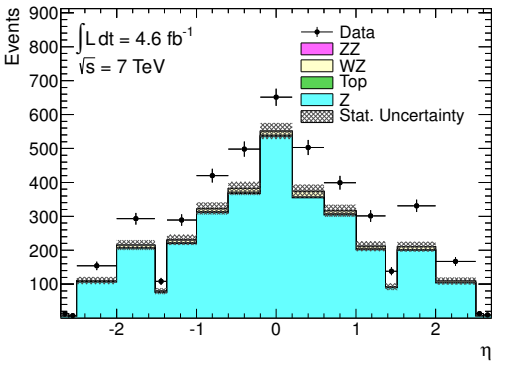

(h) Muon-Like-Jets

Figure 7.3: p_{T} and η distributions for selected muons L and lepton-like-muons J in the Z-tag sample for 7 TeV data. For the p_{T} distributions, central, forward and calorimeter-tagged muons are shown separately; for the η distributions all muons are shown in the same plot.

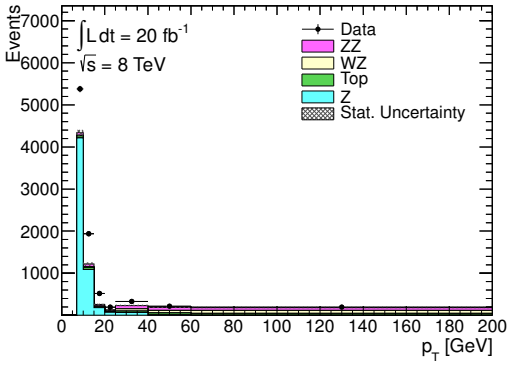

(a) Selected Central Muons

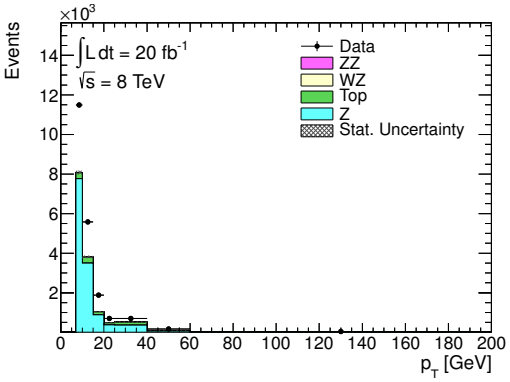

(b) Central Muon-Like-Jets

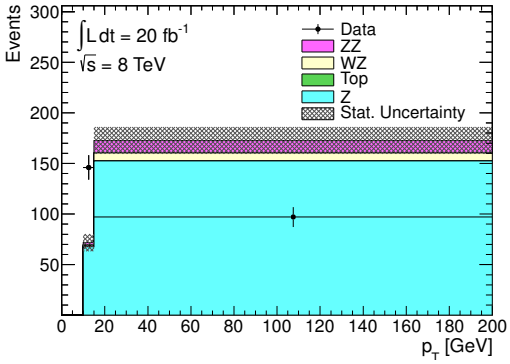

(c) Selected Forward Muons

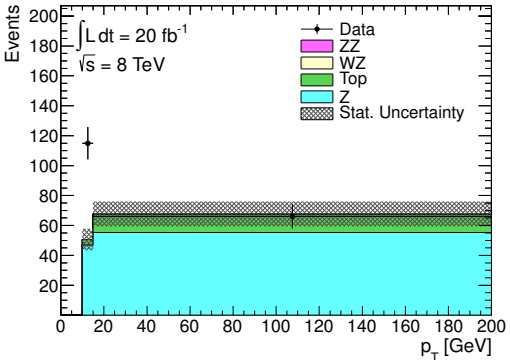

(d) Forward Muon-Like-Jets

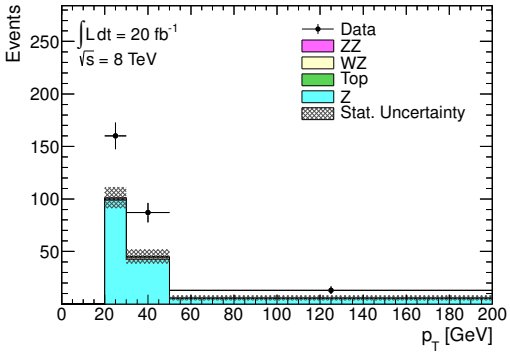

(e) Selected Calorimeter-Tagged Muons

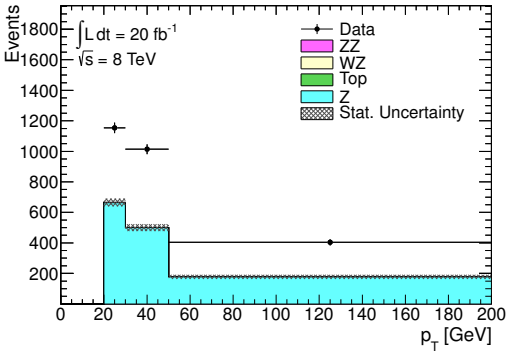

(f) Calorimeter-Tagged Muon-Like-Jets

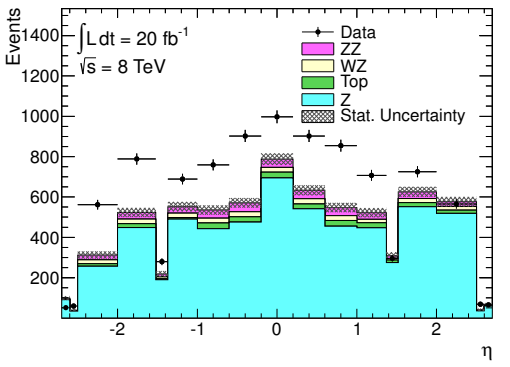

(g) Selected Muons

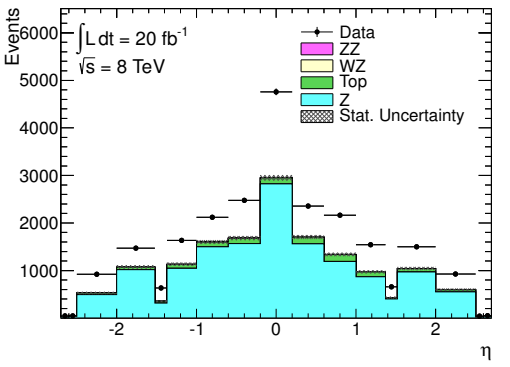

(h) Muon-Like-Jets

Figure 7.4: p_{T} and η distributions for selected muons L and lepton-like-muons J in the Z-tag sample for 8 TeV data. For the p_{T} distributions, central, forward and calorimeter-tagged muons are shown separately; for the η distributions all muons are shown in the same plot.

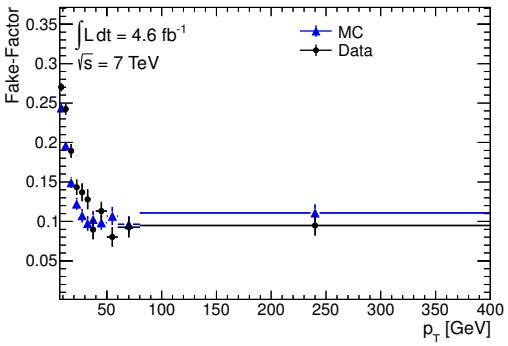

(a) Central Electrons

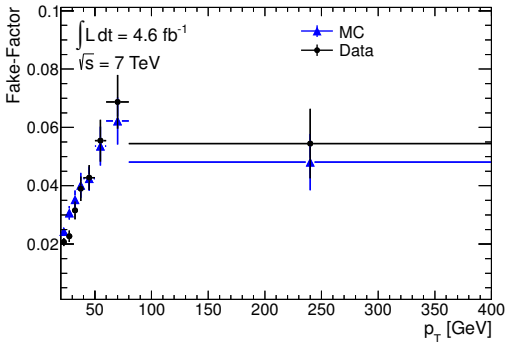

(b) Forward Electrons

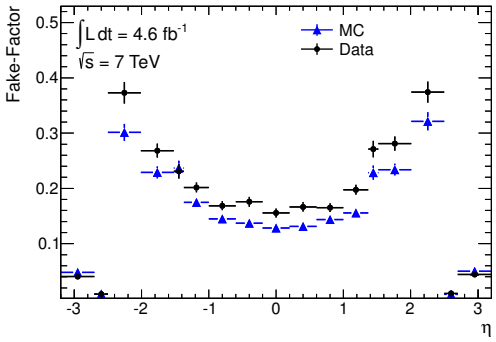

(c) All Electrons

Figure 7.5: Electron Fake-Factors as a function of p_{T} and η for 7 TeV data. For the distributions as a function of p_{T} central and forward electrons are shown separately; for the η distributions the fake-factor for central and forward electrons are shown in the same plot. The black points show the fake-factor measured in data; the blue triangles show the value estimated by Monte Carlo simulation.

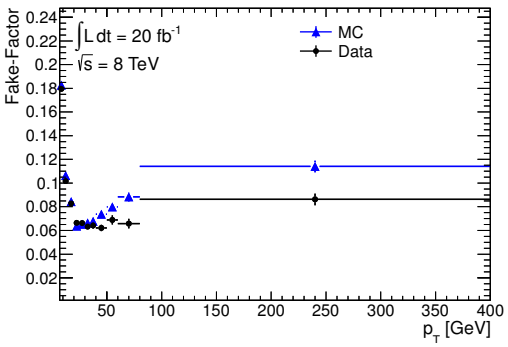

(a) Central Electrons

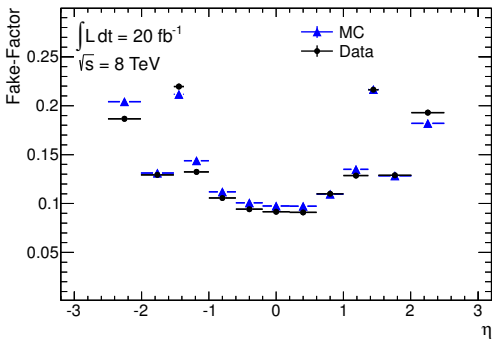

(b) Central Electrons

Figure 7.6: Electron Fake-Factors as a function of p_{T} and η for 8 TeV data. The black points show the fake-factor measured in data; the blue triangles show the value estimated by Monte Carlo simulation.

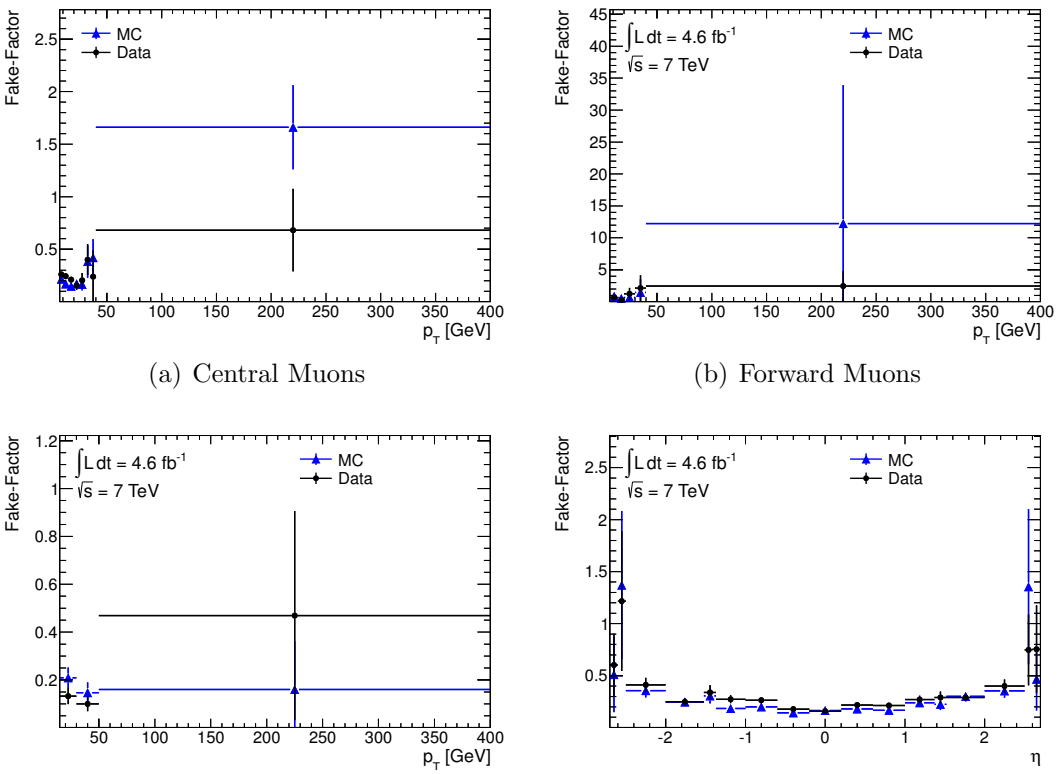

(a) Central Muons

(b) Forward Muons

(c) Calorimeter-Tagged Muons

(d) All Muons

Figure 7.7: Muon Fake-Factors as a function of p_{T} and η for 7 TeV data. For the distributions as a function of p_{T} central, forward and calorimeter-tagged muons are shown separately; for the η distributions the fake-factor all muons are shown in the same plot.The black points show the fake-factor measured in data; the blue triangles show the value estimated by Monte Carlo.

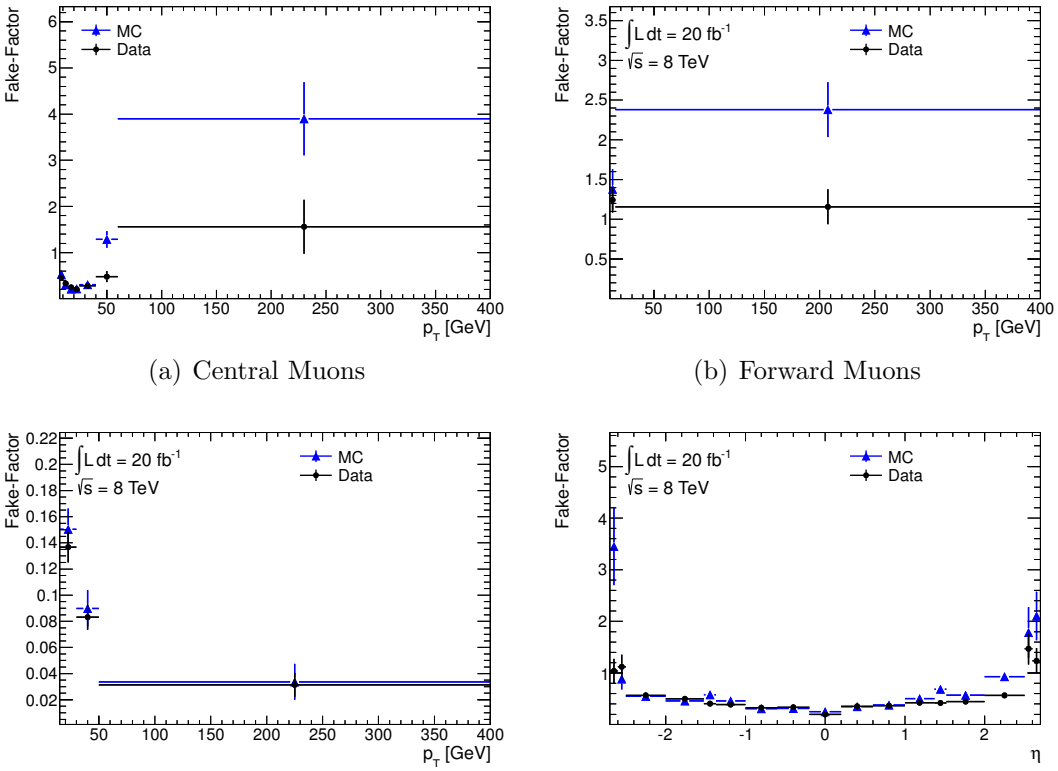

(a) Central Muons

(b) Forward Muons

(c) Calorimeter-Tagged Muons

(d) All Muons

Figure 7.8: Muon Fake-Factors as a function of p_{T} and η for 8 TeV data. For the distributions as a function of p_{T} central, forward and calorimeter-tagged muons are shown separately; for the η distributions the fake-factor all muons are shown in the same plot.The black points show the fake-factor measured in data; the blue triangles show the value estimated by Monte Carlo.

7.3 Background Shape

Due to the lack of statistics in the background Monte Carlo samples it is not possible to obtain a background shape using the full event selection. In the 7 TeV data, there are also not enough statistics in the data control regions to obtain a background shape. For the 7 TeV analysis, the background shape is therefore taken from Monte Carlo with a loosened selection. For the background shape, events are required to have an opposite-sign pair of leptons passing all of the selection requirements. The second pair is not required to be opposite-signed, and the lepton isolation and d_0-significance requirements are not applied. Apart from this, the full event selection, including mass cuts, is applied. Applying this selection, sufficient statistics are obtained from Monte Carlo to give reasonable shapes in distributions of interest (e.g. Z boson mass and p_{T}, four-lepton mass, four-lepton p_{T}).

To account for the different efficiencies in the loosened selection criteria in events with a "loose" electron pair and a "loose" muon pair, events of each type are scaled by the ratio of the number of events which pass the nominal selection to the number of events which pass the loosened selection. The "loose" electron pair efficiency was measured to be 0.051 while the "loose" muon pair efficiency was measured to be 0.012. This scaling is used to account for any difference in shape between events with a "loose" electron pair and a "loose" muon pair. The distributions thus obtained are then normalised to the data-driven background estimates shown in Table 7.14.

For the 8 TeV analysis, the background shape is taken from data, using $LLJJ$ events but treating the lepton-like jets are treated as fully selected leptons. The events are weighted by the fake factors for the lepton-like jets, and the overall normalisation of the distribution is scaled to the data-drive background estimate as shown in Table 7.14.

7.4 Final Background Estimate

The final background estimate is given in Table 7.14.

	$e^-e^+e^-e^+$	$\mu^-\mu^+\mu^-\mu^+$	$e^-e^+\mu^-\mu^+$	$\ell^-\ell^+\ell^-\ell^+$
ZZ, 7 TeV				
Reducible (D.D)	$0.3^{+0.6}_{-0.5} \pm 0.1$	< 0.7	$0.5^{+1.2}_{-0.8} \pm 0.3$	$0.2^{+1.3}_{-1.1} \pm 0.4$
Irreducible (MC)	$0.1 \pm 0.1 \pm 0.1$	$0.1 \pm 0.1 \pm 0.1$	$0.2 \pm 0.1 \pm 0.1$	$0.4 \pm 0.1 \pm 0.1$
Total	$0.4\ ^{+0.6}_{-0.5} \pm 0.1$	$0.1\ ^{+0.7}_{-0.8} \pm 0.2$	$0.7\ ^{+1.2}_{-0.8} \pm 0.3$	$0.6\ ^{+1.3}_{-1.1} \pm 0.4$
ZZ^*, 7 TeV				
Reducible (D.D)	$3.5^{+1.6}_{-1.6} \pm 0.2$	< 1.3	$8.2^{+2.9}_{-2.3} \pm 0.6$	$10.3^{+3.2}_{-2.8} \pm 0.6$
Irreducible (MC)	$0.3 \pm 0.1 \pm 0.1$	$0.3 \pm 0.1 \pm 0.1$	$0.6 \pm 0.1 \pm 0.1$	$1.2 \pm 0.1 \pm 0.1$
Total	$3.7\ ^{+1.6}_{-1.6} \pm 0.2$	$0.3\ ^{+1.2}_{-1.1} \pm 0.3$	$8.7\ ^{+2.9}_{-2.3} \pm 0.6$	$11.4\ ^{+3.2}_{-2.8} \pm 0.6$
ZZ, 8 TeV				
Reducible (D.D)	$9.3^{+1.8}_{-1.6} \pm 0.3$	$1.5^{+3.1}_{-1.5} \pm 0.8$	$6.6^{+4.5}_{-2.8} \pm 2.5$	$17.4^{+7.7}_{-4.0} \pm 3.3$
Irreducible (MC)	$0.4 \pm 0.1 \pm 0.1$	$0.5 \pm 0.1 \pm 0.1$	$0.7 \pm 0.1 \pm 0.1$	$1.6 \pm 0.1 \pm 0.1$
Total	$9.7\ ^{+1.8}_{-1.6} \pm 0.3$	$2.0\ ^{+3.1}_{-2.0} \pm 0.8$	$7.3\ ^{+4.5}_{-2.8} \pm 2.5$	$19.0\ ^{+7.7}_{-4.0} \pm 3.3$

Table 7.14: Final background estimates. The irreducible background estimate is taken from Monte Carlo, whilst the reducible background is estimated using the data driven (D.D.) technique described in this chapter.

Chapter 8

Observed Events and Cross Section Measurement

8.1 Observed Events

The expected and observed event yields after applying the ZZ and ZZ^* selections are shown in Table 8.1 for the 7 TeV analysis and in Table 8.2 for the 8 TeV analysis. A total of 66 events are observed in 4.6 fb^{-1} of 7 TeV data for the ZZ selection, and a total of 84 events for the ZZ^* selection. In the 8 TeV data, which corresponds to an integrated luminosity of 20 fb^{-1}, 305 events are observed for the ZZ selection.

7 TeV, ZZ	$e^-e^+e^-e^+$	$\mu^-\mu^+\mu^-\mu^+$	$e^-e^+\mu^-\mu^+$	$\ell^-\ell^+\ell^-\ell^+$
Observed	16	23	27	66
Exp. Signal	$10.8 \pm 0.2 \pm 1.0$	$17.5 \pm 0.2 \pm 1.0$	$27.1 \pm 0.2 \pm 1.7$	$55.4 \pm 0.3 \pm 3.4$
Exp. Bg.	$0.4\ ^{+0.6}_{-0.5} \pm 0.1$	$0.1\ ^{+0.7}_{-0.8} \pm 0.2$	$0.7\ ^{+1.2}_{-0.8} \pm 0.3$	$0.6\ ^{+1.3}_{-1.1} \pm 0.4$

7 TeV, ZZ^*	$e^-e^+e^-e^+$	$\mu^-\mu^+\mu^-\mu^+$	$e^-e^+\mu^-\mu^+$	$\ell^-\ell^+\ell^-\ell^+$
Observed	21	30	33	84
Exp. Signal	$13.1 \pm 0.2 \pm 1.3$	$22.0 \pm 0.3 \pm 1.4$	$32.6 \pm 0.3 \pm 2.3$	$67.7 \pm 0.4 \pm 4.5$
Exp. Bg.	$3.7\ ^{+1.6}_{-1.6} \pm 0.2$	$0.3\ ^{+1.2}_{-1.1} \pm 0.3$	$8.7\ ^{+2.9}_{-2.3} \pm 0.6$	$11.4\ ^{+3.2}_{-2.8} \pm 0.6$

Table 8.1: Number of observed events passing the ZZ (top table) and ZZ^* (bottom table) selections in 4.6 fb^{-1} of 7 TeV data, as well as the expected number of signal events (Exp. Signal) and the expected background (Exp. Bg.). The expected background is the sum of the data driven estimate for the reducible background and the Monte Carlo estimate for the irreducible background. The first uncertainty is statistical, while the second is systematic; uncertainties on the integrated luminosity (3.9%) are not included.

8 TeV, ZZ	$e^-e^+e^-e^+$	$\mu^-\mu^+\mu^-\mu^+$	$e^-e^+\mu^-\mu^+$	$\ell^-\ell^+\ell^-\ell^+$
Observed	62	85	158	305
Exp. Signal	$59.5 \pm 0.5 \pm 5.0$	$90.2 \pm 0.6 \pm 5.3$	$142.7 \pm 1.0 \pm 9.1$	$292.5 \pm 1.3 \pm 18.4$
Exp. Bg.	$9.7\ ^{+1.8}_{-1.6} \pm 0.3$	$2.0\ ^{+3.1}_{-2.0} \pm 0.8$	$7.3\ ^{+4.5}_{-2.8} \pm 2.5$	$19.0\ ^{+7.7}_{-4.0} \pm 3.3$

Table 8.2: Number of observed events passing the $ZZ \to \ell^-\ell^+\ell^-\ell^+$ (top table) and $ZZ^* \to \ell^-\ell^+\ell^-\ell^+$ (bottom table) selections in 20 fb^{-1} of 8 TeV data, as well as the expected number of signal events (Exp. Signal) and the expected background (Exp. Bg.). The expected background is the sum of the data driven estimate for the reducible background and the Monte Carlo estimate for the irreducible background. The first uncertainty is statistical, while the second is systematic; uncertainties on the integrated luminosity (2.8%) are not included.

8.2 Kinematic Distributions

Figures 8.1 and 8.2 show the mass of the subleading lepton pair versus the mass of the leading lepton pair for the 7 TeV and 8 TeV analyses respectively (ordered in p_{T}; see Section 6.5.1). In both cases the solid red box represents the region defined by the mass requirements of the ZZ selection and the dashed blue box the region defined by those of the ZZ^* selection. The events are seen to cluster in the regions where both masses are near m_Z, in agreement with the Monte Carlo prediction for the signal (shown as pink boxes, with the size of the box proportional to the number of expected events).

Figure 8.3 shows the correlation between the transverse momentum of the lepton pairs and the opening-angle between the leptons forming the pair in the 7 TeV data. It is observed that for higher transverse momentum di-lepton pairs the opening-angle tends to be smaller, in good agreement with the Monte Carlo predictions.

Figures 8.4 and 8.5 show the di-lepton invariant mass distributions for the leading and subleading lepton pair for the 7 TeV and 8 TeV analyses. Figure 8.6 shows the transverse momentum p_{T}^{ZZ} and invariant mass m^{ZZ} of the four-lepton system, the transverse momentum of the leading di-lepton pair p_{T}^{Z1}, and the transverse momentum of the subleading di-lepton pair p_{T}^{Z2}, for events passing the ZZ selection in the 7 TeV data; Figure 8.7 shows equivalent figure for the 8 TeV data. Figure 8.8 shows the corresponding distributions for events passing the ZZ^* selection in the 7 TeV data. In each case, the prediction from Monte Carlo for the ZZ signal is shown as a pink histogram and the prediction for the background is shown as a light blue histogram. The shapes of the distributions observed in data are consistent with the predictions.

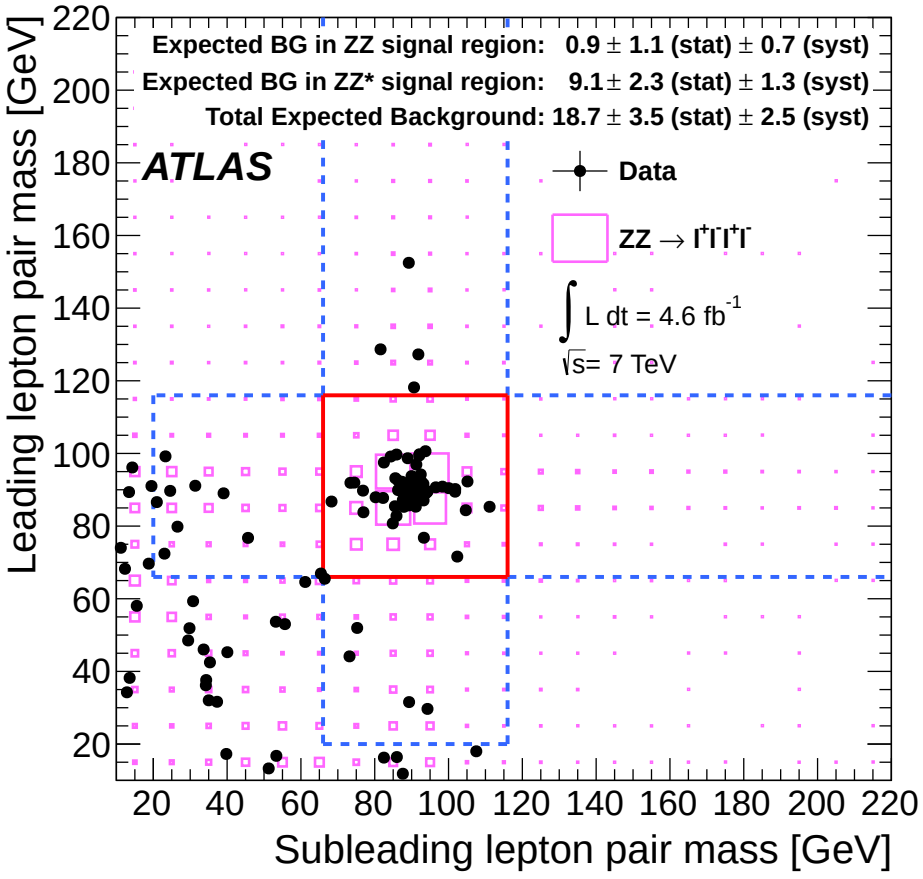

Figure 8.1: Mass of the leading lepton pair versus the mass of the sub-leading lepton pair for candidate ZZ events in the 7 TeV data after applying all of the selection requirements apart from the di-lepton mass requirements. The events observed in the data are shown as solid circles and the $ZZ^* \to \ell^-\ell^+\ell^-\ell^+$ signal prediction from simulation as boxes, with the size of each box is proportional to the expected number of events in each bin. The region enclosed by the solid (dashed) lines indicates the signal region defined by the di-lepton mass requirements for ZZ (ZZ^*) events. The expected backgrounds quoted in the label are slightly different to those quoted in Table 7.14 as they refer to the numbers in the published ATLAS analysis [4] which used a different background estimate; the expectations are consistent within the uncertainties.

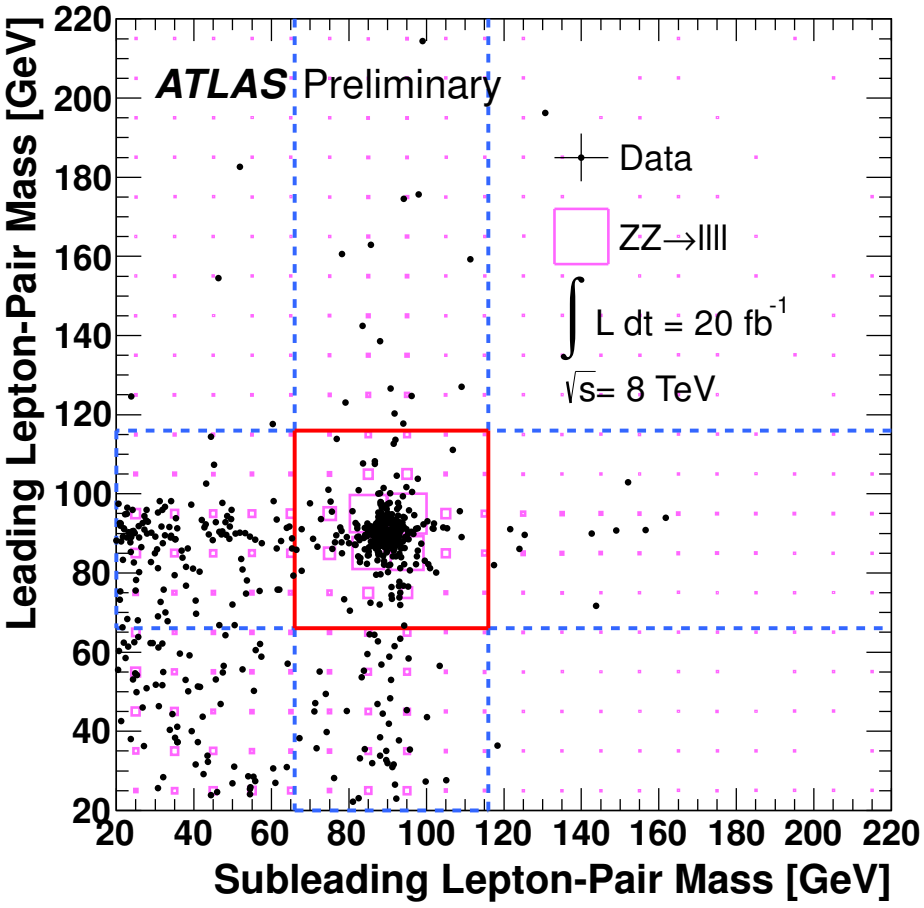

Figure 8.2: Mass of the leading lepton pair versus the mass of the sub-leading lepton pairfor candidate ZZ events in the 8 TeV data after applying all of the selection requirements apart from the di-lepton mass requirements. The events observed in the data are shown as solid circles and the $ZZ^* \to \ell^-\ell^+\ell^-\ell^+$ signal prediction from simulation as boxes, with the size of each box is proportional to the expected number of events in each bin. The region enclosed by the solid (dashed) lines indicates the signal region defined by the di-lepton mass requirements for ZZ (ZZ^*) events.

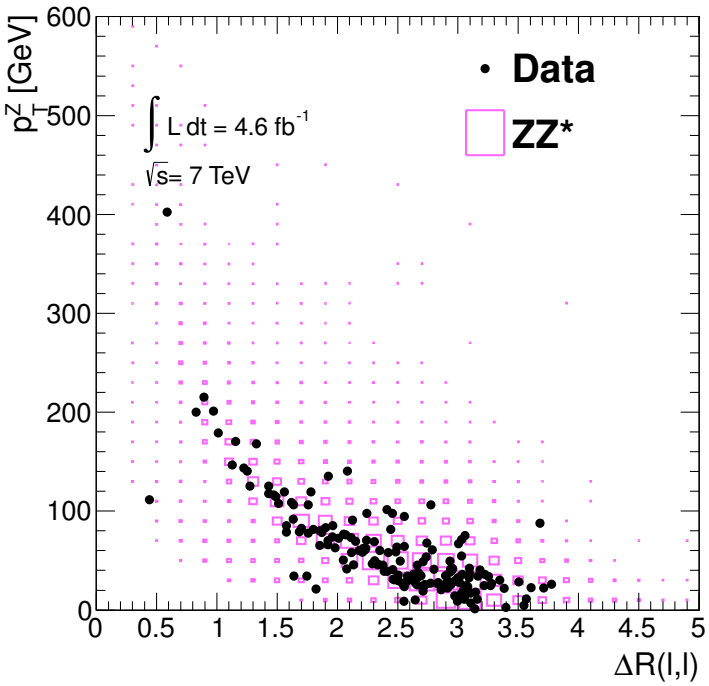

Figure 8.3: Transverse momentum of lepton pairs versus the opening angle between the leptons forming the pair, for events passing the ZZ^* selection in 7 TeV data (two entries per event).

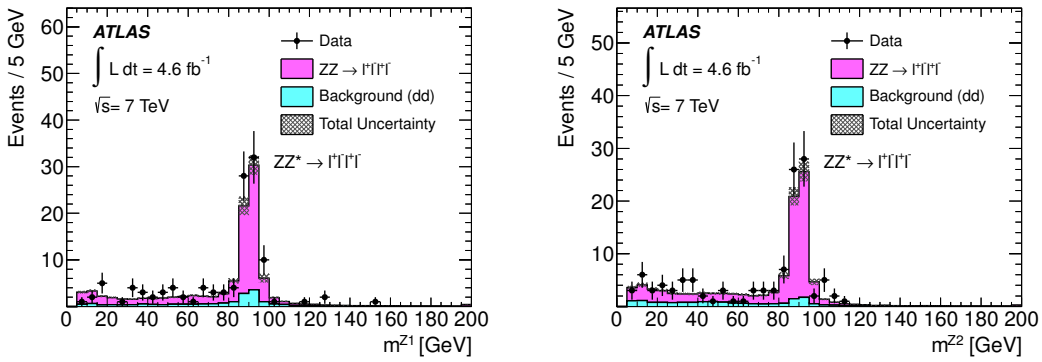

(a) (b)

Figure 8.4: Invariant masses of the (a) leading and (b) subleading lepton pair in candidate ZZ events in the 7 TeV data. In each plot, the lepton pair not shown in the plot is required to pass the $66 < m_{\ell^-\ell^+} < 116$ GeV requirement. The points represent the observed data and the histograms show the prediction from simulation, where the background is normalised to the total background estimate as described in Chapter 7. The shaded band shows the combined statistical and systematic uncertainty on the prediction.

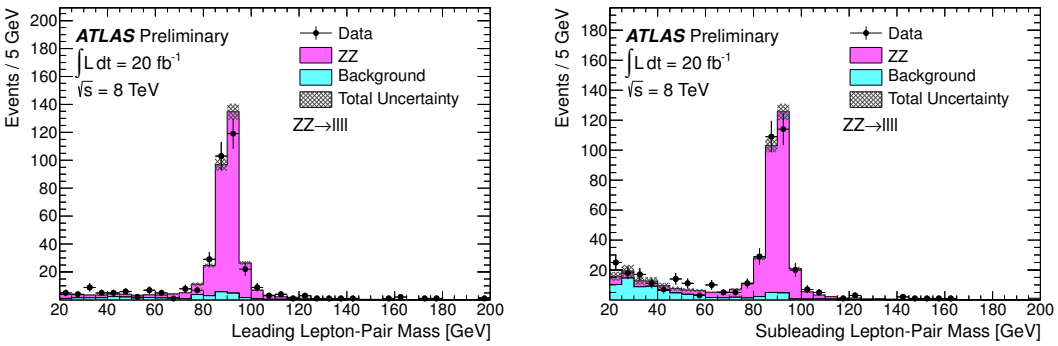

(a) (b)

Figure 8.5: Invariant masses of the (a) leading and (b) subleading lepton pair in candidate ZZ events in the 8 TeV data. In each plot, the lepton pair not shown in the plot is required to pass the $66 < m_{\ell^-\ell^+} < 116$ GeV requirement. The points represent the observed data and the pink histogram shows the prediction for the signal from simulation. The light blue histogram shows the background shape obtained from data, normalised to the total background estimate as described in Chapter 7. The shaded band shows the combined statistical and systematic uncertainty on the prediction.

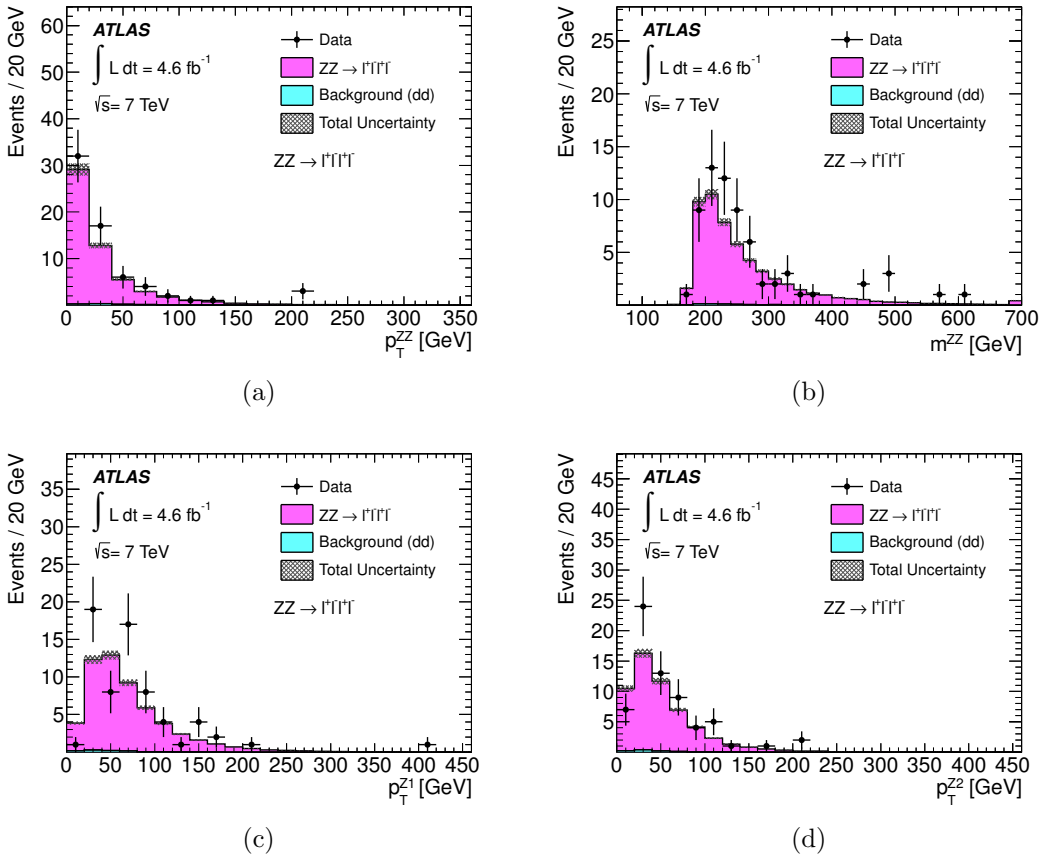

(a) (b)

(c) (d)

Figure 8.6: Kinematic distributions for events passing the ZZ selection in the 7 TeV data: (a) transverse momentum p_{T}^{ZZ} and (b) invariant mass m^{ZZ} of the four-lepton system, (c) transverse momentum of the leading di-lepton pair p_{T}^{Z1}, and (d) transverse momentum of the subleading di-lepton pair p_{T}^{Z2}. The points represent the observed data and the histograms show the prediction from simulation, where the background is normalised to the total background estimate as described in Chapter 7. The shaded band shows the combined statistical and systematic uncertainty on the prediction.

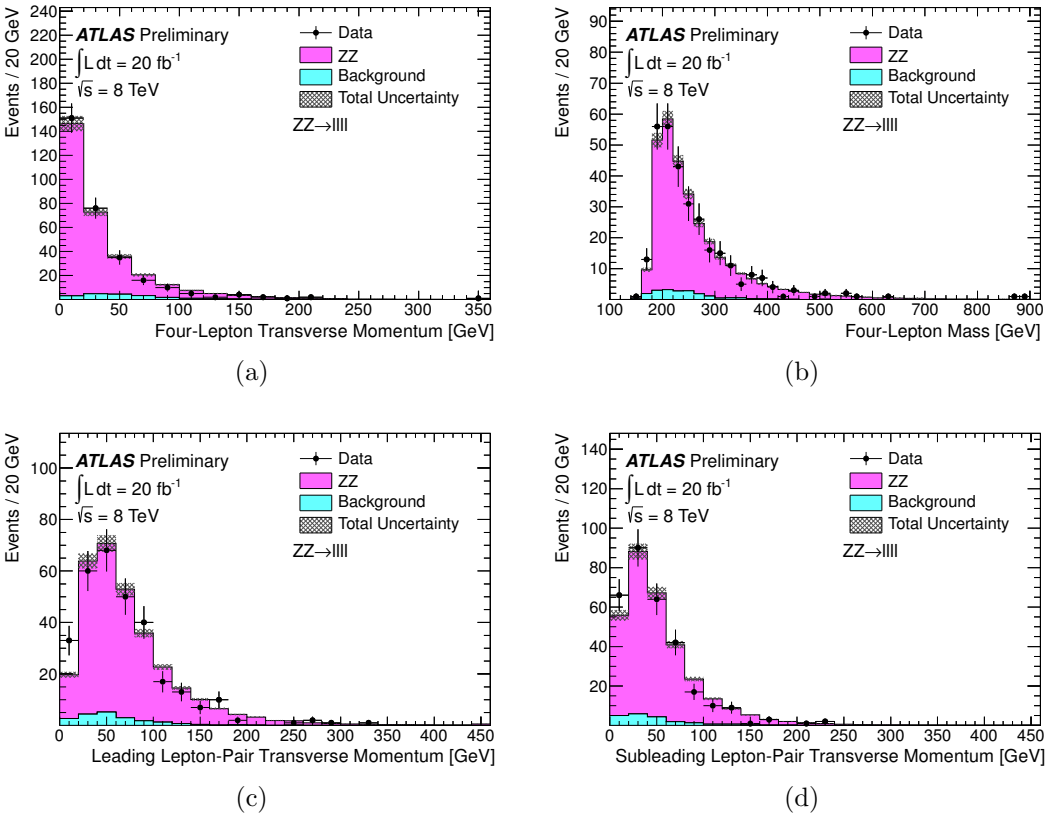

Figure 8.7: Kinematic distributions for events passing the ZZ selection in the 8 TeV data: (a) transverse momentum p_{T}^{ZZ} and (b) invariant mass m^{ZZ} of the four-lepton system, (c) transverse momentum of the leading di-lepton pair p_{T}^{Z1}, and (d) transverse momentum of the subleading di-lepton pair p_{T}^{Z2}. The points represent the observed data and the pink histogram shows the prediction for the signal from simulation. The light blue histogram shows the background shape obtained from data, normalised to the total background estimate as described in Chapter 7. The shaded band shows the combined statistical and systematic uncertainty on the prediction.

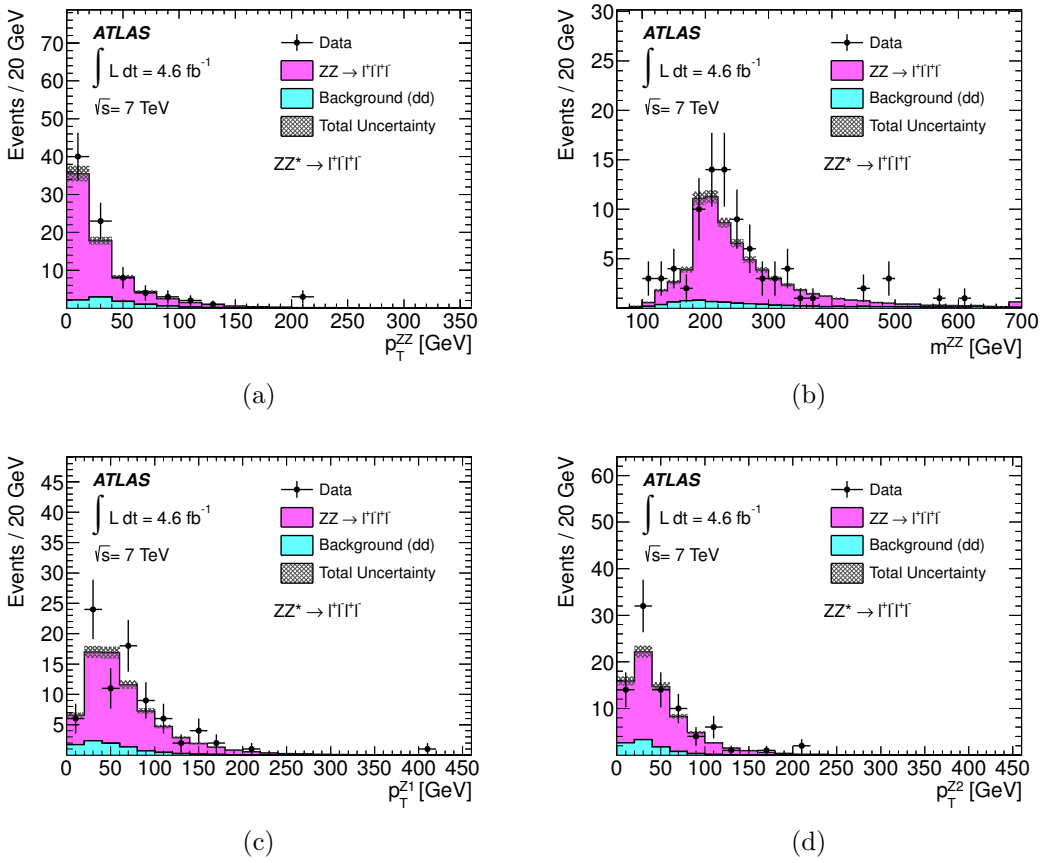

Figure 8.8: Kinematic distributions for events passing the ZZ^* selection in the 7 TeV data: (a) transverse momentum p_{T}^{ZZ} and (b) invariant mass m^{ZZ} of the four-lepton system, (c) transverse momentum of the leading di-lepton pair p_{T}^{Z1}, and (d) transverse momentum of the subleading di-lepton pair p_{T}^{Z2}. The points represent the observed data and the histograms show the prediction from simulation, where the background is normalised to the data-driven estimate as described in Chapter 7. The shaded band shows the combined statistical and systematic uncertainty on the prediction.

8.3 Cross Section Measurement

As discussed in Section 2.1.2, the cross section is first measured in a fiducial phase-space corresponding to the experimental selections (the *fiducial cross section*), in order to reduce systematic uncertainties associated with extrapolation. The fiducial cross section is then extrapolated to the total ZZ cross section, correcting for the acceptance of the fiducial phase-space and the $ZZ \to \ell\ell\ell'\ell'$ branching fraction. The definition of the fiducial phase-space was given in Section 2.1.2, and is slightly different for the 7 TeV and 8 TeV analyses due to the differing experimental selections.

8.3.1 Fiducial Cross Section

For a given $ZZ \to \ell^-\ell^+\ell^-\ell^+$ final state the fiducial cross section is defined as:

$$\sigma^{\text{fid}}_{ZZ\to\ell\ell\ell'\ell'} = \frac{N^{\text{obs}}_{\ell\ell\ell'\ell'} - N^{\text{bkg}}_{\ell\ell\ell'\ell'}}{\mathcal{L} \times C^{\ell\ell\ell'\ell'}_{ZZ}} \tag{8.1}$$

where $N^{\text{obs}}_{\ell\ell\ell'\ell'}$ is the number of observed event and $N^{\text{bkg}}_{\ell\ell\ell'\ell'}$ is the expected number of background events. $\mathcal{L}$ is the integrated luminosity of the data sample and $C^{\ell\ell\ell'\ell'}_{ZZ}$ is the reconstruction acceptance factor for the $\ell\ell\ell'\ell'$ final-state, as defined in Section 6.6.3.

The cross section is estimated using a maximum profile-likelihood technique, by maximising the *profile-likelihood function,* L with respect to the cross section σ. L is the product of the Poisson probability P for observing N events given a cross section σ, reconstruction acceptance C_{ZZ} and background b; and of Gaussian distributions G to describe nuisance parameters due to uncertainties on C_{ZZ}, b and $\mathcal{L}$:

$$\begin{aligned} L(\sigma, C'_{ZZ}, b'; \Delta_b, \Delta_{C_{ZZ}}, N) = P(\sigma, C'_{ZZ}, b'; N) \times G(C'_{ZZ}; C_{ZZ}, \Delta_{C_{ZZ}}) \\ \times G(b'; b, \Delta_b) \times G(\mathcal{L}'; \mathcal{L}, \Delta_{\mathcal{L}}) \end{aligned} \tag{8.2}$$

The Poisson probability to observe N events given an expected number of signal events s and expected background b is:

$$P(\sigma, C_{ZZ}, b; N) = \frac{e^{-(s+b)} \cdot (s+b)^N}{N!}, \tag{8.3}$$

where s is given by:

$$s(\sigma^{\text{fid}}, C_{ZZ}, \mathcal{L}) = \sigma^{\text{fid}} \times \mathcal{L} \times C_{ZZ} \tag{8.4}$$

In practice, for computational convenience $-\ln(L)$ is minimised rather than maximising L, however the procedures are equivalent. The fiducial cross section for each final-state is calculated separately. For calculating the combined $ZZ \to \ell^-\ell^+\ell^-\ell^+$ fiducial cross section, the number of observed and expected events for each individual final-state are summed and the weighted average of the reconstruction acceptances in each final-state is taken. The background is estimated for all $\ell^-\ell^+\ell^-\ell^+$ final states combined (as in the last column of Table 7.14); this benefits from a lower statistical uncertainty than summing the individual final-state background estimates. This procedure for combining the final-states gives the highest weight to the highest statistics channels, and does not automatically take into account the better signal over background ratios (S/B) in different final-states. However, since the lowest statistics channel is also the channel with the worse S/B (the $e^-e^+e^-e^+$ final-state), this simpler approach is justified.

Fiducial Cross Section Results

Fiducial cross section results are presented in Table 8.3, together with the theoretical predictions. For the 7 TeV analysis, the measured fiducial cross sections are slightly higher than predicted by the theory, but are consistent within the uncertainties. For the 8 TeV analysis, the measured cross sections are in good agreement with the theory.

8.3.2 Total Cross Section

The total cross section is obtained by extrapolating the fiducial cross section from the fiducial phase-space to the total phase-space space and by correcting for the $ZZ \to \ell^-\ell^+\ell^-\ell^+$ branching fraction. The total cross section is defined by requiring both Z bosons have mass $66 < m_Z < 116$ GeV. In order to extrapolate from the fiducial to the total phase-space, the *fiducial acceptance factor*, A_{ZZ}, must be estimated. A_{ZZ} is the is fraction of ZZ events with both Z bosons passing the $66 < m_Z < 116$ GeV requirement which fall into the fiducial phase-space, and is

Channel	Measured Fiducial Cross Section	Theory
7 TeV, ZZ		
$ZZ \to e^-e^+e^-e^+$	$7.6\,^{+2.2}_{-1.9}\,(\text{stat})\,^{+0.8}_{-0.6}\,(\text{syst})\,^{+0.4}_{-0.1}\,(\text{lumi})$ fb	$5.3\,^{+0.2}_{-0.2}$ fb
$ZZ \to \mu^-\mu^+\mu^-\mu^+$	$7.0\,^{+1.6}_{-1.4}\,(\text{stat})\,^{+0.3}_{-0.3}\,(\text{syst})\,^{+0.3}_{-0.2}\,(\text{lumi})$ fb	$5.3\,^{+0.2}_{-0.2}$ fb
$ZZ \to e^-e^+\mu^-\mu^+$	$10.4\,^{+2.2}_{-1.9}\,(\text{stat})\,^{+0.7}_{-0.6}\,(\text{syst})\,^{+0.5}_{-0.3}\,(\text{lumi})$ fb	$10.6\,^{+0.5}_{-0.4}$ fb
$ZZ \to \ell^-\ell^+\ell^-\ell^+$	$25.2\,^{+3.3}_{-3.0}\,(\text{stat})\,^{+1.2}_{-1.0}\,(\text{syst})\,^{+1.1}_{-0.9}\,(\text{lumi})$ fb	$21.2\,^{+0.9}_{-0.7}$ fb
7 TeV, ZZ^*		
$ZZ^* \to e^-e^+e^-e^+$	$8.5\,^{+2.4}_{-2.1}\,(\text{stat})\,^{+1.2}_{-1.0}\,(\text{syst})\,^{+0.5}_{-0.2}\,(\text{lumi})$ fb	$6.3\,^{+0.3}_{-0.2}$ fb
$ZZ^* \to \mu^-\mu^+\mu^-\mu^+$	$8.8\,^{+1.7}_{-1.5}\,(\text{stat})\,^{+0.5}_{-0.5}\,(\text{syst})\,^{+0.4}_{-0.3}\,(\text{lumi})$ fb	$6.3\,^{+0.3}_{-0.2}$ fb
$ZZ^* \to e^-e^+\mu^-\mu^+$	$9.7\,^{+2.4}_{-2.2}\,(\text{stat})\,^{+1.2}_{-1.3}\,(\text{syst})\,^{+0.5}_{-0.3}\,(\text{lumi})$ fb	$12.6\,^{+0.6}_{-0.4}$ fb
$ZZ^* \to \ell^-\ell^+\ell^-\ell^+$	$27.8\,^{+3.6}_{-3.4}\,(\text{stat})\,^{+1.8}_{-1.6}\,(\text{syst})\,^{+1.1}_{-1.0}\,(\text{lumi})$ fb	$25.1\,^{+1.2}_{-0.8}$ fb
8 TeV, ZZ		
$ZZ \to e^-e^+e^-e^+$	$4.6\,^{+0.7}_{-0.7}\,(\text{stat})\,^{+0.4}_{-0.3}\,(\text{syst})\,^{+0.1}_{-0.1}\,(\text{lumi})$ fb	$5.3\,^{+0.2}_{-0.2}$ fb
$ZZ \to \mu^-\mu^+\mu^-\mu^+$	$4.9\,^{+0.6}_{-0.5}\,(\text{stat})\,^{+0.2}_{-0.2}\,(\text{syst})\,^{+0.1}_{-0.1}\,(\text{lumi})$ fb	$5.3\,^{+0.2}_{-0.2}$ fb
$ZZ \to e^-e^+\mu^-\mu^+$	$11.3\,^{+1.0}_{-0.9}\,(\text{stat})\,^{+0.6}_{-0.6}\,(\text{syst})\,^{+0.3}_{-0.3}\,(\text{lumi})$ fb	$10.5\,^{+0.5}_{-0.4}$ fb
$ZZ \to \ell^-\ell^+\ell^-\ell^+$	$20.8\,^{+1.3}_{-1.2}\,(\text{stat})\,^{+1.0}_{-0.9}\,(\text{syst})\,^{+0.6}_{-0.6}\,(\text{lumi})$ fb	$21.1\,^{+0.9}_{-0.8}$ fb

Table 8.3: Fiducial Cross Section measurements at 7 TeV and at 8 TeV. The second column gives the measured cross section, and the third the prediction from theory, calculated to NLO in QCD using MCFM 6.3 with PDF set CT10 and scale set to $\frac{1}{2}m(ZZ)$. The quoted theoretical uncertainties are obtained by varying the factorisation and renormalisation scales, simultaneously, up and down by a factor of two, and by using the CT10 error set.

Source (%)	7 TeV	8 TeV
PDF	0.6	0.9
Scale	0.2	0.2
Parton Shower / ISR Model	0.1	0.1
Generator Difference	1.3	0.8
Total	1.4	1.2

Table 8.4: Systematic uncertainties to the fiducial acceptance factors, A_{ZZ}, at 7 TeV and at 8 TeV.

estimated from Monte Carlo simulation as:

$$A_{ZZ} = \frac{N^{\text{MC Fiducial Volume}}_{\text{Generated } ZZ}}{N^{\text{MC All}}_{\text{Generated } ZZ}} \tag{8.5}$$

The total cross section is then defined as:

$$\sigma^{\text{tot}}_{ZZ} = \frac{N^{\text{obs}} - N^{\text{bkg}}}{\mathcal{L} \times BR\{ZZ \to \ell^-\ell^+\ell^-\ell^+\} \times A_{ZZ} \times C_{ZZ}} \tag{8.6}$$

Uncertainties on A_{ZZ} arise due to uncertainties on the PDF, the choice of the factorisation and renormalisation scales and modelling of the parton shower and ISR. A_{ZZ} is determined using the POWHEGBOX and GG2ZZ generators. The PDF errors are estimated using the 52 CT10 error sets and by taking the difference with MSTW2008, and the scale errors are estimated by varying the factorisation and renormalisation scales, simultaneously, up and down by a factor of two. The systematic due to the modelling of the parton shower and ISR is estimated by comparing the value for A_{ZZ} obtained from a POWHEGBOX sample showered with HERWIG compared to to the nominal sample which is showered with PYTHIA. Additionally, the difference with the A_{ZZ} obtained from MCFM, which does not model the parton shower, is taken as an additional systematic. The contributions of these different sources of systematic uncertainty are shown in Table 8.4, and the values of A_{ZZ} are shown in Table 8.5. The A_{ZZ} are smaller for the 8 TeV analysis reflecting the tighter lepton η requirement in the definition of the fiducial phase-space at 8 TeV with respect to 7 TeV.

Total Cross Section Results

Total cross section results are presented in Table 8.6, together with the theoretical prediction. The measured total cross section at 7 TeV is somewhat higher than the theoretical prediction, but consistent within the errors. The measured total cross section at 8 TeV is in good agreement with the Standard Model prediction.

Channel	7 TeV	8 TeV
$ZZ \to e^-e^+e^-e^+$	$0.804 \pm 0.010\,(\text{syst})$	$0.649 \pm 0.008\,(\text{syst})$
$ZZ \to \mu^-\mu^+\mu^-\mu^+$	$0.804 \pm 0.010\,(\text{syst})$	$0.649 \pm 0.008\,(\text{syst})$
$ZZ \to e^-e^+\mu^-\mu^+$	$0.804 \pm 0.010\,(\text{syst})$	$0.649 \pm 0.008\,(\text{syst})$
$ZZ \to \ell^-\ell^+\ell^-\ell^+$	$0.804 \pm 0.010\,(\text{syst})$	$0.649 \pm 0.008\,(\text{syst})$

Table 8.5: Fiducial acceptance factors, A_{ZZ}, at 7 TeV and at 8 TeV. Systematic uncertainties are shown; the statistical uncertainty is negligible.

	Measured Cross Section	Theory
$\sigma^{\text{tot}}_{ZZ}(\sqrt{s} = 7\text{ TeV})$	$7.0\,^{+0.9}_{-0.8}\,(\text{stat})\,^{+0.4}_{-0.3}\,(\text{syst})\,^{+0.3}_{-0.2}\,(\text{lumi})$ pb	$5.9\,^{+0.2}_{-0.2}$ pb
$\sigma^{\text{tot}}_{ZZ}(\sqrt{s} = 8\text{ TeV})$	$7.1\,^{+0.4}_{-0.4}\,(\text{stat})\,^{+0.4}_{-0.3}\,(\text{syst})\,^{+0.2}_{-0.2}\,(\text{lumi})$ pb	$7.2\,^{+0.3}_{-0.2}$ pb

Table 8.6: Total ZZ Cross Section measurements at 7 TeV and at 8 TeV. The second column gives the measured cross section, and the third the prediction from theory, calculated to NLO in QCD using MCFM 6.3 with PDF set CT10 and scale set to $\frac{1}{2}m(ZZ)$. The quoted theoretical uncertainties are obtained by varying the factorisation and renormalisation scales, simultaneously, up and down by a factor of two, and by using the CT10 error set.

Figure 8.9 shows a comparison of ZZ cross section measurements and theoretical predictions as a function of the centre-of-mass energy $\sqrt{s}$. The ATLAS data point for 7 TeV on this plot is the total ZZ cross section obtained after a combination with a similar measurement using $ZZ \to \ell^-\ell^+\nu\bar{\nu}$ decays [4] not described in this thesis.

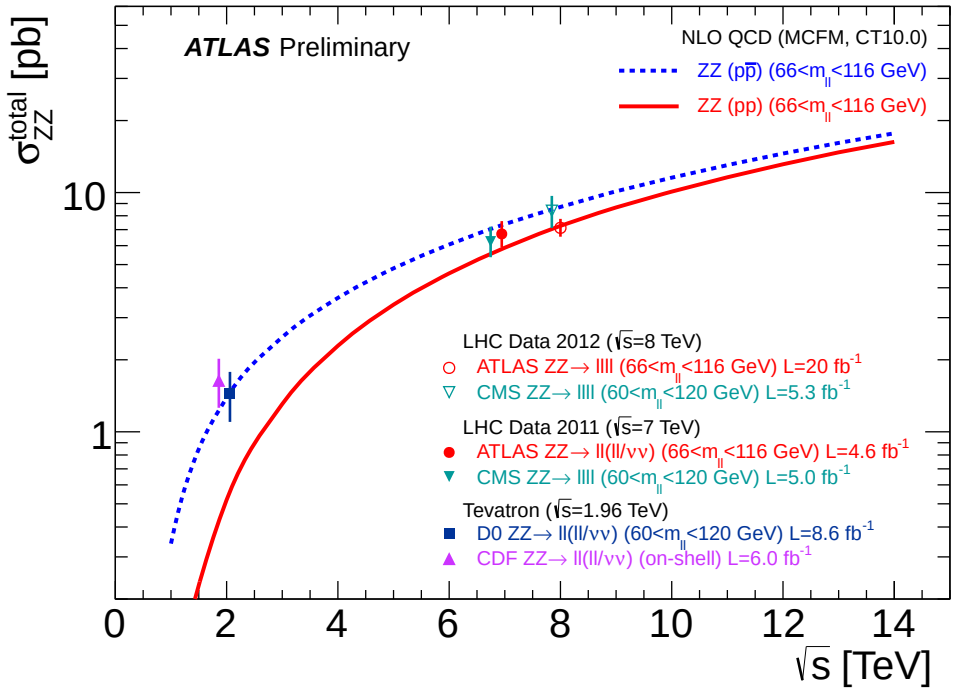

(a)

Figure 8.9: Comparison of experimental measurements and theoretical predictions of the total ZZ production cross section as a function of centre-of-mass energy $\sqrt{s}$. Shown are experimental measurements from CDF [52] and D0 [51] in $p\bar{p}$ collisions at the Tevatron at $\sqrt{s} = 1.96$ TeV, and experimental measurements from ATLAS and CMS [54, 55] in pp collisions at the LHC at $\sqrt{s} = 7$ TeV and $\sqrt{s} = 8$ TeV. The blue dashed line shows the theoretical prediction for the ZZ production cross section in $p\bar{p}$ collisions, calculated at NLO in QCD using MCFM with PDF set CT10. The solid red line shows the theoretical prediction for the ZZ production cross section in pp collisions, calculated in the same way. The theoretical curves are calculated using the natural width of the Z boson in the mass range 66 to 116 GeV.

8.4 Unfolded Kinematic Distributions

The observed kinematic distributions shown in Section 8.2 are a convolution of the underlying 'true' distribution of the parameter of interest and distortion and smearing due to detector effects. Although the detector distortion is included in the Monte Carlo simulation shown in those figures, allowing a comparison of the theoretical prediction and the observed data, it is desirable to correct the observed distributions for detector effects in order to allow model-independent comparisons between theory and observation and to allow comparison between different experiments. The correction procedure is referred to as *unfolding*.

Formally, one can consider some parameter of interest x, distributed according to a probability distribution function (pdf) $f(x)$. Due to experimental effects, one does not measure x but a different (but related) variable y, distributed according to a different pdf $g(y)$. The measured variable y is related to x by a convolution of the true distribution $f(x)$ with a response function $A(y, x)$ to account for the experimental effects:

$$g(y) = \int A(y, x) f(x) \mathrm{d}x \tag{8.7}$$

In practice, continuous distributions are generally not measured, but instead measurements are made in discretised bins. x and y can thus be rewritten as vectors $\mathbf{x}$ and $\mathbf{y}$, where each element represents the number of events in a given bin. The response function then becomes a response matrix $\mathbf{A}$, and Equation 8.7 can be rewritten as:

$$\mathbf{y} = \mathbf{A}\mathbf{x} \tag{8.8}$$

An iterative Bayesian algorithm [112] is used to perform the unfolding, using the implementation provided by the RooUnfold [113] package. The algorithm treats the response matrix $\mathbf{A}$ as a description of the probability of observing some particular data given the true distribution. From Bayes's theorem, the probability of there being in truth x_i events in bin i of the true distribution arising due to an observation of y_j events in bin j is given by:

$$P(x_i|y_j, I) = \frac{P(y_j|x_i, I) \cdot P(x_i|I)}{\sum_k P(y_j|x_k, I) \cdot P(x_k|I)} \tag{8.9}$$

where I represents the state of information under which the analysis is performed, and $P(x_i|I)$ is the prior for x_i. $P(y_i|x_j, I)$ is given by element A_{ij} of the unfolding matrix $\mathbf{A}$. $P(x_i|y_j, I)$ can be used to 'share' the events observed in a single bin of $\mathbf{y}$ between the bins of the true distribution. An estimate of the true spectrum

is obtained by 'sharing' all of the bins of the observed distribution following this formula, taking into account the efficiency. The estimate for x_i is thus given by:

$$x_i = \frac{1}{\epsilon_i} \sum_{j=1}^{n} \frac{A_{ji} \cdot P(x_i|I)}{\sum_k A_{jk} \cdot P(x_k|I)} \cdot y_j \tag{8.10}$$

where $\epsilon_i = \sum_j^n A_j$ accounts for the efficiency.

The initial set of priors $P(x_i|I)$ is taken from the simulated distribution from Monte Carlo, and the unfolding matrix $\mathbf{A}$ is also estimated using Monte Carlo simulation. The unfolding procedure is iterated, taking the posterior distribution for $\mathbf{x}$ from one iteration as a prior for the next. The choice of initial prior will tend to bias the unfolded distribution, but this bias decreases steeply with the number of iterations. Conversely, the statistical uncertainty tends to increase with the number of iterations, as fluctuations can be amplified by positive feedback inherent in the algorithm; the number of iterations must thus be chosen to balance the bias due to the choice of prior and amplification of statistical uncertainties. It is found that the difference in the results between three and four iterations is much smaller than the statistical uncertainty. The results for three iterations are thus taken as the nominal result, and the difference between three and four iterations is taken as a systematic uncertainty.

Statistical uncertainties due to the number of observed events are assessed by pseudo-experiments, in each experiment fluctuating the observed $\mathbf{y}$ by a Poisson distribution and re-running the full unfolding procedure; the RMS of 2000 pseudo-experiments is taken as the statistical uncertainty. The response matrix $\mathbf{A}$ has systematic uncertainties due to experimental uncertainties; these are handled in a similar manner to the statistical uncertainties, re-running the unfolding procedure multiple times and varying $\mathbf{A}$ according to the different sources of uncertainty. An additional systematic arises from the choice of prior. This is estimated by using the distribution predicted by Sherpa as a prior instead of the nominal PowhegBox.

Distributions of three variables sensitive to new phenomena are selected for unfolding: the transverse momentum $p_{\mathrm{T}}(Z)$ of the leading Z boson candidate, the angle $\Delta\phi(\ell^-\ell^+)$ between the decay leptons of the leading Z boson candidate, and the four-lepton invariant mass $m(ZZ)$. Bin boundaries are chosen to maximise sensitivity to nTGCs, and are in all cases larger than the detector resolution. The unfolded distributions are presented in terms of a differential fiducial cross section. This removes the effect of systematics that only affect the normalisation and not

the shape of the distribution. Unfolded distributions are only provided for the 7 TeV analysis; they are shown in Figure 8.10. The Standard Model prediction is consistent with the measurement in each case. The uncertainty on the unfolded distributions is dominated by the statistical uncertainty, which is approximately 30% in most bins. The systematic uncertainty is no more than 5% in each bin, and is dominated by the uncertainty arising due to the choice of prior.

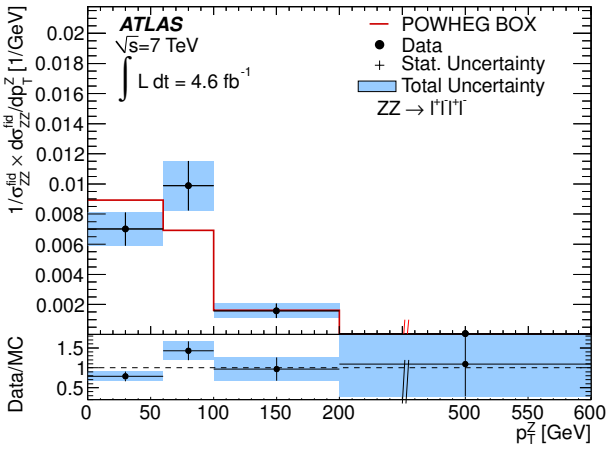

(a)

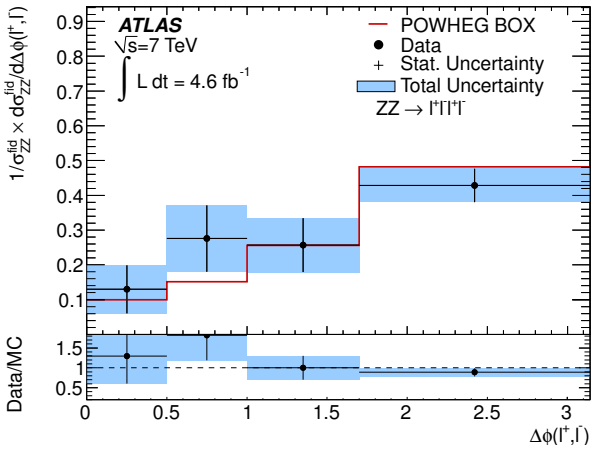

(b)

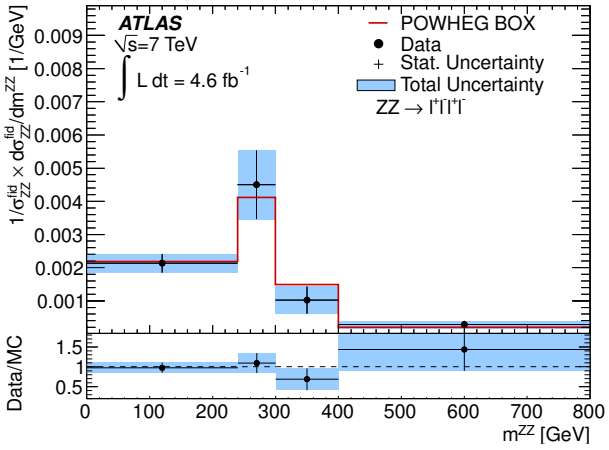

(c)

Figure 8.10: Unfolded ZZ fiducial cross sections in bins of (a) the p_{T} of the leading Z boson, (b) the angle between the decay leptons of the leading Z boson, $\Delta\phi(\ell^{-}\ell^{+})$ and (c) the four-lepton invariant mass, $m(ZZ)$. The parallel lines in (a) indicate a binning discontinuity in the final bin.

Chapter 9

Limits on Anomalous Neutral Triple Gauge Couplings

As discussed in Section 2.4, the presence of the anomalous neutral triple gauge couplings (nTGCs), ZZZ and $ZZ\gamma$, present in some models of new physics, would lead to an increase in the cross section for ZZ production, particularly at high momentum transfer. Observables such as the mass of the four-lepton system and the transverse momenta of the Z bosons and their decay products are therefore particularly sensitive to nTGCs. The observed $ZZ \to \ell^-\ell^+\ell^-\ell^+$ events are used to search for such couplings, and in the absence of any evidence for them, to set limits on the size of the couplings. The limits are obtained by performing a binned fit of the p_{T} distribution of the leading Z boson, although other variables are considered. Only the ZZ (on-shell) events are used. Separate limits are set using the 7 TeV and the 8 TeV data; for the 7 TeV analysis, limits are set in combination with observed $ZZ \to \ell^-\ell^+\nu\bar{\nu}$ events; see [4] for a description of the $ZZ \to \ell^-\ell^+\nu\bar{\nu}$ analysis. Limits are set using a form-factor with $n = 3$ and $\Lambda = 3$ TeV; these values are chosen so that expected limits are within the values allowed by requiring that unitarity is not violated at LHC energies [40]. Limits are also presented without applying a form-factor (i.e. $\Lambda = \infty$).

The limit setting procedure is described in Section 9.1. A bin optimisation study is presented in Section 9.2, and the robustness of the limits under variations in the limit setting method are described in Section 9.3. Finally, the expected and observed limits are given in Section 9.4.

9.1 Limit Setting Procedure

In order to set limits it is necessary to parametrise the expected yield in terms of the strength of the nTGCs. One method for doing this would be to generate

a grid of Monte Carlo samples at different coupling strengths. This is, however, very computationally intensive. Instead, a matrix element reweighting procedure is used to reweight a sample generated with one set of coupling strengths to another. This is described in more detail below. Once the parameterised expected yields are obtained, 95% confidence interval limits on the nTGCs are set using a frequentist likelihood-ratio method. This is also described below.

9.1.1 Matrix Element Reweighting

As described in Section 2.4, the anomalous nTGCs affecting ZZ production are described by four parameters: f_4^γ, f_4^Z, f_5^γ and f_5^Z. Since the parameters enter into the effective Lagrangian linearly (Equation 2.6), they will appear quadratically in the amplitude for the $ZZ \to \ell^-\ell^+\ell^-\ell^+$ process. The differential cross section can thus be written as:

$$\begin{aligned} \mathrm{d}\sigma_{\mathrm{SM+TGC}} &= F_{00} + f_4^\gamma F_{01} + f_4^Z F_{02} + f_5^\gamma F_{03} + f_5^Z F_{04} \\ &+ \left(f_4^\gamma\right)^2 F_{11} + f_4^\gamma f_4^Z F_{12} + f_4^\gamma f_5^\gamma F_{13} + f_4^\gamma f_5^Z F_{14} \\ &+ \left(f_4^Z\right)^2 F_{22} + f_4^Z f_5^\gamma F_{23} + f_4^Z f_5^Z F_{24} \\ &+ \left(f_5^\gamma\right)^2 F_{33} + f_5^\gamma f_5^Z F_{34} \\ &+ \left(f_5^Z\right)^2 F_{44} \end{aligned} \tag{9.1}$$

where F_{ij} are coefficients describing how the cross section changes in the presence of nTGCs. A priori, there are 25 coefficients, however, using the symmetry property of the coefficients ($F_{ij} = F_{ji}$), it is seen that only $25-10 = 15$ are independent. F_{00} corresponds to the contribution of the Standard Model diagrams and the rest consist of operator contributions associated with the anomalous couplings.

A simulated event generated assuming only Standard Model couplings can be assigned a weight corresponding to the increase in differential cross section due to nTGCs at a specific value of the four parameters:

$$\text{weight} = \frac{\mathrm{d}\sigma_{\mathrm{SM+TGC}}(f_4^\gamma, f_4^Z, f_5^\gamma, f_5^Z)}{\mathrm{d}\sigma_{\mathrm{SM}}} \tag{9.2}$$

By assigning such a weight to every event in the sample, it is possible to reweight a sample generated with only Standard Model couplings to a sample with nTGCs. This procedure can be easily extended to reweight a sample generated assuming any given set of nTGCs to any other set of nTGCs. For example, to reweight a sample generated assuming only Standard Model couplings to sample assuming

f_4^γ=0.1, one would apply to each event a weight:

$$\text{weight} = \frac{F_{00} + 0.1 \cdot F_{01} + (0.1)^2 \cdot F_{11}}{F_{00}} \tag{9.3}$$

The F_{ij} coefficients are completely specified by the kinematics of the incoming and outgoing particles, and so must be evaluated on an event by event basis, and the weight for each event must be calculated separately; the reweighting is thus fully differential. The F_{ij} are independent of the values of the anomalous coupling parameters assumed in the generation of the sample, although they do depend on the choice of form-factor.

The coefficients are determined from the matrix elements for $ZZ \to \ell^-\ell^+\ell^-\ell^+$ production in the presence of nTGCs, as follows. By using Equation 9.1 it is possible to write down 15 equations that uniquely determine the coefficients F_{ij} in terms of matrix elements assuming particular values for the nTGCs. To illustrate the procedure, it is convenient to consider the simplified situation where there is just one coupling parameter f. In this case, there are 3 coefficients to be determined:

$$\mathrm{d}\sigma_{\mathrm{SM+TGC}} = F_0 + fF_1 + f^2F_2 \tag{9.4}$$

where $F_0 = \mathrm{d}\sigma_{\mathrm{SM}}$. Using three different values of f, e.g $f = \{0, 1, -1\}$, three independent equations may be written down:

$$\begin{pmatrix} \mathrm{d}\sigma_1 \\ \mathrm{d}\sigma_2 \\ \mathrm{d}\sigma_3 \end{pmatrix} = \begin{bmatrix} 1 & 0 & 0 \\ 1 & 1 & 1 \\ 1 & -1 & 1 \end{bmatrix} \begin{pmatrix} F_0 \\ F_1 \\ F_2 \end{pmatrix} \tag{9.5}$$

Denoting the matrix containing the coupling values $\hat{A}$, the cross sections $\mathbf{d\sigma}$ and the coefficients $\boldsymbol{F}$, the equation may be inverted to give the coefficients:

$$\mathbf{d\sigma} = \hat{A}\boldsymbol{F} \qquad \Rightarrow \qquad \boldsymbol{F} = \hat{A}^{-1}\mathbf{d\sigma} \tag{9.6}$$

This requires that $\hat{A}$ must be invertible. This is the case if the coupling parameters are chosen such that the three equations in 9.5 are independent. When considering all four couplings at the same time, the matrix $\hat{A}$ is 15×15 and $\mathbf{d\sigma}$ and $\boldsymbol{F}$ are 15-dimensional vectors.

The differential nTGC matrix elements are obtained from the Baur-Rainwater code [40]; matrix elements from the BHO [114] code are also used as a cross-check.

The matrix elements are introduced into the framework described in [115], which enables a calculation of the amplitude given the four-vectors and PDG codes of the incoming partons and outgoing particles from the hard process.

Whilst it is possible to reweight a Standard Model sample to an nTGC point, this suffers from a lack of statistics in the tails of distributions such as the Z boson p_{T} and the four-lepton invariant mass, which are the regions of greatest interest when studying nTGCs. Instead, samples generated with values of the nTGC parameters set near previously derived experimental limits are used; this ensures statistics in the tails of the distributions of interest. The PowhegBox and $gg \to ZZ$ generators used to generate the nominal signal samples do not model nTGCs; instead the samples are generated using Sherpa, which does. For the 7 TeV analysis, four samples are used, with couplings $\{f_4^\gamma = 0.1\}$, $\{f_5^\gamma = -0.1\}$, $\{f_4^\gamma = 0.1$ & $f_5^\gamma = 0.1\}$, and $\{f_4^Z = 0.1$ & $f_5^Z = 0.1\}$. For the 8 TeV analysis, three sample are used, with couplings $\{f_4^\gamma = 0.1\}$ (denoted TGC0), $\{f_4^\gamma = 0.1 \,\&\, f_5^Z = 0.1\}$ (denoted TGC1), and $\{f_4^\gamma = f_4^Z = f_5^\gamma = f_5^Z = 0.1\}$ (denoted TGC2). The 7 TeV samples are generated with a form-factor of $\Lambda = 2$ TeV$, n = 3$; the 8 TeV samples are generated without a form-factor. The reweighting procedure can be used to reweight samples generated with one choice of form-factor (or no form-factor) to another choice of form-factor.

9.1.2 Validation of Reweighting Procedure

To demonstrate the performance of the reweighting procedure, the 8 TeV Sherpa samples generated with nTGCs are reweighted to the Standard Model, and compared to a sample generated assuming only Standard Model couplings. Additionally, the TGC1 and TGC2 samples are reweighted to the TGC0 sample. Figure 9.1 shows the resulting distributions of the leading Z boson p_{T}, and the ratios of the reweighted samples to the Standard Model/TGC0 distribution, separately for reweighting carried out using the BHO and the Baur-Rainwater matrix elements. For both of the codes, the reweighted samples are seen to agree well with the directly generated samples.

9.1.3 Yield Coefficients

In order to extract limits on the nTGCs, an estimate of the number of expected events passing the selection requirements as a function of the nTGC parameters must be obtained. The expected yield is parameterised by yield coefficients Y_{ij},

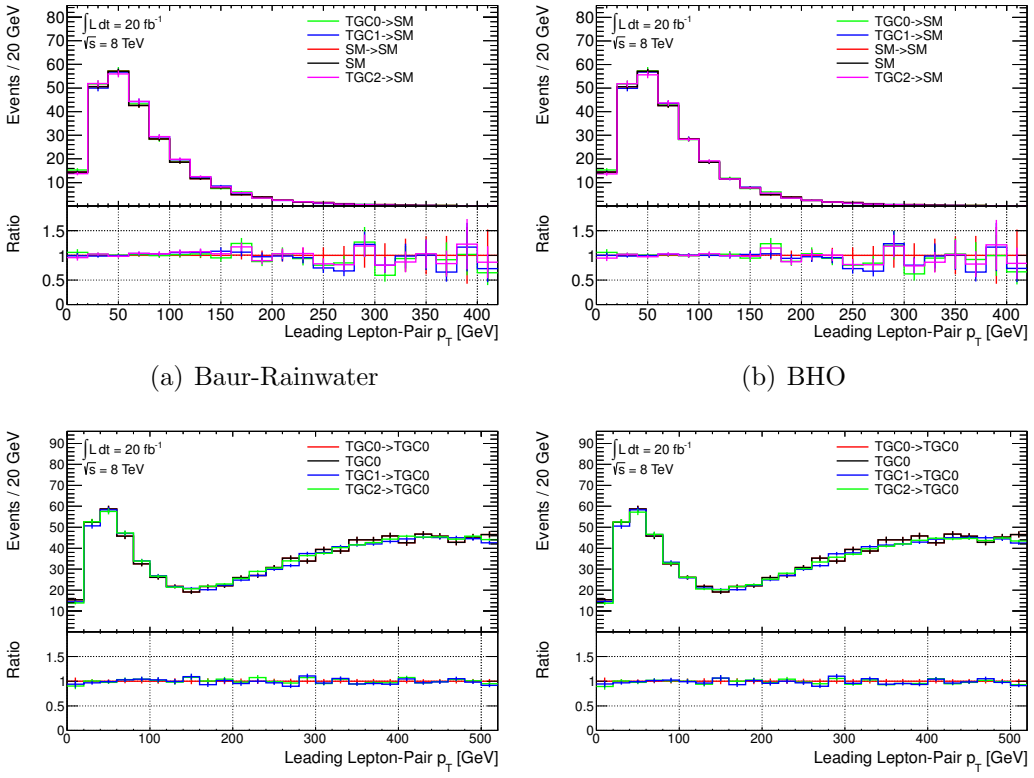

(a) Baur-Rainwater (b) BHO

(c) Baur-Rainwater (d) BHO

Figure 9.1: Validation of the TGC reweighting procedure for the 8 TeV samples. Figures (a) and (b) show the p_{T} distribution of the leading lepton pair, showing the three nTGC samples (TGC0, TGC1, TGC2; green, blue and pink lines) generated with different couplings and the Standard Model sample (red line), reweighted to the Standard Model expectation using the procedure described in Section 9.1.1, compared to the sample generated assuming only Standard Model couplings (SM, black line). In Figure (a) the matrix elements of the Baur-Rainwater code are used, and in Figure (b) the matrix elements of the BHO code are used. Figures (c) and (d) show the same distribution, showing the TGC0, TGC1 and TGC2 samples (red, blue and green lines) reweighted to the TGC0 nTGC point ($f_4^{\gamma} = 0.1$) compared to the non-reweighted TGC0 sample (black line).

which are obtained from the F_{ij} as:

$$Y_{ij} = \sum_{\text{events}} \left(\frac{F_{ij}}{\mathrm{d}\sigma_{\text{sample}}} \right) \tag{9.7}$$

where $\mathrm{d}\sigma_{\text{sample}}$ is the differential cross section for each event with the parameters set to those used to generate the sample, and the sum is over events passing the full event selection. Event-level lepton selection efficiency, energy scale, and resolution corrections are taken into account when calculating the yield coefficients. The yield coefficients are normalised to the signal expectation of PowhegBox+gg2ZZ by scaling by $N_{\text{exp}}^{\text{PowhegBox+gg2ZZ}}/Y_{00}$. A different set of yield coefficients is needed for each bin of the differential distribution used to set the limits and for each choice of form-factor. The expected yield as a function of the nTGC parameters is given by

$$\begin{aligned} N_{exp}(f_4^\gamma, f_4^Z, f_5^\gamma, f_5^Z) &= Y_{00} + f_4^\gamma Y_{01} + f_4^Z Y_{02} + f_5^\gamma Y_{03} + f_5^Z Y_{04} \\ &+ \left(f_4^\gamma\right)^2 Y_{11} + f_4^\gamma f_4^Z Y_{12} + f_4^\gamma f_5^\gamma Y_{13} + f_4^\gamma f_5^Z Y_{14} \\ &+ \left(f_4^Z\right)^2 Y_{22} + f_4^Z f_5^\gamma Y_{23} + f_4^Z f_5^Z Y_{24} \\ &+ \left(f_5^\gamma\right)^2 Y_{33} + f_5^\gamma f_5^Z Y_{34} \\ &+ \left(f_5^Z\right)^2 Y_{44} \end{aligned} \tag{9.8}$$

Tables 9.1 and 9.2 show the yield coefficients for the 8 TeV analysis for the total number of events case with a form-factor of $\Lambda = 3$ TeV, $n = 3$ and for the case of no form-factor, obtained using the Baur-Rainwater matrix-elements to reweight the TGC0 sample. Figure 9.2 shows the expected total event yield for the 8 TeV analysis as a function of the four nTGC parameters. In each case, the parameters not being varied are assumed to be at their Standard Model values of zero. The solid blue curve shows the yields with a form-factor of $n = 3, \Lambda = 3$ TeV; the dashed red curve shows the yields with no form-factor. The increase of event yield with the strength of the coupling is reduced as a result of applying the form-factor.

9.1.4 Limit Setting

The 95% confidence level (CL) intervals for the nTGC parameters are determined using a frequentist maximum profile-likelihood based method [116], combining the three $\ell\ell\ell'\ell'$ final states prior to the profile-likelihood maximisation. The likelihood function is similar to that used in the cross section calculation, but parametrised in

Y_{SM}	$Y_{f_4^\gamma}$	$Y_{f_4^Z}$	$Y_{f_5^\gamma}$	$Y_{f_5^Z}$
292.5 ± 3.1	0.6 ± 2.1	-9.0 ± 4.6	11.1 ± 2.4	-7.4 ± 5.5
	$Y_{f_4^\gamma}Y_{f_4^\gamma}$	$Y_{f_4^\gamma}Y_{f_4^Z}$	$Y_{f_4^\gamma}Y_{f_5^\gamma}$	$Y_{f_4^\gamma}Y_{f_5^Z}$
	51241.3 ± 335.4	47083.3 ± 364.1	21.8 ± 85.6	21.0 ± 46.8
	$Y_{f_4^Z}Y_{f_4^Z}$	$Y_{f_4^Z}Y_{f_5^\gamma}$	$Y_{f_4^Z}Y_{f_5^Z}$	
	71922.3 ± 624.8	20.8 ± 46.8	60.9 ± 153.6	
	$Y_{f_5^\gamma}Y_{f_5^\gamma}$	$Y_{f_5^\gamma}Y_{f_5^Z}$		
	49311.1 ± 336.1	45165.5 ± 363.4		
	$Y_{f_5^Z}Y_{f_5^Z}$			
	68920.8 ± 623.2			

Table 9.1: Yield coefficients for the 8 TeV analysis with form-factor $n = 3, \Lambda = 3$ TeV.

Y_{SM}	$Y_{f_4^\gamma}$	$Y_{f_4^Z}$	$Y_{f_5^\gamma}$	$Y_{f_5^Z}$
292.5 ± 3.1	1.1 ± 2.3	-9.6 ± 5.0	12.4 ± 2.5	-7.8 ± 5.9
	$Y_{f_4^\gamma}Y_{f_4^\gamma}$	$Y_{f_4^\gamma}Y_{f_4^Z}$	$Y_{f_4^\gamma}Y_{f_5^\gamma}$	$Y_{f_4^\gamma}Y_{f_5^Z}$
	146439.4 ± 827.9	130911.0 ± 871.3	-79.8 ± 181.2	-74.9 ± 100.7
	$Y_{f_4^Z}Y_{f_4^Z}$	$Y_{f_4^Z}Y_{f_5^\gamma}$	$Y_{f_4^Z}Y_{f_5^Z}$	
	197589.1 ± 1480.2	-75.2 ± 100.7	-213.1 ± 323.4	
	$Y_{f_5^\gamma}Y_{f_5^\gamma}$	$Y_{f_5^\gamma}Y_{f_5^Z}$		
	143338.6 ± 837.1	127865.4 ± 879.3		
	$Y_{f_5^Z}Y_{f_5^Z}$			
	192851.2 ± 1492.7			

Table 9.2: Yield coefficients for the 8 TeV analysis with no form-factor.

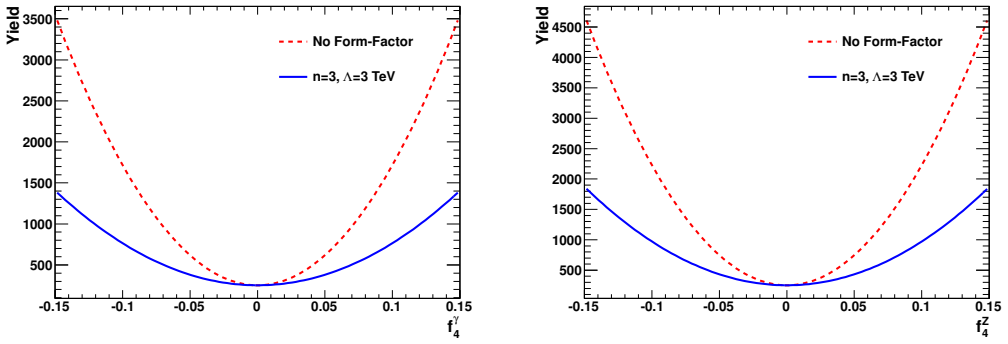

(a) f_4^γ (b) f_4^Z

(c) f_5^γ (d) f_5^Z

Figure 9.2: Expected total event yield for the 8 TeV analysis as a function of the nTGC parameters: (a) f_4^γ, (b) f_4^Z, (c) f_5^γ and (d) f_5^Z. In each case, the parameters not being varied are assumed to be at their Standard Model values of zero. The solid blue shows the yields with a form-factor of $n = 3, \Lambda = 3$ TeV; the dashed red curve shows the yields with no form-factor.

terms of the number of events in each bin instead of the cross section. Systematic uncertainties are again introduced as nuisance parameters represented as Gaussian terms (G). Since there are nuisance parameters for both signal and background, the set of nuisance parameters giving the fractional uncertainty on the signal and background expectation for a distribution of m bins is expressed as $\boldsymbol{\beta} = \{\beta_1, \beta_2, \ldots, \beta_{2m}\}$, where:

$$N^i_{\text{sig}} = N^{i,\text{nom}}_{\text{sig}} \cdot (1 + \beta_i) \tag{9.9}$$

$$N^i_{\text{bkg}} = N^{i,\text{nom}}_{\text{bkg}} \cdot (1 + \beta_{i+m}) \tag{9.10}$$

The likelihood function is:

$$L(\boldsymbol{f}, \boldsymbol{\beta}) = \prod_{i=1}^{m} P(N^i_{\text{obs}}, \mu^i(\boldsymbol{f}, \boldsymbol{\beta})) \times \frac{1}{(2\pi)^m} e^{-\frac{1}{2}(\boldsymbol{\beta} \cdot C^{-1} \cdot \boldsymbol{\beta})}, \tag{9.11}$$

where $\boldsymbol{f} = \{f_4^\gamma, f_4^Z, f_5^\gamma, f_5^Z\}$ are the nTGC parameters, C is the covariance matrix, and μ^i is the expected number of events in bin i:

$$\mu^i(\boldsymbol{f}, \boldsymbol{\beta}) = N^i_{\text{sig}}(\boldsymbol{f})(1 + \beta_i) + N^i_{\text{bkg}}(1 + \beta_{i+m}). \tag{9.12}$$

where $N^i_{\text{sig}}(\boldsymbol{f})$ is the expected signal yield in bin i as a function of the nTGC parameters, as given by Equation 9.8, but where a separate set of yield coefficients Y must be used for each bin i.

A test statistic $q(\boldsymbol{f})$ is constructed as the ratio of the maximum profile-likelihood at a specific test value of the nTGC parameters $\boldsymbol{f}$ to the full maximum profile-likelihood:

$$q(\boldsymbol{f}) = \frac{L(N|\boldsymbol{f}, \hat{\hat{\boldsymbol{\beta}}})}{L(N|\hat{\boldsymbol{f}}, \hat{\boldsymbol{\beta}})} \tag{9.13}$$

where $\hat{\hat{\boldsymbol{\beta}}}$ is the value of $\boldsymbol{\beta}$ that maximises the numerator, and $\hat{\boldsymbol{f}}$ and $\hat{\boldsymbol{\beta}}$ are the values of $\boldsymbol{f}$ and $\boldsymbol{\beta}$ that maximise the denominator. The distribution of $q(\boldsymbol{f})$ in the assumption of nTGCs at the test value of $\boldsymbol{f}$ is obtained by generating 10,000 pseudo experiments. In each pseudo experiment, the nuisance parameters $\boldsymbol{\beta}$ are Gaussian fluctuated around the mean value of $\hat{\hat{\boldsymbol{\beta}}}$ and the 'observed' number of events is drawn randomly from a Poisson distribution with a mean corresponding to the values of $\boldsymbol{f}$ and $\boldsymbol{\beta}$. The p-value at the test value of the nTGC parameters is calculated as the fraction of pseudo-experiments which have a test statistic smaller than the observed value of the test statistic $q(\boldsymbol{f})_{obs}$. This procedure is

repeated scanning possible values of $\boldsymbol{f}$, and the 95% confidence interval is defined by all values of $\boldsymbol{f}$ for which $p(\boldsymbol{f}) \geq 5\%$. In practice, the interval is determined by starting from the best fit value and working outwards in small steps of the parameters until the p-value falls below 5%.

Limits are set for one parameter at a time, holding the other parameters at their Standard Model values of zero (termed *one-dimensional limits*), and also by varying two parameters simultaneously (*two-dimensional limits*). Since the sensitivity is contained in a single bin, there is effectively only a single observable, the number of observed events in the most sensitive bin N_{obs}, which is a function of the nTGC parameters. There is therefore no sensitivity to the individual parameters but only to their combination. In this therefore not possible to set a traditional 'one-dimensional limit' on a single parameter without assuming values for the others, but only to set a limit assuming some value for all of the other parameters. For the 'one-dimensional' limits it is assumed that the other parameters are zero; this corresponds to the 'two-dimensional' limit along the line where the other parameter is zero. The two-dimensional limits are extracted by first finding the best-fit point in the two-dimensional nTGC parameter space, then working outwards along a radial line from the best-fit point and including in the exclusion region all points with a p-value $p \geq 5\%$. This is repeated for 50 evenly spaced radial lines; the 95% confidence contour is then the ellipse connecting the set of points which correspond to the 95% limits on the radial spokes.

The expected sensitivity is obtained using pseudo-experiments. In each pseudo-experiment, N^i_{sig} and N^i_{bg} are given by the Standard Model expectations but allowed to fluctuate within their uncertainties.

9.2 Bin Optimisation

For the 7 TeV analysis, limits were set using the number of events observed in bins of the leading Z boson candidate p_{T} and in bins of the mass of the four-lepton system. It was found that binning in the leading Z boson p_{T} yielded the most stringent expected limits, and that the tightest expected limits were obtained using four bins of p_{T} with boundaries 0-60, 60-100, 100-200 and $>$ 200 GeV. A combined fit with the results of a $ZZ \to \ell^-\ell^+\nu\bar{\nu}$ analysis was also carried out, using three bins of the p_{T} of the leptonically decaying Z candidate in the $ZZ \to \ell^-\ell^+\nu\bar{\nu}$ events.

For the 8 TeV analysis, a further bin optimisation was carried out, varying

the number of bins and the bin boundaries. For each variation, a set of 5,000 pseudo-experiments is carried out in order to derive the expected limit. The expected signal in each bin is re-calculated from Monte Carlo, and the reconstruction systematic uncertainties re-evaluated, as well as the theoretical uncertainties on the differential cross section. The irreducible background estimate in each bin is derived from the Monte Carlo. An estimate for the reducible background in each bin is obtained by dividing the total data-driven reducible background estimate according to the background shape obtained from data. The fractional systematic and statistical uncertainties on the data-driven background estimate are assumed to be the same in every bin. No systematic to account for uncertainties on the reducible background shape is assigned. This approximation is justified by the fact that the total background uncertainty is already large, and that the background contribution when the leading Z boson has p_{T} above 100 GeV is very small.

This procedure means that large statistical and systematic uncertainties on the expected signal and large PDF and scale errors on the fiducial cross section when the lower boundary of the last bin is set very high are taken into account in the expected limits. It does not take into account the fact that there may be insufficient Monte Carlo statistics to properly estimate the reconstruction systematic uncertainties in the last bin. Therefore before choosing a final binning it is checked that the statistics in the last bin are sufficient to properly evaluate the systematics.

A variety of choices of binning were tried, varying the number of bins from one to five, and varying the boundaries of the bins. It is observed that the expected limits are most sensitive to the choice of the lower boundary of the last bin, which is taken to be inclusive (i.e. including all events with Z boson p_{T} greater than the lower bin boundary). The limits are not observed to be very sensitive to the number of bins, or to the boundaries of the bins other than the last. Figure 9.3 shows the expected limit on f_4^γ as a function of the lower boundary of the last bin. Limits obtained using different numbers of bins are shown as different coloured markers. The expected limits become more stringent as the lower boundary of the last bin increases in p_{T}, but varying the bin boundaries other than the lower boundary of the last bin has little effect on the expected limits. The tightening of the limits as the boundary of the last bin is increased is because the relative increase in signal yield due to the existence of nTGCs is much larger at higher Z boson p_{T}. It is seen that beyond 300 GeV the limits do not significantly improve, since past this point the signal expectation in the case of Standard Model couplings only becomes very small, and so increasing the bin boundary further does little to

increase the significance of the nTGC signal. Beyond 550 GeV, the expected limits worsen; this is because the statistical, systematic, and theoretical uncertainties on the expected signal become very large, as can be seen in Figure 9.4 which shows the percentage uncertainty from different sources, for a variety of choices of binning.

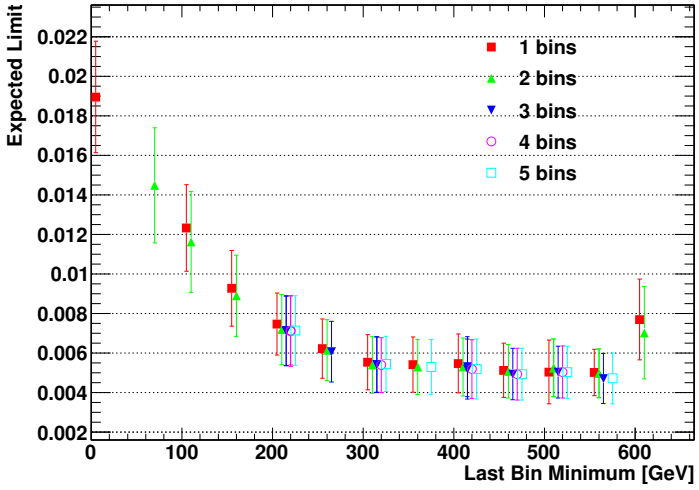

(a)

Figure 9.3: Expected limits on f_4^γ obtained in a binned fit of the p_{T} distribution of the leading Z boson candidate, as a function of the lower boundary of the last bin in p_{T}. The different coloured markers show the limits obtained using different numbers of bins.

The final limits are set using two bins of leading Z boson p_{T}: 0-300 and $>$ 300 GeV. This binning was chosen as it gives similar limits to choices of binning where the last bin boundary is higher in p_{T}, but retains sufficient statistics in the signal Monte Carlo in order to estimate the systematic uncertainties. Increasing the number of bins was not seen to give any improvement in the expected limits, so for computational convenience the binning with the lowest number of bins was chosen.

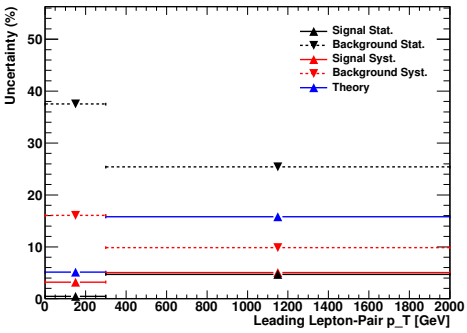

(a) 0-300, >300 GeV

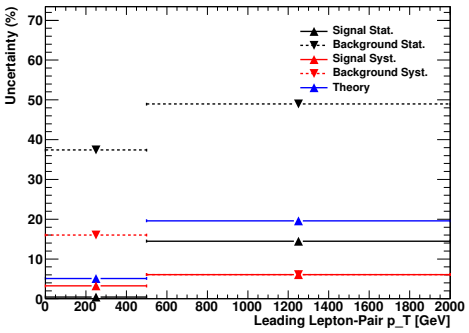

(b) 0-500, >500 GeV

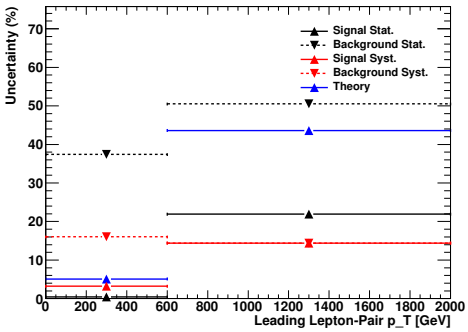

(c) 0-600, >600 GeV

Figure 9.4: Percentage uncertainties for different choices of binning in the p_{T} of the leading Z boson. The black upwards triangles show the statistical uncertainty on the signal expectation and the black downwards triangles the statistical uncertainty on the background estimate. The red upwards triangle show the systematic uncertainty on the signal expectation and the red downwards triangles the systematic uncertainty on the background. The blue upwards triangles show the theoretical uncertainty on the signal expectation.

9.3 Robustness of Limits

In order to check the robustness of the limits, the expected limits obtained using the Baur-Rainwater matrix-elements to determine the yield coefficients are compared with expected limits obtained using BHO matrix-elements to determine the coefficients. Similarly, the expected limits obtained using samples generated with different values of the nTGC parameters are compared (e.g. the TGC0 sample is compared to the TGC1 sample). Full details of the comparison are given in Appendix A.1; the changes in expected limits are smaller than the statistical uncertainties on the limit.

In order to check the effect of the assumption that the fractional statistical and systematic uncertainties on the data-driven reducible background estimate are the same in each bin of leading Z boson p_{T}, expected limits are obtained with the data-driven background uncertainties increased by a factor of five. The resulting changes in the expected limits are less than 1%, confirming the assumption that the effect of the reducible background uncertainty on the sensitivity is small. Treating the background systematic uncertainty as uncorrelated between bins leads to a negligible ($< 0.1\%$) worsening in the limits.

9.4 Expected and Observed Limits

Figure 9.5 shows expected and observed distributions of the p_{T} of the leading Z candidate with the binning used to set the nTGC limits, along with expected distributions in the case of nTGCs, with parameters set close to previously obtained experimental limits.

Tables 9.3 and 9.4 show the observed and expected 95% confidence interval limits obtained using the 7 TeV and the 8 TeV data, respectively. The limit on each coupling assumes that the other couplings are fixed at their Standard Model value of zero. In both datasets, the best fit value for all of the couplings are consistent with zero, and the observed limits are consistent with the expected limits. The expected limits from the 8 TeV data are 2.4-3.0 times more stringent than the expected limits from the 7 TeV data using both the $ZZ \to \ell^-\ell^+\ell^-\ell^+$ and $ZZ \to \ell^-\ell^+\nu\bar{\nu}$ channels, or 3.0-3.6 times more stringent than the expected limits from the 7 TeV data using only the $ZZ \to \ell^-\ell^+\ell^-\ell^+$ channel.

Figure 9.6 shows 'two-dimensional' 95% confidence level limits, allowing two of the couplings to vary simultaneously, derived without using a form-factor. The plots compare the limits set with the 7 TeV data using only the $ZZ \to \ell^-\ell^+\ell^-\ell^+$

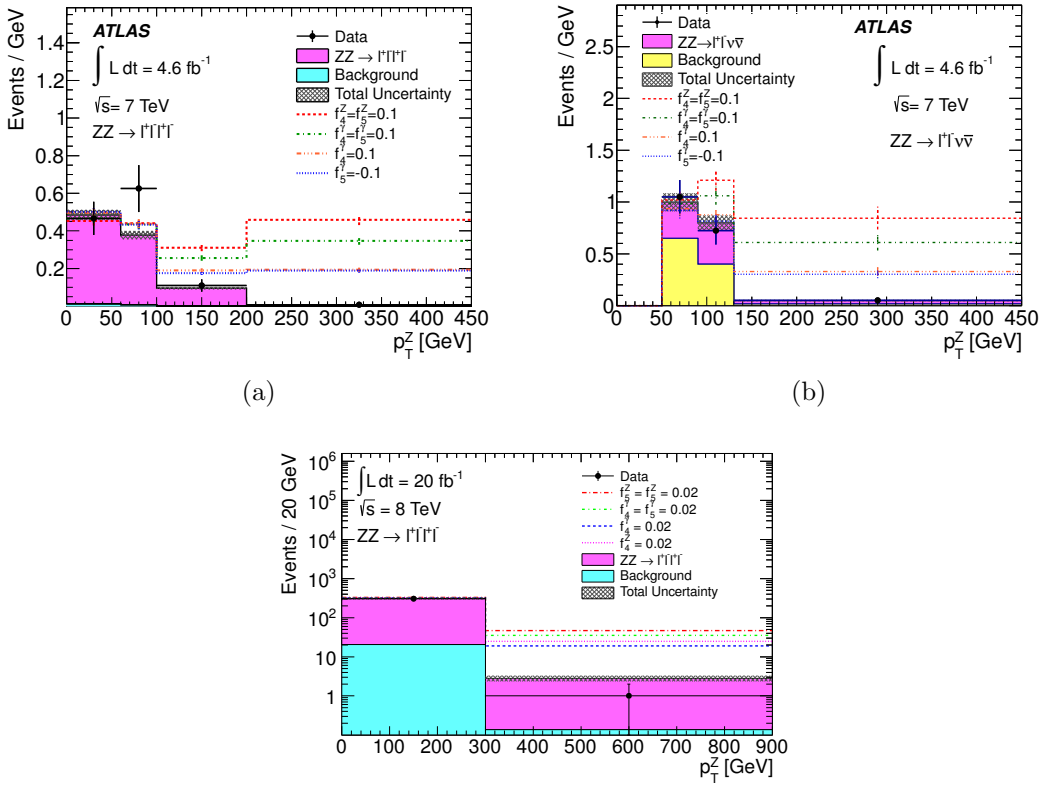

Figure 9.5: Candidate Z boson transverse momentum distributions with the binning used for nTGC limit setting. Figure (a) shows the p_T of the leading Z candidate for the $ZZ \to \ell^-\ell^+\ell^-\ell^+$ channel and (b) shows the p_T of the leptonically decaying Z candidate for the $ZZ \to \ell^-\ell^+\nu\bar{\nu}$ channel, both in the 7 TeV data. Figure (c) shows the p_{T} of the leading Z candidate in candidate $ZZ \to \ell^-\ell^+\ell^-\ell^+$ events in the 8 TeV data. The observed distributions are shown as filled circles, the SM expected signal and background are shown as filled histograms, and the predicted distributions for four different nTGC samples with form factor scales of $\Lambda = 3$ TeV are shown as dashed lines. The nTGC parameters in Figures (a) and (b) are set near the edge of the exclusion set in the 1 fb^{-1} ATLAS analysis [2]; the nTGC parameters in Figure (c) are set near the limits obtained from the 7 TeV analysis. The last bin is inclusive of the overflow.

Parameter	Expected Limit	Observed Limit
$n = 3, \Lambda = 3$ TeV, $ZZ \to \ell^-\ell^+\ell^-\ell^+$		
f_4^γ	[-0.027, 0.027] $\pm$ 0.007	[-0.031, 0.031]
f_4^Z	[-0.023, 0.023] $\pm$ 0.006	[-0.027, 0.027]
f_5^γ	[-0.028, 0.028] $\pm$ 0.007	[-0.032, 0.032]
f_5^Z	[-0.023, 0.023] $\pm$ 0.006	[-0.027, 0.027]
$n = 3, \Lambda = 3$ TeV, $ZZ \to \ell^-\ell^+(\ell^-\ell^+/\nu\bar{\nu})$		
f_4^γ	[-0.021, 0.022] $\pm$ 0.003	[-0.022, 0.023]
f_4^Z	[-0.017, 0.018] $\pm$ 0.003	[-0.019, 0.019]
f_5^γ	[-0.022, 0.022] $\pm$ 0.004	[-0.023, 0.023]
f_5^Z	[-0.018, 0.018] $\pm$ 0.003	[-0.020, 0.019]
No Form Factor, $ZZ \to \ell^-\ell^+\ell^-\ell^+$		
f_4^γ	[-0.017, 0.017] $\pm$ 0.004	[-0.020, 0.020]
f_4^Z	[-0.015, 0.015] $\pm$ 0.002	[-0.017, 0.017]
f_5^γ	[-0.018, 0.018] $\pm$ 0.004	[-0.020, 0.020]
f_5^Z	[-0.015, 0.015] $\pm$ 0.004	[-0.017, 0.017]
No Form Factor, $ZZ \to \ell^-\ell^+(\ell^-\ell^+/\nu\bar{\nu})$		
f_4^γ	[-0.014, 0.014] $\pm$ 0.001	[-0.015, 0.015]
f_4^Z	[-0.012, 0.012] $\pm$ 0.001	[-0.013, 0.013]
f_5^γ	[-0.015, 0.015] $\pm$ 0.001	[-0.016, 0.015]
f_5^Z	[-0.012, 0.012] $\pm$ 0.001	[-0.013, 0.013]

Table 9.3: Expected and observed 95% confidence interval limits for anomalous neutral gauge boson couplings (nTGCs), set using the 7 TeV data, where the limit for each coupling assumes the other couplings fixed at their SM value of zero. Limits are shown obtained using only the $ZZ \to \ell^-\ell^+\ell^-\ell^+$ channel, and using the $ZZ \to \ell^-\ell^+\ell^-\ell^+$ and $ZZ \to \ell^-\ell^+\nu\bar{\nu}$ channels in combination. Limits are given for form-factor scales of $\Lambda = 3$ TeV and $\Lambda = \infty$, the latter corresponding to not applying a form-factor.

channel, the limits set with the 7 TeV combining the $ZZ \to \ell^-\ell^+\ell^-\ell^+$ and $ZZ \to \ell^-\ell^+\nu\bar{\nu}$ channels, and the limits obtained with the 8 TeV data using only the $ZZ \to \ell^-\ell^+\ell^-\ell^+$ channel. For each pair of parameters, the other parameters are assumed to be fixed at their Standard Model value of zero.

A comparison of the one-dimensional limits presented here and those derived from measurements at at other experiments is shown in Figure 9.7. The limits are more stringent than those derived from measurements at LEP [47] and the Tevatron [53]. The ATLAS $\sqrt{s} = 7$ TeV limits are comparable to the limits from CMS [54], derived at the same centre-of-mass energy using a similarly sized dataset. It should be noted that the limits from LEP and CMS do not use a form factor, and those from the Tevatron use $\Lambda = 1.2$ TeV. The 8 TeV limits presented here are significantly tighter than any previous limits.

Parameter	Expected Limit	Observed Limit
$n = 3, \Lambda = 3$ TeV, $ZZ \to \ell^-\ell^+\ell^-\ell^+$		
f_4^γ	[-0.010, 0.010] $\pm$ 0.003	[-0.007, 0.007]
f_4^Z	[-0.008, 0.009] $\pm$ 0.002	[-0.006, 0.006]
f_5^γ	[-0.010, 0.010] $\pm$ 0.003	[-0.007, 0.007]
f_5^Z	[-0.009, 0.009] $\pm$ 0.002	[-0.006, 0.006]
No Form Factor, $ZZ \to \ell^-\ell^+\ell^-\ell^+$		
f_4^γ	[-0.005, 0.005] $\pm$ 0.001	[-0.004, 0.004]
f_4^Z	[-0.005, 0.005] $\pm$ 0.001	[-0.003, 0.003]
f_5^γ	[-0.005, 0.005] $\pm$ 0.001	[-0.004, 0.004]
f_5^Z	[-0.005, 0.005] $\pm$ 0.001	[-0.003, 0.003]

Table 9.4: Expected and observed 95% confidence interval limits for anomalous neutral gauge boson couplings (nTGCs), set using the 8 TeV data, where the limit for each coupling assumes the other couplings fixed at their Standard Model value of zero. Limits are given for form-factor scales of $\Lambda = 3$ TeV and $\Lambda = \infty$, the latter corresponding to not applying a form-factor.

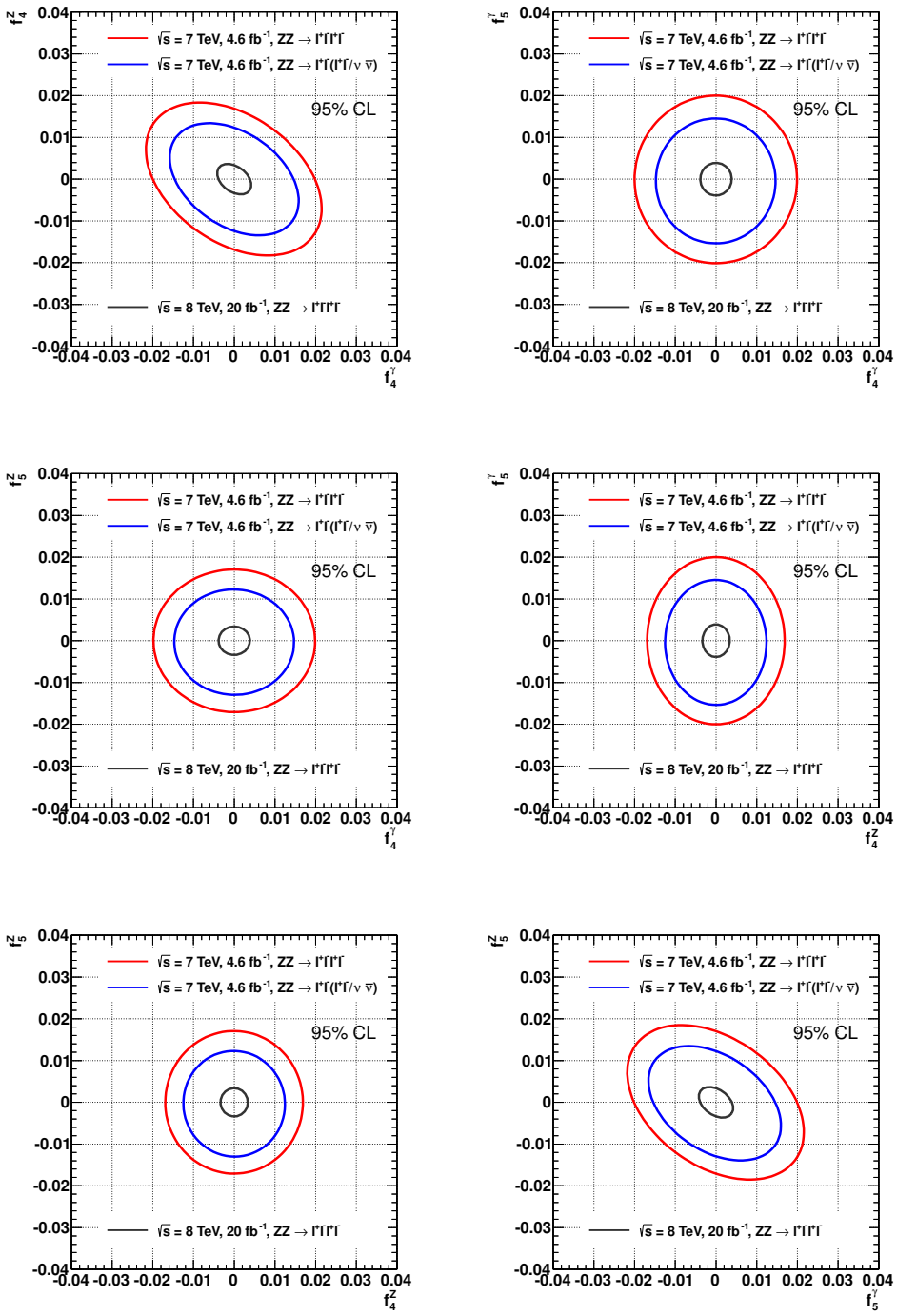

Figure 9.6: Two dimensional 95% confidence intervals for anomalous neutral gauge boson couplings (nTGCs) for form factor scale $\Lambda = \infty$. The limits set using the 7 TeV data using only the $ZZ \to \ell^-\ell^+\ell^-\ell^+$ channel are shown in red, limits set using the 7 TeV data combining the $ZZ \to \ell^-\ell^+\ell^-\ell^+$ and $ZZ \to \ell^-\ell^+\nu\bar{\nu}$ channels are shown in blue, and the limits obtained using the 8 TeV data using only the $ZZ \to \ell^-\ell^+\ell^-\ell^+$ channel are shown in black. For each pair of parameters, the other parameters are assumed to be fixed at their Standard Model value of zero.

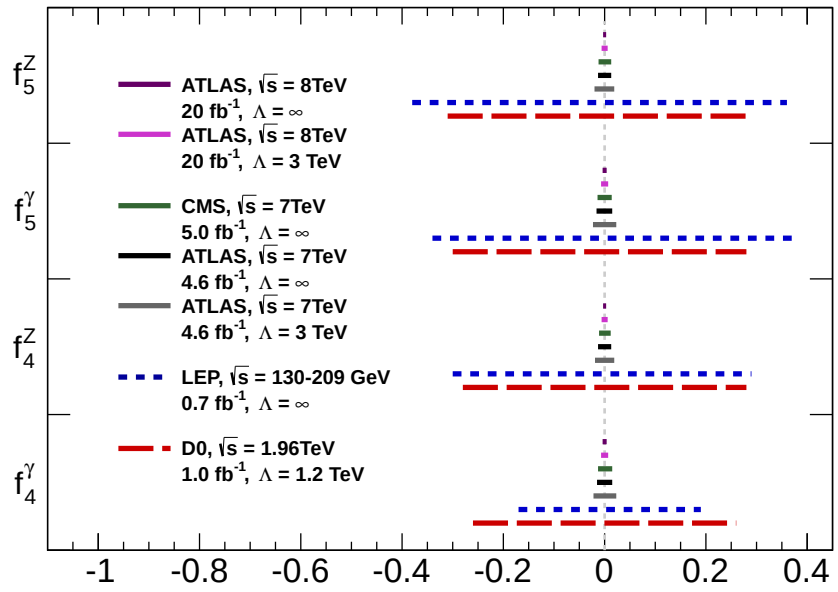

Figure 9.7: Anomalous neutral triple gauge coupling (nTGC) 95% confidence intervals from the ATLAS, CMS [54], LEP [47] and Tevatron [53] experiments. Luminosities, centre-of-mass energies and cut-offs Λ for each experiment are shown.

Chapter 10

Conclusions

Data collected by the ATLAS experiment in 2011 and 2012 were used to make measurements of ZZ production at $\sqrt{s} = 7$ TeV and $\sqrt{s} = 8$ TeV. Events were selected which were consistent with two Z bosons decaying to electrons or muons. The cross section was measured in a fiducial phase-space corresponding closely to the detector acceptance, in order to reduce theoretical uncertainties arising from extrapolating to regions where there is no experimental acceptance. The fiducial phase-space for the $\sqrt{s} = 7$ TeV measurement is defined by requiring both lepton pairs to have $66 < m_{\ell^-\ell^+} < 116$ GeV, and requiring all leptons have $p_{\mathrm{T}} > 7$ GeV, $|\eta| < 3.16$ and be separated from any other lepton with a minimum separation of $\Delta R = 0.2$. The fiducial cross section measured in a dataset corresponding to an integrated luminosity of 4.6 fb^{-1} was found to be:

$$\sigma^{\mathrm{fid}}_{ZZ\to\ell^-\ell^+\ell^-\ell^+}(\sqrt{s} = 7 \ \ \mathrm{TeV}) = 25.2\,^{+3.3}_{-3.0}\,(\mathrm{stat})\,^{+1.2}_{-1.0}\,(\mathrm{syst})\,^{+1.1}_{-0.9}\,(\mathrm{lumi})\ \mathrm{fb} \qquad (10.1)$$

to be compared with a theoretical expectation of:

$$\sigma^{\mathrm{fid,theory}}_{ZZ\to\ell^-\ell^+\ell^-\ell^+}(\sqrt{s} = 7 \ \ \mathrm{TeV}) = 21.2^{+0.9}_{-0.7}\ \mathrm{fb} \qquad (10.2)$$

Additionally, a fiducial cross section relaxing the mass requirement on one of the lepton pairs to $m_{\ell^-\ell^+} > 20$ GeV was measured to be:

$$\sigma^{\mathrm{fid}}_{ZZ^*\to\ell^-\ell^+\ell^-\ell^+}(\sqrt{s} = 7 \ \ \mathrm{TeV}) = 27.8\,^{+3.6}_{-3.4}\,(\mathrm{stat})\,^{+1.8}_{-1.6}\,(\mathrm{syst})\,^{+1.1}_{-1.0}\,(\mathrm{lumi})\ \mathrm{fb} \qquad (10.3)$$

to be compared with a theoretical expectation of:

$$\sigma^{\mathrm{fid}}_{ZZ^*\to\ell^-\ell^+\ell^-\ell^+}(\sqrt{s} = 7 \ \ \mathrm{TeV}) = 25.1^{+1.2}_{-0.8}\ \mathrm{fb} \qquad (10.4)$$

At $\sqrt{s} = 8$ TeV, the fiducial phase-space is defined similarly as for the 7 TeV

measurement, but with the lepton pseudo-rapidity requirement tightened to $|\eta| < 2.7$. The fiducial cross section measured in a dataset corresponding to an integrated luminosity of 20 fb^{-1} was:

$$\sigma^{\text{fid}}_{ZZ\to\ell^-\ell^+\ell^-\ell^+}(\sqrt{s} = 8 \text{ TeV}) = 20.8\,^{+1.3}_{-1.2}\,(\text{stat})\,^{+1.0}_{-0.9}\,(\text{syst})\,^{+0.6}_{-0.6}\,(\text{lumi})\text{ fb} \quad (10.5)$$

to be compared with a theoretical expectation of:

$$\sigma^{\text{fid,theory}}_{ZZ\to\ell^-\ell^+\ell^-\ell^+}(\sqrt{s} = 8 \text{ TeV}) = 21.1^{+0.9}_{-0.8}\text{ fb} \quad (10.6)$$

The uncertainties on the measurements at both energies are statistically dominated. The dominant systematic uncertainties arise due to uncertainties on the lepton reconstruction and identification efficiencies.

The fiducial cross sections were extrapolated to the total cross section for ZZ production with Z bosons in the mass range 66 GeV to 116 GeV, correcting for the acceptance of the fiducial phase-space and the $Z \to \ell\ell$ branching fractions. The total cross section at $\sqrt{s} = 7$ TeV was measured to be:

$$\sigma^{\text{tot}}_{ZZ}(\sqrt{s} = 7 \text{ TeV}) = 7.0\,^{+0.9}_{-0.8}\,(\text{stat})\,^{+0.4}_{-0.3}\,(\text{syst})\,^{+0.3}_{-0.2}\,(\text{lumi})\text{ pb} \quad (10.7)$$

to be compared with a theoretical expectation of:

$$\sigma^{\text{tot,theory}}_{ZZ}(\sqrt{s} = 7 \text{ TeV}) = 5.9^{+0.2}_{-0.2}\text{ pb} \quad (10.8)$$

At $\sqrt{s} = 8$ TeV the total cross section was measured to be:

$$\sigma^{\text{tot}}_{ZZ}(\sqrt{s} = 8 \text{ TeV}) = 7.1\,^{+0.4}_{-0.4}\,(\text{stat})\,^{+0.4}_{-0.3}\,(\text{syst})\,^{+0.2}_{-0.2}\,(\text{lumi})\text{ pb} \quad (10.9)$$

to be compared with a theoretical expectation of:

$$\sigma^{\text{tot,theory}}_{ZZ}(\sqrt{s} = 8 \text{ TeV}) = 7.2^{+0.3}_{-0.2}\text{ pb} \quad (10.10)$$

The theoretical expectations are calculated to next-to-leading order in QCD, and the error arises from uncertainties on the PDF and the factorisation and renormalisation scales. The 7 TeV measurement is slightly higher than the theoretical prediction, but consistent within the uncertainties. The 8 TeV measurement is in good agreement with the theoretical prediction.

The observed $ZZ \to \ell^-\ell^+\ell^-\ell^+$ events were used to set limits on anomalous

neutral triple gauge couplings (nTGCs) by performing binned fits to kinematic distributions. It was found that the differential event yield as a function of the transverse momentum of the leading (in transverse momentum) Z boson provided the greatest sensitivity to nTGCs. The observed data were consistent with the non-existence of ZZZ and $ZZ\gamma$ vertices, as predicted by the Standard Model, and so 95 % confidence level limits were set on the size of the couplings. The couplings are described by four parameters: f_4^γ, f_4^Z, f_5^γ and f_5^Z. The most stringent limits were obtained with the $\sqrt{s} = 8$ TeV data, and were found to be:

$$\begin{aligned} -0.007 < f_4^\gamma < 0.007,\ -0.006 < f_4^Z < 0.006, \\ -0.007 < f_5^\gamma < 0.007,\ -0.006 < f_5^Z < 0.006 \end{aligned} \tag{10.11}$$

where a form-factor with cutoff scale $\Lambda = 3$ TeV and strength $n = 3$ has been assumed. These are the most constraining limits on nTGCs to date.

Bibliography

[1] ATLAS Collaboration, *Measurement of the ZZ production cross section in proton-proton collisions at 7 TeV with the ATLAS detector*, ATLAS-CONF-2011-107, Aug, 2011. http://cds.cern.ch/record/1372920.

[2] ATLAS Collaboration, *Measurement of the ZZ Production Cross Section and Limits on Anomalous Neutral Triple Gauge Couplings in Proton-Proton Collisions at $\sqrt{s} = 7$ TeV with the ATLAS Detector*, Phys. Rev. Lett. **108** (2012) 041804, arXiv:hep-ex/1110.5016.

[3] ATLAS Collaboration, *Measurement of the total ZZ production cross section in the four-lepton channel with 4.7 fb^{-1} of ATLAS data*, ATLAS-CONF-2012-026, Mar, 2012. http://cds.cern.ch/record/1430735.

[4] ATLAS Collaboration, *Measurement of ZZ production in pp collisions at $\sqrt{s} = 7$ TeV and limits on anomalous ZZZ and $ZZ\gamma$ couplings with the ATLAS detector*, JHEP **1303** (2013) 128, arXiv:1211.6096 [hep-ex].

[5] ATLAS Collaboration, *Measurement of the total ZZ production cross section in the four-lepton channel using* 5.8 fb^{-1} *of ATLAS data at $\sqrt{s} = 8$ TeV*, ATLAS-CONF-2012-090 . http://cdsweb.cern.ch/record/1460409.

[6] ATLAS Collaboration, *Measurement of the total ZZ production cross section in proton-proton collisions at $\sqrt{s} = 8$ TeV in 20 fb^{-1} with the ATLAS detector*, ATLAS-CONF-2013-020, Mar, 2013. http://cds.cern.ch/record/1525555.

[7] G. Altarelli, *The Standard model of particle physics*, arXiv:hep-ph/0510281.

[8] W. Cottingham and D. Greenwood, *An Introduction to the Standard Model of Particle Physics*. Cambridge University Press, 2007. http://books.google.co.uk/books?id=Dm36BYq9iu0C.

[9] RAL, *Proceedings of the Summer School for Experimental High Energy Physics Students*. 2009. http://www.stfc.ac.uk/PPD/23413.aspx.

[10] Beringer, J et al. (Particle Data Group), *Review of Particle Physics*, Phys. Rev. D **86** (2012) 010001. http://link.aps.org/doi/10.1103/PhysRevD.86.010001.

[11] S. Weinberg, *A Model of Leptons*, Phys. Rev. Lett. **19** (1967) 1264 – 1266. http://link.aps.org/doi/10.1103/PhysRevLett.19.1264.

[12] A. Salam and J. Ward, *Electromagnetic and weak interactions*, Physics Letters **13** (1964) no. 2, 168 – 171.

[13] CMS Collaboration, *Observation of a new boson at a mass of 125 GeV with the CMS experiment at the LHC*, Phys. Lett. B **716** (2012) 30, arXiv:1207.7235 [hep-ex].

[14] ATLAS Collaboration, *Observation of a new particle in the search for the Standard Model Higgs boson with the ATLAS detector at the LHC*, Phys. Lett. B **716** (2012) 1, arXiv:1207.7214 [hep-ex].

[15] J. M. Campbell, J. Huston, and W. Stirling, *Hard Interactions of Quarks and Gluons: A Primer for LHC Physics*, Rept.Prog.Phys. **70** (2007) 89, arXiv:hep-ph/0611148.

[16] G. Altarelli and G. Parisi, *Asymptotic Freedom in Parton Language*, Nucl.Phys. **B126** (1977) 298.

[17] R. Ellis, W. Stirling, and B. Webber, *QCD and Collider Physics*. Cambridge Monographs on Particle Physics, Nuclear Physics and Cosmology. Cambridge University Press, 2003. http://books.google.co.uk/books?id=TqrPVoS6s0UC.

[18] T. Sjostrand, *Monte Carlo Generators*, arXiv:hep-ph/0611247.

[19] J. M. Campbell, R. K. Ellis, and C. Williams, *Vector boson pair production at the LHC*, JHEP **1107** (2011) 018, arXiv:1105.0020 [hep-ph].

[20] S. Alioli, P. Nason, C. Oleari, and E. Re, *A general framework for implementing NLO calculations in shower Monte Carlo programs: the POWHEG BOX*, JHEP **1006** (2010) 043, arXiv:1002.2581 [hep-ph].

[21] T. Melia, P. Nason, R. Rontsch, and G. Zanderighi, *W^+W^-, WZ and ZZ production in the POWHEG BOX*, JHEP **1111** (2011) 078, arXiv:1107.5051 [hep-ph].

[22] T. Binoth, N. Kauer, and P. Mertsch, *Gluon-induced QCD corrections to $pp \to ZZ \to lll'l'$*, arXiv:0807.0024 [hep-ph].

[23] J. M. Butterworth, J. R. Forshaw, and M. H. Seymour, *Multiparton interactions in photoproduction at HERA*, Z. Phys. C (1996) no. 72, 637, arXiv:9601371 [hep-ph].

[24] T. Binoth, M. Ciccolini, N. Kauer, and M. Kramer, *Gluon-induced W-boson pair production at the LHC*, JHEP **0612** (2006) 046, arXiv:hep-ph/0611170.

[25] T. Gleisberg et al. , *Event generation with SHERPA 1.1*, JHEP **02** (2009) 007, arXiv:0811.4622 [hep-ph].

[26] S. Hoeche, F. Krauss, S. Schumann, and F. Siegert, *QCD matrix elements and truncated showers*, JHEP **0905** (2009) 053, arXiv:0903.1219 [hep-ph].

[27] T. Sjostrand et al., *High-energy physics event generation with PYTHIA 6.1*, Comput. Phys. Commun. **135** (2001) 238–259, arXiv:hep-ph/0010017.

[28] T. Sjostrand, S. Mrenna, and P. Z. Skands, *A Brief Introduction to PYTHIA 8.1*, Comput.Phys.Commun. **178** (2008) 852–867, arXiv:0710.3820 [hep-ph].

[29] G. Corcella et al., *HERWIG 6.5*, JHEP **0101** (2001) 010, arXiv:hep-ph/0011363.

[30] M. Bahr, S. Gieseke, M. Gigg, et al., *Herwig++ Physics and Manual*, Eur.Phys.J. **C58** (2008) 639–707, arXiv:0803.0883 [hep-ph].

[31] S. Frixione and B. R. Webber, *Matching NLO QCD computations and parton shower simulations*, JHEP **0206** (2002) 029, arXiv:hep-ph/0204244.

[32] L. M. Mangano et al., *ALPGEN, a generator for hard multiparton processes in hadronic collisions*, JHEP **0307** (2003) , arXiv:hep-ph/0206293.

[33] M. L. Mangano, M. Moretti, and R. Pittau, *Multijet matrix elements and shower evolution in hadronic collisions: Wbb+n-jets as a case study*, Nuclear Physics B **632** (2002) no. 13, 343 – 362.

[34] G. J. Gounaris, J. Layssac, and F. M. Renard, *Off-shell structure of the anomalous Z and γ self-couplings*, Phys. Rev. **D62** (2000) 073012, arXiv:hep-ph/0005269.

[35] H.-L. Lai, M. Guzzi, J. Huston, et al., *New parton distributions for collider physics*, Phys.Rev. **D82** (2010) 074024, arXiv:1007.2241 [hep-ph].

[36] A. D. Martin, W. J. Stirling, R. S. Thorne, and G. Watt, *Parton distributions for the LHC*, Eur. Phys. J. **C63** (2009) 189, arXiv:hep-ph/0901.0002.

[37] P. Golonka and Z. Was, *PHOTOS Monte Carlo: A Precision tool for QED corrections in Z and W decays*, Eur.Phys.J. **C45** (2006) 97–107, arXiv:hep-ph/0506026 [hep-ph].

[38] F. Siegert, *Private communication*, .

[39] G. Gounaris, J. Layssac, and F. Renard, *Signatures of the anomalous Z_γ and ZZ production at the lepton and hadron colliders*, Phys.Rev. **D61** (2000) 073013, arXiv:hep-ph/9910395.

[40] U. Baur and D. L. Rainwater, *Probing neutral gauge boson self interactions in ZZ production at hadron colliders*, Phys.Rev. **D62** (2000) 113011, arXiv:hep-ph/0008063.

[41] G. Gounaris, J. Layssac, and F. Renard, *New and standard physics contributions to anomalous Z and gamma self couplings*, Phys.Rev. **D62** (2000) 073013, arXiv:hep-ph/0003143.

[42] The L3 Collaboration, *Study of neutral-current four-fermion and ZZ production in e+e collisions at s= 183 GeV*, Physics Letters B **450** (1999) no. 13, 281 – 293.

[43] The OPAL Collaboration, *Study of Z pair production and anomalous couplings in e^+e^- collisions at $\sqrt{s}$ between 190 GeV and 209 GeV*, Eur. Phys. J. **C32** (2003) 303, arXiv:hep-ex/0310013.

[44] The DELPHI Collaboration, *ZZproduction in e^+e^-interactions at $\sqrt{s}$ = 183 GeV to 209 GeV*, Eur. Phys. J. **C30** (2003) 447, arXiv:hep-ex/0307050.

[45] The L3 Collaboration, *Study of Z Boson Pair Production in e^+e^- collisions at LEP at $\sqrt{s}$ = 189 GeV*, Phys. Lett. **B465** (1999) 363, arXiv:hep-ex/9909043.

[46] The ALEPH Collaboration, *Measurement of Z-pair production in e + e collisions and constraints on anomalous neutral gauge couplings*, Journal of High Energy Physics **2009** (2009) no. 04, 124. http://stacks.iop.org/1126-6708/2009/i=04/a=124.

[47] The LEP Collaborations ALEPH, DELPHI, L3, OPAL, and the LEP Electroweak Working Group, *A Combination of preliminary electroweak measurements and constraints on the Standard Model*, arXiv:hep-ex/0612034.

[48] The DELPHI Collaboration, *Study of Trilinear Gauge Boson Couplings, ZZZ, ZZv and Zvv.*, DELPHI-2001-097-CONF-525, Jul, 2001. http://cds.cern.ch/record/1002930.

[49] The OPAL Collaboration, *Z boson pair production in e+ e- collisions at $\sqrt{(s)}$ = 183-GeV and 189-GeV*, Phys.Lett. **B476** (2000) 256–272, arXiv:hep-ex/0003016.

[50] D0 Collaboration, *Measurement of the ZZ production cross section in $p\bar{p}$ collisions at $\sqrt{s}$ = 1.96 TeV*, Phys.Rev. **D84** (2011) 011103, arXiv:1104.3078 [hep-ex].

[51] D0 Collaboration, *A measurement of the WZ and ZZ production cross sections using leptonic final states in 8.6 fb^{-1} of $p\bar{p}$ collisions*, Phys.Rev. **D85** (2012) 112005, arXiv:1201.5652 [hep-ex].

[52] CDF Collaboration, *Measurement of ZZ production in leptonic final states at $\sqrt{s}$ of 1.96 TeV at CDF*, Phys.Rev.Lett. **108** (2012) 101801, arXiv:1112.2978 [hep-ex].

[53] D0 Collaboration, *Search for ZZ and $Z\gamma^*$ production in $p\bar{p}$ collisions at $\sqrt{s} = 1.96$ TeV and limits on anomalous ZZZ and $ZZ\gamma^*$ couplings*, Phys.Rev.Lett. **100** (2008) 131801, arXiv:0712.0599 [hep-ex].

[54] CMS Collaboration, *Measurement of the ZZ production cross section and search for anomalous couplings in $2\ell 2\ell'$ final states in pp collisions at $\sqrt{s} = 7$ TeV*, JHEP **1301** (2013) 063, arXiv:1211.4890 [hep-ex].

[55] CMS Collaboration, *Measurement of W^+W^- and ZZ production cross sections in pp collisions at $\sqrt{s} = 8$ TeV*, arXiv:1301.4698 [hep-ex].

[56] L. Evans and P. Bryant, *LHC Machine*, Journal of Instrumentation **3** (2008) no. 08, S08001. http://stacks.iop.org/1748-0221/3/i=08/a=S08001.

[57] O. S. Brning, P. Collier, P. Lebrun, et al., *LHC Design Report*, CERN-2004-003, 2004. https://cdsweb.cern.ch/record/782076.

[58] The TOTEM Collaboration, G. Antchev, P. Aspell, I. Atanassov, et al., *First measurement of the total proton-proton cross-section at the LHC energy of 7 TeV*, EPL (Europhysics Letters) **96** (2011) no. 2, 21002. http://stacks.iop.org/0295-5075/96/i=2/a=21002.

[59] *ATLAS Luminosity Public Results*, https://twiki.cern.ch/twiki/bin/view/AtlasPublic/LuminosityPublicResults.

[60] *LHC Performance and Statistics*, https://lhc-statistics.web.cern.ch/LHC-Statistics/.

[61] D. Fournier, *Performance of the LHC, ATLAS and CMS in 2011*, EPJ Web Conf. **28** (2012) 01003, arXiv:1201.4681 [hep-ex].

[62] ATLAS Collaboration, *The ATLAS Experiment at the CERN Large Hadron Collider*, Journal of Instrumentation **3** (2008) no. 08, S08003. http://stacks.iop.org/1748-0221/3/i=08/a=S08003.

[63] J.-L. Caron, *ATLAS detector in A4 format with English captions*, https://cdsweb.cern.ch/record/841458/, Mar, 1998.

[64] ATLAS Collaboration, *Expected performance of the ATLAS experiment: detector, trigger and physics*, CERN-OPEN-2008-020, 2009. https://cdsweb.cern.ch/record/1125884.

[65] B. A. Petersen, *The ATLAS Trigger Performance and Evolution*, ATL-COM-DAQ-2012-206, Nov, 2012. https://cdsweb.cern.ch/record/1459646.

[66] S. Agostinelli, J. Allison, K. Amako, et al., *Geant4 - a simulation toolkit*, Nuclear Instruments and Methods in Physics Research Section A: Accelerators, Spectrometers, Detectors and Associated Equipment **506** (2003) no. 3, 250 – 303.

[67] ATLAS Collaboration, *Luminosity Determination in pp Collisions at sqrt(s) = 7 TeV using the ATLAS Detector in 2011*, ATLAS-CONF-2011-116, Aug, 2011. https://cdsweb.cern.ch/record/1376384.

[68] ATLAS Collaboration, *Luminosity Determination in pp Collisions at $\sqrt{s} = 7$ TeV Using the ATLAS Detector at the LHC*, Eur.Phys.J. **C71** (2011) 1630, arXiv:1101.2185 [hep-ex].

[69] M. Villa, *The Luminosity Monitor of the ATLAS Experiment*, ATL-LUM-PROC-2009-004, Nov, 2009. https://cds.cern.ch/record/1222513/.

[70] V. Cindro, D. Dobos, I. Dolenc, et al., *The ATLAS Beam Conditions Monitor*, Journal of Instrumentation **3** (2008) no. 02, P02004. http://stacks.iop.org/1748-0221/3/i=02/a=P02004.

[71] D. Belohrad, J.-J. Gras, L. K. Jensen, et al., *Commissioning and First Performance of the LHC Beam Current Measurement Systems*, http://accelconf.web.cern.ch/AccelConf/IPAC10/papers/mope059.pdf.

[72] A. Ahmad, Z. Albrechtskirchinger, P. Allport, et al., *The silicon microstrip sensors of the ATLAS semiconductor tracker*, Nuclear Instruments and Methods in Physics Research Section A: Accelerators, Spectrometers, Detectors and Associated Equipment **578** (2007) no. 1, 98 – 118.

[73] G. Lindstrm, M. Ahmed, S. Albergo, et al., *Radiation hard silicon detectors - developments by the RD48 (ROSE) collaboration*, Nuclear Instruments and Methods in Physics Research Section A: Accelerators, Spectrometers, Detectors and Associated Equipment **466** (2001) no. 2, 308 – 326. 4th Int. Symp. on Development and Application of Semiconductor Tracking Detectors.

[74] D. Attree, B. Anderson, E. C. Anderssen, et al., *The evaporative cooling system for the ATLAS inner detector*, Journal of Instrumentation **3** (2008) no. 07, P07003. http://stacks.iop.org/1748-0221/3/i=07/a=P07003.

[75] G. Viehhauser, B. Mikulec, A. Sfyrla, and A. Robichaud-Veronneau, *Temperature behaviour and uniformity of SCT barrels during assembly and reception testing*, ATL-INDET-PUB-2006-009.

[76] A. B. Poy, H. Boterenbrood, H. J. Burckhart, et al., *The detector control system of the ATLAS experiment*, Journal of Instrumentation **3** (2008) P05006. http://stacks.iop.org/1748-0221/3/i=05/a=P05006.

[77] K. Shaw and S. D'Auria, *SCT Cooling and Environment 2008 Performance: SCT Cooling and Environment 2008 Performance*, ATL-COM-INDET-2009-094, Dec, 2009. https://cdsweb.cern.ch/record/1229428.

[78] ATLAS Collaboration, *ATLAS Photo Gallery*, http://www.atlas.ch/photos/index.html.

[79] T. Cornelissen, M. Elsing, I. Gavrilenko, et al., *The new ATLAS track reconstruction (NEWT)*, Journal of Physics: Conference Series **119** (2008) no. 3, 032014. http://stacks.iop.org/1742-6596/119/i=3/a=032014.

[80] R. Frühwirth, *Application of Kalman filtering to track and vertex fitting*, Nucl.Instrum.Meth. **A262** (1987) 444–450.

[81] T. G. Cornelissen, M. Elsing, I. Gavrilenko, et al., *The global χ^2 track fitter in ATLAS*, Journal of Physics: Conference Series **119** (2008) no. 3, 032013. http://stacks.iop.org/1742-6596/119/i=3/a=032013.

[82] J. T. M. Baines, R. Bock, C. Hinkelbein, et al., *Pattern Recognition in the TRT for the ATLAS B-Physics Trigger*, ATL-DAQ-99-007, Jul, 1999. https://cdsweb.cern.ch/record/683897.

[83] G. Piacquadio, K. Prokofiev, and A. Wildauer, *Primary vertex reconstruction in the ATLAS experiment at LHC*, Journal of Physics: Conference Series **119** (2008) no. 3, 032033. http://stacks.iop.org/1742-6596/119/i=3/a=032033.

[84] W. Waltenberger, R. Frḧwirth, and P. Vanlaer, *Adaptive vertex fitting*, Journal of Physics G: Nuclear and Particle Physics **34** (2007) no. 12, N343. http://stacks.iop.org/0954-3899/34/i=12/a=N01.

[85] F. Monticelli, J. M. Lorenz, A. Tricoli, and T. Kohno, *Performance of the Electron and Photon Trigger in p-p Collisions at sqrts = 7 TeV with the ATLAS Detector at the LHC in 2011*, ATL-DAQ-INT-2012-001, May, 2012. https://cdsweb.cern.ch/record/1450947.

[86] ATLAS Collaboration, *Expected electron performance in the ATLAS experiment*, ATL-PHYS-PUB-2011-006, Apr, 2011. https://cdsweb.cern.ch/record/1345327.

[87] ATLAS Collaboration, *Electron performance measurements with the ATLAS detector using the 2010 LHC proton-proton collision data*, Eur.Phys.J. **C72** (2012) 1909, arXiv:1110.3174 [hep-ex].

[88] W. Lampl, S. Laplace, D. Lelas, et al., *Calorimeter Clustering Algorithms: Description and Performance*, ATL-LARG-PUB-2008-002, ATL-COM-LARG-2008-003, Apr, 2008. https://cdsweb.cern.ch/record/1099735.

[89] ATLAS Collaboration, *Improved electron reconstruction in ATLAS using the Gaussian Sum Filter-based model for bremsstrahlung*, ATLAS-CONF-2012-047, May, 2012. https://cdsweb.cern.ch/record/1449796.

[90] R. Frühwirth, *A Gaussian-mixture approximation of the BetheHeitler model ofelectron energy loss by bremsstrahlung*, Computer Physics Communications **154** (2003) no. 2, 131 – 142.

[91] T. M. Atkinson, *Electron reconstruction with the ATLAS inner detector. oai:cds.cern.ch:1448253.* PhD thesis, Melbourne U., 2006. https://cdsweb.cern.ch/record/1448253. Presented 2006.

[92] ATLAS Collaboration, *Search for the Standard Model Higgs boson in the decay channel $H \to ZZ^{(*)} \to 4\ell$ with 5.8 fb^{-1} of pp collision data at $\sqrt{s} = 8$ TeV with ATLAS*, ATL-COM-PHYS-2012-835, Jun, 2012. https://cdsweb.cern.ch/record/1456228.

[93] ATLAS Collaboration, *Electron efficiency measurements in early 2012 data*, https://atlas.web.cern.ch/Atlas/GROUPS/PHYSICS/EGAMMA/PublicPlots/20120611/ElectronEfficiency2012/ATL-COM-PHYS-2011-783/index.html.

[94] ATLAS Collaboration, *Electron energy response stability with time and pile-up*, https://atlas.web.cern.ch/Atlas/GROUPS/PHYSICS/EGAMMA/PublicPlots/20121403/StabilityPlots/ATL-COM-PHYS-2012-259/index.html.

[95] ATLAS Collaboration, *Electron energy response stability with time in 2012 data with 13fb^{-1}*, https://atlas.web.cern.ch/Atlas/GROUPS/PHYSICS/EGAMMA/PublicPlots/20121106/ATL-COM-PHYS-2012-1593/index.html.

[96] ATLAS Collaboration, *Electron energy response stability with pile-up in 2012 data*, https://atlas.web.cern.ch/Atlas/GROUPS/PHYSICS/EGAMMA/PublicPlots/20120611/StabilityPlots/ATL-COM-PHYS-2012-782/index.html.

[97] ATLAS Collaboration, *Calibrated $Z \to ee$ mass with 2011 data*, https://atlas.web.cern.ch/Atlas/GROUPS/PHYSICS/EGAMMA/PublicPlots/20110512/CalibratedZee/ATL-COM-PHYS-2011-1637/index.html.

[98] ATLAS Collaboration, *Electron identification efficiency dependence on pileup*, https://atlas.web.cern.ch/Atlas/GROUPS/PHYSICS/EGAMMA/PublicPlots/20121403/EfficiencyPileup/ATL-COM-PHYS-2012-260/index.html.

[99] ATLAS Collaboration, *Identification efficiency measurement for electrons with transverse energy between 7 and 50 GeV*, https://atlas.web.cern.ch/Atlas/GROUPS/PHYSICS/EGAMMA/PublicPlots/20111412/EfficiencyVsET/ATL-COM-PHYS-2011-1669/index.html.

[100] ATLAS Collaboration, *Performance of the ATLAS Trigger System in 2010*, Eur.Phys.J. **C72** (2012) 1849, arXiv:1110.1530 [hep-ex].

[101] ATLAS Collaboration, *Muon Reconstruction Performance*, ATLAS-CONF-2010-064, Jul, 2010. http://cdsweb.cern.ch/record/1281339.

[102] ATLAS Collaboration, *Muon reconstruction efficiency in reprocessed 2010 LHC proton-proton collision data recorded with the ATLAS detector*, ATLAS-CONF-2011-063, Apr, 2011. http://cdsweb.cern.ch/record/1345743.

[103] R. Nicolaidou, L. Chevalier, S. Hassani, et al., *Muon identification procedure for the ATLAS detector at the LHC using Muonboy reconstruction package and tests of its performance using cosmic rays and single beam data*, Journal of Physics: Conference Series **219** (2010) no. 3, 032052. http://stacks.iop.org/1742-6596/219/i=3/a=032052.

[104] ATLAS Collaboration, *Pile-up Depedence of the ATLAS Muon Performance*, https://twiki.cern.ch/twiki/bin/view/AtlasPublic/MuonPerformancePublicPlots.

[105] ATLAS Collaboration, *Plots of Muon Performance in 2012 Data*, https://atlas.web.cern.ch/Atlas/GROUPS/PHYSICS/MUON/PublicPlots/2012/June/index.html.

[106] M. Cacciari, G. P. Salam, and G. Soyez, *The anti- k t jet clustering algorithm*, Journal of High Energy Physics **2008** (2008) no. 04, 063. http://stacks.iop.org/1126-6708/2008/i=04/a=063.

[107] C. Doglioni, *Measurement of the inclusive jet cross section with the ATLAS detector at the Large Hadron Collider*. PhD thesis, Oxford U., 2011. http://cdsweb.cern.ch/record/1404256.

[108] ATLAS Collaboration, *Probing the measurement of jet energies with the ATLAS detector using Z+jet events from proton-proton collisions at sqrt(s) = 7 TeV*, ATLAS-CONF-2012-053, May, 2012. https://cdsweb.cern.ch/record/1452641.

[109] ATLAS Collaboration, *Probing the measurement of jet energies with the ATLAS detector using photon+jet events in proton-proton collisions at sqrts = 7 TeV*, ATLAS-CONF-2012-063, Jul, 2012. https://cdsweb.cern.ch/record/1459528.

[110] R. Gavin, Y. Li, F. Petriello, and S. Quackenbush, *FEWZ 2.0: A code for hadronic Z production at next-to-next-to-leading order*, Comput.Phys.Commun. **182** (2011) 2388–2403, arXiv:1011.3540 [hep-ph].

[111] M. Aliev, H. Lacker, U. Langenfeld, et al., *HATHOR: HAdronic Top and Heavy quarks crOss section calculatoR*, Comput.Phys.Commun. **182** (2011) 1034–1046, arXiv:1007.1327 [hep-ph].

[112] G. D'Agostini, *Improved iterative Bayesian unfolding*, arXiv:1010.0632 [physics.data-an].

[113] T. Adye, *Unfolding algorithms and tests using RooUnfold*, arXiv:1105.1160 [physics.data-an].

[114] U. Baur, T. Han, and J. Ohnemus, *QCD corrections and anomalous couplings in $Z\gamma$ production at hadron colliders*, Phys.Rev. **D57** (1998) 2823–2836, arXiv:hep-ph/9710416.

[115] G. Bella, *Weighting Di-Boson Monte Carlo Events in Hadron Colliders*, arXiv:0803.3307 [hep-ph].

[116] G. Cowan, K. Cranmer, E. Gross, and O. Vitells, *Asymptotic formulae for likelihood-based tests of new physics*, Eur.Phys.J. **C71** (2011) 1554, arXiv:1007.1727 [physics.data-an].

Appendix A

Additional Material for nTGC Limits

A.1 Robustness of nTGC Limits

In order to check the robustness of the limits, the expected limits obtained using the Baur-Rainwater generator to determine the yield coefficients are compared with the expected limits obtained using BHO to determine to coefficients. Similarly, the expected limits obtained using a samples samples generated at different TGC points are compared (e.g. the TGC0 sample is compared to the TGC1 sample). The resulting expected limits are given in Table A.1; the changes in expected limits are much smaller than the statistical uncertainties on the limit.

No. Bins	Generator	Sample	f_4^γ	f_4^Z	f_5^γ	f_5^γ
$n = 3, \Lambda = 3$ TeV						
1	BR	TGC0	[-0.0321 , 0.0320] ± 0.0048	[-0.0270 , 0.0271] ± 0.0040	[-0.0328 , 0.0326] ± 0.0048	[-0.0276 , 0.0277] ± 0.0041
1	BHO	TGC0	[-0.0321 , 0.0320] ± 0.0048	[-0.0271 , 0.0271] ± 0.0040	[-0.0327 , 0.0327] ± 0.0048	[-0.0276 , 0.0276] ± 0.0041
1	BR	TGC1	[-0.0323 , 0.0323] ± 0.0048	[-0.0272 , 0.0272] ± 0.0040	[-0.0329 , 0.0331] ± 0.0049	[-0.0274 , 0.0282] ± 0.0041
1	BR	TGC2	[-0.0320 , 0.0321] ± 0.0047	[-0.0269 , 0.0271] ± 0.0040	[-0.0327 , 0.0327] ± 0.0048	[-0.0272 , 0.0278] ± 0.0041
2	BR	TGC0	[-0.0100 , 0.0100] ± 0.0026	[-0.0086 , 0.0085] ± 0.0023	[-0.0101 , 0.0101] ± 0.0027	[-0.0086 , 0.0086] ± 0.0023
2	BHO	TGC0	[-0.0101 , 0.0100] ± 0.0027	[-0.0086 , 0.0086] ± 0.0023	[-0.0101 , 0.0101] ± 0.0027	[-0.0087 , 0.0087] ± 0.0023
2	BR	TGC1	[-0.0103 , 0.0102] ± 0.0027	[-0.0088 , 0.0088] ± 0.0023	[-0.0104 , 0.0103] ± 0.0027	[-0.0088 , 0.0088] ± 0.0024
2	BR	TGC2	[-0.0103 , 0.0102] ± 0.0027	[-0.0088 , 0.0087] ± 0.0023	[-0.0104 , 0.0103] ± 0.0027	[-0.0088 , 0.0088] ± 0.0023
No Form Factor						
1	BR	TGC0	[-0.0189 , 0.0189] ± 0.0028	[-0.0163 , 0.0164] ± 0.0024	[-0.0192 , 0.0191] ± 0.0028	[-0.0165 , 0.0165] ± 0.0025
1	BHO	TGC0	[-0.0190 , 0.0189] ± 0.0028	[-0.0163 , 0.0163] ± 0.0024	[-0.0192 , 0.0192] ± 0.0028	[-0.0165 , 0.0165] ± 0.0025
1	BR	TGC1	[-0.0190 , 0.0190] ± 0.0028	[-0.0164 , 0.0164] ± 0.0024	[-0.0192 , 0.0193] ± 0.0029	[-0.0164 , 0.0167] ± 0.0025
1	BR	TGC2	[-0.0190 , 0.0190] ± 0.0028	[-0.0162 , 0.0164] ± 0.0024	[-0.0192 , 0.0192] ± 0.0028	[-0.0164 , 0.0166] ± 0.0024
2	BHO	TGC0	[-0.0055 , 0.0054] ± 0.0014	[-0.0047 , 0.0047] ± 0.0013	[-0.0055 , 0.0055] ± 0.0014	[-0.0048 , 0.0048] ± 0.0013
2	BR	TGC0	[-0.0054 , 0.0054] ± 0.0014	[-0.0047 , 0.0047] ± 0.0012	[-0.0055 , 0.0054] ± 0.0014	[-0.0047 , 0.0047] ± 0.0013
2	BR	TGC1	[-0.0055 , 0.0055] ± 0.0015	[-0.0048 , 0.0048] ± 0.0013	[-0.0056 , 0.0055] ± 0.0015	[-0.0048 , 0.0048] ± 0.0013
2	BR	TGC2	[-0.0056 , 0.0055] ± 0.0015	[-0.0048 , 0.0048] ± 0.0013	[-0.0056 , 0.0056] ± 0.0015	[-0.0048 , 0.0048] ± 0.0013

Table A.1: Expected 95% confidence intervals for anomalous neutral gauge boson couplings (nTGCs) for the 8 TeV analysis, where the limit for each coupling assumes the other couplings fixed at their SM value of zero. Limits are given for form-factor scales of $\Lambda = 3$ TeV and $\Lambda = \infty$, the latter corresponding to not applying a form-factor. The limits obtained using yield coefficients derived using the Baur-Rainwater (BR) and BHO (BHO) generators are occured, as are limits obtained using samples generated at different TGC points (TGC0 - TGC1; see Section 9.1.1 for defintiion of the points).